Studies of the mechanical dissipation of thin films for mirrors in interferometric gravitational wave detectors

Kieran Craig

School of Physics and Astronomy,

University of Glasgow

Presented as a thesis for the degree of Ph.D
in the University of Glasgow, University Avenue,
Glasgow G12 8QQ.

July 2015

Table of contents

List of figures

List of tables

Acknowledgements

I would like to thank my supervisor, Professor Sheila Rowan, for her help and advice throughout my PhD. My second supervisor, Dr Iain Martin, has been a pleasure to work with, providing guidance, support and an insight into the side of academia that you can't learn in a lab. I am extremely grateful to have worked at the Institute for Gravitational Research (IGR), which has provided me the opportunity to travel to meetings and labs all around the world and to meet even more fantastic people. The work presented in this thesis was carried out under a scholarship from the Science and Technology Facilities Council (STFC), to whom I am grateful.

I would like to thank many of the members of the IGR. Major thanks go to Alan Cumming and Liam Cunningham for help along the way, showing me how to use many pieces of equipment and for many conversations completely unrelated to physics. I would like to thank all my office mates, Matt Abernathy, Paul Campsie, Chris Bell, Peter Murray, Keith Evans, Rahul Kumar, Martin Hart, Sean Leavey, Richard Middlemiss, Valentina Mangano, Hafizah Isa, Raymond Robie and Mark Fletcher for all of the thought-provoking physics discussions, distracting conversations and hilarious pranks. Thanks also to Stevie Craig for the endless football-related optimism.

For hospitality during my stay in Jena, I would like to thank everyone at the Solid State Physics Institute at Jena University, in particular Ronny Nawrodt for many inspiring conversations. For my time in Tokyo, I would like to thank Eiichi Hirose for showing me many restaurants, izakayas, ramen shops in the area and some of the finer sites of Kanagawa prefecture. Thanks also to Kazuhiro Yamamoto, Seiji Kawamura and Alexander Khalaidovski for their hospitality during my stays in Japan.

I want to thank the people outside of the lab who kept me sane throughout my time. Thank you to my mother, Frances Craig, my sister Michelle and

my brother Gavin. A big thanks to my friends and pub quiz team mates Steven Gladman, Gordon Sommerville, Steven Gordon and Fraser Anderson. In particular, thanks to Gordon for being my cycling companion throughout long, punishing and often swear filled rides as well as for organising weekly games of football, regardless of the antcipated weather or game quality. Thanks to everyone at the Glasgow University Karate Club for all the good times, the blood, sweat and tears, the broken fingers and the partying. I would also like to offer my sincerest thanks to Sarah Eeles for her love and support throughout.

Preface

This thesis is an account of work carried out in the Instiute for Gravitational Research at the University of Glasgow between October 2011 and April 2015, involving studies of the mechanical properties of optical materials for use in future gravitational wave detectors.

Chapter 1 presents an introduction to gravitational waves and the types of astrophysical event which produce gravitational waves. The status of current and future gravitational wave detectors is also discussed.

In Chapter 2, mechanisms of coating thermal noise are discussed. In particular, the relationship between Brownian noise and mechanical dissipation is discussed.

In Chapter 3, coating deposition methods are discussed. The methods used in this thesis to measure coating mechanical loss using a cantilever technique at room temperature and at cryogenic temperatures are described, along with sample preparation. Mechanical loss measurements using disks are described, including the suspension techniques used in this thesis.

In Chapter 4, cryogenic mechanical loss measurements of TiO_2-doped Ta_2O_5 are presented. Mechanical loss measurements of the as-deposited 55% coating were made by Dr. M. Abernathy. Measurements of the 25% as-deposited coating were made by the author, and additional measurements were made by Dr. M. Abernathy. Measurements of the heat-treated 25% and 55% doped coatings were made by the author. All measurements of uncoated control samples within the chapter were carried out by the author. The measurements were taken using data collection software written by Dr. R. Nawrodt. Ringdown times for each measurement were calculated using software written by Dr. M. Abernathy. Data analysis was carried out by the author with guidance from Dr. I. Martin. Calculations of barrier height distributions were carried out by the author using software written by Dr. I. Martin. All measurements of the

ALD tantala coating were made by the author. All measurements within this chapter were made at the suggestion and with guidance from Prof. S. Rowan and Dr. I. Martin.

In Chapter 5, the mechanical loss of several Advanced LIGO coatings are presented. This work was carried out in collaboration with Dr. M. Granata and Dr. G. Cagnoli from the coating vendor LMA, and under the supervision of Dr. I. Martin. Measurements of cantilevers coated with the ETM coating were made by the author. The FEA model used to calculate the relevant energy ratios for the ETM coating was produced by Dr. L. Cunningham. The mechanical loss of an ITM coating is presented. Measurements of this sample were made by the author, with further measurements carried out by Mr. R. Robie and Mr. M. Fletcher. The FEA model used for data analysis of the ITM coating loss was created by the author. The mechanical loss of a silica/tantala multilayer coating, deposited on a sapphire disk is presented in the second half of Chapter 5. Measurements of the uncoated disk were carried out by the author and by Dr. E. Hirose of the ICRR, University of Tokyo. Measurements of the unannealed, coated disk were carried out by the author and by Dr. E. Hirose. Heat-treatment of the coated disk was carried out by Dr. K. Waseda of the National Astronomical Observatory of Japan. Measurements of the coated disk after annealing were carried out by the author and Dr. P. Murray. Disk temperature calibration was carried out by Dr. E. Hirose. Data analysis was carried out by Dr. E. Hirose with input from the author. Calculations of the thermoelastic loss were made by the author with guidance from Dr. K. Yamamoto of the ICRR.

In Chapter 6, the mechanical loss of a silica-doped hafnia coating as a function of heat-treatment is presented. Measurements of the as-deposited, 300 °C, 400 °C and 600 °C heat-treated cantilevers were made by the author. Measurements of the control sample were carried out by the author, and additional measurements of the uncoated control sample were carried out by Dr. K. Haughian. Measurements of the 150 °C heat-treated coating were carried out by Mr. D. Dzhenkov. All data analysis and thermal noise calculations were carried out by the author. All optical absorption measurements were carried out by Dr. J. Steinlechner. Transmission electron microscopy measurements were carried out by Mr. M. Hart with assistance from Dr. I. MacLaren.

All measurements within this chapter were made at the suggestion and with guidance from Prof. S. Rowan and Dr. I. Martin.

In Chapter 7, the mechanical loss measurements of GaP/AlGaP and GaAs/AlGaAs multilayer crystalline coatings are presented. Measurements of the GaP/AlGaP coating were carried out jointly with Dr. A. Cumming. Data analysis was carried out by Dr. A. Cumming. Calculations of thermoelastic loss were carried out by Dr. D. Heinert at the University of Jena. Investigations of the GaAs/AlGaAs coating at cryogenic temperatures were done in collaboration with Dr. A. Cumming. Measurements of the GaAs/AlGaAs coated silica disk at room temperature were carried out by the author, with additional measurements carried out by Mr. R. Robie. The FEA model used for data analysis relating to the GaAs/AlGaAs coating on silica was created by the author. Measurements and data analysis within this chapter were carried out with guidance from Prof. S. Rowan and Dr. I. Martin.

In Appendix A, the mechanical loss of an ALD tantala coating is presented. Measurements of the ALD coating deposited on an unoxidised cantilever were made by the author, with additional measurements made by Mr. R. Robie. All data analysis was carried out by the author.

In Appendix B, the mechanical loss of a Niobia film is presented. Measurements of the disks were carried out in collaboration with Dr. A. Cumming. FEA models relating to the disk measurements were created by Dr. A. Cumming, and FEA models relating to the cantilever measurements were created by the author.

In Appendix C, the mechanical loss of a bonded cantilever is presented. The two cantilevers comprising the sample were bonded by Dr. A. van Veggel and Dr. N. Beveridge. Measurements were carried out under the supervision of Dr. I. Martin.

Summary

Einstein's General Theory of Relativity predicts the existence of gravitational waves, which are fluctuations in the curvature of space-time, which propagate at the speed of light. Gravitational waves arise from the asymmetric acceleration of mass. While these waves have not been directly detected, studies of the inspiral of a binary pulsar system provide strong evidence for their existence. The detection of gravitational waves would enable a new form of astronomical observations which would provide great insight into bodies such as black holes.

In order to detect gravitational waves, a world wide network of first generation interferometric detectors was built. These detector projects aim to measure the fluctuating tidal strains in space produced by gravitational waves using laser interferometry to measure fluctuations in the relative positions of highly reflective mirrors which are separated by kilometre scale distances. The second generation detector era will be formed by the American Advanced LIGO project, the French/Italian Advanced Virgo detector, the German/British GEO 600 detector and the Japanese KAGRA detector project.

The change of interferometer arm length due to a gravitational wave is expected to be very small, at the order of $\sim 10^{-20}$m for a kilometre scale long interferometer arm. This magnitude of displacement is small enough such that the thermal motion of the mirrors and their suspensions is expected to form an important limit to detector sensitivity. The magnitude of thermal noise is related to the mechanical loss of the materials used in the mirror substrates, the suspension elements and the mirror coatings.

The research presented focuses on the charaterisation of the optical mirror coatings, with the aim of reducing the magnitude of thermal noise in future gravitational wave detectors. In Chapter 1, an introduction to gravitational waves is given, along with the sources of gravitational waves. An introduction to interferometric detectors and the techniques commonly employed within

these detectors to improve upon the basic Michelson interferometer is also given in Chapter 1. Chapter 2 discusses coating thermal noise, one of the major limits to detector sensitivity in interferometric gravitational wave detectors. The different types of coating thermal noise are discussed, along with the relationship between coating Brownian noise and the mechanical loss of coating materials.

The mirror coatings used in current gravitational wave detectors are dielectric thin films composed of alternating layers of high and low refractive index materials. The predominant source of coating thermal noise is Brownian noise, which is dependent upon the mechanical loss of the coating materials. In Chapter 3, several methods used to deposit thin films are discussed. A general method of measuring mechanical loss is described, and the application of the technique to cantilever samples and disk samples is detailed. A description of the apparatus used to measure the mechanical loss in each case is given. The methods described in this chapter are used throughout the thesis.

In Chapter 4, the mechanical losses of titania-doped tantala thin films are characterised at low temperature. The doping concentration within the films is varied in order to investigate the effects of doping cation concentration on the mechanical loss. Here, tantala doped with titania to a cation concentration of 25% and 55% is studied. Additionally, different post-deposition heat-treatments are applied to investigate the effect of the types of heat-treatment regime typically used to reduce stress and optical absorption in optical coatings. The temperature dependent mechanical losses of the coatings exhibit relatively broad cryogenic loss peaks. Analysis of these peaks allows insight into the possible dissipation mechanisms in the coatings. The activation energies responsible for the loss peaks of the as-deposited 25% doped, as-deposited 55% doped and 600 °C heat-treated 55% doped coatings were calculated to be (25.3 ± 5.4) meV, (13.6 ± 1.6) meV and (35.8 ± 5) meV respectively. The rate constants calculated for these coatings were $(2.2 \pm 3.8) \times 10^{-8}$ s, $(13.6 \pm 1.6) \times 10^{-7}$ s, and $(35.8 \pm 5) \times 10^{-13}$ s respectively. The width of the loss peaks suggests that there is a broad distribution of barrier heights, which have been calculated and compared to the barrier height distribution previously calculated for pure tantala heat-treated at 600 °C. These comparisons suggest that an increase in doping concentration acts to decrease the number of barriers at each barrier energy. The calculated barrier height distributions will aid computational molecular models of tantala thin

films, and will also aid investigations of the molecular structure of the material. Tantala films deposited by different processes are expected to have radically different molecular structures. As such, the mechanical loss of a tantala film deposited by atomic layer deposition was measured, and a cryogenic loss peak was found. The associated activation energy and rate constant were calculated to be $E_a = (91 \pm 22)\,\text{meV}$ and $(0.02 \pm 1) \times 10^{-11}\,\text{s}$ respectively.

In Chapter 5, the mechanical losses of nominally identical coatings to those for use in Advanced LIGO are studied. The coatings to be used on the end mirrors of Advanced LIGO exhibit a broad low-temperature loss peak at approximately 23-28 K with a peak magnitude of $0.9\text{-}1\times10^{-3}$. The loss exhibited by the coatings at room temperature is found to be 3×10^{-4}. The room temperature mechanical loss of the coatings intended for use on the input mirrors of Advanced LIGO was found to be in the range $1\text{-}1.4\times10^{-4}$. The mechanical loss of this coating is lower than predicted from previous measurements of silica and titania-doped tantala coatings.

The mechanical loss of tantala is known to be significantly higher than that of silica. As such, the mechanical loss of multilayer coating may be improved by finding a lower loss high refractive index coating than tantala. Previous studies found that ion beam sputtered hafnia has a lower mechanical loss at cryogenic temperatures than tantala despite the coatings being partially crystalline, a property which is usually associated with increased loss. Since silica-doping is known to stabilise hafnia against crystallisation, the temperature-dependent mechanical loss of a hafnia film doped with silica to a cation concentration of 30% as a function of post-deposition heat-treatment is presented in Chapter 6. At room temperature, the mechanical loss of the coating is shown to be approximately 1×10^{-3}, which may be reduced to 3×10^{-4} by hear-treating the coating at 600 °C. However, this is a higher loss than current titania-doped tantala films. At cryogenic temperatures, the coating heat-treated at 400 °C is shown to exhibit a lower loss than comparable tantala films. The thermal noise of a silica/silica-doped hafnia coating on a silicon substrate at cryogenic temperatures is calculated to be lower than that of the Advanced LIGO end mirror coating for comparable design parameters. At 20 K, a silica/silica-doped hafnia coating offers a factor of 2.5 improvement in Brownian noise over the Advanced LIGO ETM coating at room temperature, and a factor of 1.14 improvement in Brownian noise over the Advanced LIGO ETM coating at 20 K.

In previous studies, a multilayer coatings composed of GaAs/AlGaAs exhibited a lower mechanical loss than the best silica/tantala coatings. However, these studies used either free-standing structures made from the material, or were based on calculations following thermal noise measurements. Hence, Chapter 7 presents direct room temperature mechanical loss measurements of a GaAs/AlGaAs multilayer coating bonded to a silica disk. The lowest coating loss exhibited in these measurements was $2.0 \pm 0.7 \times -5$, which is consistent with the loss found in previous investigations by other methods. The Brownian thermal noise arising from an AlGaAs coating bonded to a silica substrate would be a factor of 2.9 lower than that of the Advanced LIGO end mirrors operating under similar conditions. Investigations of an AlGaAs coating bonded to a silicon disk found that the coating delaminated after cooling to cryogenic temperatures. The mechanical loss of a crystalline GaP/AlGaP coating grown directly onto a silicon wafer is presented in Chapter 7. The coating loss was measured to be as low as 1.4×10^{-5}. The Brownian thermal noise of such a coating would be a factor of 8-13.3 lower than the Brownian noise arising from the Advanced LIGO coatings at room temperature, and a factor of 3.7-6 lower than the Brownian noise arising from the Advanced LIGO coatings operating at 20 K.

Chapter 1

Gravitational wave detection

1.1 Introduction

Gravitational waves are postulated to exist by Einstein's General Theory of Relativity, which describes gravity as a curvature in space-time in the presence of mass [9]. These waves are predicted to arise from non-axisymmetric acceleration of mass, and propagate at the speed of light as fluctuations in the curvature of space-time. Gravitational waves are quadrupole in nature, distorting space-time in the directions perpendicular to that of propagation.

Due to the weakness of the interaction of gravity with matter, extremely large astrophysical bodies are required to produce detectable gravitational waves [10]. Examples of the types of events which produce gravitational waves include black hole mergers, compact binary systems, pulsars and supernovae. It is also thought that there is a stochastic gravitational wave background analogous to the cosmic microwave background. The gravitational wave background is thought to be made up of a primordial background of cosmological origin and a background of astrophysical origin.

Gravitational waves have not yet been directly detected, though efforts to detect them have been ongoing since the 1960's. The first attempts at directly detecting gravitational waves were made by Joseph Weber at the University of Maryland [11]. Weber used long aluminium bars whose resonant modes may be excited by a passing gravitational wave. However, these resonant bar detectors were limited to a very narrow bandwidth and did not produce results which could be replicated by other bar detectors [12].

Since then, the timing of pulsar systems have provided key evidence for the existence of gravitational radiation. Specifically, studies carried out by Hulse and Taylor on the binary pulsar PSR1913+16 show that the decay rate of the binary orbital period is consistent with the system losing energy at the rate predicted by models for the emission of gravitational radiation [13–17]. While these observations do not confirm the existence of gravitational waves, they do show that the binary pulsar system is losing energy at a rate faster than can be explained by electromagnetic radiation alone. Their observations, made using the Arecibo radio observatory, showed that the orbital phase shift of the system matched that predicted by general relativity to within 1%. This work earned Hulse and Taylor the Nobel Prize in physics in 1993. Since then, great effort has been applied towards the direct detection of gravitational waves in modern broad band interferometric detectors.

A world wide network of interferometric gravitational wave detectors has since been constructed. While these detectors have not detected gravitational waves, their data have been used to place meaningful constraints on the models of gravitational wave producing sources. Many of these detectors are currently undergoing significant upgrades to improve their sensitivity, which should allow a direct detection.

The detection of gravitational waves is one of the foremost challenges of modern physical science, not only to confirm Einstein's theory but also to be able to study the universe in a new way, ushering in a new era of astronomy analogous to the boom seen in moving from the use of optical telescopes to telescopes sensitive to non-visible electromagnetic radiation.

1.2 The nature of gravitational waves

Gravitational radiation is produced by the acceleration of mass similarly to electromagnetic radiation being produced by the acceleration of charge. However, while a dipole moment can exist in electromagnetic radiation as a result of the existence of two charges, the conservation of momentum prevents dipolar gravitational radiation since there is no such thing as negative mass. There are no conservation laws to prevent higher moments of mass distributions from emitting higher numbered polarities, though the conservation of mass precludes odd-numbered polarities. It is expected however, that most gravitational radia-

tion would be emitted as quadrupolar since this is the simplest polarity under these constraints [18].

This quadrupolar nature of gravitational waves implies that they can only be emitted by the asymmetric acceleration of mass, such as in orbiting binary objects or the rotation of non-spherical bodies. The emissions are typically at twice the natural frequency of the generating system.

A gravitational wave travelling perpendicularly to two adjacent, free-falling bodies will change their separation, L, by a distance ΔL, where the amplitude, h, of the wave is

$$h = \frac{2\Delta L}{L}. \tag{1.1}$$

A visualisation of the effect of a gravitational wave passing through a ring of test-masses can be seen in figure 1.1. This figure illustrates the difference between the two polarisations of gravitational waves- the + and × polarisations, which are rotated from each other. As the gravitational wave passes through the test masses, it causes an increase in separation length in one direction, and a decrease in separation length in the perpendicular direction. This shows the quadrupolar nature of gravitational waves.

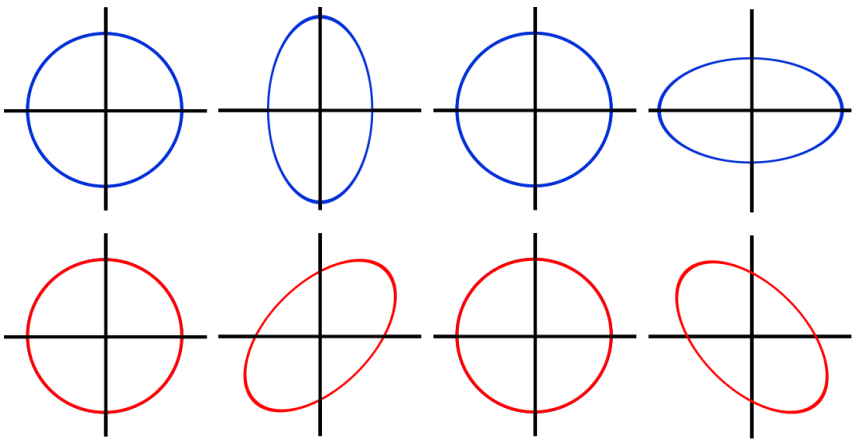

Fig. 1.1 The effect of a gravitational wave passing perpendicularly through a ring of test masses. The two possible polarisations of gravitational wave are represented, h_+ top, and $h_\times$ bottom.

1.3 Sources of gravitational waves

Saulson calculates the gravitational wave strain that would be expected to arise from rotating a simple dumbbell in the lab, demonstrating that the strain amplitude from such masses is extremely small [10]. This means that giant astrophysical bodies are required to produce strain amplitudes which could be considered to be detectable. Here, the three main types of gravitational wave sources will be discussed, with a few examples of each.

1.3.1 Continuous sources

A continuous source is classified as one which emits gravitational waves at a roughly constant amplitude and frequency for at least a few weeks [19]. The most likely sources to lie within the frequency band of ground based detectors are low mass X-ray binary systems and isolated neutron star systems such as pulsars [20]. Binary systems are those in which two stars orbit their centre of mass, with over half of all stars thought to exist within this type of system. The orbital radius of a binary system decays over time as the energy and angular momentum stored within the system is lost through gravitational radiation. The orbital decay of the pulsar PSR 1913+16 was measured to be within 0.2% of the rate expected from the emission of gravitational waves [15], which is good evidence for the emission gravitational radiation.

X-ray binary systems consist of neutron stars accreting mass from a neighbouring star. Gravitational potential energy is released by the accretion as X-rays, and asymmetries in the accretion may emit gravitational waves. The strain amplitude of the gravitational waves emitted by the X-ray binaries should be [21]:

$$h = 8.5 \times 10^{-27} \left(\frac{10\,\mathrm{kpc}}{r}\right) \left(\frac{1\,\mathrm{kHz}}{f}\right)^{\frac{1}{2}} \left(\frac{M}{10^{-8} M_{\odot} \mathrm{yr}^{-1}}\right)^{\frac{1}{2}}, \tag{1.2}$$

where r is the distance from Earth, f is the gravitational wave frequency and M is the accretion rate.

Rapidly spinning neutron stars, may be a source of gravitational waves if they feature a mass asymmetry. This mass asymmetry can form after the violent formation of a neutron star, when the internal modes of the star are excited as it cools, freezing the deformations into the surface, forming a crust

[22, 23]. If a young neutron star has a strong magnetic field which is not aligned with the spin axis, this can result in bulges at the magnetic poles [24]. A neutron star with a mass excess on both sides of the centre of mass will emit gravitational waves at twice the star's rotational frequency [25]. The strain amplitude expected from such a system can be approximated as [26]:

$$h \approx 6 \times 10^{-25} \left(\frac{f_{\mathrm{rot}}}{500\,\mathrm{Hz}}\right)^2 \left(\frac{1\,\mathrm{kpc}}{r}\right) \left(\frac{\epsilon}{10^{-6}}\right), \tag{1.3}$$

where f_{rot} is the rotational frequency of the star and ϵ is the ellipticity.

The gravitational wave amplitude of waves emitted by neutron stars may seem low, but their signal would be able to coherently summed over long periods of observation. Studies carried out using the data from LIGO, Virgo and GEO600 have placed upper limits on the emission of gravitational waves from nearby pulsars, which are highly magnetised neutron stars, bettering the limits placed as a result of electromagnetic observations [27–29].

1.3.2 Burst sources

Burst sources are classified to be those which emit a short burst of gravitational waves for about a second or less [30]. Some examples of these which are expected to lie within the detection band of ground-based detectors are coalescing compact object binary systems and supernovae [20].

As discussed in section 1.3.1, the orbital radius of a binary system decays over time. The coalescence of a binary system is a burst source of gravitational waves. As the orbital radius decays, the objects become closer and closer until they finally coalesce. As the orbital radius decreases, the period of orbit decreases, increasing the frequency of gravitational wave emissions. In the few seconds shortly before coalescence, the frequency increases from around 10 Hz to around 300 Hz [20]. The resulting chirp signal is expected to have a strain amplitude of [31]:

$$h = 10^{-23} \left(\frac{100\mathrm{Mpc}}{d}\right) \left(\frac{M_b}{1.2M_\odot}\right)^{\frac{5}{3}} \left(\frac{f}{200\mathrm{Hz}}\right)^{\frac{2}{3}}, \tag{1.4}$$

where d is the distance of the event from the Earth, M_b is known as the mass parameter of the binary system and is related to the masses, M_1 and M_2, of

the compact objects by $M_b = \frac{(M_1 M_2)^{3/5}}{(M_1+M_2)^{1/5}}$, $M_\odot$ is the solar mass and f is the frequency of the emitted wave.

Inspirals are relatively well understood compared to other sources of gravitational waves. Their signals can be filtered from the noise of the detector using a matched filter. This technique allows the detection of fainter signals than for other sources. If the time dependence of the signal's amplitude and frequency can be measured, then the distance to the inspiral event can be calculated, meaning that inspirals may be used as a standard candle, allowing an independent measurement of the Hubble Constant if the redshift of the host galaxy is known [32].

Supernovae

The death of a star is an extremely violent astrophysical event, and is commonly known as a supernova. This happens when a star can no longer sustain nuclear fusion, meaning that there is no pressure from within to prevent gravitational collapse. This collapse releases gravitational potential energy, triggering an extremely energetic explosion, during which gravitational waves may be emitted if there is an asymmetric distribution of mass during the event. It has been estimated that for a supernova within the Milky Way, at a distance of 10 kpc from Earth, emitting the energy equivalent to $10^{-7} M_\odot$, at a frequency of 1 kHz and lasting for 1 ms, the gravitational wave strain amplitude would be [25]:

$$h = 6 \times 10^{-21} \left(\frac{E}{10^{-7} M_\odot} \right)^{\frac{1}{2}} \left(\frac{1\,\mathrm{ms}}{T} \right)^{\frac{1}{2}} \left(\frac{1\,\mathrm{kHz}}{f} \right) \left(\frac{10\,\mathrm{kpc}}{r} \right), \tag{1.5}$$

where E is the energy of the wave and T is the duration of the gravitational wave burst.

1.3.3 Stochastic Background

It is expected that there is a stochastic background of gravitational waves. This will comprise of a superposition of faint, unresolved and random sources as well as events from the early universe, such as the Big Bang [33]. This is a gravitational wave analogue of the cosmic microwave background. Gravitational waves could come from as early as 10^{-35} seconds after the Big Bang, whereas the cosmic microwave background was produced approximately 10^5 years after

the Big Bang. Studies of the gravitational wave stochastic background would therefore provide insight into the very early universe.

It is thought that the strain noise power spectrum of the stochastic background would be [30]:

$$h = 4 \times 10^{-22} \sqrt{\Omega_{GW}} \left(\frac{100\,\mathrm{Hz}}{f} \right)^{\frac{3}{2}} \mathrm{Hz}^{-\frac{1}{2}}, \tag{1.6}$$

where Ω_{GW} is the energy density required for a closed universe.

Observing the gravitational wave stochastic background is a key aim of the detector projects, since it could give some insight into the very early universe. To acheive this, the data from multiple, widely separated detectors would need to be cross-correlated to remove uncorrelated instrument noise. This technique can significantly increase the senstivity of gravitational wave searches, and has been used to place constraints on cosmic string models [34].

1.4 Gravitational wave detection

1.4.1 Resonant bar detectors

The first attempts at detecting gravitational waves were made by Joseph Weber in the 1960's [11]. His detectors were resonant bars in which a passing gravitational wave could excite one of the bar's normal modes of vibration, which were resonant around 1660 Hz [35]. Weber made several claims of coincident events between bar detectors in Maryland and Illinois, separated by 1000 km [36], but these claims could not be verified by coincident events with other bar detectors [12, 37–40]. Subsequent calculations suggested that Weber's resonant bars were not sensitive enough to regularly detect gravitational waves from astrophysical sources, and that the sensitivity would need to be improved by many orders of magnitude in order for gravitational waves to be detected [10].

Variants of Weber's bars have significantly improved sensitivity over the originals. Most notably, thermally excited motions in the bars and electronic noise in the detector circuits were reduced using cryogenics. These low temperature bar setups were built at various locations including Louisiana State University, the University of Rome and the University of Western Australia, amongst others [41, 42]. While these detectors are orders of magnitude more

sensitive than the original room temperature bars, they are limited by their narrow bandwidth due to the narrow resonances of the bars. The narrow bandwidth means that they are usually chosen to be optimised for the detection of a particular type of source. Since broadband interferometric detectors have exceeded the senstivity of bar detectors, there is now much more focus on these detectors than on the resonant bar type.

1.4.2 Interferometric detectors

In 1962, Gertsenshtein and Pustovoit proposed the use of a laser interferometer as a gravitational wave detector [43]. The idea was that widely separated masses may have a measurable change in separation when a gravitational wave passes through them, causing a strain in the space occupied by the detector. The advantages of such a detector over the existing bar detectors were that they could offer broadband senstivity [44], and could be made more sensitive by lengthening the detector arms.

The first prototype gravitational wave detector to use interferometry was built by Robert Forward and his colleagues [45, 46]. The sensitivity was limited by the short arm length and the low power of the He-Ne laser used. Further developments were made at the Max Planck Institute for Astrophysics in Munich [47], where a 3 m prototype was built as well as at the University of Glasgow, where a 1m prototype was built [48]. These were followed by larger scale prototypes: a 10 m interferometer at Glasgow [49], a 40 m interferometer at the California Institute of Technology [50], a 6 m prototype at the Massachusetts Institute of Technology [51], and a 30 m prototype at the Max Planck Institute of Quantum Optics in Garching [52]. These instruments allowed the relevant technologies to be developed to the point where there was enough confidence to build an interferometer large enough to have a realistic chance of detecting gravitational waves. The construction of the first kilometre-scale interferometric detector began in 1994.

Modern laser interferometers are based on the topology of a Michelson interferometer. A laser beam is split by a beam splitter, and the two beams travel down two perpendicular arms. At the end of these arms, each of the beams reflect off of the freely suspended end mirrors and travel back toward the beam splitter, where they are recombined. They then pass through the beam

splitter and the resulting interference pattern is incident upon a photodetector at the output port. A passing gravitational wave would change the respective arm lengths, changing the interference of the recombined beams, thus changing the light intensity incident upon the photodetector.

1.5 Limiting noise sources of long-baseline detectors

Interferometric detectors are limited in sensitivity by a number of fundamental noise sources, such as quantum noise, gravity gradient noise and thermal noise. A discussion of each is detailed below, as well as details of steps taken to mitigate them.

1.5.1 Seismic noise

Continual motion of the ground, with amplitudes in the micrometer range, is a major low-frequency limit to the sensitivity of ground-based interferometers, and is known as seismic noise. In the frequency range 1-10 Hz, the vibrations largely arise from wind and human activity such as traffic and industry. Under 1 Hz, vibrations from ocean waves travelling as surface waves in the Earth's crust produce the micro-seismic background, with peaks in amplitude at 80 mHz and 160 mHz [53]. At a relatively low-noise location on the surface of the Earth, seismic vibrations will produce a noise spectrum of around $10^{-7} f^{-2}$m Hz$^{\frac{1}{2}}$ in all directions [10]. At 30 Hz, this is a factor of 10^9 greater than required for gravitational wave detection. Hence, if gravitational waves are to be detected, the mirror test masses of the detector must be isolated against both horizontal and vertical disturbances.

Suspending the test masses as pendula is a simple way of isolation against horizontal motion. It can be shown that the transfer function of a single pendulum suspension of a mass with a resonant frequency f_0 will have the form [10]:

$$\frac{x}{x_g} \approx \left(\frac{f_0}{f}\right)^2 \tag{1.7}$$

where x is the displacement of the mass, x_g is the ground motion and f is the frequency of interest, assuming that damping is negligible. This is the case for $f \gg f_0$. However, by increasing the number of pendulum stages, the attenuation can be greatly increased, as the transfer function of an N stage cascaded pendulum becomes [10]:

$$\frac{x}{x_g} \approx \left(\frac{f_0}{f}\right)^{2N}. \tag{1.8}$$

Vertical motion may be damped by the use of cantilever blade springs [54–56], and this attenuation may also be increased by the use of multiple stages [10].

1.5.2 Gravitational gradient noise

Gravitational gradient noise, also known as Newtonian noise, arises from the direct gravitational coupling between the mirror test masses and mass density fluctuations around the detector [57]. This noise source limits ground based interferometers below roughly 10 Hz. It is expected that the dominant source of this noise will arise from seismic surface waves in the upper layers of the Earth's crust, but can come from changes in mass density in the local environment including the movement of people near the test masses, clouds passing overhead or passing vehicles [58]. The gravity gradient noise is expected for form an ultimate low frequency noise source [58].

Gravity gradient noise may be reduced by choosing a site with low seismic activity for the location of the detector [19, 57]. However, this is best achieved by placing the detector somewhere other than the Earth's surface. In the case of the Japanese detector project KAGRA, an underground location was chosen in the Kamioka mines in Japan, where construction is ongoing [59]. The Einstein Telescope is designed to follow suit by incorporating underground interferometers into its design [19], while other projects have designed space-based detectors [60].

1.5.3 Thermal noise

The dominant source of noise in the range of a few tens of Hertz to a few hundred Hertz, the most sensitive frequency band of an interferometric detector, is thermal noise. Thermal noise arises from the thermally driven motion of the

molecules in the test masses, mirror coatings and suspensions. The magnitude of the thermal noise in the detection band is related to the intrinsic mechanical dissipation of the mirror test mass, coating and suspension materials and the level of thermoelastic damping [61]. The atoms of the test masses are constantly moving, and have a thermal energy of $k_B T/2$ per degree of freedom associated with them. This thermal motion can excite resonant modes of the test masses.

In order to minimise the thermal noise in gravitational wave detectors, ultra low dissipation materials such as fused silica are used for the test-masses and the suspension fibres [62, 63]. As a result, the energy of the thermally excited resonant modes of the test masses will be stored near the resonances. The suspensions and test-masses are designed such that their resonant modes are outside of the detection band.

Thermoelastic noise arises from statistical fluctuations in the temperature of a material. If one region of a material has a higher temperature than another, a temperature gradient is created. The resulting heat flow is a source of dissipation. If the material is excited by an external force, the temperature gradient is created by the cooling and heating of regions undergoing expansion and contraction. However, even in the absence of external forces, the natural statistical fluctuations in a material's temperature profile give rise to thermal noise. In the case of suspension fibres, the material properties of silica allow the thermoelastic dissipation of the fibres to be nulled with a careful choice of axial stress [64, 65].

A fuller description of coating thermal noise is presented in chapter 2.

1.5.4 Photon shot noise

As described earlier, interferometers are designed to sense the change in the interference pattern incident on the photodetector at the output port. However, there is a limit to how sensitively a small change in optical power can be observed because of the statistical fluctuation in the number of photons counted at the photodetector, also known as photoelectron shot noise. According to Poisson statistics, if N photons are counted at the output of the interferometer, the count will have an associated error of $\sqrt{N}$. Since the interferometer is operated at a 'dark fringe', where the arm lengths are set such that the beams destructively interfere at the output port, only a small number of photons reach

the detector at any instant.

Due to shot noise, the smallest strain detectable in time τ, $h_{\text{detectable}}$ in a basic Michelson interferometer is given by [66, 67]:

$$h_{\text{detectable}} = \frac{1}{L}\left(\frac{2\hbar\lambda c}{\pi P_{\text{in}}\tau}\right)^{\frac{1}{2}} \tag{1.9}$$

where $\hbar$ is the reduced Planck's constant, λ is the wavelength of the photons, P_{in} is the input power of the laser, c is the speed of light, f is the frequency, and τ is the time that the light is within the detector. From this equation, it is desirable to increase the input laser power. It is also desirable to increase the time, τ, spent within the detector by the light (with an upper limit of $\tau = 1/(2f)$ for measurement frequency f), which may be done by extending arm length, or introducing delay lines or Fabry-Perot cavities (section 1.6). Photon shot noise is an important sensitivity limit at high frequencies, since it scales almost linearly with f, and is the dominant detector noise source at frequencies greater than several hundred Hertz.

1.5.5 Radiation pressure noise

As shown in the discussion of shot noise, it is desirable to increase the input laser power. However, this has a drawback in that high laser power will contribute another noise source: radiation pressure noise. Radiation pressure noise arises from the fact that each photon incident on the mirrors of the interferometer has a momentum, which will be imparted to the mirrors upon reflection. This will displace the mirror by a tiny amount. As the laser power is increased, there will be more photons, increasing this displacement noise due to radiation pressure. The strain noise amplitude spectrum in a simple Michelson interferometer, $h_{\text{rp}}(f)$ arising from radiation pressure can be shown to be [10]:

$$h_{\text{rp}}(f) = \frac{1}{mf^2L}\sqrt{\frac{\hbar P_{\text{in}}}{8\pi^3\lambda c}}. \tag{1.10}$$

Here, m is the mass of the interferometer mirrors, and L is the interferometer arm length. Other symbols are defined similarly to those in equation 1.9. It can be seen that the effects of radiation pressure can be reduced by increasing the mirror's mass as well as the inteferometer arm length, but that the effects

are increased by increasing the input laser power. From the $1/f^2$ dependence, radiation pressure noise is most significant at low frequency.

1.5.6 The Standard Quantum Limit

In an interferometer, the Standard Quantum Limit (SQL) is defined as the point where the input laser power is such that shot noise and radiation pressure noise are optimally minimised, fulfilling $h_{\mathrm{shot}} = h_{\mathrm{rp}}$. First generation detectors did not reach the SQL, but it is believed that second generation detectors may be sensitive enough to reach the SQL. This would fundamentally limit the sensitivity of future detectors, but research has shown that the SQL may be surpassed by using squeezed light techniques [68].

While the relatively simple treatment above allows a derivation of the quantum noise, a full quantum mechanical treatment shows that the real origin of both shot noise and radiation pressure is in vacuum fluctuations, or zero point energy fluctuations in the vacuum field. Vacuum fluctuations occur when photons are randomly created and destroyed in the vacuum field, and these fluctuations enter the interferometer through the output port [68, 69]. Fluctuations in the phase quadrature, or imaginary part of the detected signal, are responsible for shot noise and fluctuations in the amplitude quadrature, or the real part of the signal are responsible for radiation pressure noise. These random fluctuations mean that the amplitude and phase of light in the arm cavities of the detector cannot both be detected with absolute accuracy. It is possible to reduce the uncertainty of one quadrature, at the expense of the other, which is done by injecting 'squeezed' vacuum into the output port. This means that, depending on the frequency of interest, the phase or amplitude uncertainty can be reduced in order to reduce the corresponding noise source below its expected noise level without changing the input laser power. Squeezed light techniques have been demonstrated at the GEO600 detector in the frequency range 10 Hz to 10 kHz [70]. As a result, squeezed light is being considered for aLIGO and future detectors such as ET in order to surpass the SQL [19, 71].

1.6 Interferometric techniques

The sensitivity of a basic Michelson interferometer can be improved by a number of techniques discussed below. As discussed above, increasing the length of the arms is desirable since it increases the absolute change in length caused by a passing gravitational wave. The same effect can be achieved by incorporating cavities or delay lines into the arms, since the apparent length change of the cavity is multiplied by the number of round trips the light performs. As discussed in section 1.5.6, there are methods of beating the SQL, by the introduction of squeezed vacuum via the output port. Finally, signal recycling allows the sensitivity to be increased by recycling a gravitational wave signal back into the interferometer.

1.6.1 Delay lines and Fabry-Perot cavities

As seen above, it is desirable to have as long an arm length as possible, but by folding the arm of an interferometer, the effective arm-length can be increased and circumvent the problems encountered by simply extending the arms of a simple Michelson [44], including the expense of extending the evacuated beam tubes, and the curvature of the Earth. An illustration of a folded arm can be seen in figure 1.2, where the light is reflected back down the beam tube to an end mirror located near the beamsplitter. A more advanced form of this is the delay line [44, 47], where shaped mirrors allow the light to bounce back and forth along the beam tube several times, shown in figure 1.3. The total phase change due to a gravitational wave increases with every reflection, provided that the light is stored within the arms for a time which is less than half the period of the gravitational wave. Some prototype gravitational wave detectors used multiple beam delay lines [47, 48, 52], but found that scattering of the laser light became a significant noise source. However, the GEO600 detector still uses a folding mirror design since much simpler control systems are required compared to interferometers with Fabry-Perot cavities.

Another topology, used by the LIGO, Virgo and TAMA detectors is the inclusion of a Fabry-Perot cavity into each of the two arms of the interferometer. A schematic of this is shown in figure 1.4. The laser beam enters the cavity through the input test mass (ITM), which is partially transmissive, and passes down the beam line towards the end test mass (ETM). Upon reflection from

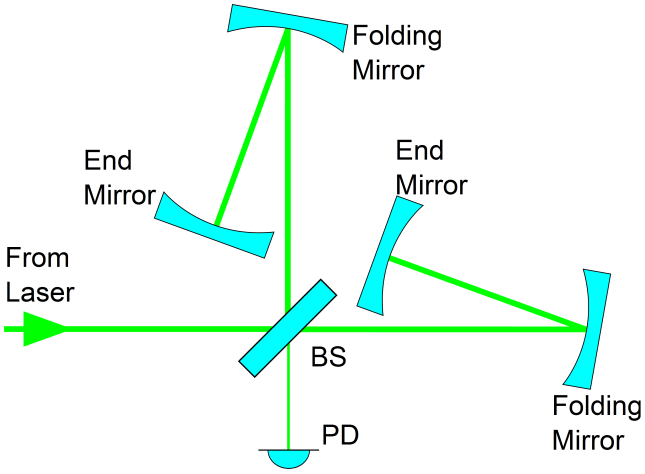

Fig. 1.2 A Michelson interferometer with a folded arm.

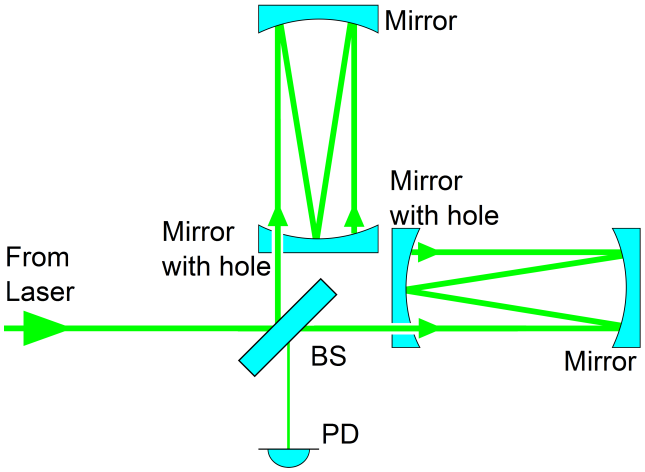

Fig. 1.3 An example configuration of a delay line. The light enters the cavities through a hole in the input mirror, near the beam splitter. The light then makes several round trips before exiting through the same hole.

the ETM, the light travels towards the ITM where it will reflect, making this round trip many times before exiting through the ITM to the beam splitter. The number of bounces along the cavity is determined by the reflectivity of each of mirrors forming the cavity. The energy stored within the arm cavities is much greater than that held in a standard Michelson and any phase change in the light from an arm length change is increased with every round trip made.

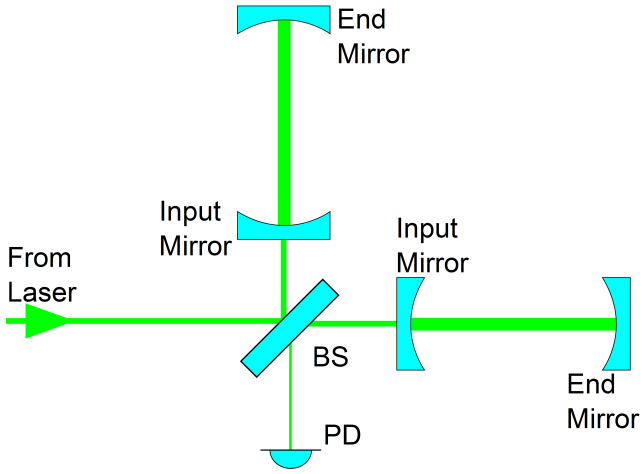

Fig. 1.4 The layout of an interferometer with a Fabry-Perot cavity in each arm. The light enters and exits the arm cavities through the partially transmissive input mirrors. This configuration vastly increases the light storage time in the arms of the interferometer.

1.6.2 Power recycling

Since interferometers are operated such that they always hold a dark output in the absence of gravitational waves, all of the light (minus that absorbed, scattered or transmitted through the end mirrors) exits the interferometer at the input port. By placing a mirror at the input port, the light which would exit at the input port can be reflected back into the interferometer. An illustration of this technique is shown in figure 1.5. This mirror is known as the power recycling mirror, and the technique known as power recycling is used to increase the light power stored in the arm cavities. This mirror creates an additional cavity, with the power recycling mirror at one end and the interferometer at the other, which can be controlled such that no light is reflected back to the laser [72].

1.6.3 Signal recycling

Signal recycling is somewhat analogous to the method of power recycling described above. A partially reflective mirror is placed between the photodetector and the beamsplitter so as to reflect light back into the interferomter [73–75], as shown in figure 1.6. When a gravitational wave changes the interferometer arm length, there is a resulting phase change in the circulating light. In frequency space, this can be represented as sidebands on a carrier signal, which in this case

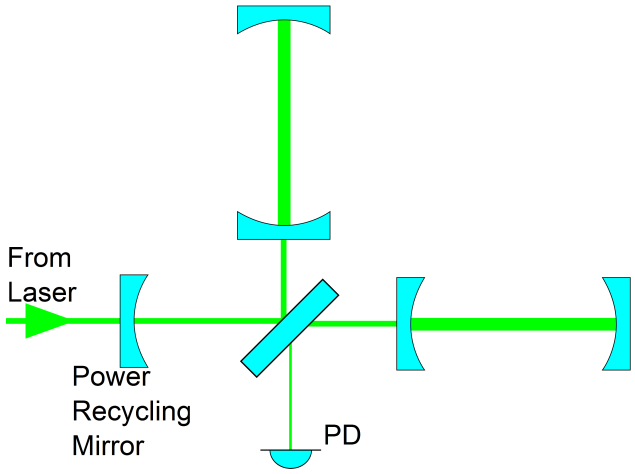

Fig. 1.5 An interferometer with a power recycling mirror, which forms a cavity between itself and the interferometer.

is the laser frequency. The main carrier signal is resonant with the Fabry-Perot cavities and hence it remains within the detector. However, the sidebands are non-resonant and exit the interferometer at the output port. The signal recycling mirror is designed to create a cavity with the mirror at one end and the interferometer at the other, building the signal strength by sending it back into the interferometer. However, signal recycling sacrifices the bandwidth over which the detector is most sensitive. The frequency range over which the enhancement takes place is determined by the reflectivity of the mirror, and the centre of the frequency band is determined by the length of the cavity formed by the mirror and the interferometer. This mirror must be quietly and precisely controled, and the reflectivity must be chosen in advance to provide the desired enhancement to detector sensitivity. Signal recycling could be useful in improving sensitivity in narrow frequency bands where continuous sources such as those discussed in section 1.3.1 are expected to produce signals. On the other hand, broadband signal recycling could be used in searches for burst sources such as supernovae and chirping sources such as inspirals.

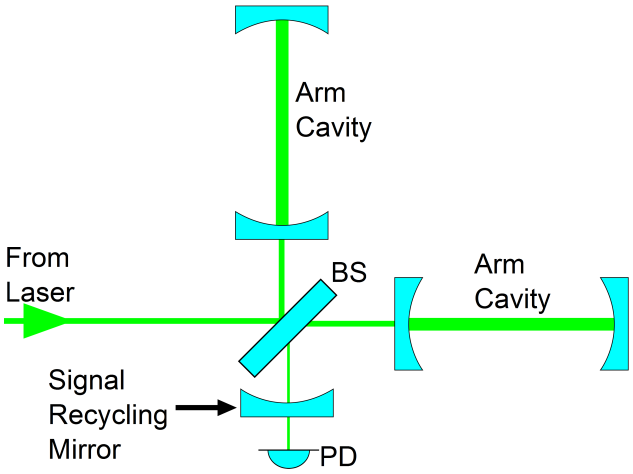

Fig. 1.6 An interferometer with a signal recycling mirror, which forms a cavity between itself and the interferometer, allowing the peak sensitivity to be tuned to specific frequency ranges.

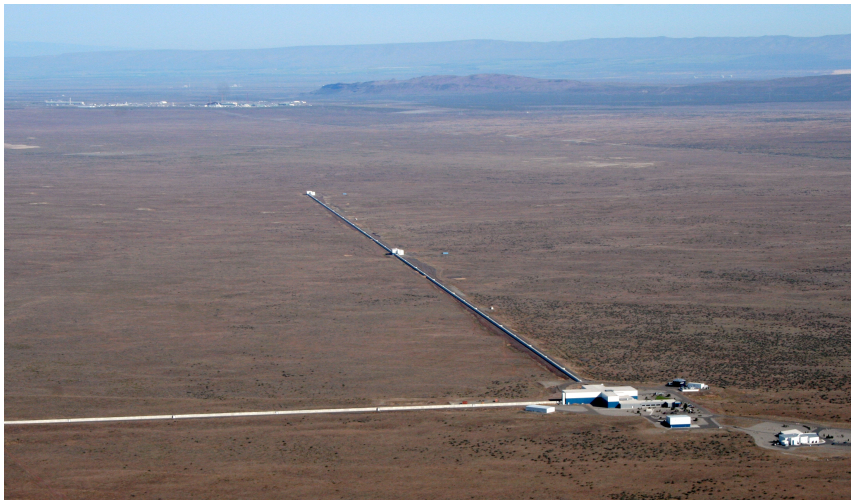

Fig. 1.7 An aerial view of the LIGO Hanford site, located in Washington, USA. Each arm is 4 km long. [1]

1.7 Current interferometric detectors

1.7.1 LIGO and Advanced LIGO

The Laser Interferometer Gravitational-wave Observatory (LIGO) is a detector project in the USA comprised of interferometers at two locations. The LIGO Livingston Observatory (LLO) is located in Livingston, Louisiana, and has one interferometer with 4 km arm cavities. The LIGO Hanford Observatory (LHO) is located in Hanford, Washington, and had two interferometers within one

vacuum system during the initial phase of operation, one of which had half sized 2 km long arms, and the other with the full 4 km long arms. An aerial view of the Hanford site is shown in figure 1.7. The construction of these facilities was completed in 1999, and detectors began operating in a configuration that was known as initial LIGO (iLIGO) two years later, with design sensitivity being reached in 2005. Initial LIGO was then partially upgraded in 2009 to become what was known as enhanced LIGO (eLIGO) and was operated for one year in this configuration before installation of Advanced LIGO (aLIGO) was begun. Advanced LIGO features a large number of upgrades with the goal of improving upon the eLIGO sensitivity by a factor of at least 10.

All three iLIGO interferometers utilised Fabry-Perot arm cavities and power recycling [30]. The cavity mirrors were 10.7 kg silica masses which were coated with alternating layers of the low refractive index material silica (SiO_2) and the high refractive index material tantala (Ta_2O_5) in a multilayer configuration which was reflective at 1064 nm. To isolate the mirrors from ground motion, the test mases were each suspended as pendula by single loops of steel wire, and there were also four-layer mass-spring isolation stacks.

The iLIGO detectors carried out five science runs and during the last of these, S5, the detector operated with a sensitivity of 2×10^{-23} at the most sensitive frequency [76]. At the end of S5, the two 4 km LIGO interferometers underwent upgrades towards the eLIGO configuration.

In 2007-2009, the eLIGO project improved upon iLIGO by increasing the input laser power from 10 Watts to 30 Watts, and moved from a heterodyne to a homodyne readout of the gravitational wave signal. The laser power upgrade meant that some optical components were also replaced. Part of the laser beam is absorbed by the optics, distorting them in a way which is not desirable, and so a thermal compensation system was also installed to heat the mirror faces to compensate for the optical distortion created by the absorbed laser light. In 2009, eLIGO was operated for one science run (S6) in coincidence with the GEO 600 and Virgo detectors (see sections 1.7.3 and 1.7.2). The S1-6 science runs concluded with no gravitational waves being detected, but were able to place meaningful upper limits on the strength of gravitational waves from various sources.

The Advanced LIGO interferometers will use the same facilities as the previous LIGO projects, but with major upgrades to the seismic isolation,

suspensions, optics and laser subsystems. This includes monolithic silica suspensions, improved mirror coatings, larger, heavier test masses to allow the reduction of thermal and radiation pressure noise, and a 200 Watt input laser [71]. These upgrades should facilitate a factor of 10 improvement in sensitivity over iLIGO, but with a larger bandwidth. The noise budget of aLIGO is shown in figure 1.8, with the major contributions to the noise also shown.

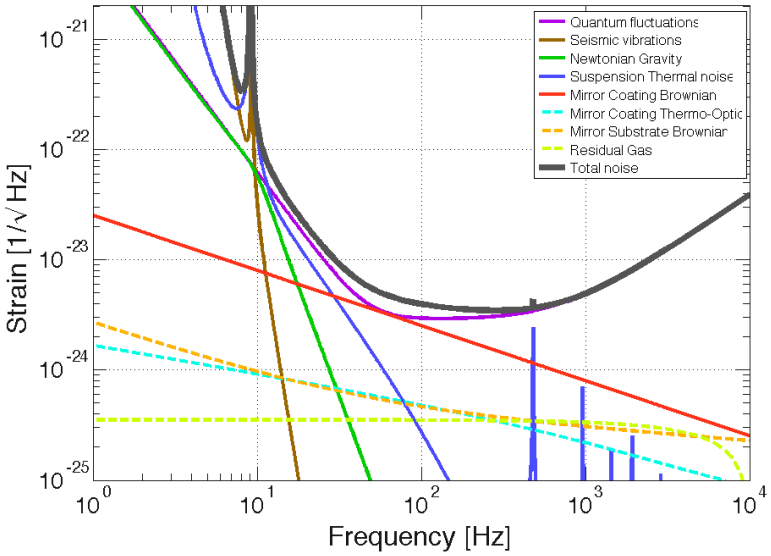

Fig. 1.8 The noise budget of Advanced LIGO, showing the contributions of individual sources.

1.7.2 Virgo

Virgo is a 3 km facility built in Cascina, near Pisa, Italy. This detector features Fabry-Perot arm cavities and a power recycling mirror. However, the interferometer has a unique feature known as the super attenuator [77], a seismic isolation system which gives Virgo an improved low frequency sensitivity over the other detectors. The initial configuration was enhanced after the first Virgo science run to incorporate a more powerful laser, a thermal compensation system on the mirrors, improved control electronics, improved input optics and monolithic fibre suspensions. Virgo is undergoing further upgrades into the Advanced Virgo phase of operation.

Advanced Virgo will use the current Virgo facilities, but will further include

signal-recycling techniques, a more powerful input laser, larger mirrors, an upgraded thermal compensation system and an improved vacuum system [78].

1.7.3 GEO600

Located near Hannover, Germany, GEO600 is a gravitational-wave detector built as part of a German/British collaboration. While only 600 m long, GEO600 uses a folded arm to double the effective arm length to 1.2 km, as well as power recycling and detuned signal recycling. The detector does not feature Fabry-Perot cavities, however, it was the first kilometre scale detector to incorporate monolithic silica suspensions and dual recycling [79]. GEO600 was upgraded to GEO-HF in order to reduce high frequency noise sources such as shot noise by increasing the input laser power and the injection of squeezed light into the output port of the interferometer [80]. After the reduction of shot noise, the limiting noise source at frequencies above 1 kHz was thermal noise from the optical coatings. To ensure that any loud transient signals were not missed, GEO-HF has been used to continue observations while the LIGO and Virgo detectors undergo their respective upgrades, and will further be used for the development of new technologies for future detectors.

1.7.4 TAMA, CLIO and KAGRA

The TAMA300 detector project was a 300 metre long interferometer operated by the Japanese gravitational wave community and is located at the National Astronomical Observatory of Japan (NAOJ) in Mitaka, Tokyo [81, 82]. The interferometer featured test masses suspended on single wire loops and Fabry-Perot arm cavities. In addition to TAMA, the Japanese also built CLIO [83], the Cryogenic Laser Interferometer Observatory as a 100 m long test-bed for the development of applying cryogenic technologies towards gravitational wave interferometers. CLIO was used to demonstrate the reduction of thermal noise using cryogenics [84].

The technologies developed and used by TAMA and CLIO are intended for use at the KAGRA (KAmioka GRAvitational wave detector) [59], previously known as the Large-scale Cryogenic Gravitational wave Telescope (LCGT) [85], which is currently under construction in the Kamioka mines of Gifu Prefecture,

Japan. The detector will have a three-stage seismic isolation system similar to Virgo's super attenuator system. KAGRA will also be the first gravitational wave detector to be located underground in order to reduce the local seismic activity and reduce gravity gradient noise [59]. The optical design of the inteferometer includes Fabry-Perot arm cavities and a power recycling [59]. The KAGRA optics will be made from sapphire test-masses with an as-yet undecided coating, suspended by sapphire fibres and sapphire blade springs. The test-masses will be placed within cryogen-free cryostats and cooled by conduction through the suspension fibres to 20 Kelvin. This will make KAGRA the first cryogenic gravitational wave interferometer [59].

1.7.5 Einstein Telescope

The Einstein Telescope (ET) is a proposed third generation ground-based gravitational wave detector [19]. ET is designed to push the limits of available materials, interferometric techniques and data analysis techniques. The detector has many ambitious design features such as 10 km arm lengths, located 100 m undergound featuring six interferometers in an equilateral triangle. Three of these detectors will be operated at 10 K to reduce thermal noise, with low laser power to reduce radiation pressure noise and greater seismic isolation to provide high sensitivity in the low frequency range 2-40 Hz. However, in order to meet thermal noise requirements, silicon will be used as the test-mass and suspension material. Since silicon is opaque at 1064 nm, the laser wavelength will be 1550 nm. Additionally, much research must be carried out in order to understand the behaviour of any materials planned for use in ET at 10 K, including crystalline silicon and any proposed mirror coatings must meet the design requirements.

The remaining three interferometers will operate at room temperature with high laser power to reduce high-frequency shot noise. These six interferometers will work in tandem as one observatory at least ten times more sensitive than second-generation detectors by using the best technologies from current detectors such as Virgo's seismic isolation system, and GEO-HF's squeezed light methods. A plot of the sensitivity of the ET design is shown in figure 1.9 to illustrate the magnitude of improvements in gravitational wave detectors through time.

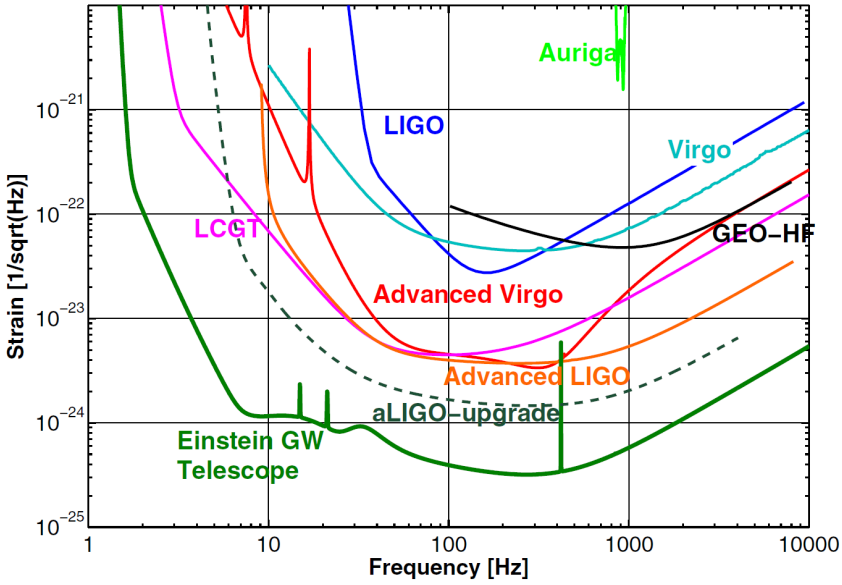

Fig. 1.9 A comparison of the sensitivities of initial configuration detectors with the sensitivities of their advanced design stages. The Einstein Telescope design study takes advantage of as many technologies as possible, giving the detector design a very low noise budget over a broad band of frequencies. This plot is reproduced from [2].

1.8 Conclusions

The detection of gravitational waves is one of the most challenging problems in experimental astrophysics, and second generation detectors will soon be in a position to detect the direct effects of violent astrophysical events on the fabric of space-time. A direct detection of gravitational waves is highly anticipated, since it was postulated in the General Theory of Relativity almost 100 years ago. Since then, the emission of gravitational radiation has been confirmed by Hulse and Taylor, and many developments have been made in the field of gravitational wave detectors, though a direct detection has not yet been made. Advanced versions of LIGO, Virgo and GEO600 will work towards this, opening a new era of astronomy not possible using only optical, radio or other electromagnetic observations. However, these detectors will be limited in sensitivity by a variety of noise sources such as gravity gradient noise, photon shot noise and radiation pressure noise. At their most sensitive frequencies, they will be limited by thermal noise. To reduce thermal noise, further research of the materials comprising the suspensions, mirror test masses and optical coatings must be carried out. This is essential in order to improve current

gravitational wave detectors, and to meet the ambitious design requirements of the Einstein Telescope, or any other future detectors. Chapter 2 will further discuss the sources and importance of thermal noise, and the remainder of this work is focussed on the investigation of optical coatings for the reduction of coating thermal noise.

Chapter 2

Coating thermal noise in gravitational wave detectors

2.1 Introduction

Under the equipartition theorem, a mechanical system will have a mean thermal energy of $\frac{1}{2}k_BT$ per degree of freedom. This energy is stored in the molecules of the system in the form of vibrations, which results in thermally induced motion of the macroscopic system. In the mirrors of a gravitational wave detector, this takes the form of excitations of the resonant modes of the test masses and their suspensions. These thermally induced vibrations induce displacement noise in the interferometer which may be of the same order of magnitude as the signal from a passing gravitational wave. Displacement noise arising from this mechanism is known as thermal noise.

The sensitivities of second generation gravitational wave detectors are expected to be limited in their most sensitive frequency bands by the thermal noise in the mirror coatings [86]. This noise source was not a limiting factor for the first generation detectors since they were limited by technical noise sources, which will be reduced in the second generation detectors by implementing a host of new developments and technologies. While measures such as expanding the beam size of the laser can be taken to reduce the coating thermal noise (see Section 2.3), this cannot be done arbitrarily as manufacturing limits will dictate how large the mirrors may be. Even with these measures, coating thermal noise is expected to form a strong upper limit to the sensitivity of detectors such as

aLIGO. The Japanese KAGRA detector and the planned Einstein Telescope project will both utilise cryogenic cooling to reduce coating thermal noise, a technique which has been demonstrated by the CLIO detector [84]. However, cooling does necessarily reduce thermal noise since it is dependent upon several material properties, some of which vary strongly with temperature. In order to reduce the thermal noise of all future detectors, understanding the underlying cause of thermal noise and the relevant material properties is highly important.

Coating thermal noise is the combination of three different noises: Brownian noise (section 2.3), thermoelastic noise (section 2.4.1) and thermo-refractive noise (section 2.4.2). Thermoelastic and thermo-refractive may be combined coherently into what is known as thermo-optic noise [87]. The effect of thermo-optic noise is small in comparison to Brownian noise for the materials planned for use in advanced gravitational wave detectors [87]. Thermo-optic noise may dominate over coating Brownian noise if alternative coating materials are used, in particular crystalline coatings [88]. Brownian noise is expected to be the most significant component of coating thermal noise within advanced gravitational wave detectors and will be one of the limiting noise sources for advanced detectors in their most sensitive frequency band between a few tens and a few hundreds of Hertz.

2.1.1 Brownian noise

Brownian thermal noise arises from thermally induced motion in the mirror test-masses, coatings and suspensions. Brownian motion was first observed in 1828 by the botanist Robert Brown, who noticed irregular patterns of motion of dust and pollen grains suspended in water [89]. A full mathematical treatment of this was given in 1905 by Einstein, who showed that these irregular patterns of movement were due to stochastic collisions of the water molecules with the pollen grains [90]. Einstein also described how the pollen grains lost their kinetic energy as a result of these collisions as they passed through the water. This was the first time that a dissipation process had been described as being the result of random fluctuations.

2.1.2 The Fluctuation-Dissipation Theorem

The idea of dissipation in a linear system was further explored by Callen et al. [91]. The Fluctuation-Dissipation Theorem states that in any linear system in equilibrium which is capable of undergoing a dissipation process, there will be fluctuations in a measurable parameter which characterises the state of the system. The power spectral density of the thermal driving force, $S_F(\omega)$ is related to the dissipative (real) part of the mechanical impedance of the system $Z(\omega)$:

$$S_F(\omega) = 4k_B T \Re\{Z(\omega)\}, \tag{2.1}$$

where the impedance is defined as

$$Z(\omega) \equiv F(\omega)/v(\omega), \tag{2.2}$$

where a force $F(\omega)$ has been applied to the system and results in a velocity $v(\omega)$. This can also be expressed in terms of the power spectral density of the thermal displacement $S_x(\omega)$:

$$S_x(\omega) = \frac{4k_B T}{\omega^2} \Re\{Y(\omega)\}, \tag{2.3}$$

where $Y(\omega)$ is the mechanical admittance of the system, which is equivalent to $Z(\omega)^{-1}$. It is therefore possible to estimate the thermal noise spectrum of a mechanical system if the real part of the macroscopic mechanical impedance is known. The real part of the mechanical impedance is more commonly known as the damping coefficient. In a gravitational wave detector, the external sources of damping such as gas damping and recoil damping [92], where energy from the suspensions is lost into a recoiling support structure, have been reduced by means of evacuating the beamline and by an appropriate suspension design. As a result, the dominant source of dissipation which contributes to the thermal noise is the internal friction of the materials which comprise the mirrors and their suspensions.

2.2 Anelasticity and mechanical loss

Internal friction in a material is caused by its anelasticity. When a stress is applied to an ideal elastic material it should respond instantaneously. However, in real (anelastic) materials, the strain response is not instantaneous and builds in the material over a relaxation time [61, 93]. In the case of an oscillating stress of frequency f and magnitude σ_0 applied to a material [93]:

$$\sigma = \sigma_0 e^{i2\pi ft}. \tag{2.4}$$

Here, σ is the stress in the material. The resulting strain will also be oscillating with the same frequency as the applied stress, but will have a phase lag, ϕ in relation to the applied stress, which arises from the strain developing over a finite relaxation time. The anelastic strain would be:

$$\epsilon = \epsilon_0 e^{i(2\pi ft-\phi)}. \tag{2.5}$$

The angle of phase lag is also commonly known as the mechanical loss angle or simply the mechanical loss of the material. The mechanical loss, or internal friction of the material is a measure of the fractional energy dissipated per cycle of oscillation.

The phase lag of the strain may arise from a number of causes such as changes in molecular arrangement, point defects, dislocations or grain boundaries in crystalline materials [61]. These types of rearrangement are sources of dissipation as they take thermal energy from the material in order to make the transitions. Another source of dissipation is the thermal gradient which may be induced by the bending of a material, known as the thermoelastic dissipation [61].

2.2.1 Thermal noise associated with a single resonant mode

Mechanical dissipation in a material arises due to the delay between a stress applied to a material and the resulting strain. In an oscillating system, this delay takes the form of a phase lag, ϕ, between the applied force F and the displacement x. An example of this can be represented by mass on a spring

with some anelasticity. In this case, the system can be modelled by a modified version of Hooke's law, where the spring constant is a complex number:

$$F = -k(1 + i\phi)x. \tag{2.6}$$

Here, F is the restoring force of the spring. If the resonant modes of the suspended mirror system in a gravitational wave detector are modelled as a driving force F applied to harmonic oscillators with internal damping, the equation of motion is:

$$m\ddot{x} = -k(1 + i\phi)x + F. \tag{2.7}$$

The displacement and acceleration of a harmonic oscillator are related to its velocity by:

$$x = \frac{\dot{x}}{i\omega} \quad \text{and} \quad \ddot{x} = i\omega\dot{x}, \tag{2.8}$$

which can be inserted into equation 2.7. The force on the oscillator, F, is then:

$$F = i\omega m\dot{x} + \frac{k}{i\omega}(1 + i\phi)\dot{x}. \tag{2.9}$$

Using the definition of impedance, equation 2.2, the expression:

$$Z = \frac{k + i\phi k - \omega^2 m}{i\omega} \tag{2.10}$$

may be obtained. Taking the reciprocal of the impedance and rationalising the denominator, the admittance of the system can be expressed as:

$$Y = \frac{i\omega(k - \omega^2 m - i\phi k)}{(k - \omega^2 m)^2 + \phi^2 k^2}. \tag{2.11}$$

From equation 2.3, the power spectral density of the noise is proportional to the real part of the admittance. From equation 2.11, the real part of the admittance is:

$$\Re\{Y\} = \frac{\omega\phi k}{(k - \omega^2 m)^2 + \phi^2 k^2}, \tag{2.12}$$

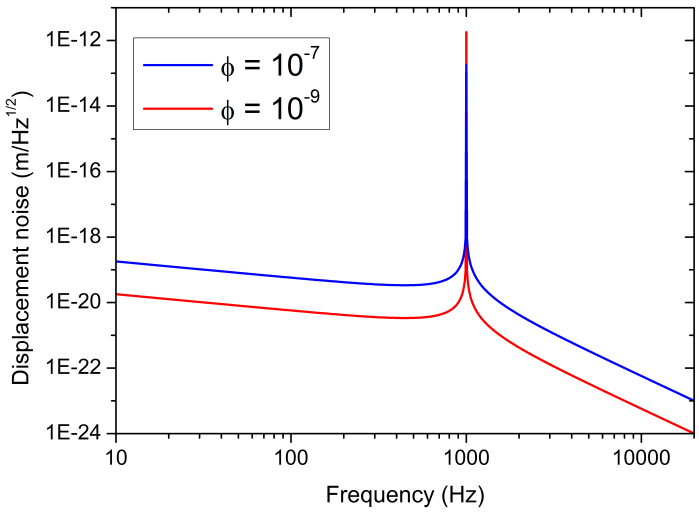

Fig. 2.1 Thermal noise displacement spectra for two oscillators with mechanical losses of $\phi = 1 \times 10^{-7}$ and $\phi = 1 \times 10^{-9}$. The two oscillators have resonant frequency $f_0 = 1\,\mathrm{kHz}$, $m = 20\,\mathrm{kg}$ and $T = 290\,\mathrm{K}$. The lower loss oscillator exhibits lower off-resonance thermal noise, but higher on-resonance thermal noise than the higher loss oscillator.

from which the power spectral density of the displacement noise is obtained and may be simplified by the relation $k = \omega_0^2 m$ to give:

$$S_x(\omega) = \frac{4k_\mathrm{B}T}{\omega} \frac{\omega_0^2 \phi(\omega)}{m[\phi^2(\omega)\omega_0^4 + (\omega_0^2 - \omega^2)^2]}. \tag{2.13}$$

This is the thermal noise power spectral density of an oscillator of resonant frequency ω_0 and dissipation ϕ. Equation 2.13 may be used to calculate the thermal noise of two oscillators which are identical apart from their mechanical dissipations. Figure 2.1 shows the displacement thermal noise spectrum for two mechanical oscillators with different mechanical loss factors. The oscillator with lower mechanical loss has a lower off-resonance thermal noise than the oscillator with higher mechanical loss. However, on resonance, the oscillator with lower loss has the higher thermal noise. That is, the low-loss resonator confines more of the thermal motion into a narrow frequency band around the resonant frequency, giving a narrower but higher peak. In gravitational wave detectors, it is favourable to have the suspensions, test-masses and coatings to be made from low loss materials so that off-resonance thermal noise is minimised.

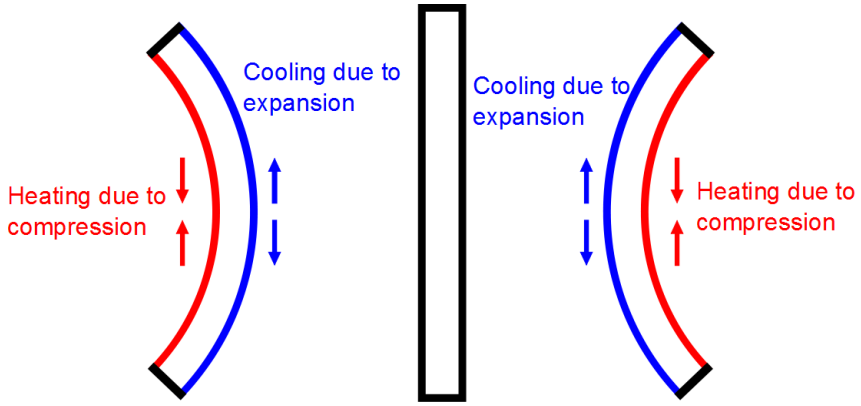

Fig. 2.2 A bending beam experiences simultaneous expansion and contraction which induce localised changes in temperature. The thermal gradient created causes heat flow from the relatively hot to cold areas of the beam. This heat flow is responsible for thermoelastic dissipation.

2.2.2 Thermoelastic Dissipation

Thermoelastic dissipation occurs when a material is deformed in such a way as to create a thermal gradient, for example in a bending beam, shown in figure 2.2. In this example, the bending induces an expansion on one side of the beam, and a compression on the other. Where the beam is expanded, it becomes slightly cooler than the mean temperature of the beam, and where it is compressed, the material becomes slightly hotter. This creates a thermal gradient through the thickness of the beam, which gives rise to energy dissipation through heat-flow. This was studied by Zener, who calculated the differential heating across a fibre as it vibrates [5, 94]. If we extend the static case described above to that of an oscillating beam, then each side of the beam will be expanded and compressed in turn. The dissipation from the resulting heat flow will have a peak at a frequency related to the time it takes for the thermal gradient across the beam to relax.

Zener calculated that for a beam of rectangular cross section, the mechanical dissipation, ϕ due to the heat flow through the thickness of the beam during oscillation at an angular frequency, ω, is given by:

$$\phi(\omega) = \frac{Y\alpha^2 T}{\rho C}\frac{\omega\tau}{1+\omega^2\tau^2}, \tag{2.14}$$

where Y is the Young's modulus of the beam, α is the coefficient of thermal expansion, defined as $\alpha = l^{-1}\frac{dl}{dT}$, ρ is the density of the material, and C is the

specific heat capacity. Here, τ is known as the thermal relaxation time and is related to the time taken for the thermal gradient across the thickness of the beam to relax. This is geometry dependent, and for a beam with rectangular cross-section is given by [61]:

$$\tau = \frac{\rho C t^2}{\pi^2 \kappa}. \tag{2.15}$$

Here, κ is the thermal conductivity of the material. Equation 2.14 features a peak where the angular frequency of vibration is equal to the reciprocal of the thermal relaxation time.

2.2.3 Mechanical loss and quality factor

A common physical descriptor of a resonance in a system is the dimensionless quality factor. For a resonant frequency, f_0, the quality factor, Q, of the resonance may be calculated from:

$$Q(f_0) \equiv \frac{f_0}{\Delta f} \equiv \frac{2\pi E_{\text{stored}}}{E_{\text{lost per cycle}}}. \tag{2.16}$$

Here, the full-width half-maximum of the power spectrum, Δf of a resonance peak is related to the energy stored in the system and the energy dissipated per cycle of oscillation. By comparison, the mechanical loss of a system is the energy lost per cycle as a fraction of the energy stored in the oscillating system. That is,

$$\phi(\omega) = \frac{E_{\text{lost per cycle}}}{2\pi E_{\text{stored}}} = \frac{\Delta f}{f_0}, \tag{2.17}$$

where the symbols are defined similarly to those in equation 2.16. The loss angle of a system is simply the reciprocal of a system's quality factor. The dissipation of a system is most easily measured at the resonant frequencies.

2.3 Brownian noise from mirror coatings

Initial models for calculating the Brownian noise in gravitational wave detectors took each resonant mode of the suspended mirror test mass in turn, and applied the Fluctuation-Dissipation Theorem to each, summing over many modes [92, 95]. In theory, all modes should be included in the summation, but in

practice the calculation can be approximated by choosing an appropriate high frequency cutoff, reducing the computational expense of the calculation. This technique is known as normal-mode expansion and formed the basis for thermal noise estimation for interferometric gravitational wave detectors. This model breaks down when the dissipation is not distributed evenly throughout the test-mass [96]. This inhomogeneous loss distribution creates correlations between fluctuations in the motions of different modes, which is not taken into account by normal-mode expansion. When the loss is homogeneously distributed, the displacement mode shape does not change during decay.

However, when loss is inhomogeneously distributed, the motion at the high loss region lags in phase with respect to the rest of the body, and the shape of the displacement mode shape during decay is therefore different from that of the resonant mode [97]. In the case of the mirrors used in gravitational wave detectors, the coatings applied to only one surface have a dissipation higher than that of the substrate by several orders of magnitude. This means that the normal-mode expansion severely underestimates the Brownian thermal noise arising from lossy coatings. To remedy this problem, several approaches have been developed.

The method most similar to normal-mode expansion is the so-called advanced mode expansion. Advanced mode expansion introduces cross-mode coupling terms which arise due to inhomogeneous dissipation distribution [97]. In the case where dissipation is evenly distributed, these terms become zero, giving the same results as normal mode expansion. However, this method and normal mode expansion are both computationally expensive, particularly as more modes are included in the summation [96], providing motivation to develop more direct methods to calculate Brownian thermal noise.

A direct approach for calculating the thermal noise arising from a mirror with inhomogeneous loss was presented by Levin in 1998 [96]. Levin's approach considers a notional pressure, of the same profile as the laser beam, upon the front face of the mirror and directly applies the Fluctuation-Dissipation Theorem to the readout of the interferometer [96]. This intensity profile is thought of as a notional pressure applied to the front face of the mirror, and the thermal noise is calculated from the power dissipated in the mirror. This

approach results in the following formula for the thermal noise power spectral density:

$$S_x(f) = \frac{2k_B T}{\pi^2 f^2} \frac{W_{\text{diss}}}{F_0^2}, \tag{2.18}$$

where F_0 is the peak amplitude of the notional oscillatory force, and W_{diss} is the power dissipated in the mirror. Here, W_{diss} can be shown to be [98]:

$$W_{\text{diss}} = 2\pi f \int_{vol} \varepsilon(x, y, z)\phi(x, y, z, f)dV, \tag{2.19}$$

where ε is the energy density of elastic deformation when the test mass is maximally deformed under the notional applied pressure. If the laser beam radius is small compared to the radius of the mirror surface, the mirror can be approximated as half-infinite. In this case, the power spectral density of the Brownian thermal noise, $S_x^{\text{ITM}}(f)$ can be shown to be [99]:

$$S_x^{\text{ITM}}(f) = \frac{2k_B T}{\sqrt{\pi^3} f} \frac{1 - \sigma^2}{Y w_0} \phi_{\text{substrate}}(f), \tag{2.20}$$

where Y and σ are the Young's modulus and Poisson's ratio of the mirror material respectively, $\phi_{\text{substrate}}$ is the mechanical loss of the mirror material, w_0 is the distance over which the electric field amplitude of the laser beam falls to $1/e$ of the peak value. Equation 2.20 requires some modification to correct for cases where the laser beam radius does not allow the mirror to be treated as a half-infinite body. A calculation of thermal noise power spectral density arising from a finite sized test mass was carried out by Bondu et al. [99] and corrected by Liu and Thorne [100]. For an Advanced LIGO mirror, they calculated that for a laser beam of radius varying between 1 and 6 cm, the correction factor varies between 0.96 and 0.66 respectively.

One of the most important ideas to come from Levin's work is that the position of mechanical loss within the mirror with respect to the laser is key when calculating thermal noise. A source of dissipation close to the mirror surface upon which the laser is incident should contribute more thermal noise than an identical one which is placed far from the reflecting surface. This is because the dissipation on the front surface would directly influence the readout of the laser beam, whereas the same dissipation on the back surface would require its effects to propagate through the entire test mass in order to influence

the laser beam. For this reason, the dissipation of the mirror coatings is of particular significance in calculating the thermal noise in an interferometer.

In a treatment by Nakagawa et al., a mirror coating was approximated as being a thin surface layer of thickness d and mechanical loss ϕ_{coating} and the same material properties as the test-mass substrate [101]. This allowed the power spectral density of the coating and the mirror substrate to be calculated:

$$S_x^{\text{total}}(f) = \frac{2k_BT}{\pi^{3/2}f}\frac{1-\sigma^2}{w_0 Y}\left(\phi_{\text{substrate}} + \frac{2}{\sqrt{\pi}}\frac{(1-2\sigma)}{(1-\sigma)}\frac{d}{w_0}\phi_{\text{coating}}\right). \tag{2.21}$$

Typical values of $\phi_{\text{substrate}}$ and ϕ_{coating} are 1×10^{-8} and 3×10^{-4}. While this calculation takes into account the dissipation inhomogeneity of the mirrors by separating the coating and the substrate, it assumes that the coating itself is homogeneous. However, the highly reflective coatings of gravitational wave detectors consist of a multilayer stack, usually of two materials, which have different thermo-mechanical properties and mechanical dissipations. A more detailed calculation, in which this structure is taken into account, was carried out by Harry et al. [86]. Careful use of the fluctuation dissipation theorem gives the power spectral density of Brownian thermal noise from a coated mirror to be [86]:

$$\begin{aligned} S_x(f) = \frac{2k_BT}{\pi^{3/2}f}\frac{1-\sigma^2}{w_0 Y}\Bigg\{&\phi_{\text{substrate}} + \frac{1}{\sqrt{\pi}}\frac{d}{w_0}\frac{1}{YY'(1-\sigma'^2)(1-\sigma^2)} \\ &\times [Y'^2(1+\sigma)^2(1-2\sigma)^2\phi_{\parallel} \\ &+ Y'\sigma'(1+\sigma)(1+\sigma')(1-2\sigma(\phi_{\parallel}-\phi_{\perp}) \\ &+ Y^2(1+2\sigma')^2(1-2\sigma')^2\phi_{\perp}]\Bigg\} \end{aligned} \tag{2.22}$$

where Y' and σ' are the Young's modulus and Poisson's ratio of the coating respectively. $\phi_{\parallel}$ and $\phi_{\perp}$ are the mechanical loss values of the multilayer coating for strains parallel and perpendicular to the mirror surface respectively. This equation can be simplified under the approximation that $\sigma = \sigma' = 0$ to give:

$$S_x(f) = \frac{2k_BT}{\pi^{3/2}f}\frac{1}{w_0 Y}\left\{\phi_{\text{substrate}} + \frac{1}{\sqrt{\pi}}\frac{d}{w_0}\left(\frac{Y'}{Y}\phi_{\parallel} + \frac{Y}{Y'}\phi_{\perp}\right)\right\}. \tag{2.23}$$

This equation is correct to around 30% for the materials used in initial LIGO. If the $\phi_{\text{substrate}}$ term is removed from this equation, it provides an estimate of the Brownian thermal noise solely due to the coatings. The power spectral density of the thermal noise due to the coating varies as $1/{w_0}^2$, meaning that thermal noise reduces quickly as the laser beam radius increases. This is because the laser beam radius determines the area over which the test-mass vibrations are averaged. It should also be noted that the coating part of the Brownian thermal noise depends on the elastic modulus of the substrate. That is, the same coating will exhibit different levels of thermal noise on different substrates.

2.4 Coating thermo-optic noise

2.4.1 Thermoelastic noise

Statistical temperature fluctuations across a coating induce deformation due to the coupling of the temperature with the dimensions of the coating through the thermal expansion coefficient. If a particular region of the coating experiences a slight increase in temperature relative to the mean temperature of the coating, it will expand in the direction of the interrogating laser beam. Hence, a certain portion of the beam will sense a shortening of the interferometer arm, and vice versa for a decrease in temperature. The resulting displacement noise is known as thermoelastic noise. Braginsky et al. calculated the thermoelastic noise arising from the substrate, although this approach approximates the mirror to be half-infinite with respect to the incident laser beam [102]. Liu and Thorne later applied a correction factor to Braginsky's formulation to correct for the finite dimensions of real test masses, although this factor is of the order of unity for typical test masses.

The thermoelastic noise of a coated mirror requires an additional term, which is a result of the difference between the thermo-mechanical properties of the coating and the substrate [103]. This is referred to as coating thermoelastic noise, and the power spectral density of this noise was calculated by Fejer and Braginsky to be [102, 103]:

$$S_x(f) \approx \frac{8k_BT^2}{\pi\sqrt{\pi f}}\frac{d^2}{w_0^2}(1+\sigma_{\text{s}})^2\frac{C_{\text{f}}^2}{C_{\text{s}}^2}\frac{\alpha_{\text{s}}^2}{\sqrt{\kappa_{\text{s}}C_{\text{s}}}}\tilde{\Delta}^2, \tag{2.24}$$

where the subscript s refers to the substrate, the subscript f refers to the thickness-averaged properties of the coating materials discussed below, σ is the Poisson's ratio, C is the specific heat capacity, α is the coefficient of thermal expansion and κ is thermal conductivity. Here, $\tilde{\Delta}$ is an averaging of material properties, defined by Fejer to be:

$$\tilde{\Delta} \equiv \left\{ \frac{C_\mathrm{s}}{2\alpha_\mathrm{s} C_\mathrm{f}} \left[\frac{\alpha}{1-\sigma} \left(\frac{1+\sigma}{1+\sigma_\mathrm{s}} + (1-2\sigma)\frac{E}{E_\mathrm{s}} \right) \right]_\mathrm{avg} - 1 \right\}^2, \tag{2.25}$$

where the square brackets are evaluated for each of the materials in the coating before being averaged, weighted by the total thickness of each material within the coating, using the equation:

$$[X]_\mathrm{avg} \equiv \frac{d_a}{d_a + d_b} + \frac{d_b}{d_a + d_b}. \tag{2.26}$$

We can see from equation 2.25 that in the case where there is no difference between the thermo-mechanical properties of the substrate and those of the coating that $\tilde{\Delta}$ becomes zero. This means that where the coating and substrate are identical, there is no coating thermoelastic noise.

2.4.2 Thermo-refractive noise

Thermo-refractive noise arises from the temperature dependence of the refractive index of coating materials. Local statistical fluctuations in the temperature of the coating result in changes to the refractive index, changing the optical path length of the laser beam within the coating. The resulting fluctuations in refractive index are governed by the thermo-optic coefficient $\beta = \frac{dn}{dT}$. These fluctuations in the refractive index of the coating create fluctuations in the optical path length of the laser beam, which penetrates the coating to a depth which is of the order of the optical thickness of one bilayer [104].

The power spectral density of thermo-refractive noise was calculated by Braginsky et al. to be:

$$S_{x,\beta}^\mathrm{TD}(\omega) = \frac{\sqrt{2}\beta_\mathrm{eff}^2 \lambda^2 k_B T^2}{\pi r_0^2 \sqrt{\omega \rho C \kappa}} \tag{2.27}$$

where λ is the wavelength of the laser, k_B is Boltzmann's constant, T is the mean temperature of the coating, r_0 is the radius over which the gaussian beam

amplitude falls to $1/e$ of the maximum, ω is angular frequency, ρ is the density of the coating, C is the specific heat capacity and κ is the thermal conductivity. β_{eff} is the effective temperature dependence of the refractive index of the whole coating, which is calculated from the individual coefficients of the high and low index layers from:

$$\beta_{\text{eff}} = \frac{n_{\text{L}}^2 \beta_{\text{L}} + n_{\text{H}}^2 \beta_{\text{H}}}{4(n_{\text{L}}^2 - n_{\text{H}}^2)} \tag{2.28}$$

in the case where the coating is composed of quarter-wavelength layers only. Here, n is the refractive index of either the high, H, or low, L, index material.

2.4.3 Thermo-optic noise

As discussed in the previous two sections, thermoelastic noise arises from thermo-mechanical fluctuations in the physical thickness of the mirror coating and thermo-refractive noise arises from fluctuations in refractive index, changing the optical path length of the mirror coatings. Both of these noise sources may introduce phase noise into the signal of the interferometer, but their root cause is the same: statistical fluctuations in temperature within the coating. As such, while the two noise sources are distinct, they may be added coherently. However, studies by Evans et al., who applied the Levin approach, found that for the materials planned for use in Advanced LIGO, the two noise sources serve to partially cancel each other [87]. Firstly, they calculated the power spectral density of coating thermal fluctuations as observed by a laser beam with a Gaussian profile:

$$S_{\text{TO}}^{\Delta T} = \frac{2\sqrt{2}}{\pi} \frac{k_B T^2}{r_G^2 \sqrt{\kappa C \omega}} \tag{2.29}$$

where the symbols here are defined similarly to those in equation 2.27, except r_G which is the radius over which the Gaussian laser beam falls to $1/e^2$ in power. The authors subsequently calculated the phase fluctuations induced in the laser beam by the thermal fluctuations, combining the thermoelastic and thermo-refractive mechanisms. The power spectral density of thermo-optic noise is given, in the most complete form, by:

$$S_{\text{TO}}^{\Delta z} \simeq S_{\text{TO}}^{\Delta T} \Gamma_{tc} \left(\Delta \bar{\alpha}_{fsm} d - \bar{\beta} \lambda \right)^2 \tag{2.30}$$

where $S_{\mathrm{TO}}^{\Delta T}$ is the power spectral density of thermal fluctuations in the coating given in equation 2.29, and Γ_{tc} is a correction factor which takes account of the coating's thickness. The first and second terms inside the brackets represent the thermoelastic and thermo-refractive terms respectively. $\Delta\bar{\alpha}_{fsm}$ is a term derived from the effective thermal expansions of the coating and substrate materials, multiplied by a correction factor which accounts for the finite size of the test mass. Finally, $\bar{\beta}$ is the effective thermo-refractive coefficient given as:

$$\bar{\beta} \simeq \frac{n_{\mathrm{L}}^2 B_{\mathrm{L}} + n_{\mathrm{H}}^2 B_{\mathrm{H}}}{4(n_{\mathrm{L}}^2 - n_{\mathrm{H}}^2)}, \tag{2.31}$$

in the case that the coating is comprised purely of quarter-wavelength layers, or:

$$\bar{\beta} \simeq \frac{B_{\mathrm{H}} + B_{\mathrm{L}}(2(n_{\mathrm{H}}/n_{\mathrm{L}})^2 - 1)}{4(n_{\mathrm{H}}^2 - n_{\mathrm{L}}^2)} \tag{2.32}$$

in the case where there is a half-wavelength thick cap layer of the low index material on the surface of the coating. In both equations 2.31 and 2.32, B is calculated from the change of refractive index over temperature, $\beta = \frac{dn}{dT}$, of the subscripted material, its effective thermal expansion and its refractive index, n. For a given material X:

$$B_{\mathrm{X}} = \beta_{\mathrm{X}} + \bar{\alpha}_{\mathrm{X}} n_{\mathrm{X}}. \tag{2.33}$$

It is important to note that in the power spectral density of thermo-optic noise, equation 2.30, that the sign of the thermo-refractive term inside the brackets is the opposite to the sign of the thermo-elastic term. This means that the two terms act to cancel one another when added coherently, assuming a positive thermo-optic coefficient. This reduces the effect of thermo-optic noise within a gravitational wave detector, and it may be the case that with materials chosen to have appropriate material properties, the two noise sources could cancel completely.

2.5 Conclusions

Thermal noise is expected to form a significant limit to the sensitivity of interferometric gravitational wave detectors. The coupling of dissipation-

induced motion into the interferometer signal is strongest for dissipation located near the laser beam, such as that in the coatings on the mirrors. The magnitude of coating thermal noise in the second generation detectors will be dominated by Brownian thermal noise, and will be a sensitivity limit to detectors in their most sensitive frequency bands. This noise source is related to the mechanical dissipation of the coating materials, with low mechanical loss corresponding to low thermal noise. Coating Brownian noise may be reduced by decreasing the temperature of the mirror and increasing the radius of the laser beam used to measure the position of the mirror. However, the laser beam radius cannot be increased arbitrarily due to the finite size of the mirror. The mirror test masses are limited in size by manufacturing constraints, as well as the requirements of the suspension systems. Cryogenic cooling of the mirrors will be implemented by the KAGRA detector, but this requires vastly increasing the complexity of the detector.

However, another method of reducing coating thermal noise is to choose materials which have a lower mechanical dissipation than the currently used materials, as well as appropriate values for the other material properties. The mechanical loss of many materials is temperature dependent, and hence the measurement of coating mechanical loss at cryogenic temperatures as well as at room temperature is important for future detectors. Measuring the temperature dependence of mechanical loss is also a useful tool to investigate the microscopic structure of coatings for a better understanding of the mechanisms which cause dissipation.

Chapter 3

Coating mechanical loss measurement techniques and sample preparation

3.1 Introduction

As discussed in Chapter 2, the thermal noise in an interferometric gravitational wave detector is dependent upon the mechanical dissipation of the materials used for the mirrors and their suspensions. In particular, the reflective mirror coatings applied to the front surface of the mirrors are a major source of thermal noise. Therefore, the mechanical loss of the mirror coatings is of particular importance.

The mirrors used in the first generation of gravitational wave detectors comprised of silica (SiO_2) test masses, coated with alternating quarter-wavelength ($\lambda = 1064\,\mathrm{nm}$) optical thickness layers of the high refractive index material tantalum pentoxide (also known as tantala, Ta_2O_5) and low refractive index silica. These layers are repeated in order to achieve the required reflectivity. Research has shown that most of the mechanical loss, and therefore also the thermal noise of such a coating, originates from the tantala layers [105]. Therefore, it is of interest to reduce the dissipation of these layers. Studies have shown that by doping the high index tantala layers with titania (TiO_2) to a concentration of around 25%, the dissipation of multilayer silica/tantala coatings may be reduced by as much as 40% [105, 106]. For this reason, titania-doped tantala

($Ti:Ta_2O_5$) was adopted as the high-index material for the coatings used for the Advanced LIGO detector [107]. These coatings are studied in detail in Chapter 5.

In this chapter, a general method of measuring coating mechanical loss is described. This measurement technique involves exciting resonant modes of coated samples and monitoring the decay of their vibrations. This technique can be applied to samples of many geometries. In this thesis, two types of sample have been studied: cantilevers and disks. This chapter will discuss the details of sample preparation as well as how this measurement is applied to each geometry of sample.

3.2 Coating deposition methods

3.2.1 Ion beam sputtering

There are many techniques by which amorphous coatings may be deposited. The coatings used in the first generation of gravitational wave detectors were deposited by ion beam sputtering (IBS). This technique was also used to deposit the coatings to be used in Advanced LIGO and Advanced Virgo. This technique involves accelerating a beam of ions towards a sputtering target, which is composed of the desired coating material. The ions impact with the surface of the target and eject atoms from the material. These atoms then condense on the surface of the substrate, and slowly form a uniform coating layer. A schematic diagram of a simple IBS coating chamber is shown in figure 3.1. Tantala coatings are typically deposited using a tantalum target with a small amount of oxygen in the deposition chamber [108]. The sputtered tantalum atoms react with the oxygen en route to the substrate and are deposited as tantalum pentoxide. IBS coatings also exhibit relatively low optical scattering.

Compared to other thin-film deposition techinques, ion beam sputtering has several advantages. The sputtered ions typically have a relatively high kinetic energy (several eV), which means that the coating atoms tend to adhere more strongly to the substrate and the coating has a relatively high density compared to coatings deposited by other techniques [109]. Ion beam sputtering produces coatings with fewer impurities than other techniques, and the coatings

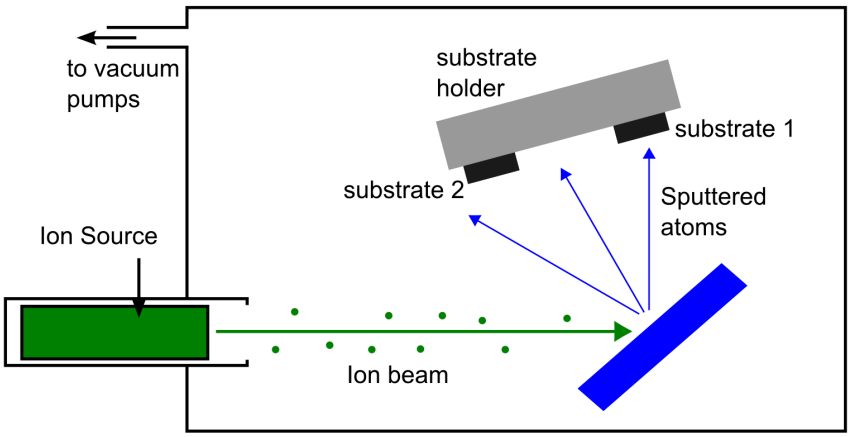

Fig. 3.1 A schematic diagram of a simple ion beam sputtering chamber

produced exhibit lower optical absorption than comparable coatings deposited by other techniques [106].

3.2.2 Atomic layer deposition

It is of interest to study coatings deposited by different deposition processes, since advances in the respective technologies may result in better coatings over time. It is also of interest to study changes in mechanical loss as a result of the differences in atomic stucture due to the deposition process used, since this may give information as to how to create low loss coatings.

As described in [110], atomic layer deposition (ALD) is a coating deposition process in which a coating is grown layer by layer, rather than sputtered. The substrate is typically treated to functionalise the surface, making it chemically reactive. Once placed into an evacuated coating chamber, a precursor gas is fed into the chamber, which reacts with the substrate surface. Once the precursor has reacted with the entire surface to be coated, the excess precursor and reaction by-products are flushed from the chamber by means of an inert carrier gas. A second precursor gas is then injected into the chamber, reacting with the surface of the coating formed by the first precursor. The excess precursor and reaction by-products from the second stage of deposition are then purged from the chamber. The process then repeats, injecting each precursor sequentially until the desired coating thickness has been reached. Each precursor stage is referred to as a half-reaction, with half of the desired coating material deposited during each stage. The ALD process is typically carried out with the substrate

held at temperatures below 350 °C [110]. This is significantly higher than the substrate temperature during IBS deposition which is typically 50-100 °C, depending on the material being deposited.

The ALD technique has the advantage that the coating is deposited layer by layer, giving good control over the thickness of the film. The thickness of a coating may easily be tailored by changing the number of ALD cycles, with coating typically deposited at a rate of less than 1 Å/cycle [110].

3.2.3 Magnetron sputtering

The basic sputtering process involves bombarding a target with ions, as described in section 3.2.1. The ions are generated in a glow-discharge plasma in front of the target, bombard the target surface and eject atoms which later condense on the substrate surface, forming the coating. The ions also eject secondary electrons from the target. These electrons are essential to maintaining the plasma which generates the sputtering ions [111]. The basic sputtering process is limited by low deposition rates and low ionisation efficiencies within the plasma [111].

Magnetron sputtering improves upon the basic sputtering process through the use of magnetic fields, aligned parallel to the target surface in order to constrain the motion of the electrons emitted by the target [111]. This magnetic field traps the electrons in a region close to the target in order to increase the probability of an ionising electron-atom collision. This creates a dense plasma, which causes higher rates of ion bombardment of the target, increasing the sputtering rate [111].

3.2.4 Molecular beam epitaxy

The methods of coating deposition already discussed are typically used to produce amorphous thin films. However, crystalline coatings are also of interest, and are discussed in detail in Chapter 7. Molecular beam epitaxy is a method of growing single-crystal coatings on a crystalline substrate. During coating growth, the substrate is placed in a vacuum chamber. A molecular beam of the coating material is typically produced by the evaporation or sublimation of a suitable material within an ultra-pure crucible. The coating material adsorbs onto the surface of the substrate, where it then migrates on the heated

surface until it interacts in proximity of a vacant lattice site, and condenses. The coating is grown layer by layer, and the lattice parameter of the coating typically matches that of the substrate to within 10%.

3.3 Previous measurements of coating mechanical loss

The mechanical loss of thin films has been subject to investigation at the University of Glasgow for over a decade [112]. Examples of measurements of a similar format to those carried out within this thesis are listed here.

The mechanical loss of silica cantilevers manufactured by laser welding silica ribbons to a thicker clamping block were developed and studied by I. Martin [113]. These samples were later used to characterise the mechanical loss of tin oxide (SnO) conductive coatings [113].

The mechanical loss of silicon cantilever substrates in the temperature range 77-300 K were characterised by S. Reid [114]. The substrates were later characterised in the temperature range 10-300 K by I. Martin [113]. I. Martin characterised the mechanical loss of silica, tantala and titania-doped tantala coatings deposited by IBS on silicon cantilevers [4, 115, 116]. M. Abernathy characterised the mechanical loss of IBS hafnia coatings deposited on silicon cantilevers [6].

Coating loss measurement techniques using silica disks suspended by wires were developed by A. Cumming [3]. This technique was used to measure the mechanical loss of a diffractive coating fabricated from silicon [3].

3.4 Cantilever measurements

3.4.1 Technique

The use of cantilevers to measure coating loss was first described by Berry and Pritchett in 1975 [7]. Mechanical loss is the fraction of the total energy which is lost per cycle of oscillation, normalised over the energy stored in the system. The mechanical loss of a cantilever may be measured by exciting its resonant

bending modes in turn, and monitoring the decay of oscillation amplitude in each case. During decay, the amplitude of oscillation takes the form:

$$A(\omega_0) = A_0 \exp\left(\frac{-\phi(\omega_0)\omega_0 t}{2}\right), \tag{3.1}$$

where A is the amplitude of the oscillations at time t, ω_0 is the angular resonant frequency, and A_0 is the amplitude at $t = 0$. The mechanical loss can be found by measuring the time that the amplitude takes to decay to $1/e$ of the initial amplitude.

The n^{th} bending mode of a cantilever, of frequency f_n can be calculated from [117]:

$$f_n = (k_n L)^2 \frac{a}{2\sqrt{3}L^2}\left(\frac{Y}{\rho}\right)^{\frac{1}{2}}, \tag{3.2}$$

where the cantilever has thickness a, length L and has a Young's modulus and density of Y and ρ respectively. Here, $k_n L$ is a mode dependent constant and has the values 1.875 ($n = 1$), 4.694 ($n = 2$), 7.853 ($n = 3$), 10.996 ($n = 4$), and 14.137 ($n = 5$). For $n > 5$, $k_n L$ can be approximated as $k_n L = \frac{\pi}{2}(2n - 1)$. In order to measure the mechanical loss of a cantilever, one must excite the vibration of these modes. The practical method for this is discussed in section 3.4.2.

So far, we have discussed how to measure the mechanical loss of a cantilever. However, we are interested in the mechanical loss of coatings, from which full cantilevers may not be easily fabricated. The mechanical loss of coating materials may be measured by creating free-standing structures by etching away part of the substrate after deposition. However, any dissipation arising from the adhesion of the coating to a substrate is of interest since mirror coatings are deposited upon substrates, and these free-standing structures typically have resonant frequencies much higher than the detection band of gravitational wave detectors. Therefore, the coatings studied here are applied to cantilever substrates and the mechanical loss of the coating is calculated from the loss of the coated sample. First, the mechanical loss of the cantilever substrate is measured before the coating deposition, or the loss of a nominally identical uncoated cantilever control sample is measured. Next, the coated cantilever is measured. During the amplitude decay of the coated cantilever's vibrations,

the energy lost is a combination of the energy lost in both the substrate and the coating:

$$E_{\text{lost,coated}} = E_{\text{lost,substrate}} + E_{\text{lost,coating}}. \tag{3.3}$$

Dividing both sides by a factor of 2π times the energy stored in the coated cantilever during oscillation, we find the dissipation of the coated cantilever:

$$\frac{E_{\text{lost,coated}}}{2\pi E_{\text{stored,coated}}} = \frac{E_{\text{lost,substrate}}}{2\pi E_{\text{stored,coated}}} + \frac{E_{\text{lost,coating}}}{2\pi E_{\text{stored,coated}}} \tag{3.4}$$

However, when the coating is thin compared to the substrate, we can approximate that $E_{\text{stored,substrate}} \approx E_{\text{stored,coated}}$. With this approximation and the definition of mechanical loss given in equation 2.16, we can see that:

$$\phi_{\text{coated}} \simeq \phi_{\text{substrate}} + \frac{E_{\text{lost,coating}}}{2\pi E_{\text{stored,substrate}}}, \tag{3.5}$$

where the second term is the mechanical loss of the coating multiplied by the ratio of energy stored in the coating to that stored in the cantilever:

$$\phi_{\text{coated}} \simeq \phi_{\text{substrate}} + \frac{E_{\text{stored,coating}}}{E_{\text{stored,substrate}}}\phi_{\text{coating}}. \tag{3.6}$$

Therefore, the mechanical loss of the cantilever may be calculated if we measure the loss of a cantilever before and after coating from:

$$\phi_{\text{coating}} \simeq \frac{E_{\text{stored,substrate}}}{E_{\text{stored,coating}}}(\phi_{\text{coated}} - \phi_{\text{substrate}}). \tag{3.7}$$

Under the assumption, stated above, that the substrate is much thicker than the coating, the energy storage ratio in this equation may be calculated from the Young's moduli and thicknesses of the substrate and coating [118]:

$$\frac{E_{\text{stored,substrate}}}{E_{\text{stored,coating}}} = \frac{Y_{\text{substrate}} t_{\text{substrate}}}{3 Y_{\text{coating}} t_{\text{coating}}}. \tag{3.8}$$

As shown in [118] and explained below, the energy storage ratio in the case where the substrate is much thicker than the coating, may be derived. However, in the case where the coating cannot be assumed to be thin compared to the substrate, this ratio must be calculated by a numerical method such as by Finite Element Analysis (FEA).

The ratio of elastic energy stored in the substrate to the energy stored in the coating may be calculated by considering a beam of thickness a, width b, and length L. The beam has a thin coating of thickness t, and is bent into the arc of a circle of radius R. A diagram of the system is shown in figure 3.2.

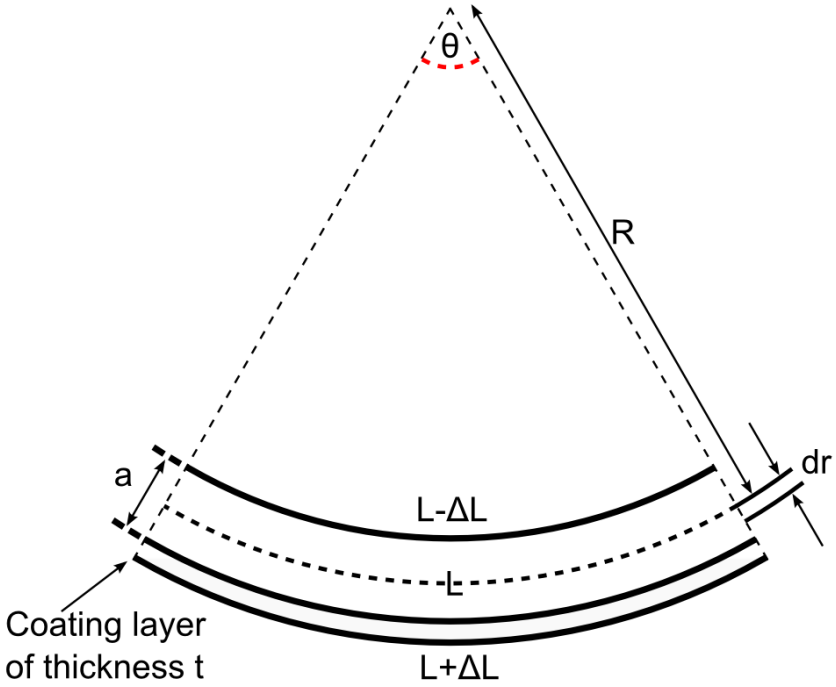

Fig. 3.2 A beam of width b and thickness a with a thin coating of thickness t applied to one face. The beam is bent into the arc of a circle of radius R.

The elastic strain energy stored in the coating layer, E_c, is given by:

$$E_c = \frac{Y_c t b}{2L} \Delta L^2, \tag{3.9}$$

where Y_c is the Young's modulus of the coating, and the change in length Δ_L is given by:

$$\Delta L = \frac{a}{2}\theta. \tag{3.10}$$

The energy stored in the half of the beam under compression may be expressed as:

$$dE = \frac{Y_s b \Delta L^2}{2L} dr, \tag{3.11}$$

where Y_s is the Young's modulus of the substrate and $\Delta L = (r-R)\theta$. Integrating over the half of the beam under compression gives:

$$\frac{E_s}{2} = \int_R^{R+\frac{a}{2}} \frac{Y_s b\theta^2}{2L}(r-R)^2 dr = \frac{1}{48}\frac{Y_s b\theta^2 a^3}{L}. \tag{3.12}$$

Under the assumption that the energy stored in the half of the beam under tension is the same as the energy stored under compression, the total energy in the beam is double that calculated in 3.12. Combining the expressions for the energy stored in the coating layer with that stored in the substrate (equations 3.9 and 3.12 respectively), it can be shown that the ratio of elastic energy stored in the substrate to that stored in the coating is given by [118]:

$$\frac{E_s}{E_c} = \frac{Y_s a}{3Y_c t}. \tag{3.13}$$

3.4.2 Apparatus

A schematic diagram of a loss measurement setup is shown in figure 3.3. The cantilevers are clamped in stainless steel clamps inside vacuum tanks which are subsequently evacuated to a pressure of $< 1 \times 10^{-5}$ mbar. This reduces the effect of gas-damping which would otherwise be the dominant source of dissipation [119]. The tightness of the stainless steel clamps are crucial to measuring mechanical loss. If they are too loose, excess energy from the oscillating cantilever will be dissipated by motion at the clamping interface, while if they are too tight, the cantilevers are liable to break. After several cantilever breakages, the surfaces of the clamp were mirror polished to reduce surface roughness, and reduce the probability of a fracture. This polishing was carried out using a Struers Labo-Pol-4 [120] lapping machine, combined with 1μm MicroPolish [121].

The following process is followed in order to clamp a cantilever. The bolts of the clamp are loosened and removed. The top block of the clamp is also removed. A cantilever is placed on top of the clamp, with the clamping block of the cantilever in the position desired after clamping. The top block of the clamp is then placed on top of the cantilever, and pressure applied centrally to ensure the top block is level during clamping. One bolt is then inserted through each side of the top block, and screwed into the main body of the clamp. If the top block is not level when the bolts are tightened, a differential pressure may

break the clamping block of the cantilever. The bolts are tightened as much as possible without breaking the cantilever.

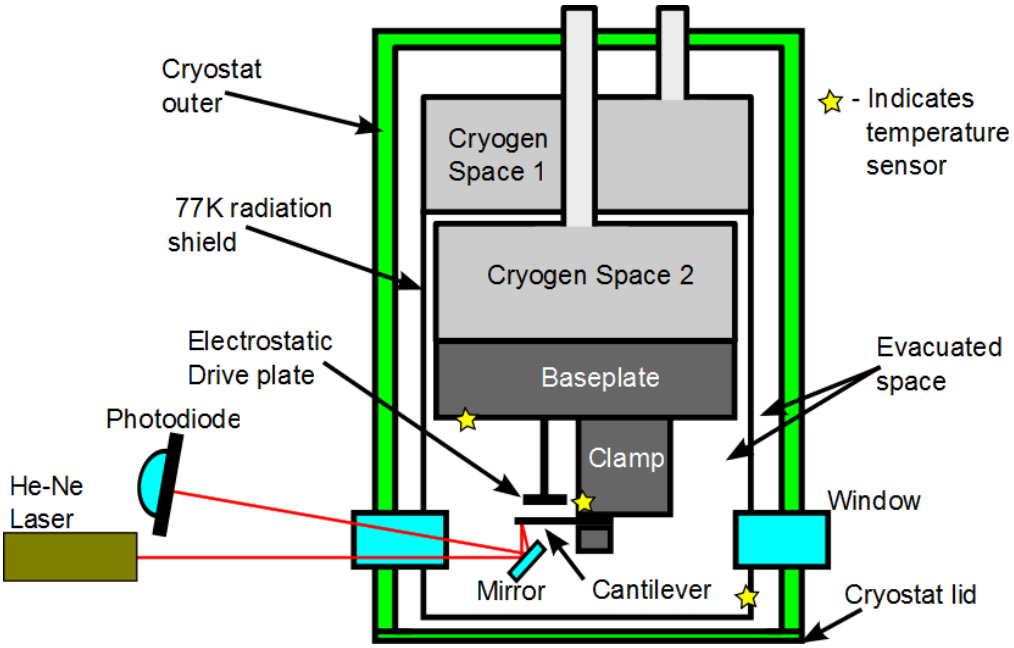

Fig. 3.3 A schematic diagram of the cryostats used for mechanical loss measurements. Cryogen spaces 1 and 2 are filled with nitrogen and helium respectively to cool the sample by conduction to ~10 K. This allows mechanical loss to be characterised in the region 10-300 K. The sample temperature is taken to be the same as that of the clamp as measured near the clamping block of the cantilever. The experimental volume is evacuated during measurement, and an electrostatic drive plate is used to excite the resonant modes of the cantilever.

The temperature of the clamp is measured in close proximity to the cantilever using a Lakeshore DT-670 silicon diode temperature sensor. The same type of sensor is also used elsewhere in the cryostat and are typically accurate to ± 0.01 K at 10 K, and to ± 0.03 K at room temperature [122]. The free end of a silicon cantilever is assumed to be the same temperature as the clamped section because silicon has a relatively high thermal conductivity of 140 W/(m K). Additionally, two heaters are connected to the clamp to control the temperature of the cantilever during cryogenic measurements. The cantilever temperature is regulated using the PID control function of a Lakeshore 340 temperature controller, which changes the power of the heaters attached to the clamps to acheive the desired temperature. Measurements are only carried out once the sample temperature has stabilised, when the rate of change of clamp temperature has reduced to below $\frac{dT}{dt} = 0.01\,\mathrm{K hr}^{-1}$.

One bending mode of the cantilever is excited by applying a high voltage oscillating signal at the frequency of interest, with a d.c. offset on the order of 1 kV to an electrostatic drive plate, which is placed around 5 mm above the cantilever. The d.c. offset acts to polarise the sample, and the applied a.c. signal provides a driving force at the chosen frequency.

In this thesis, two methods have been used to read out the relative amplitude of vibration of cantilevers: shadow sensing and the use of an optical lever. Each method is described below. In both cases, the laser and photodiodes used are placed outside of the vacuum chamber to allow easy adjustments to be made to the optical alignment. Once the amplitude of a bending mode is excited to as high an amplitude as possible, which is typically at least a factor of 10 above the background noise of the sensors, the excitation signal is switched off. The amplitude then decays with the form given in equation 3.1.

The cryostats used are capable of being cooled using liquid nitrogen and liquid helium. This allows the mechanical loss of coatings to be measured in the region of approximately 10-300 K. The process for measurement of samples at low temperature is as follows. A cantilever is secured firmly in the stainless steel clamp. Next, the tank is closed and evacuated. The relevant optics, described in sections 3.4.2 and 3.4.2, are aligned for a relative displacement amplitude measurement. The resonant frequency of the fundamental bending mode is found by connecting the photodiode output to a spectrum analyser, which displays a Fourier transform of the time series. From the cantilever dimensions, the fundamental mode is known to be in the range 50-100 Hz for all cantilevers used in this thesis. The higher order bending mode frequencies are then calculated from the frequency of the fundamental mode using equation 3.2. Mechanical loss measurements are carried out to test the quality of the clamping by checking that the loss of the silicon cantilever is dominated by thermoelastic dissipation. This is carried out by comparing the room temperature mechanical loss as a function of frequency with the thermoelastic dissipation calculated for a cantilever of the same dimensions. If the mechanical loss is not dominated by the thermoelastic dissipation, the cantilever is reclamped to reduce clamping loss until the thermoelastic dissipation is the dominant source of loss. Cooling is then carried out by filling cryogen spaces 1 and 2 (as labelled in figure 3.3) with liquid nitrogen. A stable temperature at the clamp, baseplate and nitrogen shield is typically reached approximately six hours after the spaces have been

filled with nitrogen. The liquid nitrogen is then removed from cryogen space 2 by blowing it out with nitrogen gas. Cryogen space 2 is then filled with liquid helium. After filling with liquid helium, the sample reaches temperatures as low as 10 K after approximately 90 minutes. Ringdown measurements of several bending modes are then carried out at the lowest temperature reached by the cryostat. The sample is then heated and its temperature stabilised at a desired measurement temperature where further ringdown measurements of each bending mode are carried out. This process is carried out in temperature increments of 1 K in the range 10-50 K, increments of 2 K in the range 50-100 K and then increments of 5 K until 300 K is reached. The entire process, from clamping a cantilever to the end of mechanical loss measurements, typically lasts 5 days.

Shadow sensors

A shadow sensing arrangement is a method of vibrational amplitude readout which senses the motion of the shadow of a cantilever. A schematic diagram of such a system is shown in figure 3.4. A laser beam illuminates the edge of the cantilever such that a shadow of the cantilever is cast onto a split photodiode sensor. The equilibrium point of the cantilever is aligned with the split between the photodiodes. A lens is used so that the gap between the photodiodes is much thinner, by a factor of at least ten, than the cantilever shadow. The split photodiode is positioned such that the cantilever shadow is centered around the gap between the photodiodes. This is represented by the time series having zero d.c. offset. The current created by one photodiode is subtracted from that created by the other photodiode. As the cantilever moves from its equilibrium position to the upper extremity of its motion, the shadow covers the upper photodiode and the lower photodiode produces a relatively larger current, producing a positive peak in the output signal. The shadow then moves to its lower extremity, covering the lower photodiode and the difference between the signals is now a negative peak (it is arbitrary which photodiode is designated as positive and negative). In time, this produces a sum of sinusoidal waves which can be deconstructed using Fourier methods so that the frequencies of oscillation may be recorded. This subtraction method removes most of the background noise such as that from the room lighting, daylight etc.

The shadow sensor does not require the cantilever to have a high reflectivity. This is particularly beneficial for measurements involving silica cantilevers, where the cantilever would transmit most of the incident laser power if an optical lever was used.

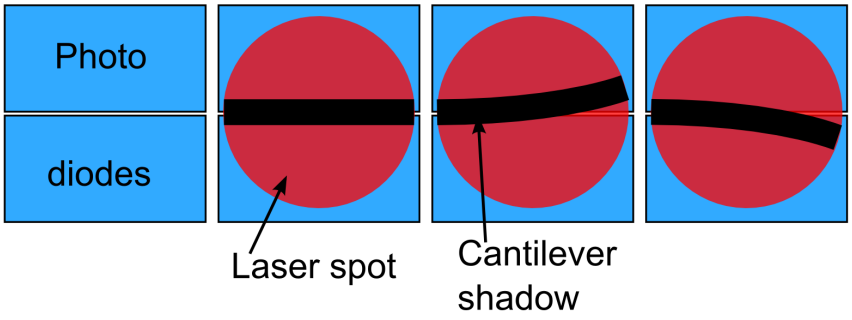

Fig. 3.4 A shadow sensor measures the displacement of a cantilever by the difference in currents created by two photodiodes. The current difference is due to the difference in incident light intensity created by the cantilever shadow.

Optical levers

A schematic of an optical lever is shown in figure 3.5. A laser beam is incident upon the surface of a cantilever, ideally at a vibrational antinode. As the cantilever oscillates at some frequency, the reflected laser beam will vary in position with the same frequency. A folding mirror is used so that the laser beam can enter and exit the cryostat through the same window. The reflected laser beam is then focussed onto a split photodiode sensor, and the laser beam position is read out by subtracting the signal of one photodiode and then amplified in a similar fashion to that used in a shadow sensor system.

The optical lever readout has the advantage that it is more sensitive at higher frequencies than the shadow sensor. This is in part due to the fact that laser spot samples a small area of the face of the cantilever, whereas the shadow sensor is sensitive to the average motion of a finite section of the cantilever length. For higher frequency bending modes, the shadow readout begins to be sensitive to additional vibrational antinodes. This acts to reduce the sensed signal since the sensor is averaging over motions in two different directions. The shadow sensor used here is capable of measuring the motions of bending modes with frequencies below approximately 9 kHz. The optical lever readout is capable of measuring modes with frequencies as high as 18 kHz.

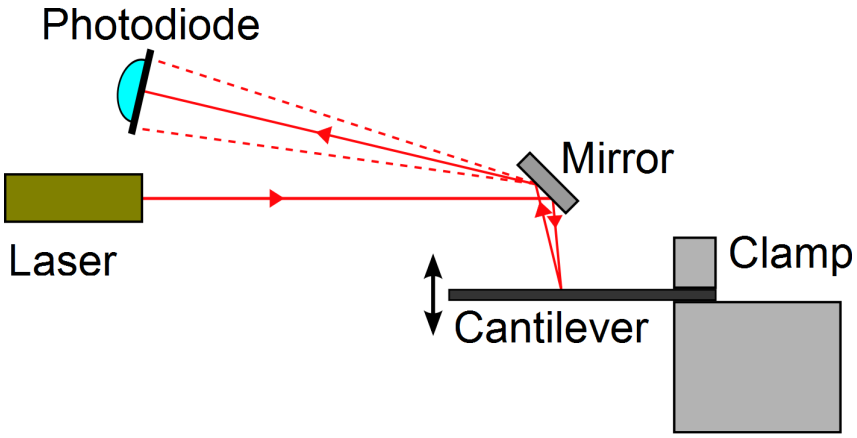

Fig. 3.5 A shadow sensor measures the displacement of a cantilever by the difference in currents created by two photodiodes. The current difference is due to the difference in incident light intensity created by the cantilever shadow.

3.4.3 Silica cantilevers

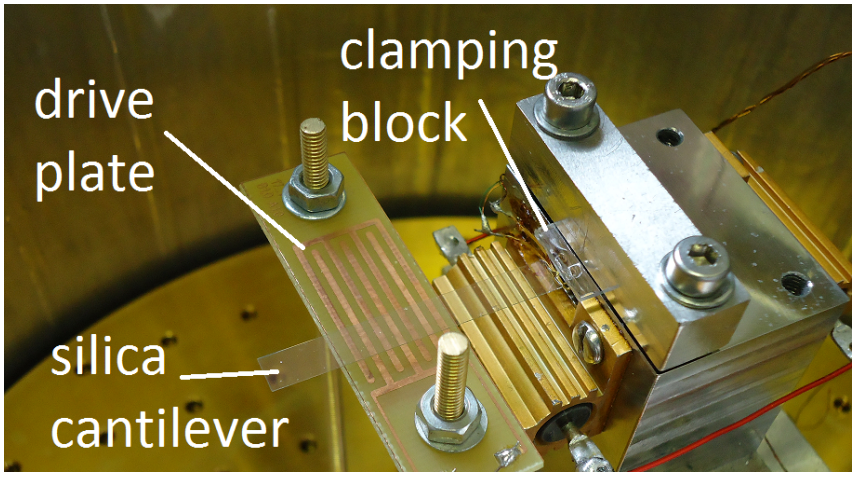

Fig. 3.6 A silica cantilever is shown, clamped at one end. The electrostatic drive plate used to excite the bending modes of the cantilever may be seen underneath the cantilever as a combed design printed on a circuit board.

The choice of geometry and material for the cantilever substrate is important. For thin, low-loss coatings, it is important to ensure that a sufficient fraction of the total energy in the system is stored in the coating to allow the coating dissipation to be probed. In particular, the cantilever substrate must be of low mechanical loss.

At room temperature, bulk fused silica has been shown to exhibit a mechanical loss as low as 1×10^{-8} [123, 124]. Fused silica also has a low thermoelastic

loss, meaning that silica exhibits low loss at room temperature. The dissipation of silica cantilevers is typically a few 10^{-6} at low frequency at room temperature. As a result, this is the substrate material of choice for determining the mechanical loss of coatings for measurements at room temperature. The cantilevers consist of a thin section of dimension $42 \times 5\,\mathrm{mm}$ and are of thicknesses between $\sim$100-160 μm. The thin section is the oscillating part of the cantilever, which is welded at one end to a silica block of dimensions $\sim 10 \times 10 \times 1\,\mathrm{mm}$. This thick section is referred to as the clamping block, and is the end which is clamped in the stainless steel clamp. The use of a clamping block reduces stick-slip loss at the clamping interface, which may arise from some degree of freedom of movement of the cantilever in the clamp [125]. A study by Quinn showed that having a clamping block much thicker than the flexure ensures that the bending point occurs outwith the jaws of the clamp, which reduces the tendency of the flexure to slip within the clamp [125]. Additionally, the clamping block can be used for handling the sample without damaging the surface of the cantilever or any coatings deposited, it is less likely to break during clamping than if the thin section were to be clamped, and it defines the cantilever length during clamping, ensuring that the resonant frequencies of the cantilever do not change significantly with reclamping. A clamped silica cantilever is shown in figure 3.6

3.4.4 Silicon cantilevers

While silica cantilevers are used for mechanical loss measurements at room temperature, they have several features which make them unsuitable for cryogenic measurements. Firstly, silica has a low thermal conductivity, $1.4\,\mathrm{W/(m\,K)}$, meaning that if the sample is being temperature controlled via conduction from its clamped end, this can lead to long timescales being needed to reach the desired temperatures along the complete sample. Secondly, previous studies have shown that the loss of silica increases at low temperature, exhibiting a large, broad dissipation peak at around 40 to 60 K [123, 126, 127], decreasing the sensitivity to any coating dissipation. For these reasons, a different material must be used for cryogenic coating loss measurements.

Crystalline silicon is used to make cantilever substrates for cryogenic coating loss measurements since it exhibits relatively low mechanical loss at low temperatures, which minimises the substrate contribution to the measured loss when

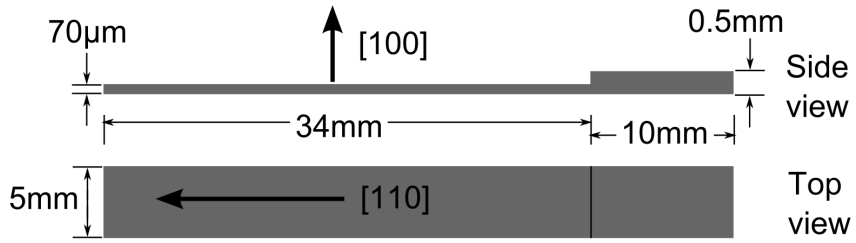

Fig. 3.7 A schematic diagram of a silicon cantilever with the relevant crystal axes shown. The thin, flexing part of the cantilever is 34 mm long, 5 mm wide, and typically around 70 μm thick. The thicker protrusion on the right is the clamping block, which is typically 500 μm thick. Coatings are applied to the largest face of the cantilevers.

cooled [128]. A study by Nawrodt et al. shows that at 10 K, uncoated silicon cantilevers of the approximate dimensions of interest here may reach losses of 1×10^{-7} or below, depending upon sample preparation [129]. Uncoated silicon cantilevers in this thesis typically reach losses of 2×10^{-6} or below at 10 K, which is sufficiently low to be sensitive to the loss of coatings. These cantilevers are manufactured from single crystal silicon wafers, which are double side polished, and with the [110] crystal axis oriented parallel to the long dimension of the cantilever, and the [100] axis oriented perpendicular to the long dimension of the cantilever. The cantilevers used have dimensions approximately 34×5 mm and thicknesses of their flexing part which are usually between 50-70 μm. As is the case for silica cantilevers, they also have a clamping block on one end that is approximately 10×5×0.5 mm in size. A diagram of a silicon cantilever is shown in figure 3.7.

The mechanical loss of a silicon cantilever at room temperature is shown in figure 3.8, alongside the loss of a silica cantilever. The loss of the silicon cantilever shows the same frequency dependence as the thermoelastic loss, which is the dominant source of loss for the cantilever. It can be seen that the mechanical loss of the silica cantilever is lower than that of the silicon cantilever at all frequencies. The loss of the silica cantilever is not dominated by the thermoelastic loss, and shows a different frequency dependence to the calculated thermoelastic loss.

Discussions with commercial vendors of IBS coatings have indicated that some IBS coatings do not adhere properly to the surface of silicon, and that the growth of a very thin thermal oxide layer on the surface of the sample

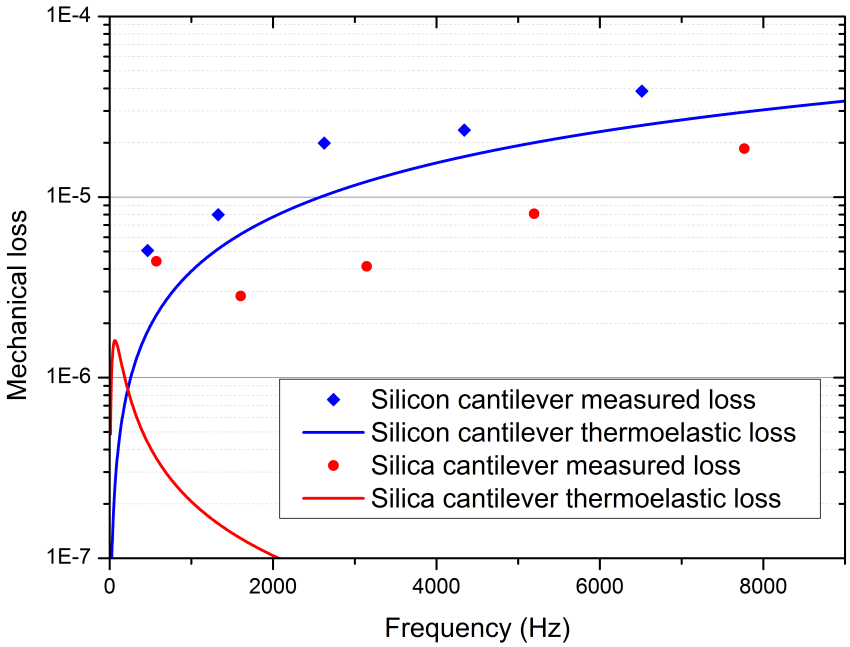

Fig. 3.8 The room temperature mechanical loss of a silica and a silicon cantilever at room temperature, showing that the loss exhibited by the silica cantilever is lower at all frequencies.

can significantly improve adhesion [130]. Silicon typically has a native surface oxide layer ∼2-3 nm thick. Before coating deposition, the silicon cantilevers studied here were typically placed into an oven at 1000 °C for 15 minutes. This creates a ∼20 nm thick layer of amorphous silicon dioxide on all surfaces of the cantilever, which is measured by ellipsometry. The hypothesis that oxidising silicon cantilevers prior to coating promotes adhesion is tested in Appendix A.

3.5 Disk measurements

The mechanical loss of coatings may also be measured by comparing the dissipation of coated and uncoated disks. This may be done where cantilever substrates cannot be manufactured from a chosen material, or in the case where coating vendors are not able to deposit coatings onto cantilevers.

Two methods of supporting disks are presented here, both of which support the disk by the vibrational nodes of particular sets of modes to minimise energy loss into the support structure and thus enable an accurate measurement of the loss of the disk.

The frequencies of vibration for these disks are obtained by finite element analysis, and the resonant modes are excited using an electrostatic drive method similar to that used in cantilever measurements.

3.5.1 Nodal suspension

The nodal suspension technique was developed by A. Cumming, and involves suspending the disk between two 50 µm thick tungsten wires, which contact the disk at vibrational nodes for the modes of interest [3]. Since the disk is contacted by the wires at vibrational nodes, the energy lost into the suspensions is minimised. A schematic diagram of a disk suspended by this technique is shown in figure 3.9, and a photo of a 76 mm diameter suspended silica disk is shown in figure 3.10. The method of suspending a disk is as follows: the two clamps are loosened to allow wires to be inserted and clamped. Additionally, one of the clamps is loosened from the baseplate to allow initial longitudinal motion along a slot cut into the base-plate. Two wires are held taut and clamped at each end, parallel to each other and separated by ∼1-2 mm. The wires are then slackened by moving one clamp towards the other, so that a disk may fit between them. Next, the disk is inserted between the wires, around halfway between the two clamps, and resting on a temporary support. The wires are then tensioned by pulling the loose clamp, ensuring that the contact points of the wires with the disk are diametrically opposite each other. The wire tension is adjusted by altering the position of the loose clamp before it is bolted down. The tension must be high enough to ensure that the disk is adequately supported, but not so tight that the wires break [3].

Mechanical loss measurements presented in this thesis using the nodal suspension technique use an interferometric read out to obtain the amplitude of disk vibration.

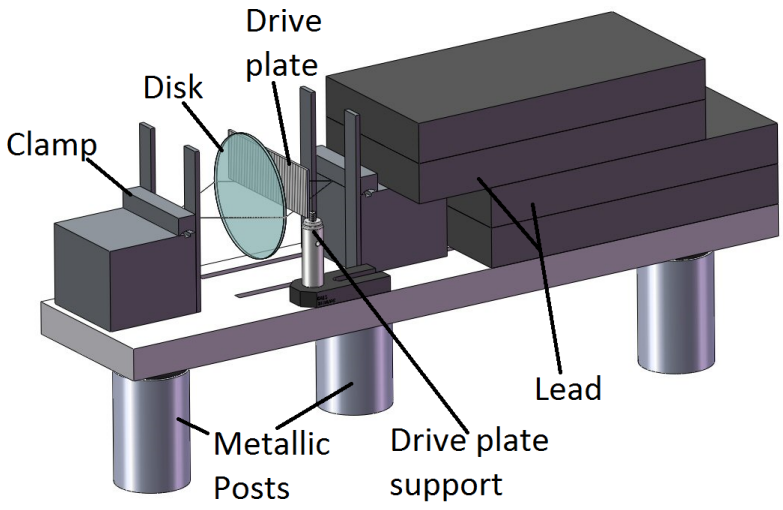

Fig. 3.9 A schematic diagram of the nodal suspension system. A disk is suspended by two wires, which are placed under tension and each clamped at both ends. An electrostatic drive plate is placed behind the disk and used to excite the resonant modes of the disk. To reduce the effect of any external vibrations on the system, the setup is placed on metal posts, with rubber rings placed between the baseplate and the tops of the posts. Additionally, lead is placed on top of the baseplate to prevent the system from moving. Figure reproduced from [3].

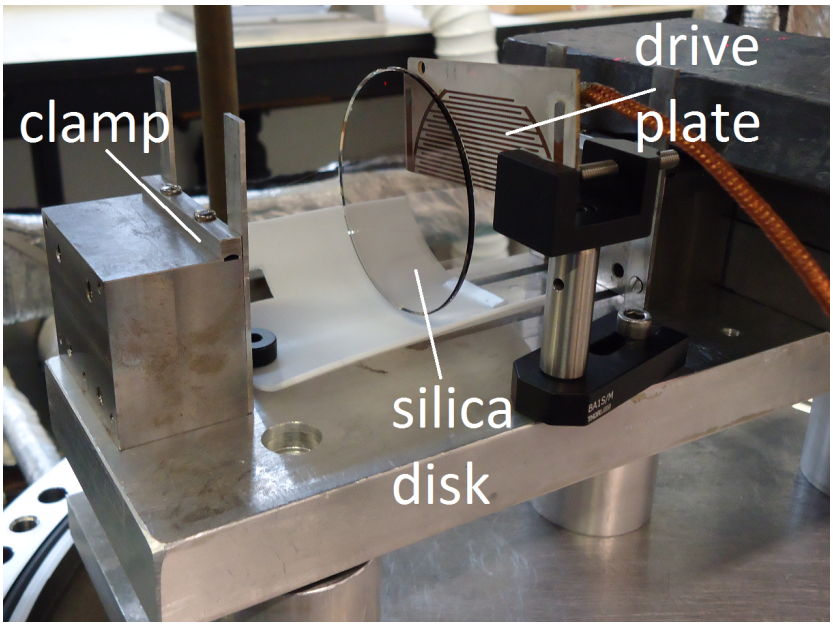

Fig. 3.10 A photo of a silica disk in the nodal suspension.

Interferometric displacement readout

Mechanical loss measurements of suspended disks were carried out using an interferometer to sense the ringdown of the resonant motion of the disk. The interferometer used was constructed by A. Cumming [3]. A schematic diagram of the interferometer read-out is shown in figure 3.11. The interferometer has two arms. One of these arms uses the disk sample being measured as the end mirror. The other arm is folded with three mirrors which are mounted on two different types of actuator, which compensate for the low frequency motions of the disk. Two of the mirrors are mounted on small loudspeakers which filter out motions below approximately 30 Hz, and one is mounted on a piezoelectric transducer which correct for motions at frequencies below ∼100 Hz. The interferometer is locked halfway up an interference fringe so that length changes in the arm containing the disk result in both positive and negative feedback signals to the actuators.

To increase the accuracy of the mechanical loss measurements, a constant amplitude 10 kHz reference signal is injected into the interferometer through one of the loudspeakers. Any variation in light intensity at the photodiode due to fluctuations in laser power, or from random vibrations will be present in both the reference signal and the ringdown signal. The 10 kHz reference signal can be used as to remove these effects, acting as a correction signal. To record the reference signal, an additional lock-in amplifier and signal generator are required.

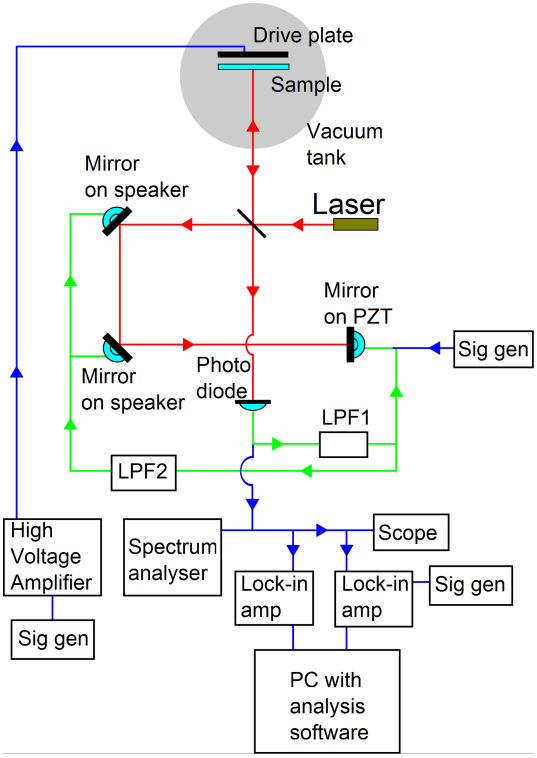

Fig. 3.11 A schematic of the interferometer used to measure the vibration of suspended disks. Red lines show the path of the laser, green lines show the path of the locking system and blue lines denote the detection, correction and excitation system.

3.5.2 Nodal support

The nodal support technique was developed by Numata et al. [131], who supported cylindrical bulk samples on ruby spheres. The technique was later adopted by Yamamoto et al. [132], who used a nodal support made entirely of copper. The nodal support system made by staff at the University of Tokyo and used in studies by Yamamoto was reused within this thesis, and is described below.

The nodal support technique uses a copper support system, shown in figure 3.12, to hold a disk such that the centre of the disk is the only part touching the support. This means that the mechanical loss of the disk may be measured only for modes which have a vibrational node at the centre of the disk. This has the disadvantage that fewer vibrational modes may be measured compared to the nodal suspension technique, but the advantage that a larger region of contact means that the disk temperature may be controlled by conduction. This is particularly useful for cryogenic measurements of large disks, which may become difficult to suspend in a nodal suspension. The vibrational amplitlude is measured using an optical lever.

During cryogenic measurements using the nodal support, three calibrated silicon diode temperature sensors were attached to the parts of the system shown in figure 3.12. A constant current source was connected to them, and the voltage across the diodes cross-referenced with the calibration curves for each, supplied by the manufacturer. The film heater on the top plate is used to change the disk temperature.

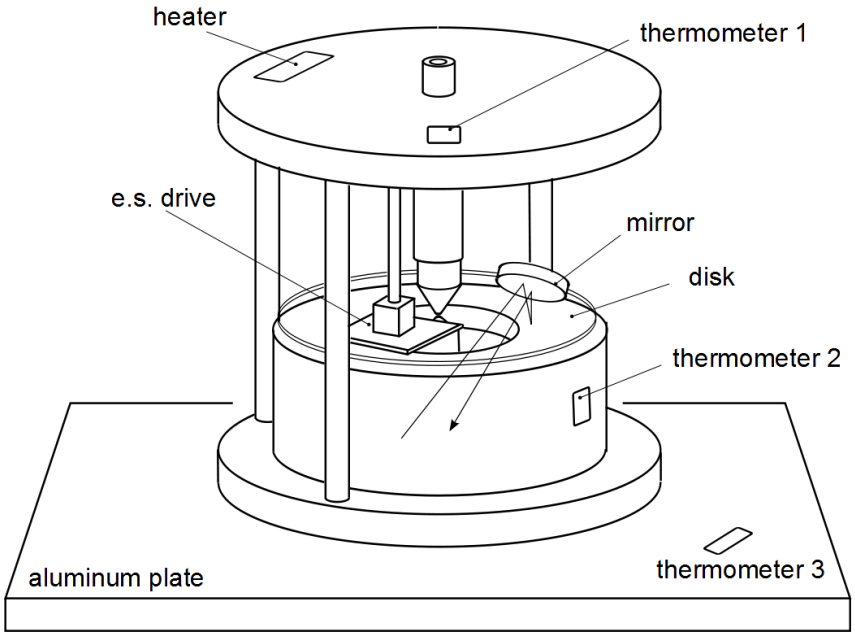

Fig. 3.12 A schematic of the nodal support. The support structure is made from copper to allow good thermal conductivity during cryogenic measurements.

3.6 Conclusions

The mechanical loss of coatings may be measured using a variety of sample geometries and measurement techniques. Using the silicon cantilevers described here, the mechanical loss of a coating may be measured with small temperature increments in the temperature range 10-300 K. Silicon cantilevers are generally treated in such a way as to grow a thermal oxide on their surfaces prior to deposition. For room temperature coating loss measurements, silica cantilevers must be used due to the relatively high thermo-elastic damping of silicon cantilevers, which reduces senstivity to coating dissipation.

Thin disks may also be used for coating loss measurements. Disks may be used for both room temperature and cryogenic mechanical loss measurements. This chapter has covered room temperature measurements only, with two different cryogenic disk measurement techniques described in chapters 6 and 7.

In Appendix C, the mechanical loss of a coating is presented as a function of coating thickness and substrate geometry in order to compare the methods described in this chapter. The mechanical loss of a DC magnetron niobia coating deposited on two silica cantilevers and two silica disks show that the coating mechanical loss is independent of both substrate geometry and coating thickness for this coating, within experimental error.

Chapter 4

Mechanical loss measurements of IBS titania-doped tantala thin films

4.1 Introduction

Detector projects such as KAGRA [59], and the planned Einstein Telescope [19] intend to use cryogenics to cool the detector mirrors to reduce thermal noise. However, studies have shown that both silica and tantala deposited by IBS show dissipation peaks at low temperatures [4, 115, 116]. The decrease in thermal noise gained by reducing the mirror temperature is therefore not as great as would be expected if these dissipation peaks were not present. In studies of bulk silica, a large, broad dissipation peak was observed, which is thought to arise from re-orientations of the Si-O bonds within a double-well potential [123, 126].

The nature of the loss peak observed in tantala is postulated to be similar to that seen in silica. However, the cause of the room temperature reduction in the mechanical loss of tantala due to titania-doping is not well understood. Research comparing the properties of tantala doped with titania to a cation concentration of 14.5%, and heat treated to 600 °C, to pure tantala heat-treated to the same temperature show that doping changes the distribution of activation energies associated with the low temperature loss peak observed in pure tantala [4].

Studies of pure tantala have shown that the distribution of activation energies associated with the low temperature dissipation peak is also affected by post-deposition heat-treatment. In this chapter, the mechanical loss of titania-doped tantala coatings are characterised, studying the effect of both heat-treatment and doping concentration. These measurements are of interest for future low-temperature detectors, since the magnitude of coating Brownian noise is determined by the dissipation of the coatings used. It is also of interest to study the low-temperature dissipation peaks exhibited by the coatings, which may give insight into the dissipation processes within the coatings, and thus aid design of future coatings intended for room temperature detectors. Here, the mechanical loss of an as-deposited 25% coating is compared to the same coating heat-treated to 400 °C. Additionally, the 55% as-deposited coating is compared to a 55% coating heat-treated to 600 °C.

While the mirror coatings used in gravitational wave detectors are deposited by ion beam sputtering (IBS), the exploration of alternative deposition methods is important for two reasons. Firstly, an alternative deposition method may produce a coating with a lower dissipation than an IBS coating. Secondly, coatings produced by different methods may show loss peaks from different dissipation processes which may be related to the differences in their respective atomic structures. Studying loss peaks may therefore allow a deeper understanding of the underlying loss mechanisms possible in a given material, depending on its structure.

Measurements of the metal-metal and metal-oxygen nearest neighbour distances in tantala as a function of heat-treatment may be found in [133–135]. This can be used to construct a detailed atomic model, constructed using molecular dynamics and reverse Monte Carlo modelling [133, 134]. This model allows access to information such as bond angle distributions and bond types [133, 134]. It may be possible to compare the bond angle and barrier height distributions in these models with those found from mechanical loss measurements. This would enable correlations between changes in the local structure of the coating materials with changes in the mechanical loss, which may be a result of changes in the deposition parameters, post-deposition heat-treatments, dopant, and doping concentration. Additionally, different deposition methods may produce coatings with radically different structures. Hence, it is of interest to study coatings deposited by different processes. In

Titania-doped tantala cantilever mode frequencies (Hz)				
Mode	AD 25%	400 °C 25%	AD 55%	600 °C 55%
2	505			
3	1411	1390	1224	1140
4	2750	2725	2390	2330
5	4547	4500	3940	3679
6		6717	5878	
7	9434	9374	8224	7707
8			10900	
9				13132
10				16392

Table 4.1 Resonant frequencies of the cantilevers using which an array of titania-doped tantala coatings were measured. AD stands for as-deposited, temperatures denote the temperature of heat-treatment and percentages refer to the level of titania doping within the coating.

this Chapter, mechanical loss measurements of a thin film of tantala fabricated by an atomic layer deposition process is studied. In table 4.1, a summary of the titania-doped tantala coatings studied is shown, along with the vibrational mode frequencies of the respective cantilevers upon which the coatings were deposited.

4.2 25% titania-doped tantala

Silicon cantilevers were prepared by the methods described in Chapter 3, with an oxide layer grown on the cantilever surfaces prior to coating deposition. A 25% titania-doped tantala coating was deposited by IBS a commercial vendor, CSIRO [136], with a coating thickness of 500 nm applied to the largest (bottom) face of the cantilever samples. One of these samples was left with the coating in an as-deposited condition. Other samples were heat-treated post-deposition to 300, 400 and 600 °C. One bottom-coated cantilever underwent each heat-treatment. The heat-treated samples were typically heated at a rate of 2 °C min^{-1} and kept at the desired temperature for 24 hours, after which the samples were allowed to cool naturally over night. Additionally, for each heat-treatment, one cantilever was chosen to remain uncoated, but was put through the same thermal cycle as its coated counter-part. This means that

any potential changes to the mechanical loss of the substrates as a result of heat-treatment are taken into account.

The mechanical loss of the as-deposited and 400 °C heat-treated coatings are presented below followed by a comparison of the two coatings.

4.2.1 As-deposited 25% titania-doped tantala

The temperature dependence of the mechanical loss of the as-deposited coating was measured using techniques described in Chapter 3. The mechanical loss of the coated cantilever, along with the calculated coating loss is shown in figures 4.1, 4.2, 4.3, and 4.4 for bending modes 3, 4, 5 and 7 respectively, with the modes in the frequency range 1.4-9.5 kHz. These figures also show the mechanical loss of an uncoated control sample, which was used to calculate the coating loss. Error bars are not shown, but are small on the scale of the graphs. Each point representing the mechanical loss of the coated cantilever and control sample at each temperature is an average of multiple measurements. A description of how data is combined is given in Appendix A. The variation in losses measured at each temperature point typically contributes a few per cent, while the uncertainty in substrate thickness contributes a further 3 per cent to the error in coating loss. The total uncertainty in coating loss from this combination is typically around 4%.

The coating losses were calculated using the mechanical loss of a control sample which was heat-treated to 600 °C. This sample was chosen as the control sample because the uncoated cantilever corresponding to the as-deposited coating was found to be much thinner than the coated cantilever. The heat-treated uncoated sample was chosen as a more appropriate control sample since at measurement temperatures above 150 K the dominant source of loss in the control sample is the thermoelastic loss, which is governed by the cantilever substrate thickness. Previous studies of uncoated silicon cantilevers by M. Abernathy show that the loss of an uncoated silicon cantilever heat-treated at 400 °C agrees with the loss of a silicon cantilever which did not go through the heat-treatment [137]. Also, since the control sample was placed in an oven at 1000 °C prior to coating, the additional heat-treatment at 600 °C is unlikely to change the mechanical loss significantly. The temperature dependent mechanical loss of the uncoated control sample was fitted with a piecewise

cubic Hermite polynomial to enable interpolation of the loss onto the same temperature points as the coated sample. The coating loss was calculated by subtracting the interpolated control data from the loss of the coated cantilever, and scaling by the appropriate energy ratio using equations 3.7 and 3.8.

The coating loss shows a dissipation peak at temperatures in the range 30-42 K, with the temperature at which the peak occurs increasing at higher frequencies.

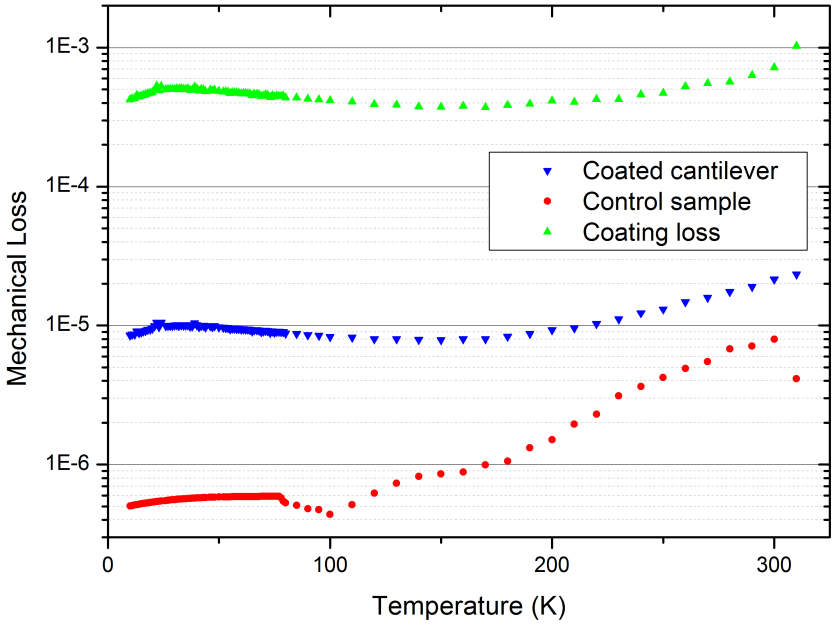

Fig. 4.1 The mechanical loss of a silicon cantilever coated with an as-deposited 25% titania-doped tantala coating, and the calculated coating loss for the third bending mode (1.4 kHz).

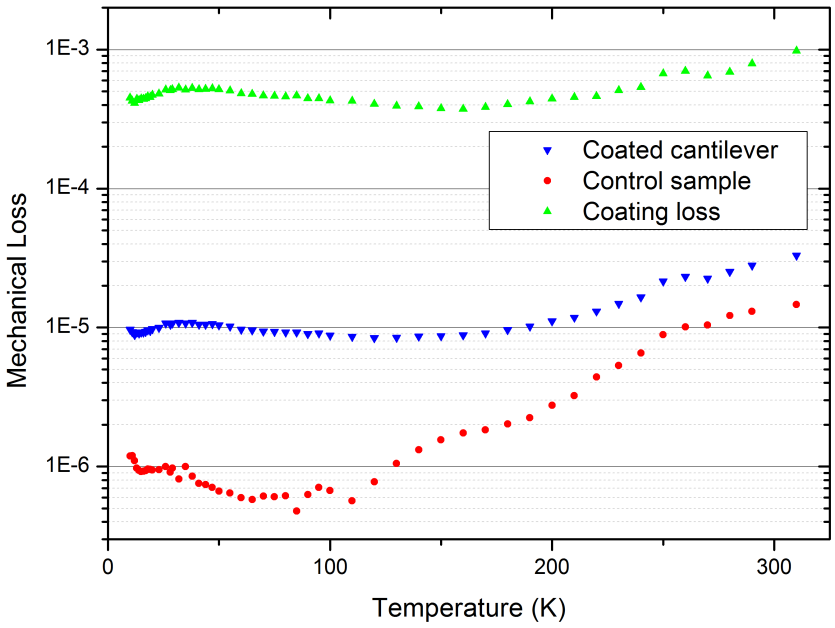

Fig. 4.2 The mechanical loss of a silicon cantilever coated with an as-deposited 25% titania-doped tantala coating, and the calculated coating loss for the fourth bending mode (2.8 kHz).

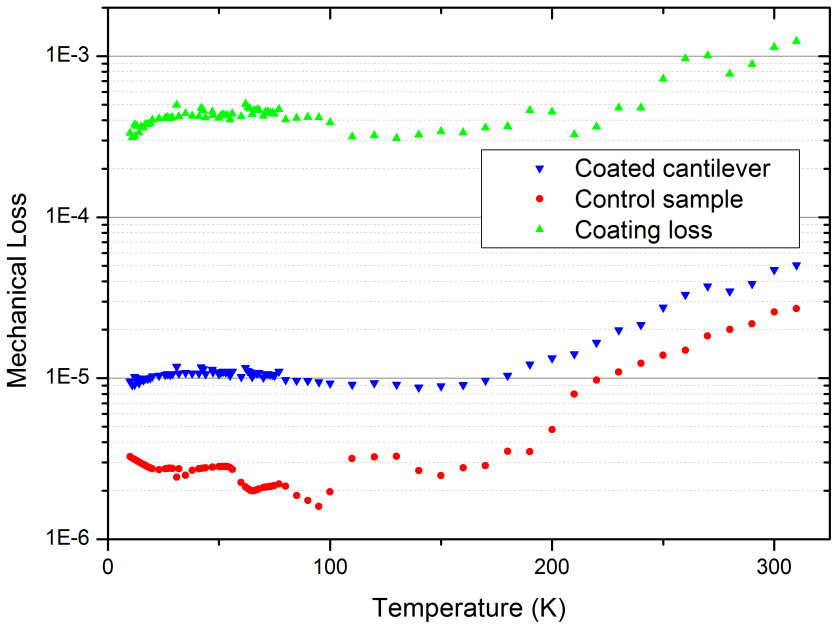

Fig. 4.3 The mechanical loss of a silicon cantilever coated with an as-deposited 25% titania-doped tantala coating, and the calculated coating loss for the fifth bending mode (4.5 kHz).

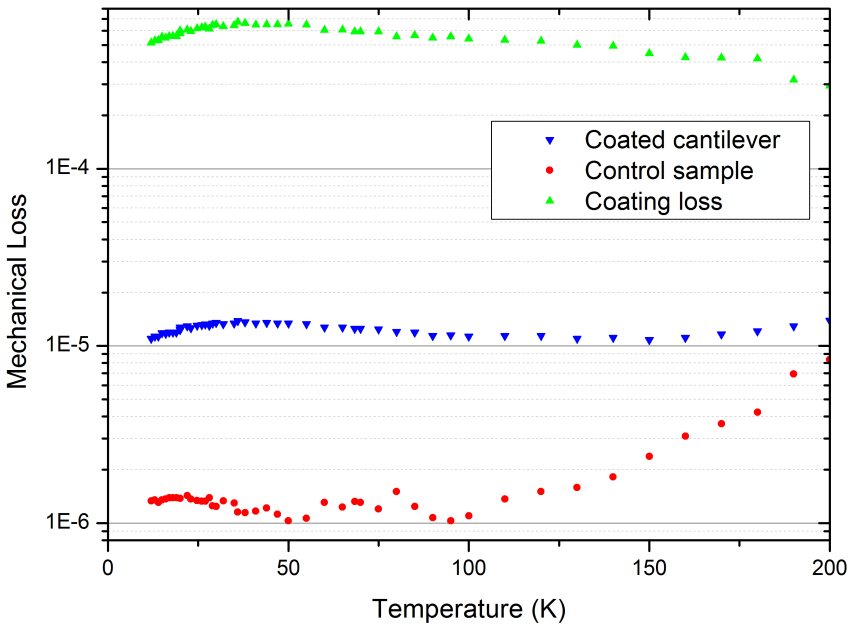

Fig. 4.4 The mechanical loss of a silicon cantilever coated with an as-deposited 25% titania-doped tantala coating, and the calculated coating loss for the seventh bending mode (9.5 kHz).

4.2.2 Analysis

The mechanical loss of the as-deposited 25% titania-doped tantala coating presented in figures 4.1, 4.2, and 4.4 shows a broad low temperature peak in each case. Dissipation peaks may arise if the cantilever resonance frequency is close a resonance of the clamp structure. However, observation of similar peaks in several modes across a wide range of frequencies generally indicates that the peaks are unlikely to be due to such coupling. If one assumes that the dissipation takes the form of a Debye peak, which is the case for most dissipation mechanisms [61], the loss may be expressed as:

$$\phi(\omega) = \Delta \frac{\omega\tau}{1 + (\omega\tau)^2}, \tag{4.1}$$

where Δ is a constant related to the magnitude of the dissipation, and τ is the relaxation time of the dissipation process [61]. One characteristic of dissipation peaks arising from a thermally activated process is that the temperature at which maximum dissipation occurs is a function of the resonant frequency. In a thermally activated process, the relaxation time is related to the activation energy E_a of the process by the Arrhenius equation [61]:

$$\tau^{-1} = \tau_0^{-1} e^{-E_a/k_B T}, \tag{4.2}$$

where τ_0 is the relaxation constant of the dissipation mechanism and k_B is the Boltzmann constant. Analysis of equation 4.1 shows that the dissipation peak occurs when $\omega\tau = 1$. Combining this condition with equation 4.2 gives the relation:

$$\ln(\omega) = -\ln(\tau_0) - \frac{E_\mathrm{a}}{k_\mathrm{B}} \frac{1}{T}. \tag{4.3}$$

Thus, a plot of the natural logarithm of the angular frequency of each resonant mode against the reciprocal of the peak temperature should be a straight line of gradient $E_\mathrm{a}/k_\mathrm{B}$, and y-intercept equal to the logarithm of the relaxation constant.

Peak fitting using a Gumbel probability density function was used to determine the temperature at which each peak occurred. The Gumbel probability density function was chosen because the fit parameters may be chosen such

that the fit closely matches the asymmetry of the peak. The functional form of the Gumbel probability density function used is:

$$y = y_0 + A\mathrm{e}^{-\mathrm{e}^{\frac{T-T_c}{w}} - \frac{T-T_c}{w} + 1}, \tag{4.4}$$

where y_0 is a constant, which may be adjusted to account for the background level of loss, A is the peak amplitude, T_c is the temperature at which the peak occurs and w is the width of the peak. The commercial fitting package used quotes each parameter with a standard error. For the fit parameters given by the package, a chi-squared value was calculated and the value of T_c changed in order to verify that the standard error quoted was an uncertainty of one sigma. Additionally, the value T_c quoted may change depending upon the data window included in the fit. Hence, the fitting process was carried out multiple times for each peak, changing the boundaries of the region included in the fit each time in order to determine the uncertainty in the peak temperature T_c. The mode 3 data, including three peak fits each with different values of T_c are shown in figure 4.5. The error calculated from refitting was combined in quadrature with the error calculated by the fitting package used.

The mechanical loss of bending mode 2 of the coated sample was measured, but no control data was measured for this mode. As for the other modes studied, the loss of the coated sample shows a peak at approximately 30 K. The loss of the uncoated control sample around 30 K shows a frequency dependence, with lower frequencies exhibiting lower loss. For mode 2, the loss of the control sample would be far below the loss of the coated cantilever, and so the temperature at which the peak occurs is assumed to be unaffected by the subtraction of control data for this mode. Hence, the peak has been fitted using the mechcanical loss of the coated sample and included in the Arrhenius analysis of the 25% coating. A peak could not be fitted to he coating loss calculated from measurements of the fifth bending mode.

The fitted curves used to obtain values of T_{peak} are shown in figure 4.7 and the peak temperature at each frequency is summarised in table 4.2. These values were used to produce figure 4.8, a plot of $\ln(\omega)$ against $1/T$. A linear regression fit to the data is also shown, with the gradient giving an activation energy of $E_{\mathrm{a}} = 25.3 \pm 5.8\,\mathrm{meV}$ and a relaxation constant of $\tau_0 = (2.2 \pm 3.8) \times 10^{-8}\,\mathrm{s}$.

25% As-deposited		
Mode	Frequency (Hz)	T_{peak} (K)
2	507	30.4 ± 1.7
3	1417	34.3 ± 1.1
4	2765	39.5 ± 1.2
7	9464	41.6 ± 0.9

Table 4.2 Dissipation peak temperatures for the as-deposited 25% titania-doped tantala coating used to calculate the activation energy of the loss mechanism responsible for the peak.

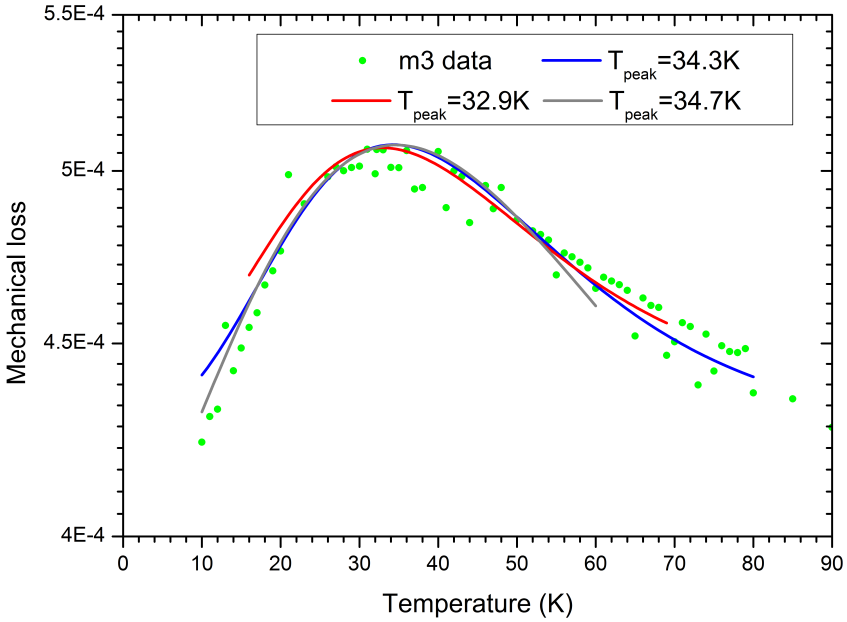

Fig. 4.5 The coating loss of the as-deposited 25% titania-doped tantala coated, calculated from measurements of the third bending mode. Also shown are three fits used to determine the temperature at which the loss peak occurs, as well as the uncertainty arising from the choice of data window used in the fitting process. The chi-sqared values of each fit are: 21.1 (red curve, 38 points included in fit window), 29.8 (blue, 68 points included in fit) and 23.3 (grey, 48 points included in fit).

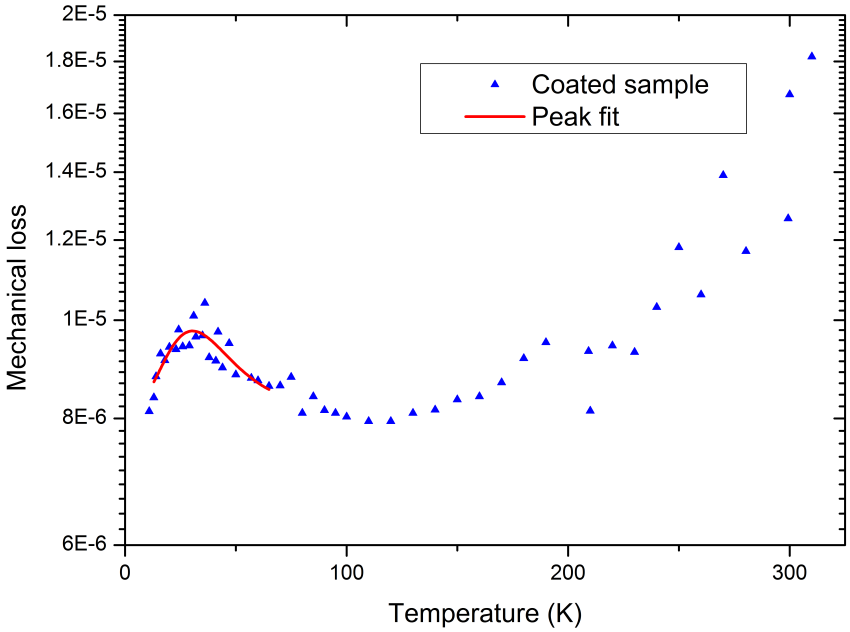

Fig. 4.6 The mechanical loss of a silicon cantilever coated with an as-deposited 25% titania-doped tantala coating for the second bending mode (0.5 kHz).

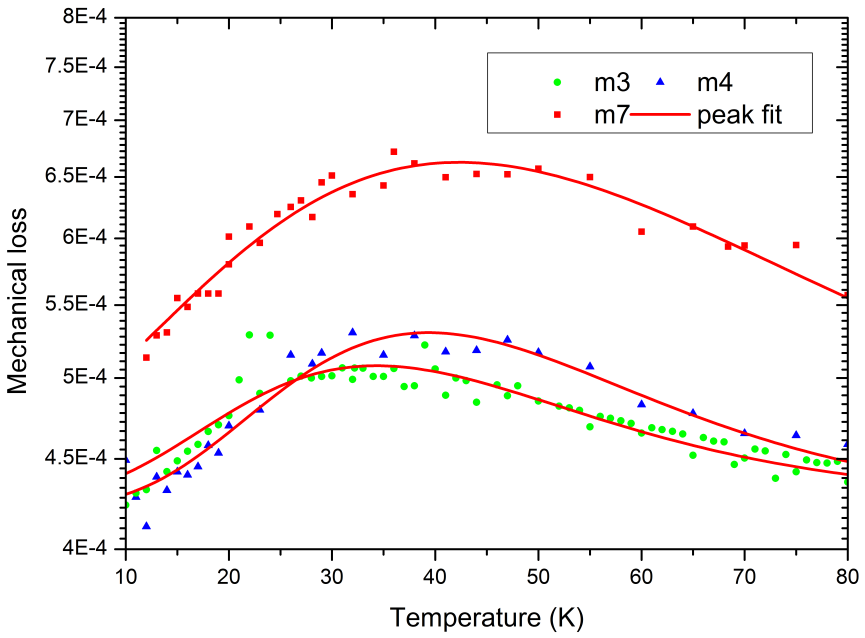

Fig. 4.7 The curves fitted to the temperature dependent loss to obtain temperature values at each peak for the as-deposited 25% doped coating

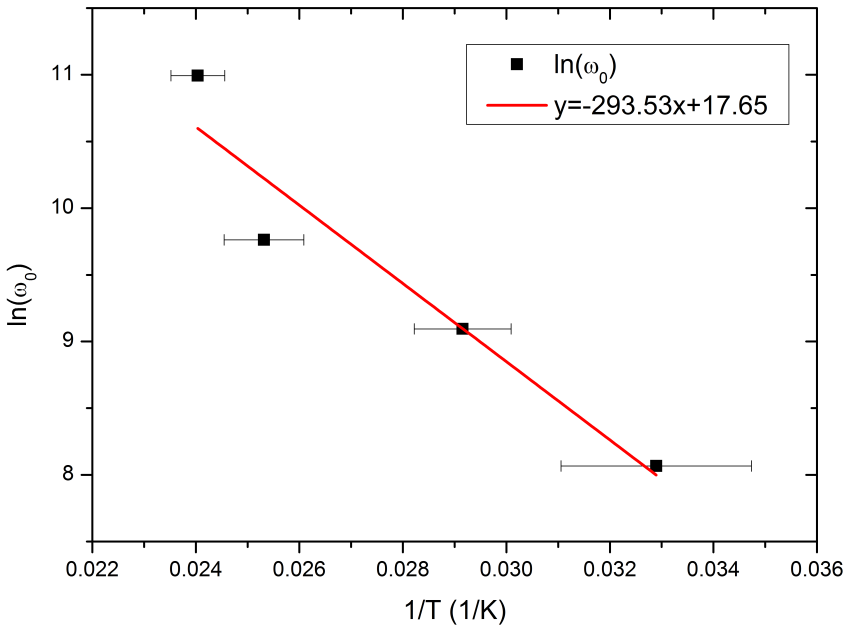

Fig. 4.8 An Arrhenius plot for the dissipation peaks observed in the as-deposited 25% titania-doped tantala coating.

4.2.3 400 °C heat-treated 25% titania-doped tantala

A cantilever upon which a 25% titania-doped tantala coating was applied was heat-treated to 400 °C. The mechanical loss of this cantilever was measured in the temperature range 10-300 K. The data from the 600 °C heat-treated control sample was used for coating loss calculations. The mechanical loss of the coated cantilever, the coating loss and the control data used for the calculations are presented for the 3rd to the 7th bending modes, with a frequency range of 1.4-9.4 kHz, in figures 4.9 - 4.13. Error bars are again not shown, but are of the same order as those of the as-deposited sample.

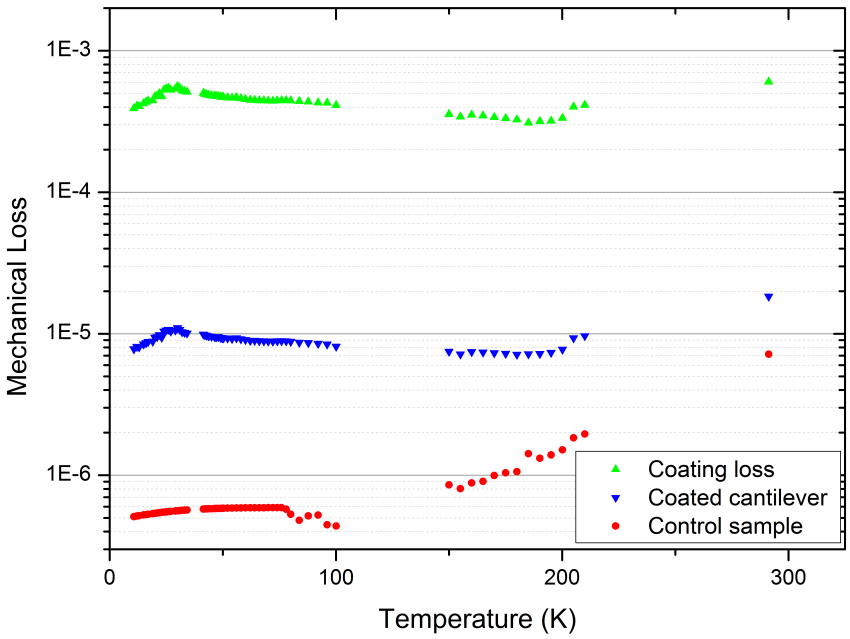

Fig. 4.9 The mechanical loss of a silicon cantilever coated with a 400 °C heat-treated 25% titania-doped tantala coating, and the calculated coating loss for the third bending mode (1.4 kHz).

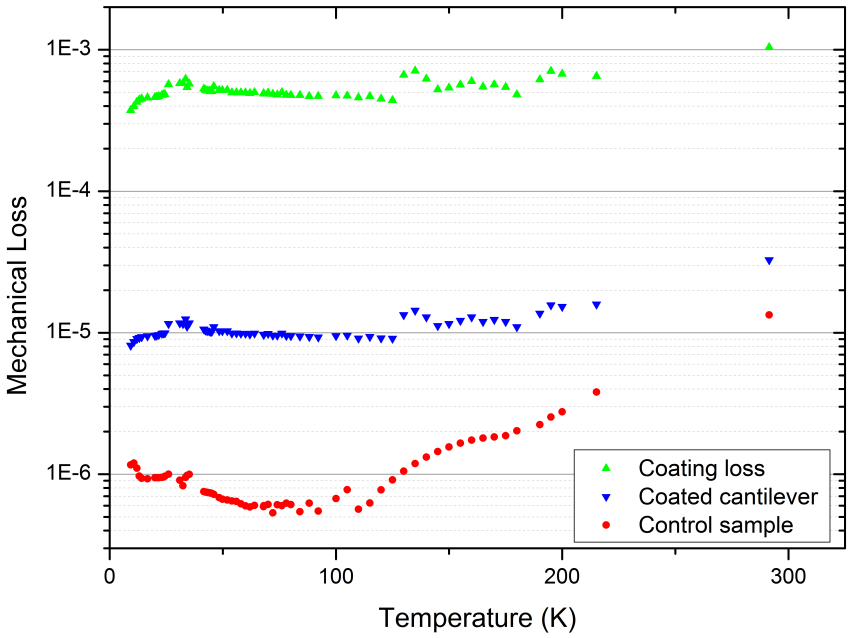

Fig. 4.10 The mechanical loss of a silicon cantilever coated with a 400 °C heat-treated 25% titania-doped tantala coating, and the calculated coating loss for the fourth bending mode (2.7 kHz).

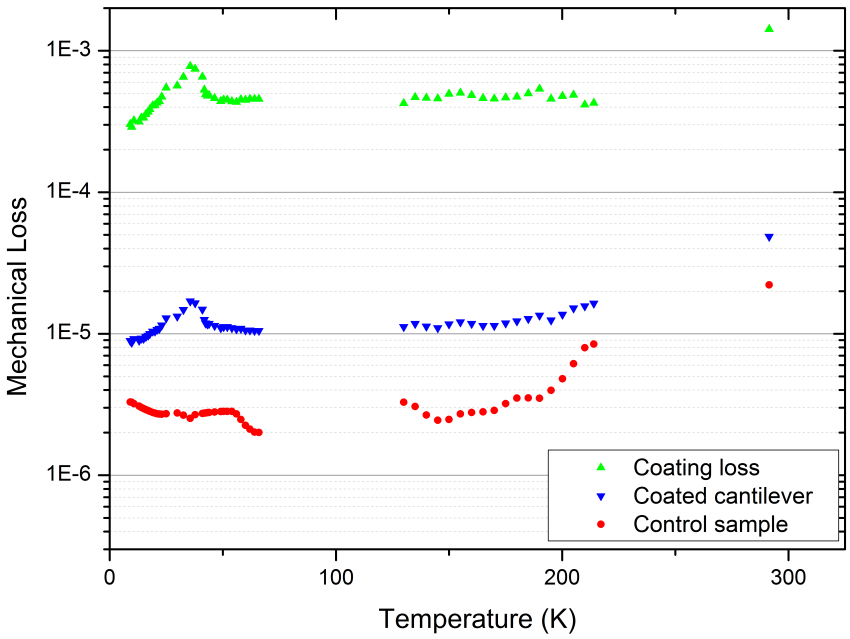

Fig. 4.11 The mechanical loss of a silicon cantilever coated with a 400 °C heat-treated 25% titania-doped tantala coating, and the calculated coating loss for the fifth bending mode (4.5 kHz).

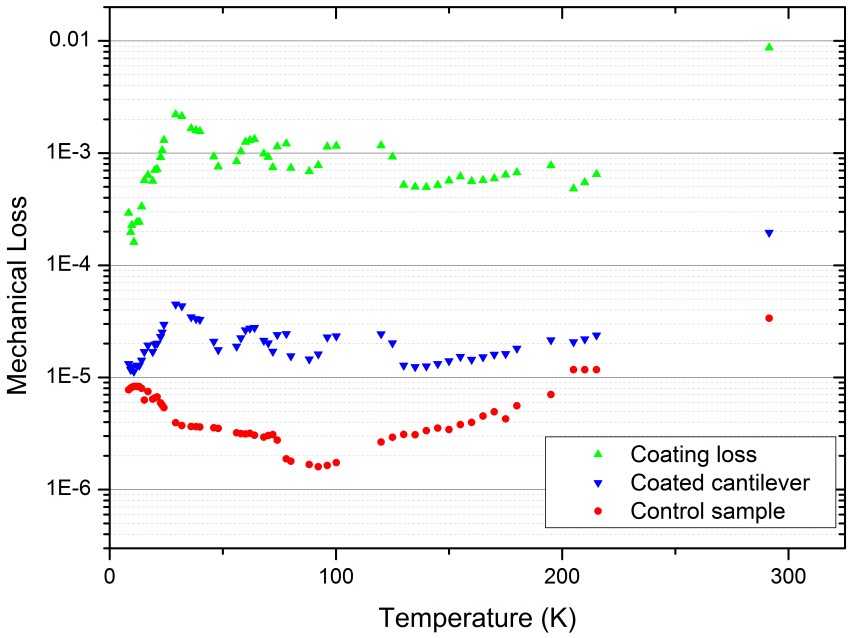

Fig. 4.12 The mechanical loss of a silicon cantilever coated with a 400 °C heat-treated 25% titania-doped tantala coating, and the calculated coating loss for the sixth bending mode (6.7 kHz).

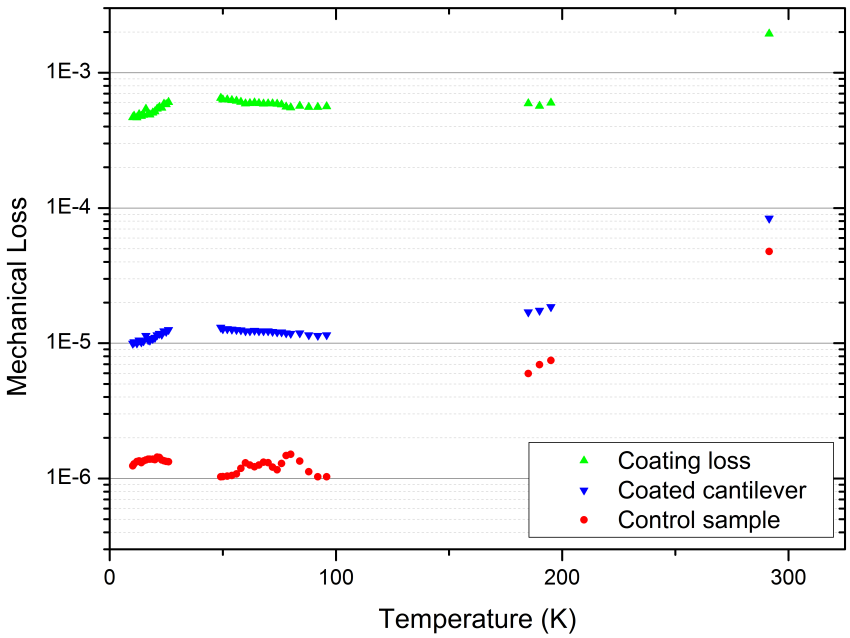

Fig. 4.13 The mechanical loss of a silicon cantilever coated with a 400 °C heat-treated 25% titania-doped tantala coating, and the calculated coating loss for the seventh bending mode (9.4 kHz).

4.2.4 Comparison of As-deposited and 400 °C 25% titania-doped tantala

The coating losses of the as-deposited and 400 °C 25% titania-doped tantala coating are compared for bending modes 3, 4, 5, and 7 are compared in figures 4.14 - 4.17 in order of increasing frequency. For all modes, the magnitude of both coating losses are very similar, however modes 3, 4 and 5 show that the 400 °C coating has increased loss in a narrow range between 20 and 40 K. However, mode 7 has a lack of data for the 400 °C heat-treated coating in this temperature range.

Modes 2, 3, 4 and 7 of the as-deposited coating were used to calculate an activation energy for the low temperature dissipation peak. By comparing the two coatings, it can be seen that the loss of the coating heat-treated at 400 °C displays a similar dissipation peak for modes 3, 4 and 7. Heat-treatment at 400 °C therefore does not remove the dissipation mechanism responsible for this peak, and appears, from inspection of the loss for modes 3 and 5 of the 400 °C coating to have introduced an additional dissipation peak.

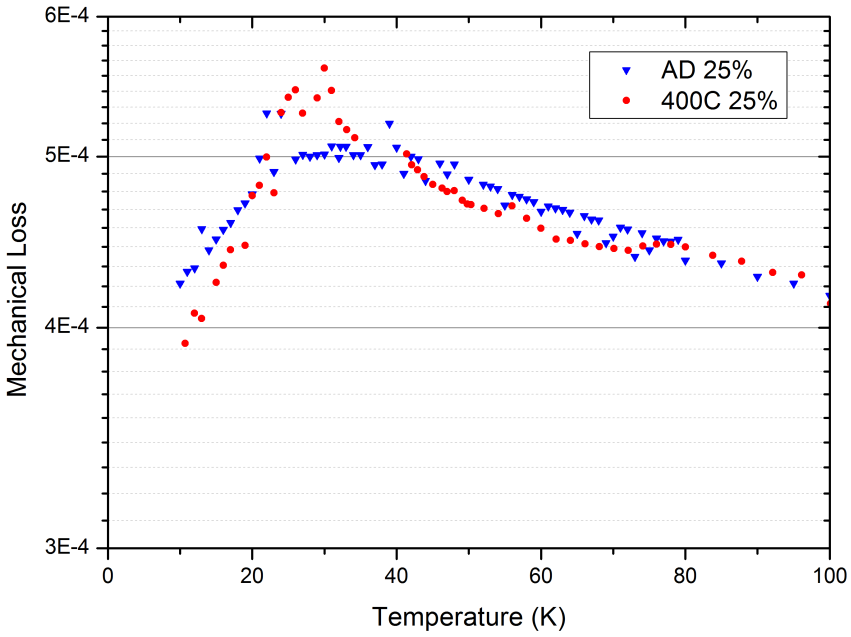

Fig. 4.14 A comparison of the coating loss of an as-deposited and 400 °C heat-treated 25% titania-doped tantala coating for bending mode 3, at 1.4 kHz

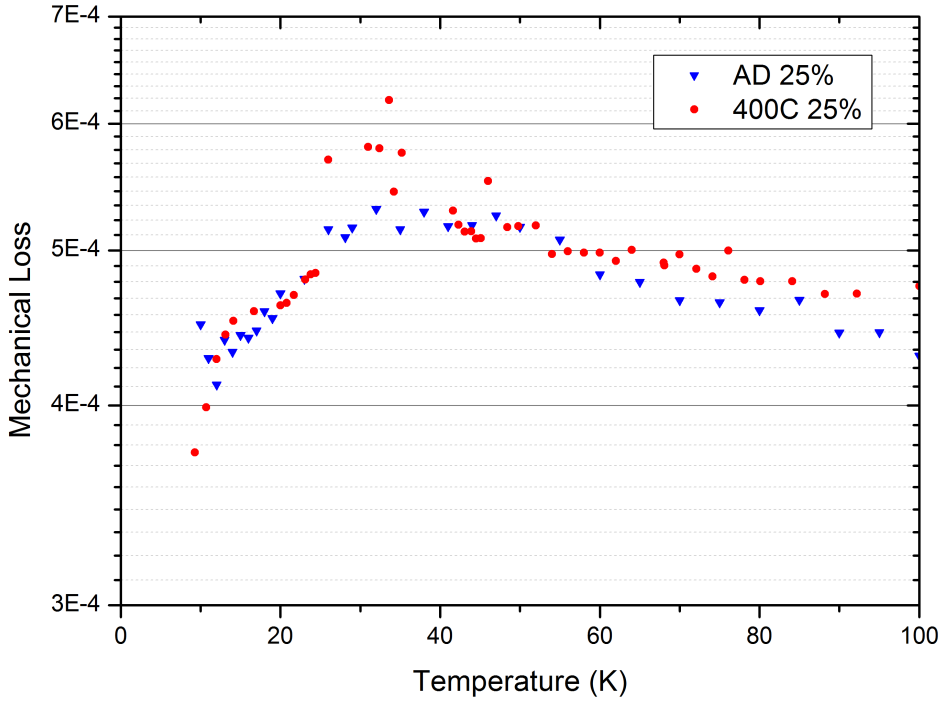

Fig. 4.15 A comparison of the coating loss of an as-deposited and 400 °C heat-treated 25% titania-doped tantala coating for bending mode 4, at 2.7 kHz

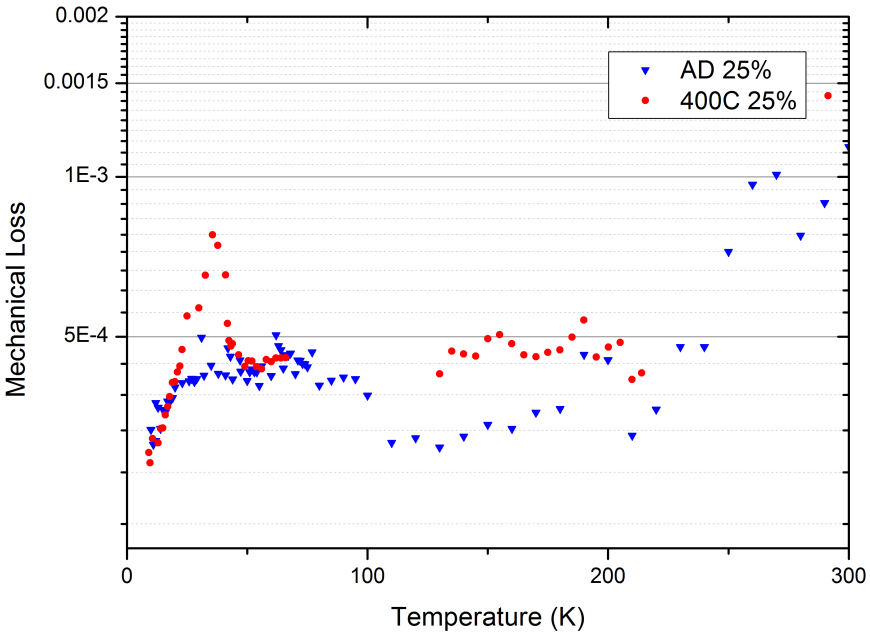

Fig. 4.16 A comparison of the coating loss of an as-deposited and 400 °C heat-treated 25% titania-doped tantala coating for bending mode 5, at 4.5 kHz

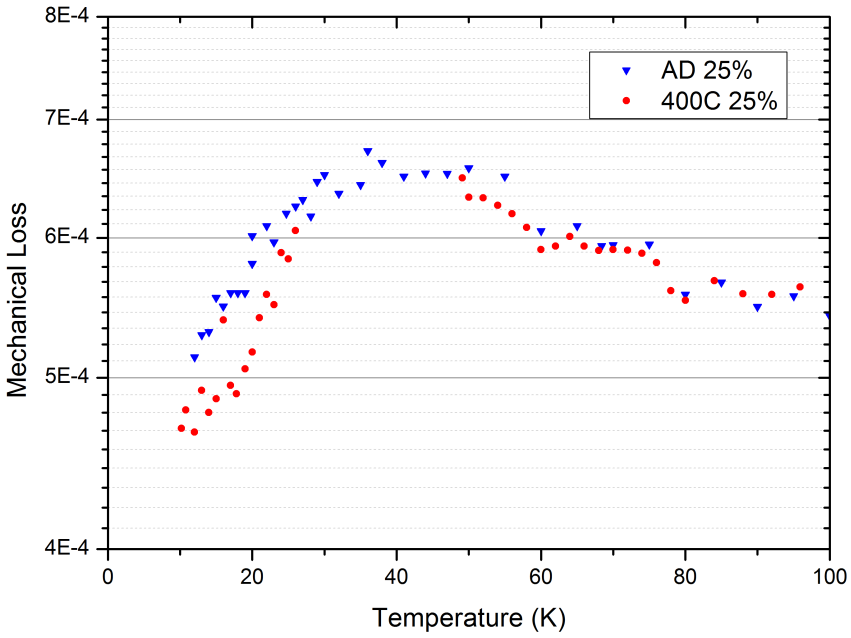

Fig. 4.17 A comparison of the coating loss of an as-deposited and 400 °C heat-treated 25% titania-doped tantala coating for bending mode 7, at 9.5 kHz

4.3 55% titania-doped tantala

4.3.1 As-deposited 55% titania-doped tantala

Cantilevers from a further silicon wafer were oxidised in air and sent to CSIRO for coating. A 500 nm thick 55% titania-doped tantala coating was deposited on the cantilevers. One of these cantilevers was heat-treated to 600 °C. In this section, and section 4.3.2, mechanical loss measurements of the the as-deposited and 600 °C coatings are presented.

The mechanical loss of the as-deposited 55% doped coating is shown for modes 3-8, with a frequency range of 1.1-10.9 kHz, in figures 4.18-4.23 in order of increasing mode number. Modes 4, 5, 7 and 8 show mechanical loss peaks in the range 27-37 K. These peaks were fitted using the method described in section 4.2.2. The peaks fitted to the data are shown in figure 4.24. The values of the peak temperatures and the corresponding frequencies are catalogued in table 4.3, and figure 4.25 shows an Arrhenius plot constructed from these values. The activation energy and time constant for this peak were found to be $E_a = (13.6 \pm 1.8)$ meV, and $\tau_0 = (2.3 \pm 0.4) \times 10^{-7}$ s respectively.

This activation energy is somewhat lower than that calculated for the peak observed in the 25% as-deposited coating. However, the magnitude of loss of the 55% doped coating is up to 20% higher than that of the 25% coating for all modes. This suggests that the increase in doping concentration decreases the activation energy of the dissipation mechanism responsible for the low-temperature peak, but also increases the overall level of loss.

55% As-deposited		
Mode	Frequency (Hz)	T_{peak} (K)
4	2402	27.4 ± 1.5
5	3962	31.4 ± 1.3
7	8246	35.7 ± 0.6
8	10945	37.0 ± 1.1

Table 4.3 Dissipation peak temperatures for the as-deposited 55% titania-doped tantala coating used to calculate the activation energy of the loss mechanism responsible for the peak.

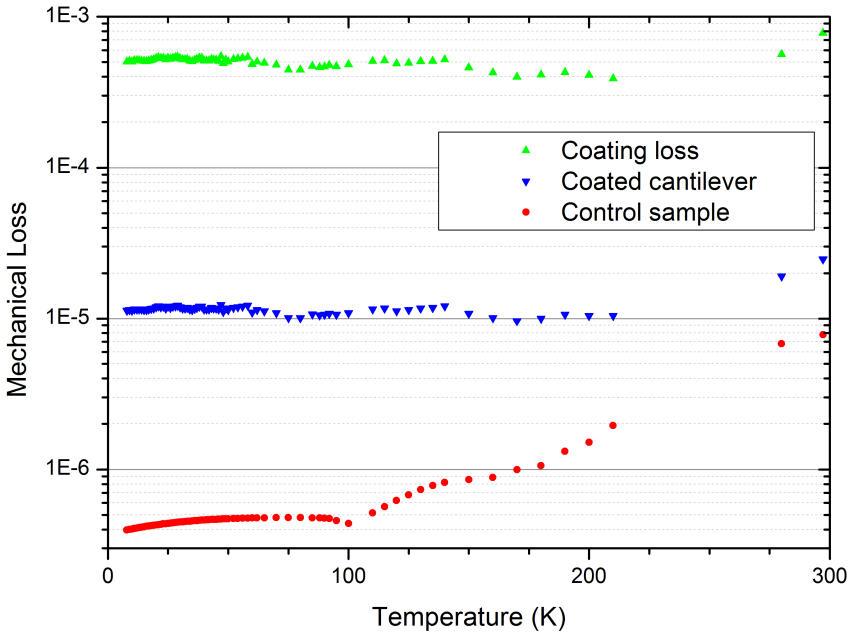

Fig. 4.18 The mechanical loss of a silicon cantilever coated with an as-deposited 55% titania-doped tantala coating, and the calculated coating loss for the third bending mode (1.2 kHz).

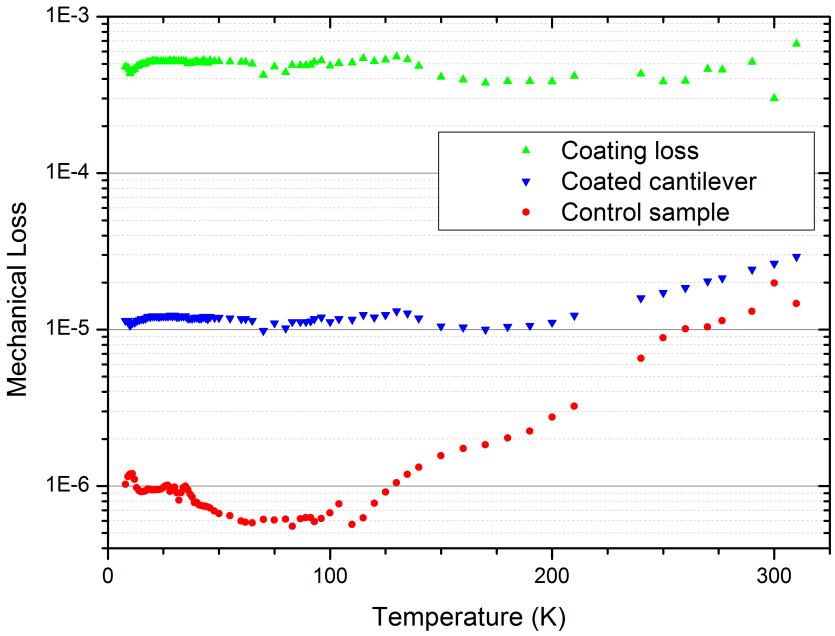

Fig. 4.19 The mechanical loss of a silicon cantilever coated with an as-deposited 55% titania-doped tantala coating, and the calculated coating loss for the fourth bending mode (2.4 kHz).

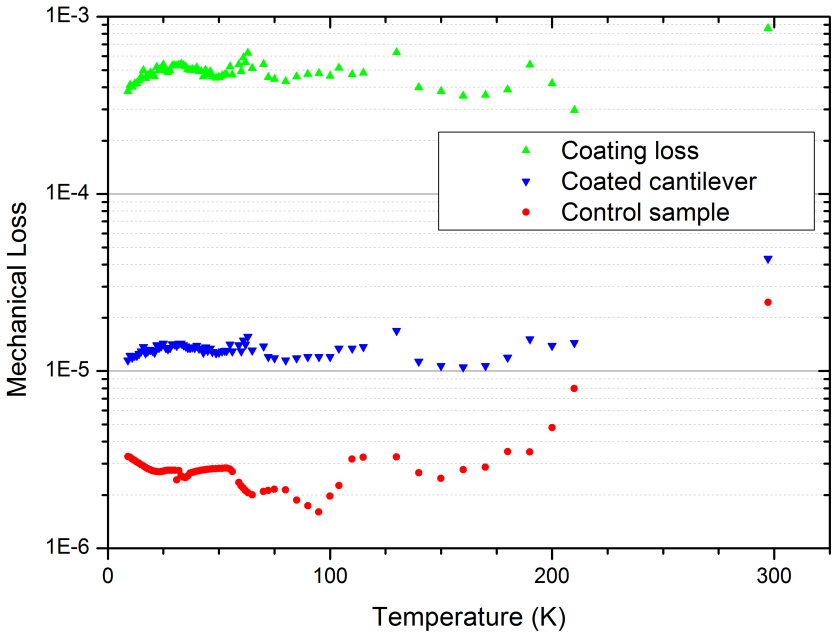

Fig. 4.20 The mechanical loss of a silicon cantilever coated with an as-deposited 55% titania-doped tantala coating, and the calculated coating loss for the fifth bending mode (3.9 kHz).

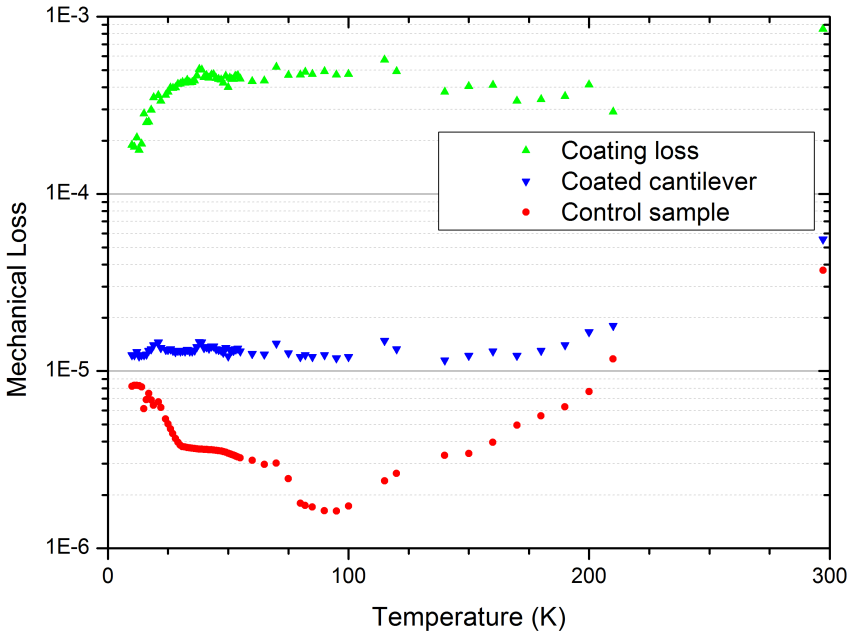

Fig. 4.21 The mechanical loss of a silicon cantilever coated with an as-deposited 55% titania-doped tantala coating, and the calculated coating loss for the sixth bending mode (5.9 kHz).

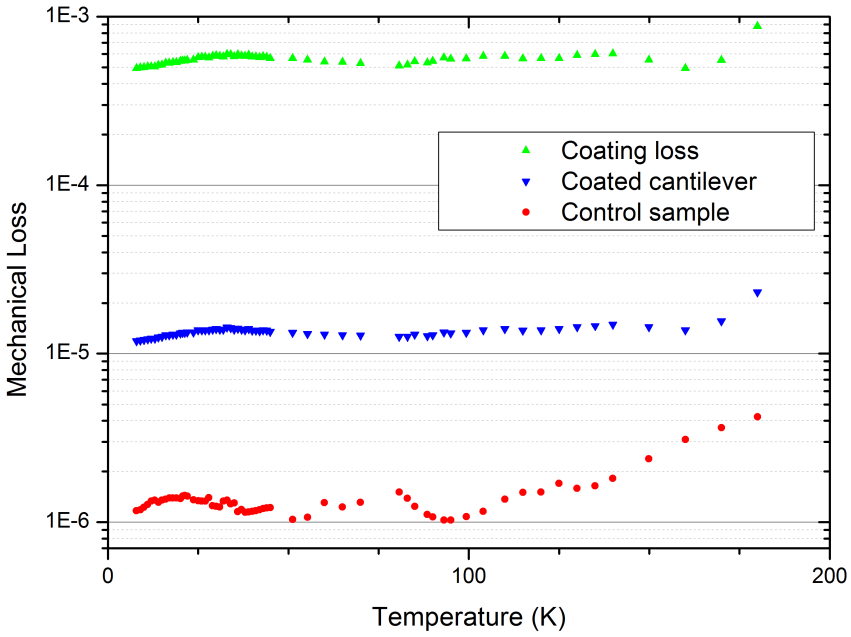

Fig. 4.22 The mechanical loss of a silicon cantilever coated with an as-deposited 55% titania-doped tantala coating, and the calculated coating loss for the seventh bending mode (8.2 kHz).

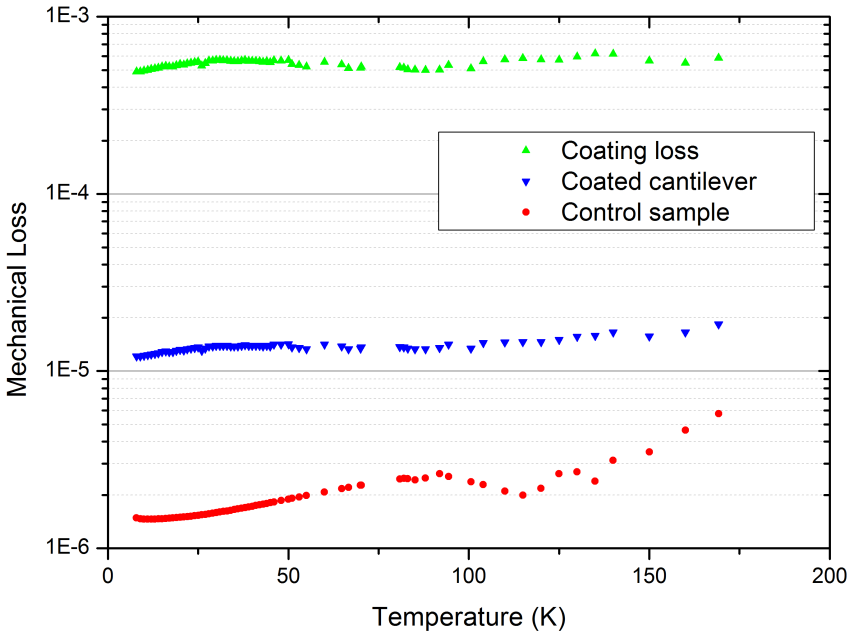

Fig. 4.23 The mechanical loss of a silicon cantilever coated with an as-deposited 55% titania-doped tantala coating, and the calculated coating loss for the eighth bending mode (10.9 kHz).

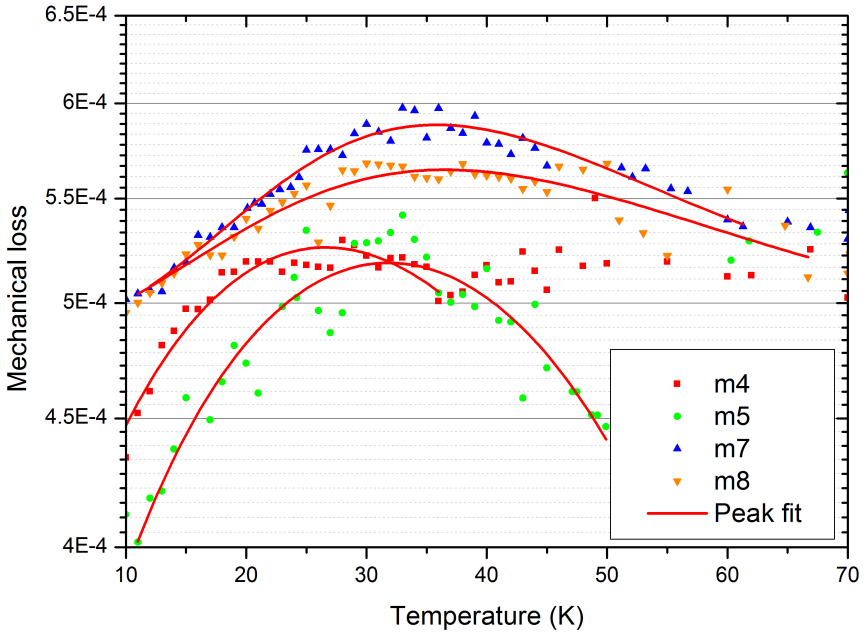

Fig. 4.24 The dissipation peaks observed in the as-deposited 55% doped coating, with the peaks fitted for Arrhenius analysis. Peak temperature values are given in table 4.3.

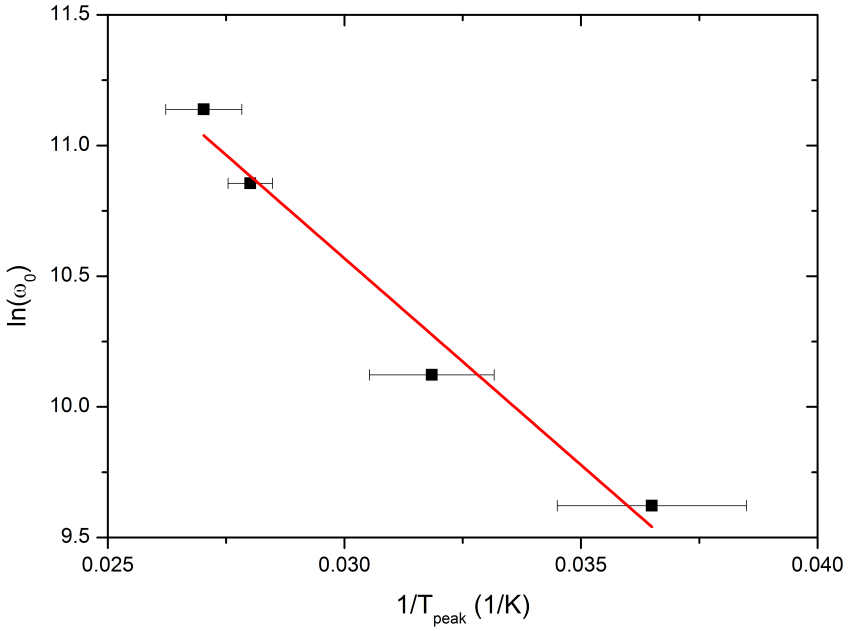

Fig. 4.25 An Arrhenius plot for the loss peaks observed in the as-deposited 55% titania-doped coating.

4.3.2 600 °C heat-treated 55% titania-doped tantala

The mechanical loss of the 600 °C heat-treated 55% titania-doped sample was measured for bending modes 3, 4, 5, 7, 9, and 10 in the frequency range 1.1-16.4 kHz. The measured losses, along with the calculated coating losses are shown in figures 4.26-4.31 in order of increasing frequency.

For mode 10, there is only loss data under 60 K, the main region of interest for this coating. In calculating the coating loss for mode 10, it has been assumed that the substrate makes no contribution to the measured loss. From the other modes of this sample, it can be seen that the substrate should only contribute around 10% of the loss measured for mode 10. This adds extra uncertainty to the magnitude of the coating loss of mode 10, but the temperature at which the dissipation peak occurs should not be affected.

For all of the modes studied, a dissipation peak in the temperature range 18-22 K is observed in the extracted coating loss. These peaks are shown in figure 4.32 for clarity. The temperature at each peak, along with the corresponding frequencies are recorded in table 4.4. These values were used for the Arrhenius plot, shown in figure 4.33. The best fit line gives the values $E_a = (35.8 \pm 5)$ meV and $\tau_0 = (0.3 \pm 2.4) \times 10^{-13}$ s for the activation energy of the dissipation mechanism and relaxation constant respectively. This activation energy is somewhat higher than that obtained in section 4.3.1 from measurements of the as-deposited coating. This could suggest that either the heat-treatment leads to an increase in activation energy for a certain dissipation mechanism, or that the heat-treatment introduces a different loss causing process. However, the activation energy of the dissipation process responsible for the peak in 600 °C heat-treated 55% is very close to that found in 600 °C heat-treated pure tantala, (35.6 ± 2.5) meV [4]. Comparing the peak heights of the coating studied here and that by Martin et al. [4], the doped coating features a lower peak magnitude. Hence, it appears that, with doping, the underlying loss process is still present but its effects have been reduced.

However, the activation energy is consistent with measurements of a pure tantala coating, heat-treated to 600 °C. This would suggest that titania-doping, even as much as 55%, does not remove the dissipation mechanism responsible for the low temperature loss peak observed in 600 °C heat-treated tantala coatings. However, in comparing the peak magnitudes of the 600 °C pure tantala and

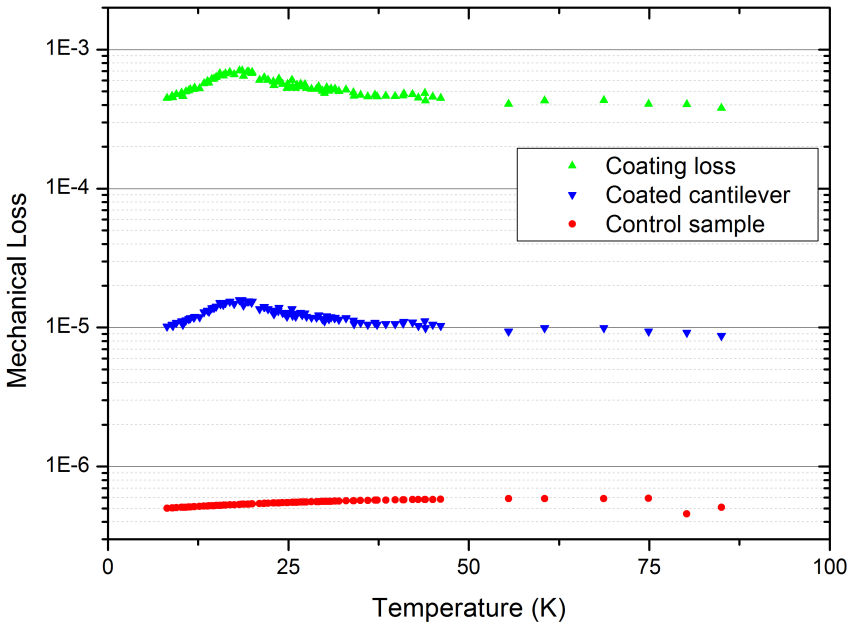

Fig. 4.26 The mechanical loss of a silicon cantilever coated with a 600 °C heat-treated 55% titania-doped tantala coating, and the calculated coating loss for the third bending mode (1.1 kHz).

55% titania-doped coatings, doping appears to reduce the magnitude of the peak.

The magnitude of loss of the 600 °C heat-treated coating is compared to that of the as-deposited 55% coating in figures 4.34, 4.35, 4.36, and 4.37. It can be seen that the peak, first observed in the 400 °C heat-treated coating, is present here and at this peak, the magnitude of loss of the 600 °C heat-treated coating is a factor of 1.2-1.5 higher than that of the as-deposited coating at the same temperatures.

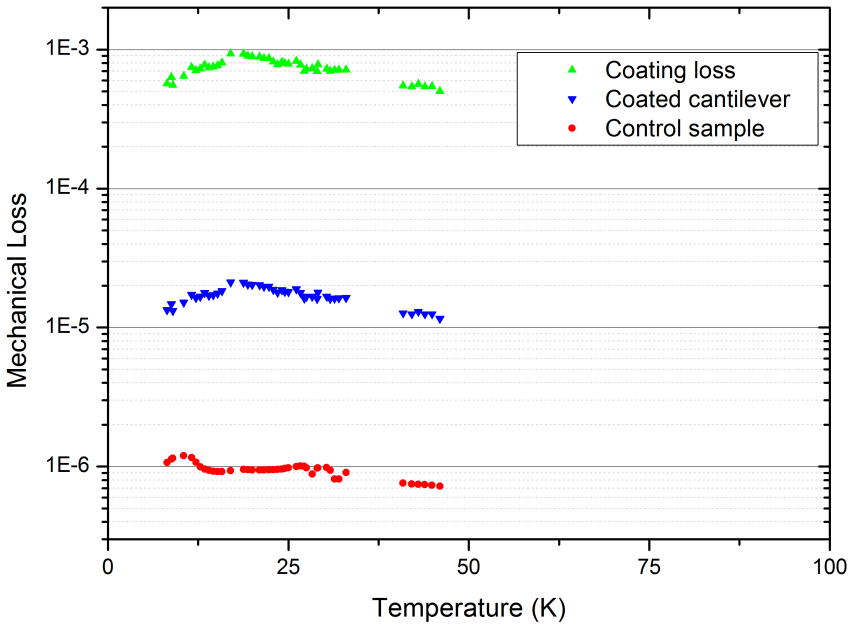

Fig. 4.27 The mechanical loss of a silicon cantilever coated with a 600 °C heat-treated 55% titania-doped tantala coating, and the calculated coating loss for the fourth bending mode (2.2 kHz).

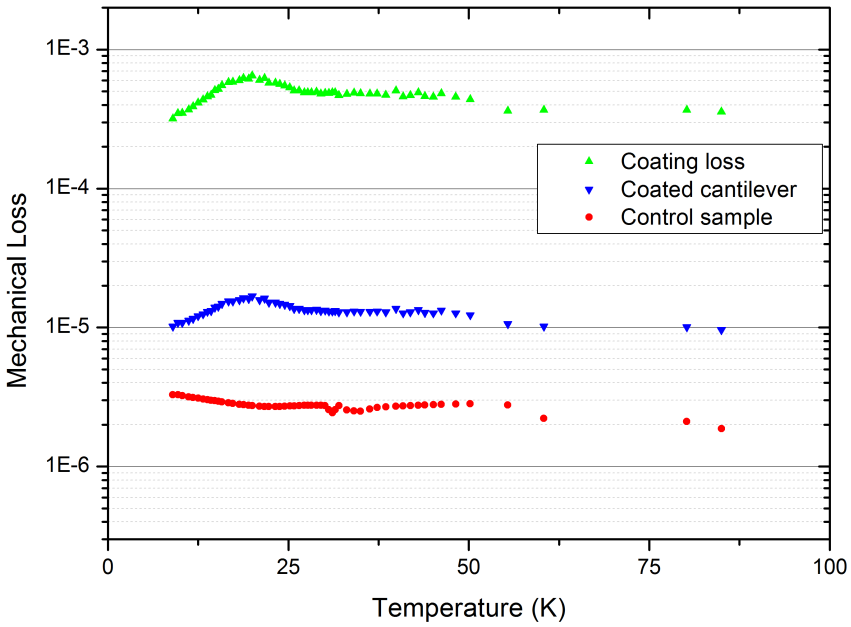

Fig. 4.28 The mechanical loss of a silicon cantilever coated with a 600 °C heat-treated 55% titania-doped tantala coating, and the calculated coating loss for the fifth bending mode (3.7 kHz).

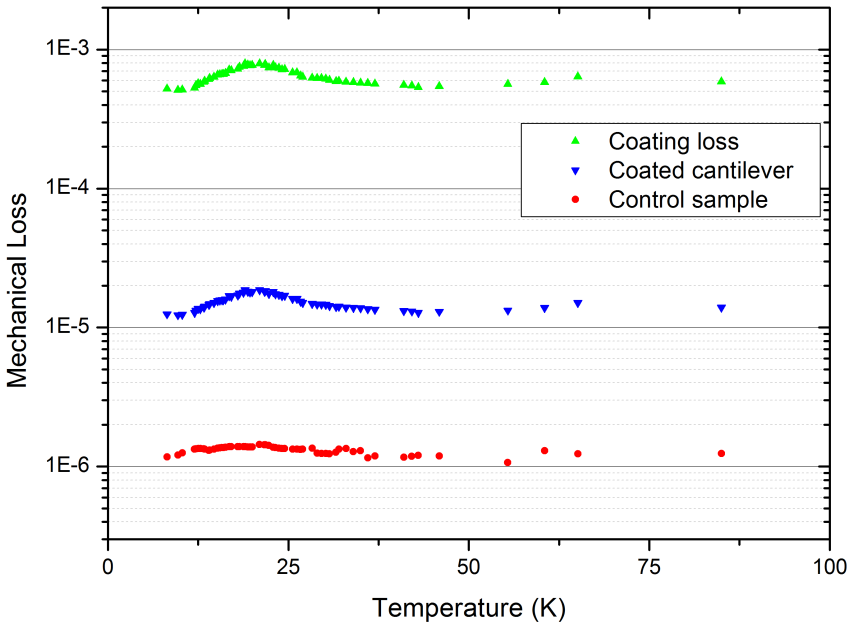

Fig. 4.29 The mechanical loss of a silicon cantilever coated with a 600 °C heat-treated 55% titania-doped tantala coating, and the calculated coating loss for the seventh bending mode (7.7 kHz).

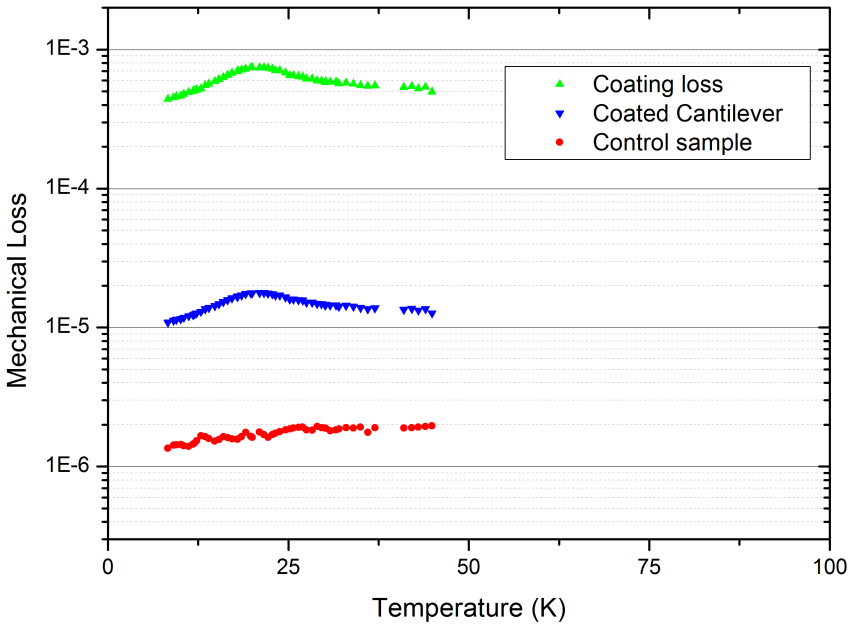

Fig. 4.30 The mechanical loss of a silicon cantilever coated with a 600 °C heat-treated 55% titania-doped tantala coating, and the calculated coating loss for the ninth bending mode (13.1 kHz).

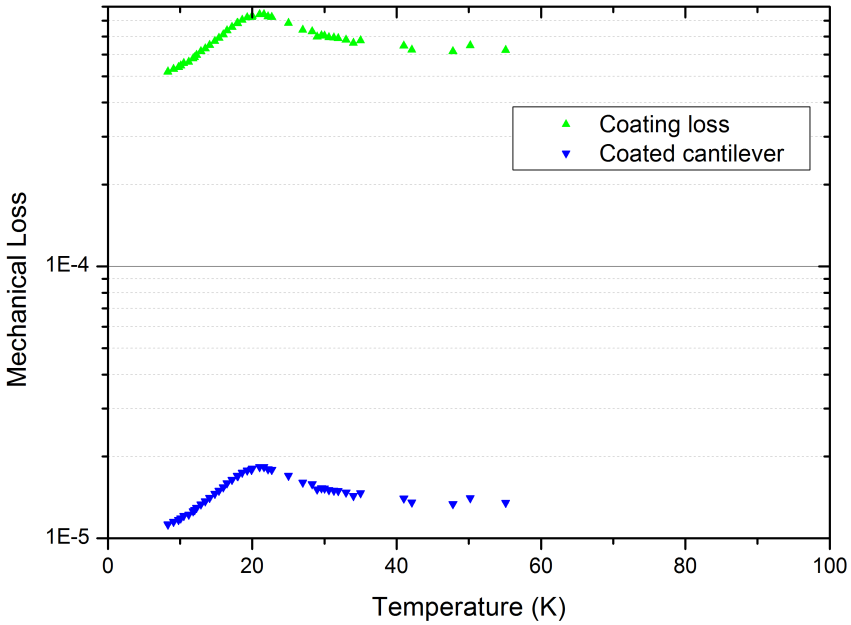

Fig. 4.31 The mechanical loss of a silicon cantilever coated with a 600 °C heat-treated 55% titania-doped tantala coating, and the calculated coating loss for the tenth bending mode (16.4 kHz).

55% 600 °C		
Mode	Frequency (Hz)	T_{peak} (K)
3	1148	18.6 ± 0.3
4	2240	19.3 ± 0.4
5	3703	19.9 ± 0.2
7	7705	20.6 ± 0.2
9	13145	20.4 ± 0.1
10	16394	21.3 ± 0.3

Table 4.4 Dissipation peak temperatures for the 600 °C heat-treated 55% titania-doped tantala coating used to calculate the activation energy of the loss mechanism responsible for the peak.

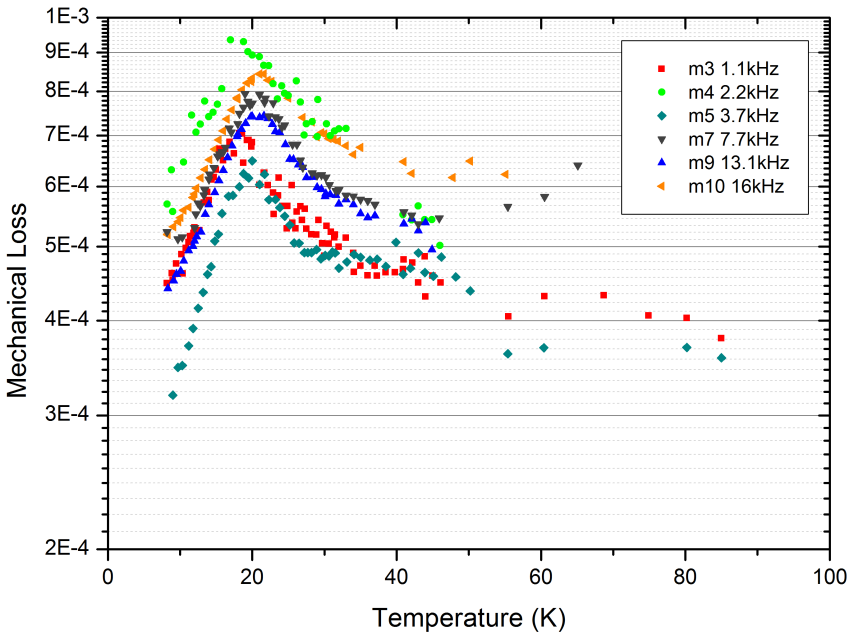

Fig. 4.32 The mechanical loss of a silicon cantilever coated with a 600 °C heat-treated 55% titania-doped tantala coating, and the calculated coating loss for the tenth bending mode (16.4 kHz) under the assumption that the substrate loss is negligable under 100 K.

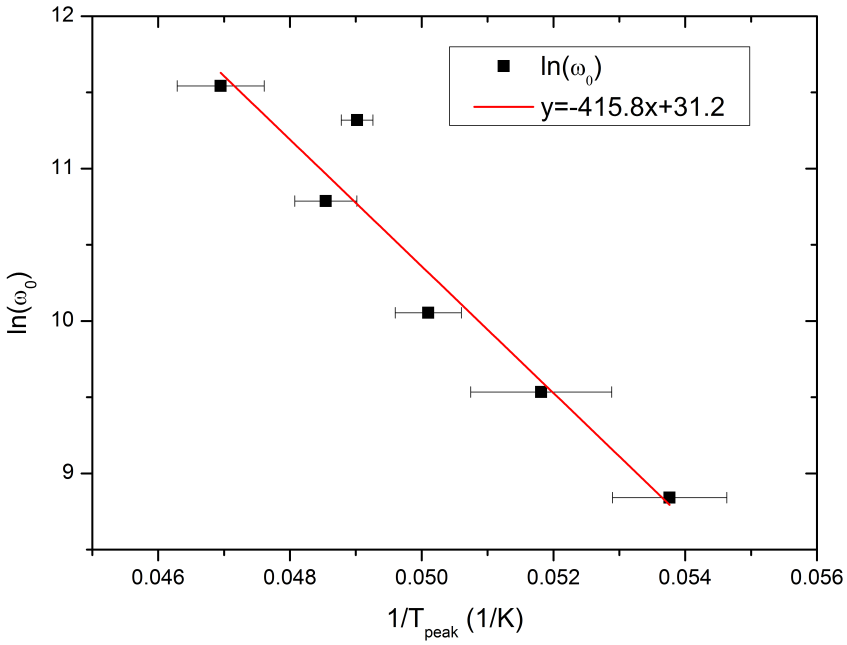

Fig. 4.33 An Arrhenius plot for the loss peaks observed in the 600 °C heat-treated 55% doped coating.

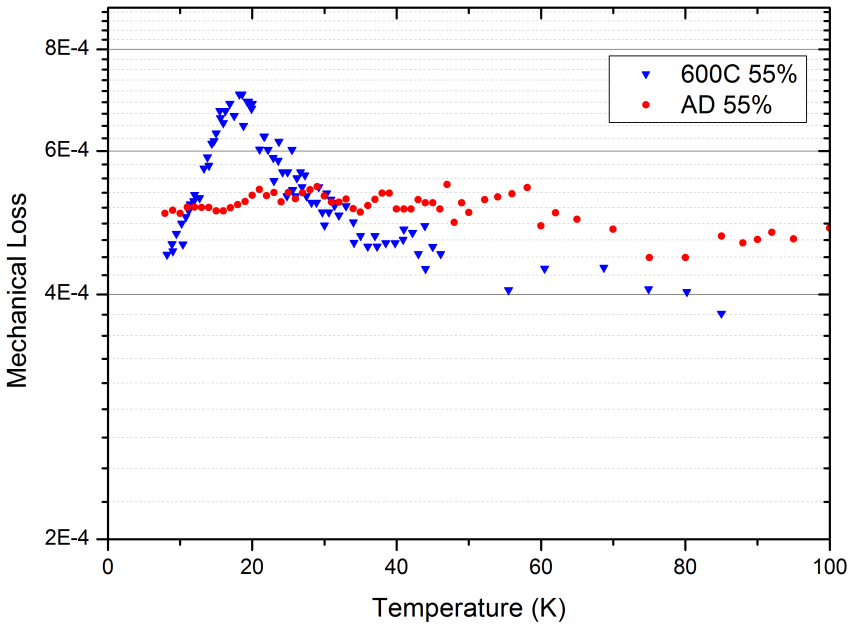

Fig. 4.34 A comparison of the coating loss of an as-deposited and 600 °C heat-treated 55% titania-doped tantala coating for bending mode 3, at 1.2 kHz

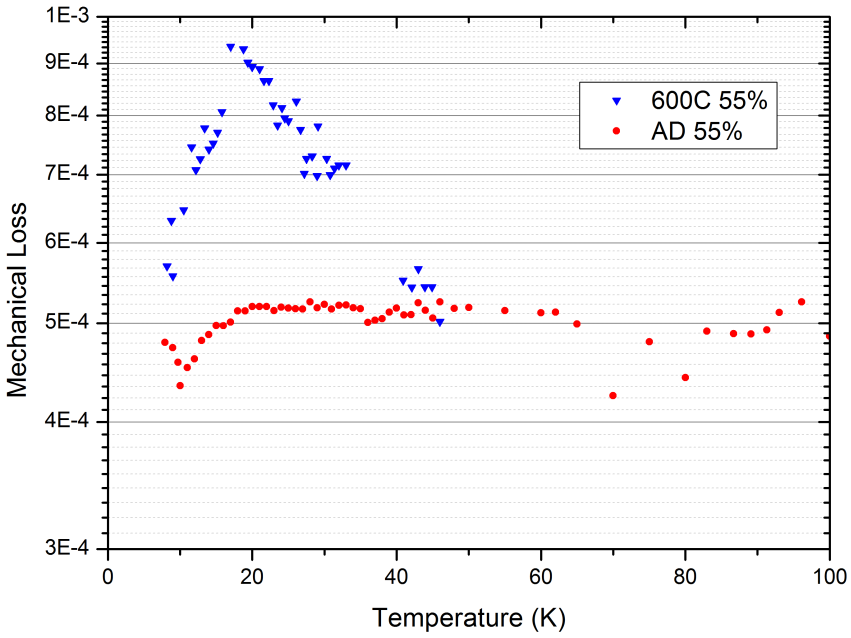

Fig. 4.35 A comparison of the coating loss of an as-deposited and 600 °C heat-treated 55% titania-doped tantala coating for bending mode 4, at 2.4 kHz

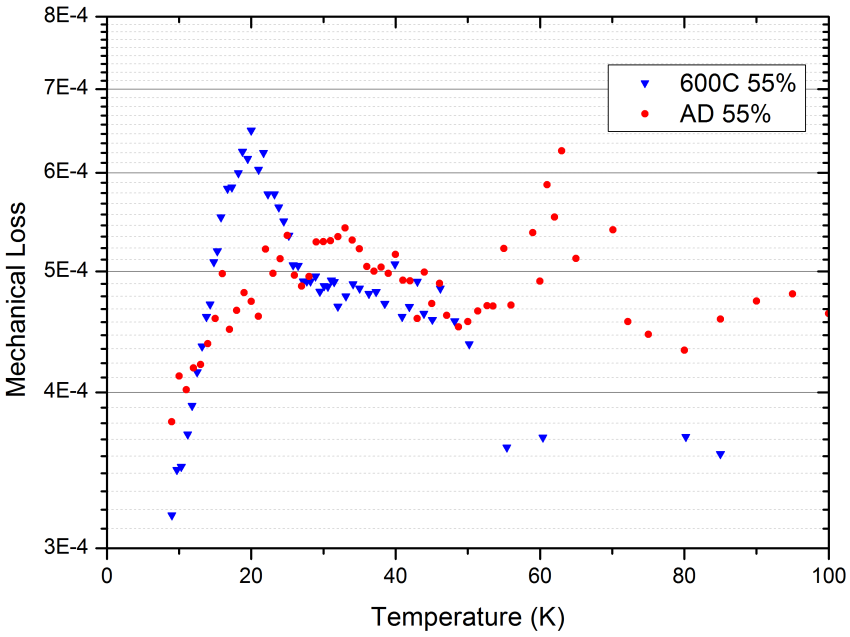

Fig. 4.36 A comparison of the coating loss of an as-deposited and 600 °C heat-treated 55% titania-doped tantala coating for bending mode 5, at 3.9 kHz

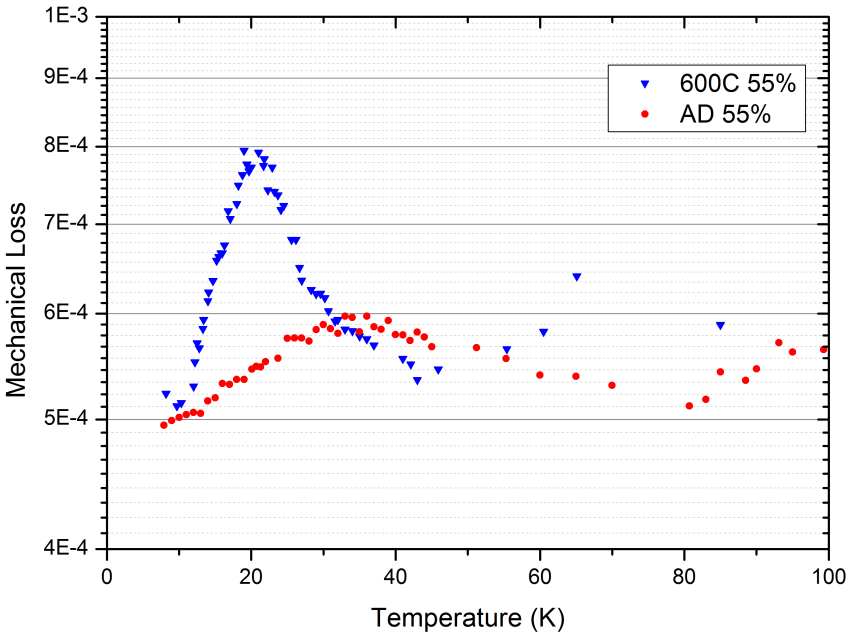

Fig. 4.37 A comparison of the coating loss of an as-deposited and 600 °C heat-treated 55% titania-doped tantala coating for bending mode 7, at 8.2 kHz

4.4 Further Analysis

In many amorphous solids such as fused silica, the mechanical loss peaks above 10 K are thought to arise from thermally activated reorientations of bonds between stable positions [138]. These stable orientations can be represented as a double-well potential, with a barrier of height V separating two minimum energy states [126]. However, the amorphous nature of these materials gives rise to a wide range of barrier heights, which accounts for the broad loss peaks observed in measurements of these materials. Initial models assumed that these double-well potentials were symmetric, with the barrier separating two minima of equal energy [126, 127, 139, 140]. However, several shortcomings of this model were pointed out by Gilroy and Phillips [141]. For a dissipation peak to occur, the model must include a low energy cut-off in the distribution of barrier heights. The symmetric model also fails to explain the linear scaling of peak loss with measurement frequency observed in fused silica. It was also suggested that the same structural variations which lead to the distribution of barrier heights would also be expected to produce asymmetric potential wells.

In an asymmetric double-well potential, V is the difference between the lowest possible energy and the top of the potential barrier and Δ is the energy difference between the two wells. An amorphous solid will have a distribution of potential barrier heights, $g(V)$, and a distribution of well asymmetries, $f(\Delta)$. Gilroy and Phillips showed that the mechanical loss predicted by their model is given by [141]:

$$\phi = \frac{\gamma^2}{k_\mathrm{B} T C_{ii}} \int_0^\infty \int_0^\infty \frac{\omega\tau}{1+(\omega\tau)^2} \mathrm{sech}^2\left(\frac{\Delta}{2k_\mathrm{B}T}\right) f(\Delta) g(V) d\Delta dV, \tag{4.5}$$

where ω is the angular frequency of the measurement, C_{ii} is the appropriate elastic constant for the mode shape under consideration, γ is the elastic coupling constant which represents the coupling between the defect (such as the re-orientation of a bond within the asymmetric double well potential) and the applied strain. The relaxation time τ is related to the barrier height V by equation 4.2.

Taking equation 4.5 and making the assumptions that $g(V)$ is independent of temperature and that $f(\Delta) = f_0 = constant$ [141], Topp and Cahill show that the mechanical loss is related to $g(V)$ by [142]:

$$\phi = \frac{\pi\gamma^2 f_0}{C_{ii}} k_B T g(V), \tag{4.6}$$

where

$$V = -k_B T \ln(\omega\tau_0). \tag{4.7}$$

Hence, the distribution of barrier heights may be calculated from the measured mechanical loss as a function of temperature. This calculation was carried out for the as-deposited 25% and 55% titania-doped coatings and the 600 °C heat-treated 55% titania-doped tantala coating. The values of τ used for these three coatings were 2.2×10^{-8}, 2.3×10^{-7} and 3.0×10^{-14} respectively, as found from the analyses in the previous sections.

A value of γ related to tantala could not be found in literature. In the absence of specific data for tantala, previous calculations of the barrier height distributions in heat-treated tantala by Martin et al. [4] use the value $\gamma = 0.9\,\text{eV}$ matching that of silica. Experimental data in Topp and Cahill suggests that for most amorphous materials, gamma is in the range $0.6\,\text{eV} < \gamma < 1.1\,\text{eV}$. Thus, the value of gamma used for calculations presented here was $\gamma = 0.9\,\text{eV}$, and is assumed to be similar for titania-doped, and pure, tantala.

The value of the elastic constant C_{ii} used in tantala barrier height distribution calculations in [4, 113] was approximated using data from Topp and Cahill. The elastic constant for silica, $C_{ii} = 3.3 \times 10^4$ MPa [143], was multiplied by the ratio of Young's Modulii of tantala and silica, giving a value of $C_{ii} = 6.2 \times 10^4$ MPa. The same value is used here for titania-doped tantala since the values for tantala and titania-doped tantala are likely to be similar. The values used for both γ and C_{ii} are thus estimates. Any variation between the values assumed and the real values will not affect the shape of the barrier height distributions calculated, and the distributions may still be compared.

The barrier height distribution function, $g(V)f_0$, calculated for as-deposited 25 and 55% titania-doped tantala coatings as well as that of the 600 °C heat-treated 55% doped coating are shown as a function of barrier height in figure

4.38. This plot shows the distribution of activation energies for the transition between potential wells in the asymmetric double well potential.

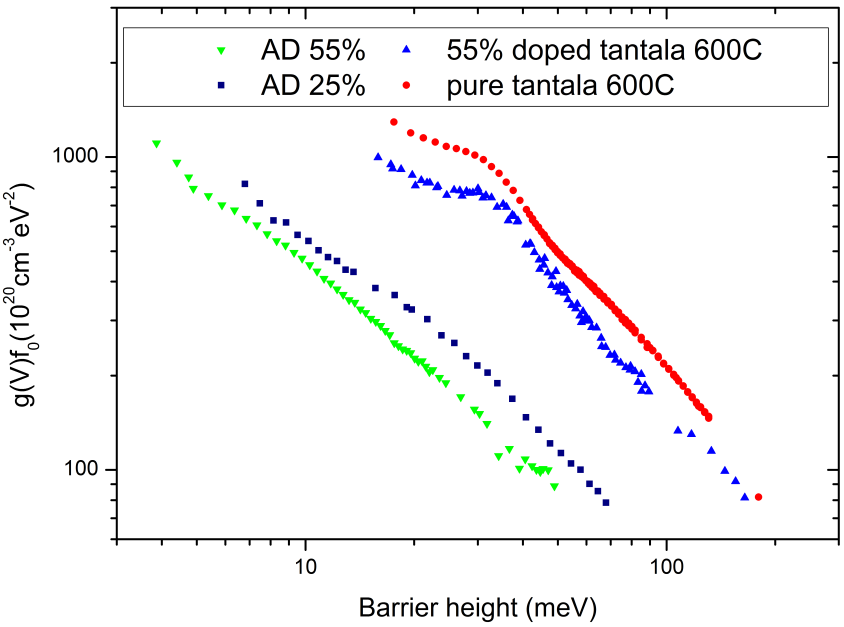

Fig. 4.38 A comparison of the barrier height distribution function $g(V)f_0$ as a function of barrier height for as-deposited 25 and 55% titania-doped tantala, 600 °C heat-treated pure and 55% titania-doped tantala coatings. The pure tantala data were reproduced from Martin [4].

In comparing the two as-deposited coatings, it can be seen that the effect of further doping from 25 to 55% is to reduce the number of barriers at each potential. This trend is also seen in comparing the 55% 600 °C heat-treated coating with the 600 °C heat-treated pure tantala coating measured by Martin et al. [4].

Comparing the 600 °C heat-treated 55% coating with the as-deposited 55% coating, it can be seen that the effect of heat treatment to 600 °C is to shift the barrier height distribution to significantly higher barrier heights. It is likely that the barrier height distribution of a 25% titania-doped tantala coating heat-treated at 600 °C would lie somewhere between the barrier height distributions of the pure tantala and the 55% titania-doped tantala, each heat-treated at 600 °C. An important piece of future work would be to verify this with measurements of the 25% titania-doped tantala coating heat-treated at 600 °C.

Mechanical loss calculations may be made by building computational atomic models of dielectric materials such as tantala. However, for these calculations to be accurate, it is essential to have good estimates of the interatomic potentials and barrier height distributions within the model. The barrier height distributions obtained by mechanical loss measurements and subsequent calculations are crucial to guiding and improving these computational models [144]. Additionally, material properties such as the specific heat [145] and thermal conductivity [146] may be calculated from the barrier height distribution for a given amorphous material.

Electron energy loss spectroscopy (EELS) is a form of vibrational spectroscopy, which may be used to probe the vibrational spectra of materials. Recent developments in the field have greatly improved the energy resolution of this type of measurement by monochromating the electron beam used to probe the sample material [147]. A study by Krivanek features measurements of materials including silica, in which the measurement background rises significantly at energies under 100 meV [147]. This type of measurement may be of interest where the activation energy of a dissipation process garnered from mechanical loss measurements is above 100 meV, or if the EELS measurement technique is developed to the point where energies of the order of a few tens of meV may be resolved. Cross correlating EELS spectra with activation energies from mechanical loss measurements would allow futher insight into the structure of coating materials. Measurements of the Raman spectra of these coatings are also of interest, and it may be expected that the activation energies of dissipation processes would appear on the Raman spectra as peaks. Both EELS and Raman spectra would allow correlations between changes in mechanical loss and the changes of peak heights observed as a result of heat-treatment of the coatings. This would provide a deeper understanding of the structural changes taking place during heat-treatment and how these changes affect the mechanical loss of a coating.

4.5 ALD tantala

A 500 nm thick tantala layer was deposited onto a silicon cantilever by atomic layer deposition (ALD). Since this process is radically different from IBS, it is expected to produce coatings with a different molecular structure to

those produced by IBS. In particular, IBS produces highly dense coatings by impacting the sputtered material into the substrate, whereas ALD deposits the coating by a self-limiting chemical reaction which limits the coating density. IBS also produces the purest coating materials [106].

The mechanical loss as a function of temperature for an ALD tantala coating was measured in the temperature range 10-300 K. At low temperatures, dissipation peaks could be observed in almost all modes of the coating loss as measured on the coated oxidised cantilever. These peaks occur at different temperatures depending on the measurement frequency, allowing an Arrhenius analysis to be performed. In the proceeding sections, the coatings deposited on the two cantilevers are treated separately before a comparison is made.

The mechanical loss of a silicon cantilever (which was oxidised prior to coating) for the third to the ninth bending modes is presented in figures 4.39, 4.40, and 4.41 in order of increasing frequency.

The coating loss, as measured on the oxidised cantilever is generally between 1×10^{-3} and 3×10^{-3}. The losses of all modes of the oxidised cantilever showed the same broad peak exhibited around 50 K as the unoxidised cantilever. The loss shows a dip in the range 150-200 K, and shows a rise in the range 200-300 K where the thermoelastic loss of the substrate becomes dominant. The coating losses exhibited the same peak as the coating on the unoxidised cantilever, with the same peak magnitudes.

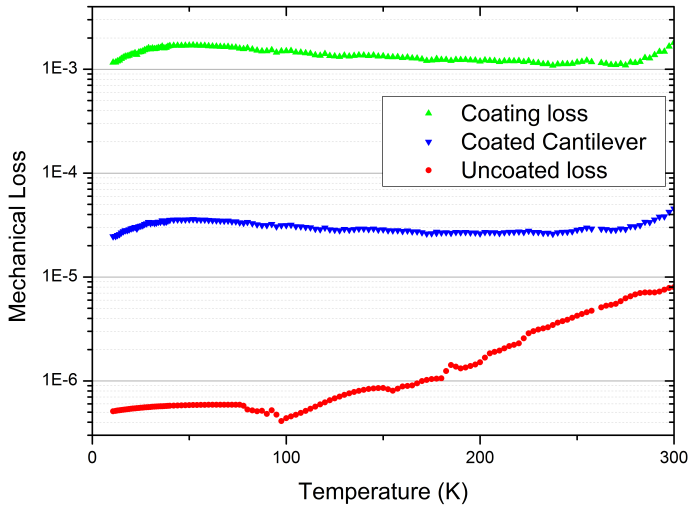

Fig. 4.39 Temperature dependent mechanical loss of an ALD tantala coating for bending mode 3 at 1.3 kHz, measured on the oxidised cantilever. Also shown is the mechanical loss of the coated, oxidised cantilever and the control data used in the coating calculation.

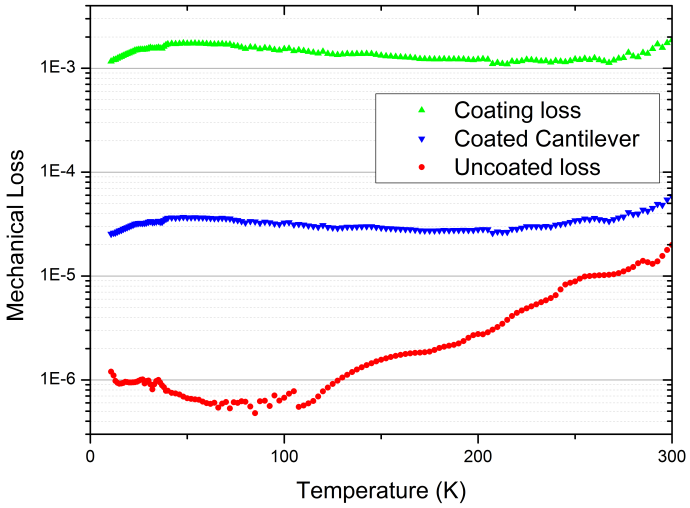

(a) Bending mode 4, 2.5 kHz

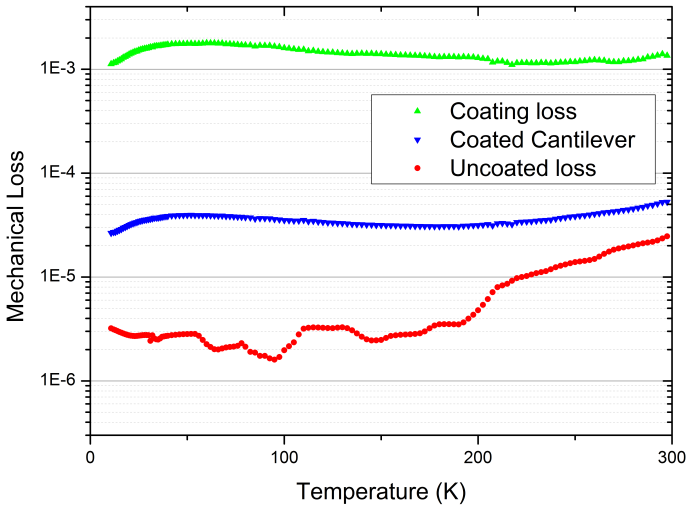

(b) Bending mode 5, 4.1 kHz

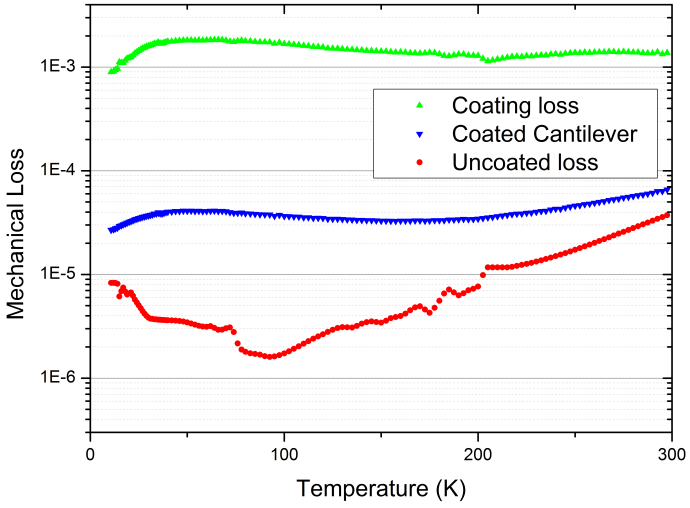

(c) Bending mode 6, 6.1 kHz

Fig. 4.40 Temperature dependent mechanical loss of an ALD tantala coating for several bending modes, measured on the oxidised cantilever. Also shown is the mechanical loss of the coated cantilever and the control data used in the coating calculation.

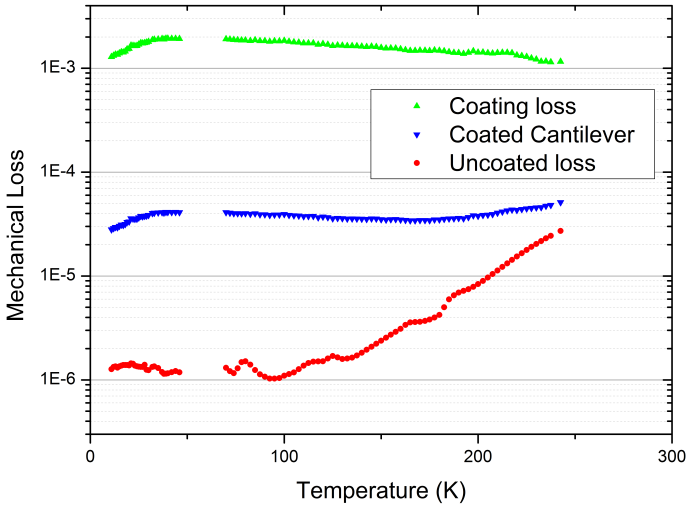

(a) Bending mode 7, 8.6 kHz

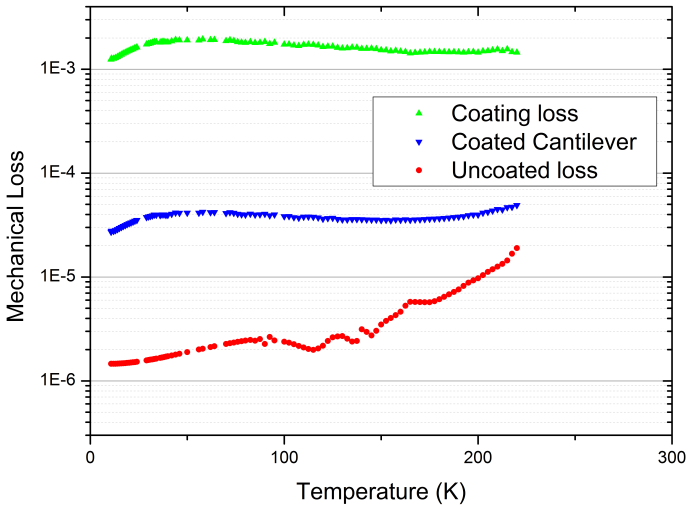

(b) Bending mode 8, 11.4 kHz

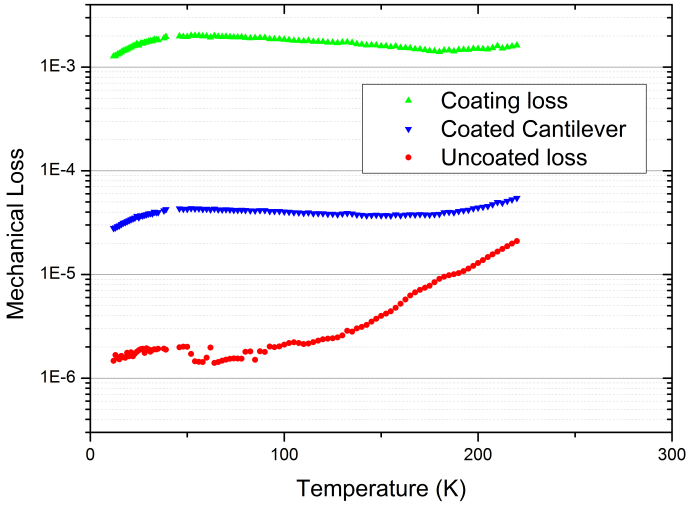

(c) Bending mode 9, 14.6 kHz

Fig. 4.41 Temperature dependent mechanical loss of an ALD tantala coating for several bending modes, measured on the oxidised cantilever. Also shown is the mechanical loss of the coated cantilever and the control data used in the coating calculation.

Dissipation peaks were observed in loss measurements of the ALD tantala coating. An Arrhenius analysis may be perfomed since the peaks do not appear at the same temperature for all measurement frequencies. For this data set, it was found that the Gumbel distribution did not give a good match to the shape of the peaks, which have a sharp decline at low temperature. The peaks were fitted with a fourth order polynomial which was later differentiated to locate the temperature at which each peak occured. As with the previous method using a Gumbel distribution, the uncertainty in temperature was calculated by changing the boundaries of the data included in the fit, and repeating the fitting process multiple times. Examples of the peaks, along with the curves fitted to extract the peak temperatures are shown in figure 4.42. The temperatures at which each peak occurs, along with the measurement frequencies, are catalogued in table 4.5.

The activation energy and rate constant obtained are $E_a = (91 \pm 22)\,\mathrm{meV}$ and $\tau_0 = (0.02 \pm 1) \times 10^{-11}\,\mathrm{s}$ respectively. The ALD tantala coating studied was deposited with the substrate temperature held at approximately 300 °C. For this reason, ALD tantala may be most directly compared with IBS tantala heat-treated to this temperature. The activation energy of the dissipation process responsible for the loss peak observed in ALD tantala is significantly higher than the activation energy of the dissipation process observed in pure tantala deposited by IBS, and heat-treated to 300 °C. In studies of pure tantala heat-treated at 300 °C, Martin et al. calculated the activation energy of the dissipation process responsible for the observed low-temperature peak to be $E_a = (66 \pm 10)\,\mathrm{meV}$ and $\tau_0 = (9.4 \pm 0.9) \times 10^{-14}\,\mathrm{s}$. This difference in activation energies may be due to differences in structure at the atomic level, which may be studied by structural measurements. Examples of the types of structural measurements which may be carried out are described in a study by Bassiri et al. [135], which compares the structures of IBS pure tantala heat-treated to 300 °C and 600 °C.

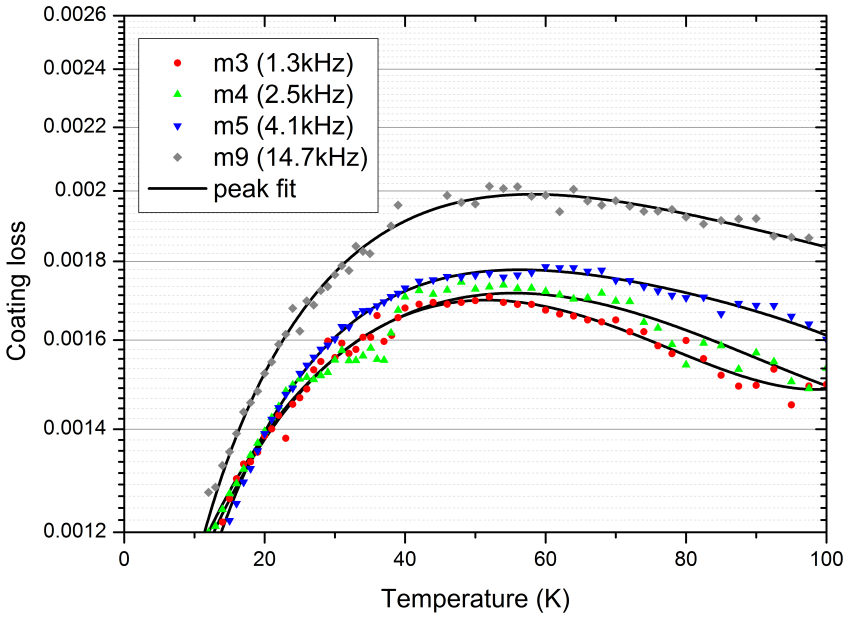

Fig. 4.42 Examples of the peaks fitted to the coating loss obtained from the oxidised cantilever measurements. The modes with the least overlap in coating loss were chosen for clarity.

ALD, oxidised cantilever		
Mode	Frequency (Hz)	T_{peak} (K)
3	1252	51.6 ± 0.1
4	2476	54.7 ± 0.1
5	4107	56.3 ± 0.2
9	14684	58.2 ± 0.2

Table 4.5 Measurement frequencies and peak temperatures used in the Arrhenius analysis of the ALD tantala coating deposited on the oxidised cantilever

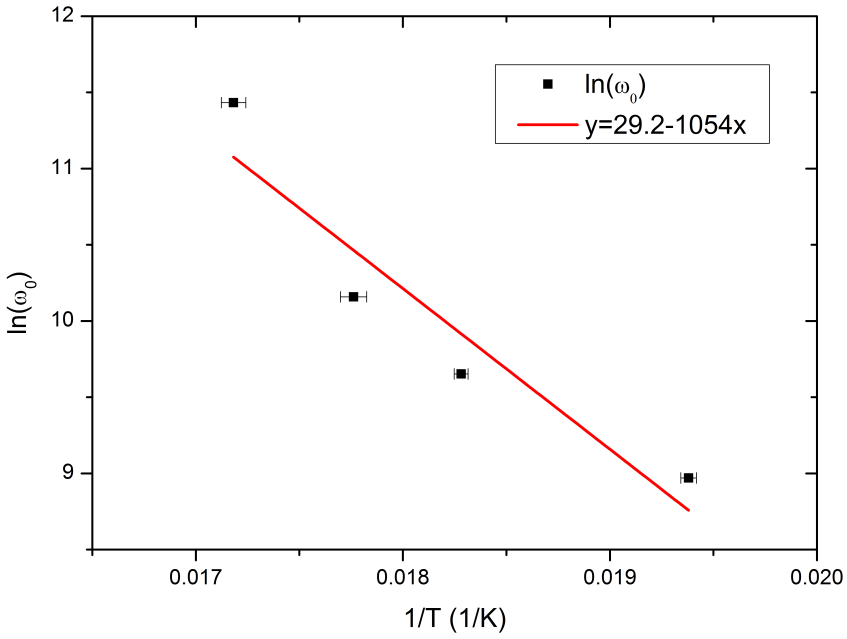

Fig. 4.43 An Arrhenius plot for the coating loss of an ALD tantala coating deposited on a cantilever which was oxidised prior to coating. A goodness of fit value of $R^2 = 0.84$ was obtained.

4.6 Conclusions

Mechanical loss measurements of titania-doped tantala coatings have been made using a variety of titania dopings and post-deposition heat-treatment. Dissipation peaks have been shown at low temperatures for the 25% doped as-deposited, and the 55% as-deposited and 600 °C heat-treated coatings. The frequency dependence of the peak temperatures indicate that the dissipation peaks arise from thermally activated relaxation processes which can be described by the Arrhenius equation.

Applying the Arrhenius equations to the 25% as-deposited coating indicates that the activation energy of the loss process responsible for the peak is $E_a = (25.3 \pm 5.4)$ meV, with a relaxation constant of $\tau_0 = (2.2 \pm 3.8) \times 10^{-8}$ s. Heat-treating the 25% doped coating to 400 °C increases the loss of the coating at low temperatures for a narrow temperature band for some modes, however this is not exhibited for all modes measured.

Heat-treating the 55% doped coating to 600 °C increases the loss of the coating at low temperatures, creating a dissipation peak similar to that seen in previous measurements of a 600 °C heat-treated pure tantala coating. The dissipation peak of the 600 °C 55% doped coating has a lower peak magnitude than that of the pure tantala coating heat-treated to the same temperature, indictating that the dissipation may be reduced by doping.

Comparison of the distribution of barrier heights indicates that further doping the 25% as-deposited coating to 55% reduces the number of barriers at all potential energies. This is reinforced by the doping of a pure tantala coating heat-treated to 600 °C, where the effect of titania-doping to a concentration of 55% is also to reduce the number of barriers at all barrier height energies. However, the number of barriers of each potential appears to be increased by heat-treatment to 600 °C.

Measurements of an ALD tantala coating have shown that the dissipation peaks follow the behaviour of the Arrhenius equation. Using this equation, the activation energies for the loss process observed in ALD tantala is $E_a = (91 \pm 22)$ meV. This is significantly higher than the activation energy of the loss process observed in IBS pure tantala heat-treated to 300 °C.

Chapter 5

Mechanical loss measurements of amorphous multilayer coatings

5.1 Introduction

The measurements of single layers of the materials used in IBS coatings are key to choosing the optimum materials for multilayer coatings. Such studies enable investigation of the effect of changing a single parameter, such as the dopant, doping concentration or post-deposition heat-treatment regime, on the mechanical loss of a coating material. It is also necessary to perform the same types of measurements on multilayer coatings since these then form the highly reflective coatings to be used in gravitational wave detectors and must be characterised in their final form in order to reliably evaluate the thermal noise expected to arise from them. Secondly, measurements of single and multilayer coatings are performed to verify the equations used to predict the loss of multilayer coating loss from single layer coating losses.

There are many previous studies of the mechanical loss of multilayer coatings in the literature oriented towards gravitational wave detectors [105, 132, 148, 149]. Most of these measurements were performed using substrates of a cylindrical geometry of varying proportions and a variety of substrate materials. Penn et al. [148] and Harry et al. [105] use silica disks, suspended at a vibrational node by flame-welding the disks to a silica fibre. With this method, care

must be taken to mask the disk around the weld area during coating deposition so that heat from the welding process does not damage the coating. Silica substrates also limit the measurement to being carried out at room temperature, due to the increased substrate loss at cryogenic temperatures.

Measurements by Yamamoto et al. [132] have sapphire as the substrate material, which has a very low loss at cryogenic temperatures. In the study, cryogenic mechanical loss measurements of two 30-layer silica/tantala stacks deposited by two commercial vendors were presented. These measurements suggested the mechanical loss of the stack to be independent of temperature, seemingly in contradiction to later studies by Martin et al., which showed the mechanical loss of single layers of both silica and tantala to have low temperature dissipation peaks [4, 115, 116].

In this chapter, measurements of the Advanced LIGO ETM and ITM coatings are presented, along with further measurements of the disks studied by Yamamoto in [132], in order to investigate the apparent discrepancy between the previous measurements and previous single layer measurements.

5.2 Advanced LIGO coatings

The highly reflective mirror coatings designed for the Advanced LIGO gravitational wave detector systems improve upon those used in initial LIGO by incorporating a few key features. The coatings depart from a conventional stack of quarter-wave optical thickness layers through studies carried out by Villar et al. [150], which showed that the thermal noise arising from a multilayer silica/tantala coating may be reduced by tailoring the layer thicknesses to reduce the overall thickness of the higher loss tantala layers within the stack. The coating Brownian noise is also improved by the larger mirror diameter used in aLIGO compared to iLIGO, but this is not a noise improvement from a change to a property of the coating itself. Each Fabry-Perot arm cavity of the aLIGO detectors is formed by an input test mass (ITM) and an end test mass (ETM). The ITM requires a higher transmission ($T = 1.4\%$ at $\lambda = 1064\,\mathrm{nm}$) compared to the ETM ($T = 5\,\mathrm{ppm}$). This is acheived simply by depositing fewer coating layers.

Assuming that the coating losses of multilayer coatings are due entirely to the dissipation of the single layers which comprise them, the mechanical

loss of the multilayer may be calculated from the material properties of the individual layers. For a multilayer coating, comprised of high and low refractive index materials (subscripted H and L respectively), the mechanical loss, ϕ_{multi}, Young's modulus, Y_{multi}, and thickness, t_{multi}, are related to those of the single layers by [118]:

$$Y_{\text{multi}} t_{\text{multi}} \phi_{\text{multi}} = Y_{\text{H}} t_{\text{H}} \phi_{\text{H}} + Y_{\text{L}} t_{\text{L}} \phi_{\text{L}}, \tag{5.1}$$

where t_{X} is the total thickness of material X within the multilayer, Y_{X} is the Young's modulus, and ϕ_{X} is the loss of the material. The loss of the multilayer may be calculated from:

$$\phi_{\text{multi}} = \frac{Y_{\text{H}} t_{\text{H}} \phi_{\text{H}} + Y_{\text{L}} t_{\text{L}} \phi_{\text{L}}}{t_{\text{H}} + t_{\text{L}}}, \tag{5.2}$$

where Y_{multi} is a weighted average of the values of the layers:

$$Y_{\text{multi}} = \frac{Y_{\text{H}} t_{\text{H}} + Y_{\text{L}} t_{\text{L}}}{t_{\text{H}} + t_{\text{L}}}. \tag{5.3}$$

If the mechanical losses of two multilayer coatings, with different relative amounts of the high and low refractive index materials, are measured, the losses of the individual materials may be calculated using the equations above. Previous studies by Crooks [151], of silica/pure tantala multilayer coatings manufactured by LMA showed the loss of the silica layers to be $\phi_{\text{SiO}_2} = (1.0 \pm 0.2) \times 10^{-4}$. Further studies by Harry et al. [105], were carried out to examine the loss of multilayers composed of silica and titania-doped tantala. These studies found that the loss of the multilayer was reduced by doping tantala with titania. The mechanical losses of the two coatings consisting of 30 alternating quarter-wavelength optical thickness layers of silica and titania-doped tantala, deposited in the large coating chamber of LMA, were $\phi_{\text{multilayer}} = (2.0 \pm 0.1) \times 10^{-4}$ and $\phi_{\text{multilayer}} = (2.1 \pm 0.2) \times 10^{-4}$. The large coating chamber at LMA is also used to fabricate the Advanced LIGO ETM and ITM mirror coatings. Additionally, a titania-doped tantala single layer from this vendor was studied, exhibiting a loss of $\phi_{\text{Ti:Ta}_2\text{O}_5} = (3.5 \pm 0.4) \times 10^{-4}$.

The mechanical losses of the aLIGO ETM and ITM mirror coatings may be predicted using equation 5.2, by inserting values from previous measurements of similar coatings by the same vendor. The Young's moduli and thicknesses of

both silica and titania-doped tantala within the ETM and ITM coatings are shown in table 5.1. The mechanical loss of silica within the coatings is taken to be $\phi_{SiO_2} = (1.0 \pm 0.2) \times 10^{-4}$ [152]. The loss of silica was used to evaluate the loss of the titania-doped tantala layers within the coatings studied by Harry [105] as $\phi_{Ti:Ta_2O_5} = (2.7 \pm 0.1) \times 10^{-4}$. The mechanical loss of a single layer titania-doped tantala coating was found to be $\phi_{Ti:Ta_2O_5} = (3.5 \pm 0.4) \times 10^{-4}$ [105]. The loss of the titania-doped tantala layer calculated from the multilayer measurements and the loss from the single layer measurements were used to predict the mechanical loss of the ETM and ITM coatings. The values predicted for the mechanical loss of the ITM and ETM coatings are shown in table 5.2.

The mechanical loss of the ITM coating at room temperature is expected, from the calculations above, to be in the range $(1.7 \pm 0.1) \times 10^{-4}$ to $(2.0 \pm 0.3) \times 10^{-4}$. The mechanical loss of the ETM coating at room temperature is expected to be in the range $(1.9 \pm 0.1) \times 10^{-4}$ to $(2.3 \pm 0.2) \times 10^{-4}$.

ETM and ITM coating properties		
	ETM	ITM
Y_H	140 GPa	140 GPa
t_H	2.1 μm	734 nm
Y_L	72 GPa	72GPa
t_L	3.8 μm	2092 nm

Table 5.1 The properties of the silica and titania-doped tantala layers within the aLIGO mirror coatings.

ETM and ITM coating loss predictions		
$\phi_{Ti:Ta_2O_5}$	$(2.7 \pm 0.1) \times 10^{-4}$	$(3.5 \pm 0.4) \times 10^{-4}$
ϕ_{ITM}	$(1.7 \pm 0.1) \times 10^{-4}$	$(2.0 \pm 0.3) \times 10^{-4}$
ϕ_{ETM}	$(1.9 \pm 0.1) \times 10^{-4}$	$(2.3 \pm 0.2) \times 10^{-4}$

Table 5.2 The mechanical loss of titania-doped tantala used in multilayer loss predictions for the aLIGO ETM and ITM, along with the predicted values of loss. The mechanical loss of silica used was $\phi_{SiO_2} = (1.0 \pm 0.2) \times 10^{-4}$.

5.2.1 Advanced LIGO ETM coatings

Two silicon cantilevers were placed in an oven at 900 °C for 10 hours prior to coating by the coating vendor, LMA [153]. The cantilever was then placed

inside the vendor's coating chamber alongside two aLIGO ETM substrates to be coated by ion beam sputtering. Two silica cantilevers were also coated to allow better sensitivity to the coating loss at room temperature. However, one silica cantilever broke in transit, and one silicon cantilever was broken while handling.

The total thickness of an aLIGO ETM coating is 5.9 µm, of which a total of 3.8 µm is silica, and 2.1 µm is titania-doped tantala. A titania-doping concentration of around 33% is used in the high-index layers. After deposition, the coating was heat-treated in air at 500 °C for 10 hours. A photo of the coated cantilevers is shown in figure 5.1

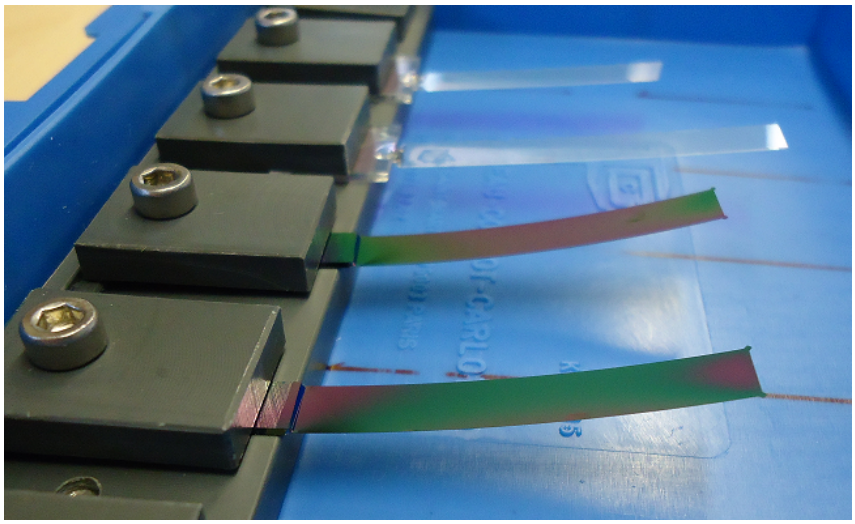

Fig. 5.1 Two silicon cantilevers coated on the underside with the aLIGO ETM coating (foreground), and two silica cantilevers with the same coating (background).

A coated silicon cantilever was clamped in a cryostat and its loss measured in the temperature range 10-300 K. The mechanical loss as a function of temperature of the coated cantilever is shown in figure 5.2, along with the loss of an uncoated cantilever of similar thickness. In the absence of control data for the second bending mode, control data for the third mode was used. Since the third bending mode has a higher frequency than the second, it exhibits a higher substrate thermoelastic loss. Therefore, in order to not under-estimate the coating loss, the thermoelastic loss of the third mode frequency was subtracted from the control data, and the thermoelastic loss of the second mode frequency added to the residual loss to provide control data for the second mode. A plot of the mechanical loss of the third mode of the uncoated cantilever, the

calculated control data for the second mode and the thermoelastic loss of both modes are shown in figure 5.3.

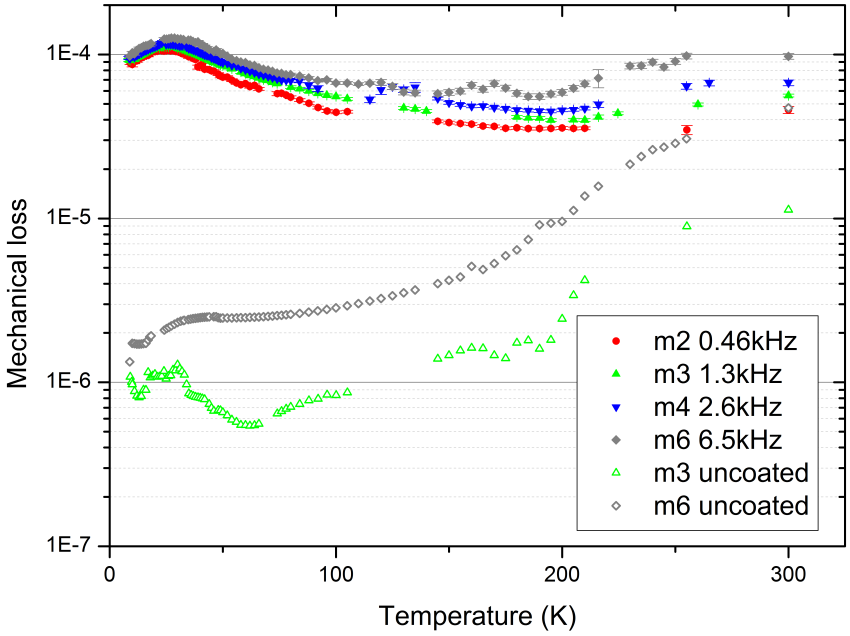

Fig. 5.2 The measured mechanical losses of a silicon cantilever coated with the Advanced LIGO ETM coating, and the loss of a silicon cantilever of similar thickness with no coating.

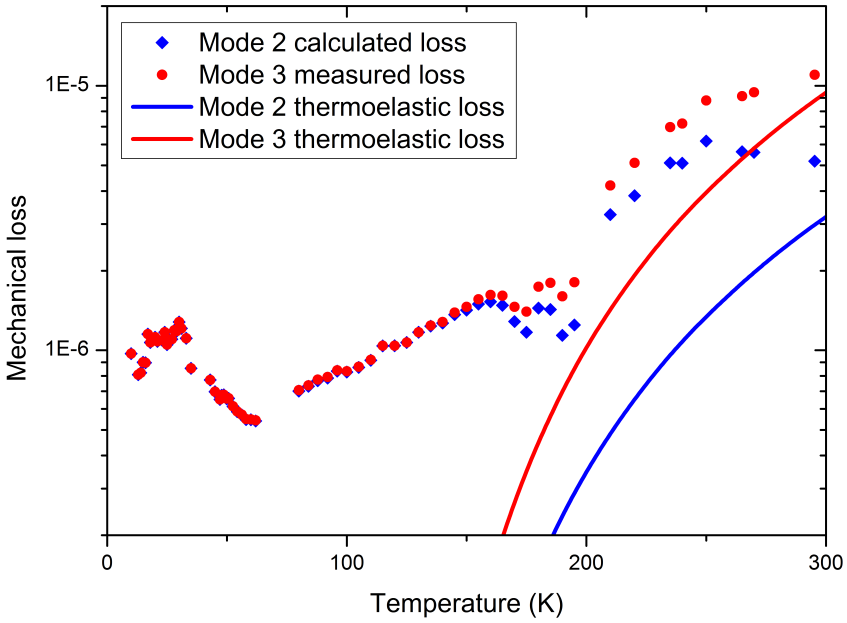

Fig. 5.3 The control data for mode 2 were calculated from the measurements of mode 3. First, the mode 3 thermoelastic loss was subtracted from the data. Then, the mode 2 thermoelastic loss was added.

To calculate the coating loss, the ratio of energy stored in the substrate to that in the coating was evaluated using the finite element analysis package ANSYS. This technique is employed when the coating thickness is not negligible compared to the cantilever thickness. The model used to calculate this energy ratio assumed that the coating consisted of only two layers, one each of silica and tantala. This was cross-checked with a similar calculation carried out by the vendor and was found to be in good agreement.

The coating losses calculated for all four modes throughout the temperature range are shown in figure 5.4. All four modes show a clear peak around 25 K. The loss also has a frequency dependence, tending towards higher loss with higher frequency. A closer view of the 25 K dissipation peak is shown in figure 5.5. The coating loss of the sixth mode shows a small peak at 170 K, and increases over 200 K. This behaviour is not exhibited by the other modes, and is likely to be due to excess loss into the clamp.

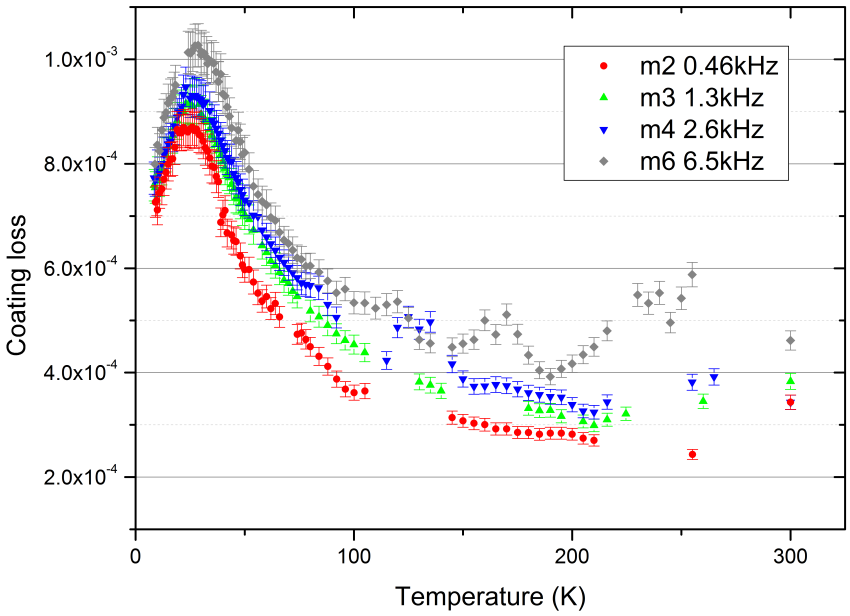

Fig. 5.4 The calculated mechanical loss of the Advanced LIGO ETM coating throughout the temperature range 10-300 K.

The aLIGO ETM coating may be expected, from measurements of single layer silica and tantala coatings on silicon cantilevers, to feature the peak exhibited. However, calculations of the mechanical loss of a 31 layer silica/pure tantala stack by Martin show a sharp peak at 20 K with a shoulder to the loss peak at around 50 K, originating from the silica layers [113]. The absence of the

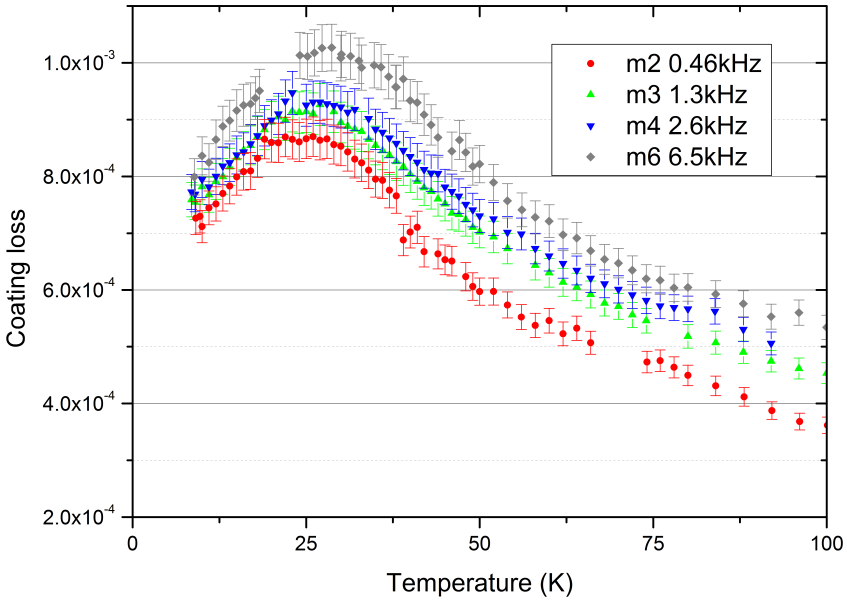

Fig. 5.5 A closer view of the dissipation peak exhibited by the Advanced LIGO ETM coating at low temperature. The temperature and level of the peak shows some frequency dependence.

shoulder in the aLIGO ETM measurements may be due to differences between the atomic structure of the coatings studied. In the calculations by Martin, the silica loss was from measurements of a coating from a different vendor, which may give rise to a different coating density since different vendors use different deposition energies. Additionally, the single layers of silica and tantala used for the calculations had been heat-treated at a higher temperature, 600 °C [113].

The temperature of the dissipation peak around 25 K shows a frequency dependence, and may be analysed in the same fashion as was carried out in Chapter 4 for titania-doped tantala single layer coatings. The curves fitted to each peak are shown in figure 5.6, and the temperature of the peaks are catalogued in table 5.3. An Arrhenius plot made using these values is shown in figure 5.7. The line of best fit gives the values of the gradient and y-intercept, which allow the activation energy and relaxation constant associated with the dissipation process to be calculated to be $E_a = (31.8 \pm 7.0)$ meV and $\tau_0 = (0.4 \pm 5.0) \times 10^{-10}$ s respectively. The activation energy calculated for the aLIGO ETM coating agrees, within error, with that observed in silica [116], tantala [4], and the titania-doped tantala measurements of Chapter 4.

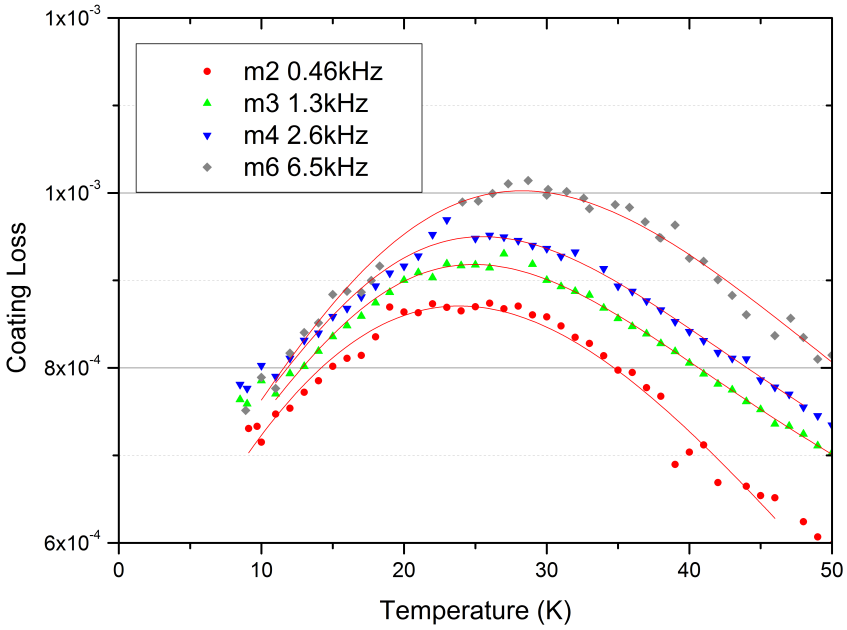

Fig. 5.6 Curves fitted to the dissipation peaks of the aLIGO ETM coating.

aLIGO ETM		
Mode	Frequency (Hz)	T_{peak} (K)
2	469	23.7 ± 0.3
3	1337	25.1 ± 0.2
4	2643	25.3 ± 0.3
6	6544	28.3 ± 0.3

Table 5.3 Dissipation peak temperatures for the Advanced LIGO ETM coating, used to calculate the activation energy of the loss mechanism responsible for the peak.

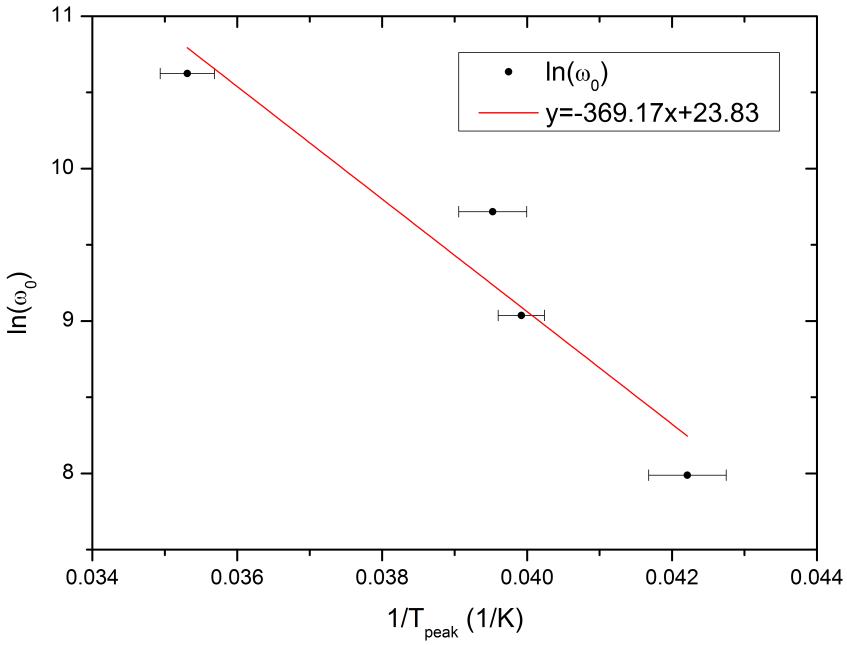

Fig. 5.7 An Arrhenius plot of the dissipation peak observed in the Advanced LIGO ETM coating, with a line of best fit.

5.2.2 Room temperature measurements of the aLIGO ETM coating

The mechanical loss of both the coated silicon and silica cantilevers were measured at room temperature. The mechanical loss of the coated silicon cantilever was compared to the mechanical loss of another, uncoated silicon cantilever of similar thickness used as a control sample to allow calculations of coating loss. The mechanical loss of the silica cantilever was measured prior to coating.

The mechanical loss of the uncoated silica cantilever, the coated silica cantilever and the calculated coating loss are shown in figure 5.8. It should be noted that for the lowest mode of the cantilever, no measurements were taken prior to coating. Therefore, the calculated coating loss for this mode is an upper limit where the dissipation of the coated cantilever is assumed to be entirely due to the coating. From the measurements, a loss of 3×10^{-4} for the first four modes, and 4×10^{-4} for the two higher frequency modes is found for the coating loss. The two highest frequency modes also exhibit increased substrate loss, which may reduce the sensitivity to the coating loss.

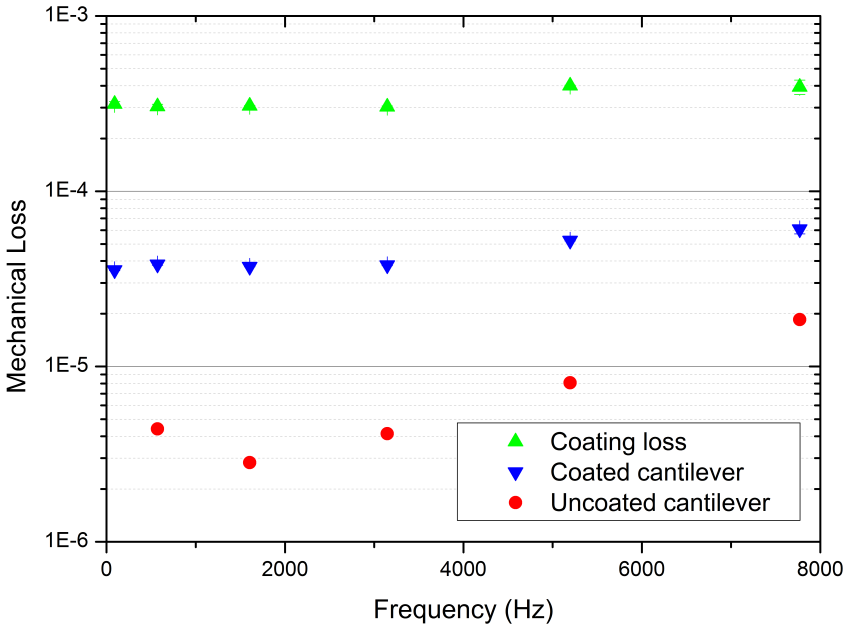

Fig. 5.8 The mechanical loss of a silica cantilever before and after being coated with the aLIGO ETM coating. The calculated coating loss is also shown.

The results of a similar set of measurements for the silicon cantilever are shown in figure 5.9. Analysis of these measurements shows that at the lowest frequencies, the coating loss tends towards the level of coating loss exhibited on the silica cantilever. However, at higher frequencies the coating exhibits a higher loss on the silicon cantilever. The lowest coating loss exhibited was $(3.4 \pm 0.2) \times 10^{-4}$ and the average was $(4.6 \pm 1.2) \times 10^{-4}$.

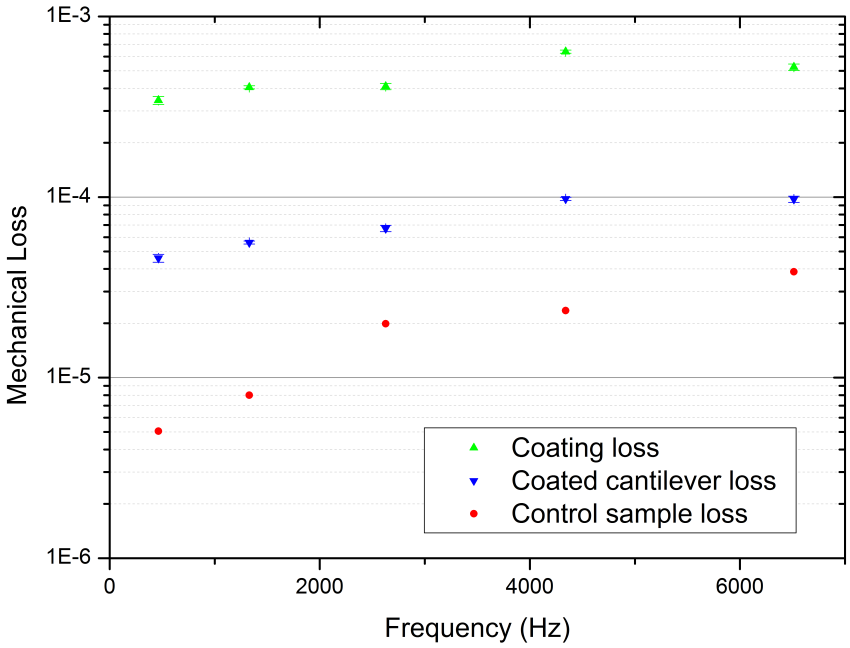

Fig. 5.9 The mechanical loss of a silica cantilever coated with the aLIGO ETM coating. The loss of an uncoated silicon cantilever of similar thickness was used to calculate the coating loss.

The lowest coating loss measured for the aLIGO ETM coating was 3×10^{-4}, which was exhibited on the first four modes of the silica cantilever. Since these modes show the lowest substrate loss, giving the best sensitivity to the coating loss, these measurements are more reliable than the coating losses calculated from the modes with higher substrate loss.

5.2.3 Advanced LIGO ITM coatings

A nominally identical coating to the ITM coatings was deposited by the vendor onto one side of a silica disk measuring 75 mm in diameter by 2.5 mm thick. This disk was suspended using the nodal suspension technique, placed in a vacuum chamber and measured using an interferometric displacement readout, as described in Chapter 3.

The measured mechanical loss of the disk for four suspensions is shown in figure 5.10. For some modes such as the 6.1 kHz and 10.6 kHz modes, two resonant frequencies exist for the same mode shape. These frequencies are separated by a few Hertz, and the mode shapes are simply rotated from each other. This rotation means that one of the two modes is limited by suspension loss, since the suspension points are not at vibrational nodes. Where these mode pairs exist, the higher loss member of the pair is not used for coating loss calculations, since it is known to be suspension-limited. At each frequency, the data from the suspension exhibiting the lowest loss is used. A mean of the measured losses from that suspension is taken, and the standard deviation of five ring-downs from that suspension is evaluated.

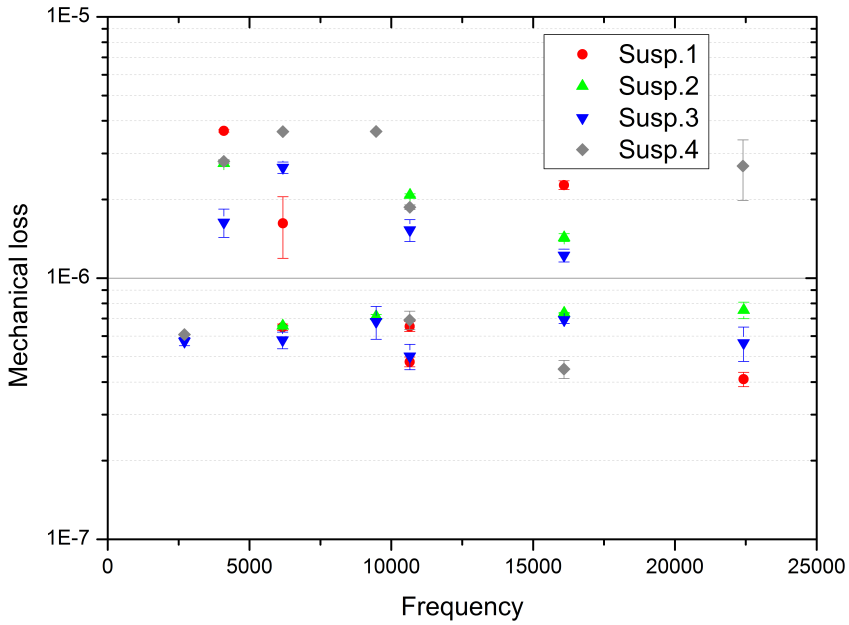

Fig. 5.10 The measured loss of a silica disk with the aLIGO ITM coating on one face for several suspensions.

The mechanical loss of the disk was not measured prior to the coating deposition, and for coating loss calculations, the dissipation was assumed to be entirely due to the coating. The coating loss values presented are therefore an upper limit. The measured mechanical loss of the coated disk and the calculated coating losses are shown in figure 5.11. The calculated coating losses are in the range 0.9-1.4$\times 10^{-4}$ for all modes except for one. The mechanical loss of this mode is limited by the suspension, since the mode shape features no vibrational nodes at the edges of the disk. This mode may therefore be excluded from consideration. The mean coating loss evaluated without this mode is $(1.18 \pm 0.18) \times 10^{-4}$. The coating loss appears to reduce slightly with increasing frequency.

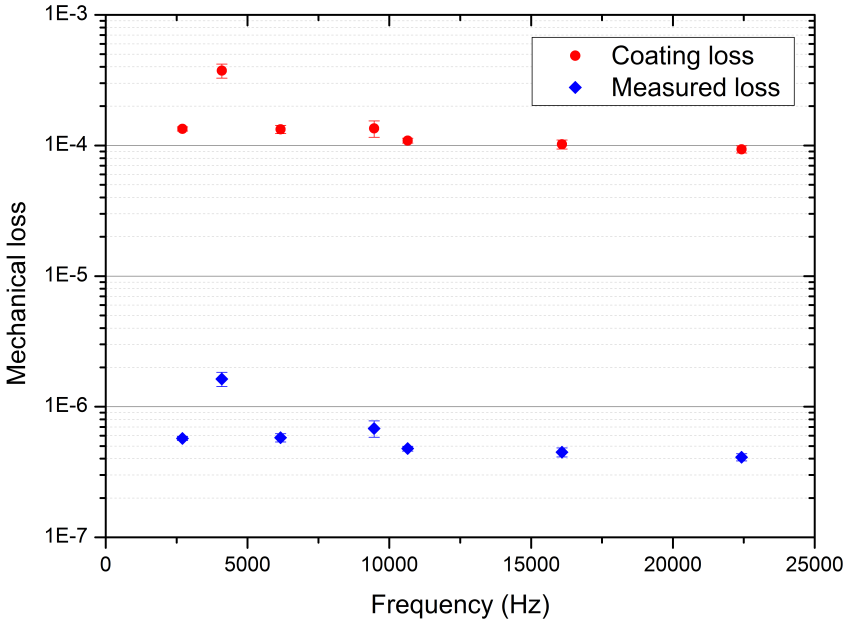

Fig. 5.11 The measured loss of a silica disk with the aLIGO ITM coating on one face. Coating loss calculations assume all measured loss to arise from the coating.

Previous measurements of a silica disk with polished edges by Cumming found the loss of the disk to be of the level 5×10^{-8} [3]. This is of the order of 10% of the loss of the coated disk. Assuming this level of substrate loss, the coating loss was recalculated, and is shown in figure 5.12, alongside the original calculated coating loss. It can be seen that the recalculated loss is slightly lower than the original coating loss, with a mean loss of $(1.06 \pm 0.19) \times 10^{-4}$. This loss agrees within error with the loss calculated from the assumption of zero substrate loss.

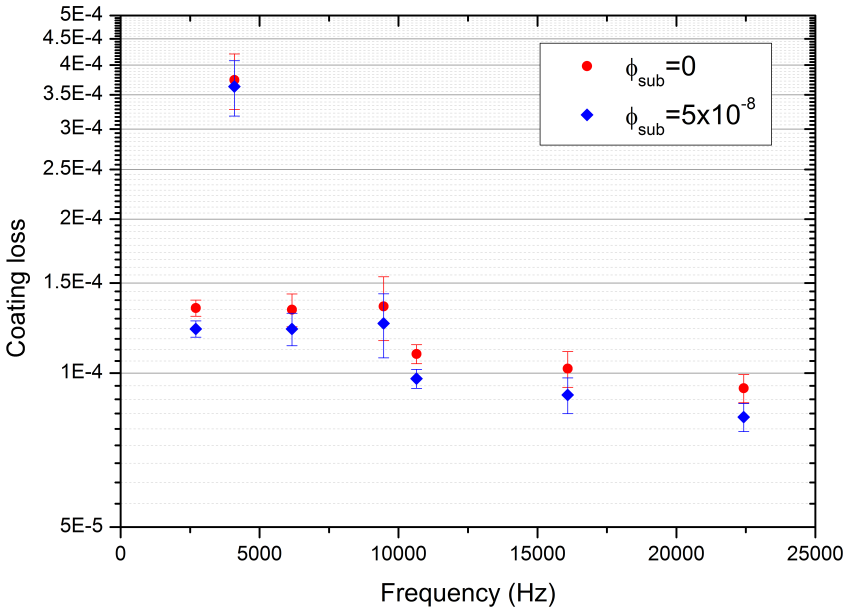

Fig. 5.12 The mechanical loss of the aLIGO ITM coating, calculated assuming that all of the loss exhibited was due to the coating (red), and assuming that the substrate exhibits a loss of $\phi_{\text{sub}} = 5 \times 10^{-8}$ (blue).

5.2.4 Analysis and discussion of the ETM and ITM coating loss

Using equation 5.2, the mechanical loss of a multilayer coating may be predicted from the material properties of the individual layers. Since the relevant properties of the ETM and ITM coatings are known, they may be used to evaluate the mechanical loss of the silica and tantala layers within the coating. This is possible since the ETM and ITM coatings each feature a different ratio of silica to tantala thickness within the full coatings. The values filling these equations are presented in table 5.1. Two values are given for the ITM coating loss: that calculated as an upper limit from the original measurements, and that calculated from the assumption that the substrate loss is 5×10^{-8}.

From the system of equations using the zero-loss substrate ITM values, the loss of the tantala within the coating is calculated to be $6.2{\times}10^{-4}$, and the loss of the silica layers calculated to be -2.3×10^{-4}. This result is clearly non-physical since a negative loss means that the silica layers would be generating energy during oscillation. However, this may mean that there is an additional loss which the system of equations used to obtain these values does not take

into account. An example could be any loss terms arising due to the interfaces between coating layers, or between the coating and the substrate.

The calculations were carried out again with the ITM coating loss calculated from the assumption that the substrate contributed a loss of 5×10^{-8} to the measured values. Under this assumption, the tantala was calculated to exhibit a loss of 6.7×10^{-4}, and the silica a loss of -2.8×10^{-4}. This is, again, a non-physical result.

Mechanical loss measurements carried out by the coating vendor, LMA [153], of silica and silicon cantilevers coated with the ETM coating agree with those carried out by the author. Measurements by the vendor of an ITM coating deposited onto a cantilever suggest that the mechanical loss of the ITM coating is 2.1×10^{-4} [154]. The coating losses predicted by the vendor for the ITM and ETM coatings were $(1.2 \pm 0.2) \times 10^{-4}$ and $(1.5 \pm 0.2) \times 10^{-4}$ respectively [154]. Further measurements of an ITM coating deposited on one silica disk and one silicon disk suggested that the coating loss of the ITM coating was $(1.5 \pm 0.1) \times 10^{-4}$, which is closer to the predicted values than found from cantilever measurements [154]. These measurements show an apparent discrepancy between the loss of one coating when deposited upon disks and a cantilever, with the coating loss found from disk measurements appearing closer to the expected coating loss than found using cantilevers. From this, it was suggested that the cantilever measurement loses accuracy when the coatings deposited upon them are relatively thick, and highly stressed. However, more information about the studies carried out by the vendor is required in order to draw a full conclusion.

Initial measurements, characterising the mechanical loss of a niobia film as a function of film thickness and substrate geometry are presented in Appendix B. These measurements conclude that, for a monolayer coating with a relatively high loss, there appears to be no effect of substrate geometry or film thickness on the calculated coating loss. However, futher studies are required using low loss coatings of the type used in Advanced LIGO for futher information.

5.3 A silica/tantala multilayer on a sapphire disk

Early mechanical loss measurements of coatings designed for future gravitational wave detectors include those made on coatings deposited on sapphire disk substrates [132]. The disks were 10 cm in diameter and 0.5 mm thick. The coatings were deposited by ion-beam sputtering at the National Astronomical Observatory of Japan (NAOJ) and consisted of 30 alternating silica and tantala layers, each of quarter wavelength optical thickness for a wavelength of 1064 nm. The coating was left in an as-deposited state, with no additional post-deposition heat-treatment. Mechanical loss measurements were carried out at several temperatures in the range 4-300 K and concluded that the coating mechanical loss is independent of temperature [132].

However, independent measurements were also carried out on coatings deposited by Japan Aviation Electronics Industry Ltd. (JAE) upon sapphire disks 1 mm in thickness and 10 cm in diameter [132]. One coating from this batch was heat-treated after deposition, however the heat-treatment regime is not specified by the vendor. From these measurements, the authors also conclude that the coating loss is almost constant with temperature.

Measurements of 0.5 μm thick monolayers of both silica and tantala, deposited by CSIRO upon silicon cantilevers, showed that the mechanical losses of both coating materials vary strongly with temperature and that both materials show dissipation peaks around 20 K [4, 116], the main temperature of interest for the KAGRA detector. Using the measured losses of the individual materials, and calculating the losses expected when they are combined into a multilayer coating suggests that the thermal noise reduction exhibited after lowering the temperature of the mirror coatings would be less than if the coating loss was constant with temperature.

Measurements of the multilayer coatings designed and deposited by LMA [153] for the Advanced LIGO mirrors presented in section 6.2 show that the mechanical loss of these coatings are also strongly dependent upon temperature, with a dissipation peak similar to that of silica and tantala at low temperatures. However, there are numerous differences between these coatings and those deposited by the NAOJ and JAE. Firstly, the Advanced LIGO coatings are all heat-treated, with a known temperature and of known duration. Secondly, the

aLIGO coatings all feature tantala doped with titania to a cation concentration of around 33%, whereas the NAOJ and JAE coatings contain pure tantala. Thirdly, these coatings were all made by different vendors. This means that the coatings may have been made with significantly different deposition parameters, changing the structure of each of the coatings, which may affect the mechanical loss. Additionally, the NAOJ and JAE coatings were deposited upon sapphire substrates, whereas the aLIGO coatings studied at cryogenic temperatures were deposited upon silicon.

KAGRA will operate with mirrors cooled to 20 K [59]. It is therefore of interest to resolve the apparent discrepancy between the measurements of the NAOJ and JAE coatings and those deposited upon silicon cantilevers. Measurements in this chapter were carried out by the author at the Institute for Cosmic Ray Research (ICRR), University of Tokyo by the author in collaboration with staff at the ICRR.

5.3.1 Sample details

The studies of Yamamoto et al. [132] used six sapphire disks, each of 10 cm diameter. From this set, the 0.5 mm thick disk coated by the NAOJ and its corresponding uncoated counterpart were selected for further measurements due to availability. The coating is composed of 15 layers of pure tantala, each quarter-wavelength optical thickness (for $\lambda = 1064\,\mathrm{nm}$), and 14 quarter-wavelength optical thickness layers of silica, and one half-wavelength thick silica layer. Mechanical loss measurements of both the coated and uncoated disk were carried out before the coated disk was heat-treated in air for 10 hours at 500 °C at the NAOJ, and further measurements taken. This heat-treatment regime was chosen to match that of the Advanced LIGO coatings.

5.3.2 Measurements

Measurements of the disks were carried out using the nodal support described in Chapter 3. Additionally, a photo of the nodal support system inside the cryostat is shown in figure 5.13. The disk balances on a copper cone, and the system is built with a moveable ring for sample mounting such that the cone is exactly centered on a 10 cm disk. After the disk has been balanced, a second, spring-loaded cone is lowered onto the disk from above to pin the disk

in place at the central node. Examples of vibrational mode shapes for which this support may be used are shown in figure 5.14. The exciter plate is then placed a few millimetres away from the disk and the nodal support structure is transferred into a cryostat.

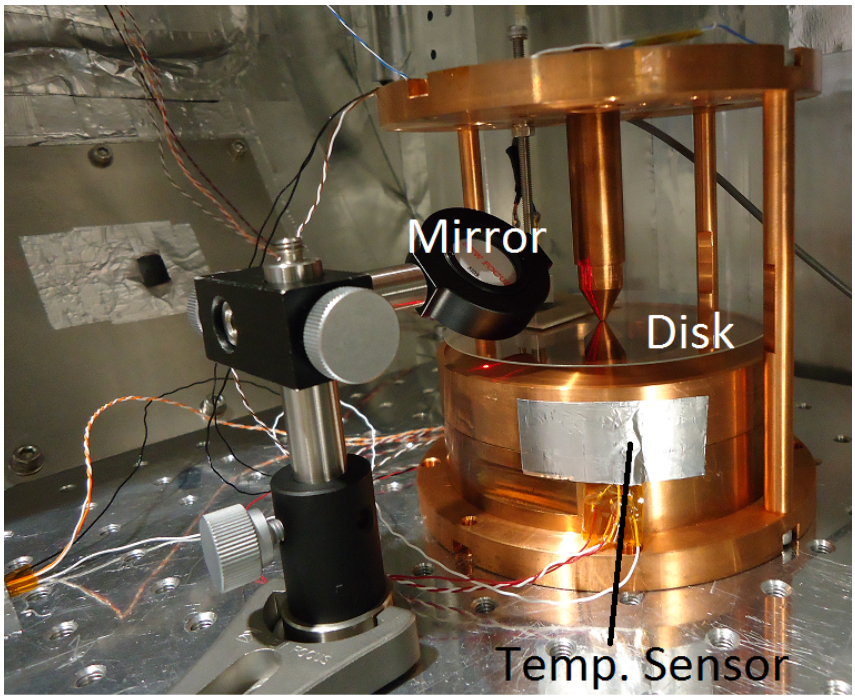

Fig. 5.13 A photo of the nodal support system used to measure the mechanical loss of sapphire disks, shown inside the cryostat at the ICRR.

Inside the cryostat, a mirror is positioned above the disk to allow an optical lever displacement readout to be used to sense the displacement of the disk as each of its resonant modes is excited in turn. The laser and photodiode for this readout was positioned outside the cryostat for any adjustments required during cooling/heating. The photodiode signal was passed through a lock-in amplifier and the lock-in signal was recorded using a computer. The cryostat was evacuated to pressures which were typically below 10^{-6} mbar during measurement to minimise the effects of gas-damping [119]. The cryostat was cooled using a Gifford-McMahon cryocooler.

Three temperature sensors were used - one was placed on the top plate of the nodal support, one placed on the bottom half of the nodal support and one on the aluminium plate on which the complete nodal support sits during

measurements. A heater attached to the top plate was used to change the temperature of the disk by changing the heater power incrementally.

The temperature of the disk was calibrated by attaching a temperature sensor to a blank disk, and measuring the disk temperature as a function of heater power and the other temperatures measured. It was found that the disk temperature closely matched the temperature of the top plate of the support. A graph of the disk temperature as a function of the top plate temperature is shown in figure 5.15. A polynomial was fitted to the data collected so that the disk temperature could be calculated during loss measurements when no temperature sensor is attached to the disk. The temperature difference between the polynomial and the data, dT, is also shown to illustrate the magnitude of uncertainty in the estimation of disk temperature. In the temperature range where a dissipation peak would be expected for a silica/tantala coating (under 30 K), dT is typically below 0.1 K.

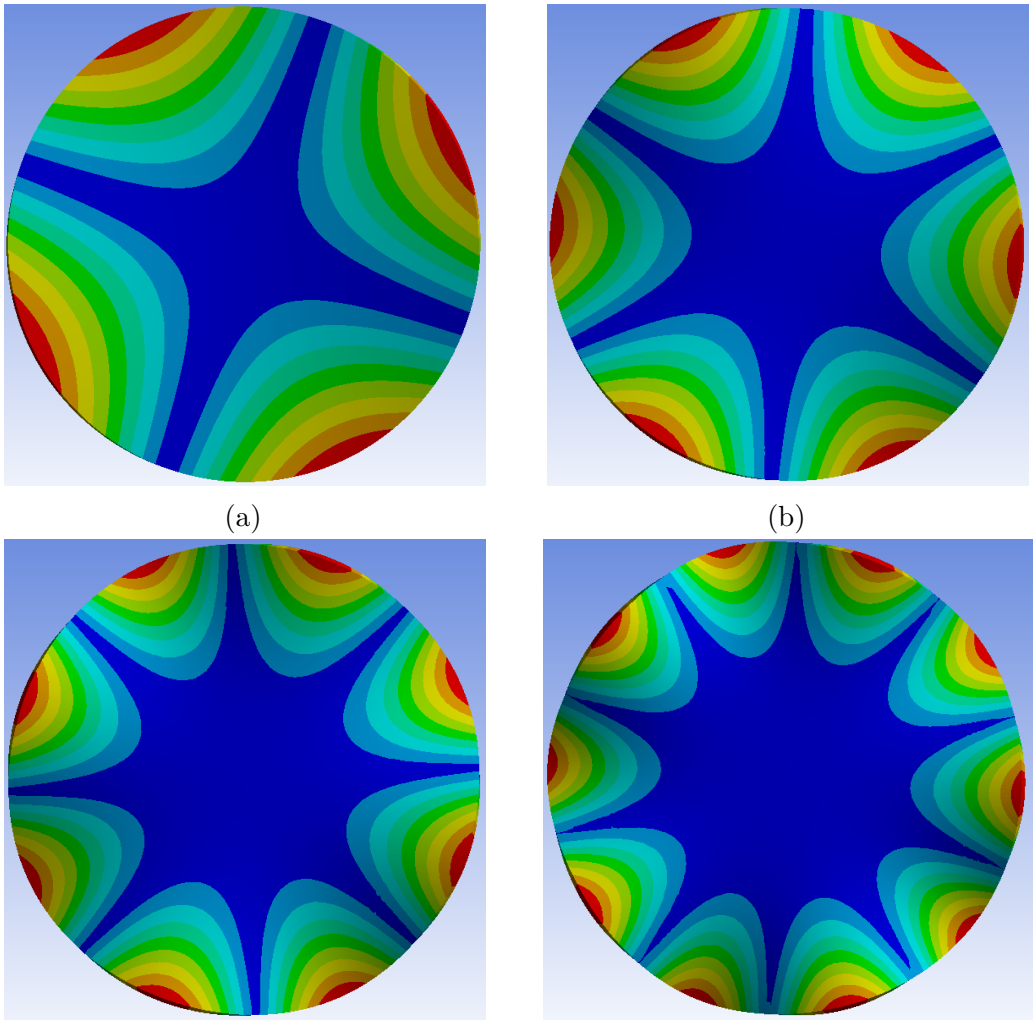

(a) (b)

(c) (d)

Fig. 5.14 ANSYS finite element models showing the shapes of several vibrational modes of a sapphire disk. The blue areas indicate minimal motion, while red areas indicate maximum motion during oscillation. Shown are (a) the 520 Hz, (b) the 1204 Hz, (c) the 2115 Hz, and (d) the 4594 Hz vibrational modes. All modes feature minima at the centre of the disk, which is necessary for the nodal support technique.

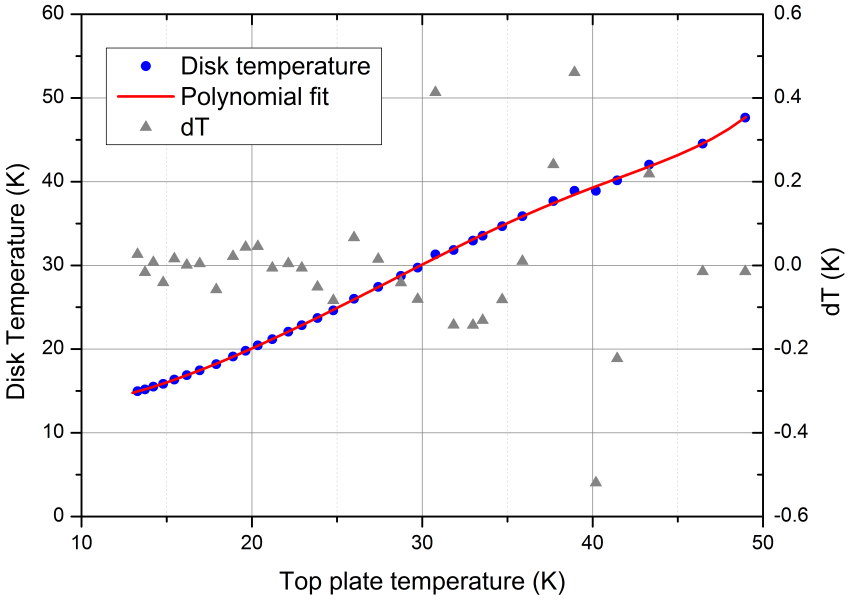

Fig. 5.15 The measured temperature of a sapphire disk as a function of the top-plate of the nodal support. A polynomial was fitted to the data so that the temperature of the disk could be calculated from the top plate temperature during loss measurements. The difference in temperature between the polynomial and the disk temperature, dT is also shown, demonstrating the uncertainty in temperature to be small, particularly below 30 K.

The temperature dependent mechanical loss of the 520 Hz mode of an uncoated sapphire disk is shown in figure 5.16. Also shown is the mechanical loss of a sapphire disk coated with the multilayer silica/tantala coating, and the mechanical loss of the coated disk, after heat-treatment. The thermoelastic loss of the disk is also shown. The thermoelastic loss of the disk was calculated from the modified version of Zener's function found in Blair and Ferreirinho [155], and the material properties of sapphire found in Touloukian [156]. The mechanical loss of all three disks are limited above 100 K by the thermoelastic loss of the substrate.

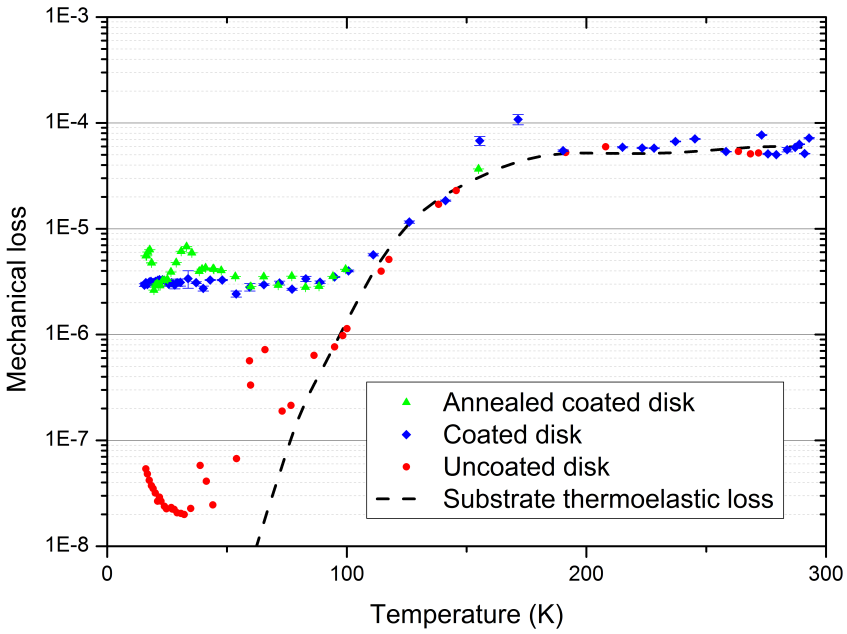

Fig. 5.16 The temperature dependent mechanical loss of a sapphire disk with no coating, with an as-deposited 30-layer silica/tantala coating, and a disk with a heat-treated 30-layer silica/tantala coating. Also shown is the thermoelastic loss of the substrate, which can be seen to limit the loss of all three disks above 100 K.

Below 50 K, the level of loss of the disks with the as-deposited and heat-treated coatings can be seen to be similar, with both far above the level of substrate loss.

The coating loss was calculated from these measurements using an FEA model, used to calculate the energy storage ratios. For this model, the coatings were assumed to be single layers with thickness-averaged mechanical properties. The mechanical losses of the as-deposited and heat-treated coatings are shown in figure 5.17. The coating loss of the as-deposited coating can be seen to

have a consistent level of around 4×10^{-4}. However, the heat-treated coating shows a larger variation with temperature. In the range 60-100 K, the loss matches that of the as-deposited coating. At 33 K, the heat-treated coating shows a sharp peak in loss, which is followed by a lower, broader peak around 42 K. Additionally, the loss shows a sharp rise below 20 K. These features are present on the first set of measurements made of the mechanical loss of the heat-treated coating. However, dissipation peaks are typically considered 'real' when they are demonstrated to be present across multiple vibrational modes, and for multiple measurement runs. That is, dissipation peaks found in a single vibrational mode can arise through frequency and temperature dependent couplings of the resonant mode being studied to a resonant mode of its support stucture [114]. For this reason, the heat-treated disk was measured again.

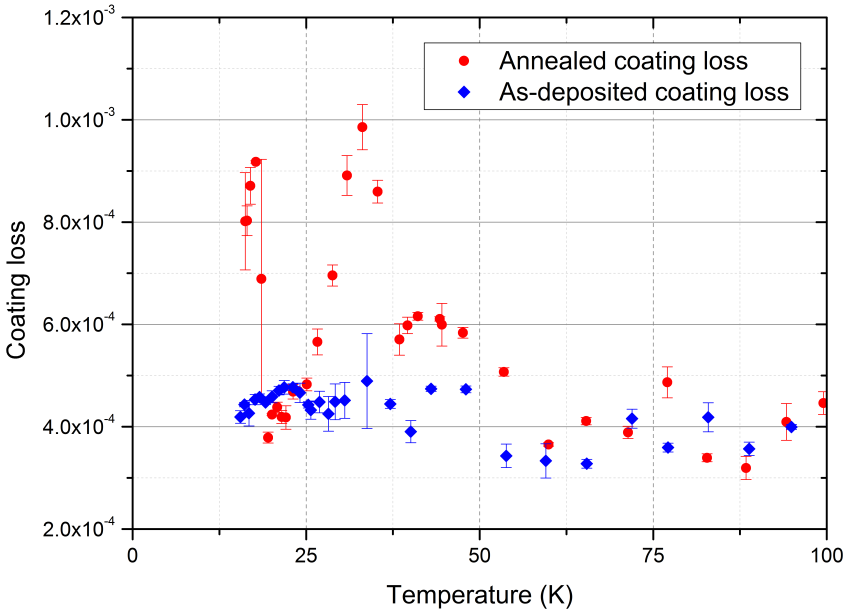

Fig. 5.17 The mechanical loss of an as-deposited 30-layer silica/tantala coating, and the loss of a heat-treated 30-layer silica/tantala coating. The as-deposited coating shows little variation with temperature, whereas the heat-treated coating shows several peaks.

The heat-treated disk was re-measured with an additional three modes being measured. In total, the 520 Hz, 1204 Hz, 2115 Hz and 4594 Hz modes were measured. The mode shapes of each are shown in figure 5.14. The coating losses of the first, second and fourth mode are shown in figure 5.18. The coating

loss of each mode shows a little scatter, with losses in the range 4-7$\times 10^{-4}$, but are largely flat with temperature and show no clear frequency dependence.

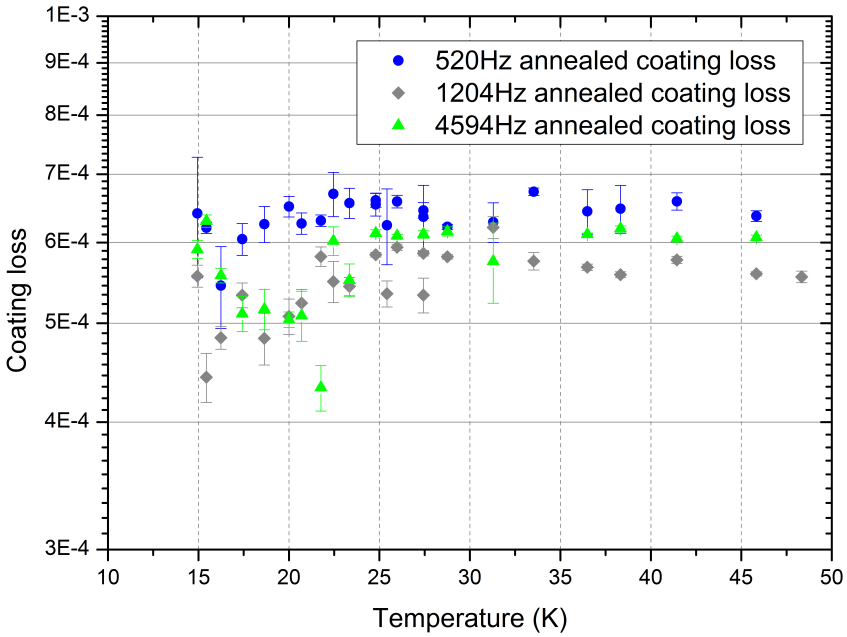

Fig. 5.18 The loss of the annealed 30-layer silica/tantala coating measured on a sapphire disk.

However, the coating loss calculated from the mechanical loss of the 2115 Hz mode showed a variation with temperature similar to the coating loss of the annealed disk in the first run. The two are shown in figure 5.19. The mechanical loss of the 2115 Hz mode shows a distinct peak at a temperature similar to that of the 520 Hz mode. The mechanical loss of the 2115 Hz mode was found, at the temperature of the peak, to reduce to the background level of loss (a coating loss of 6×10^{-5}) when the cryocooler was turned off. However, with the cryocooler off, the disk temperature rose too quickly for repeatable measurements to be made. When the cryocooler was turned back on, the level of loss rose again. This suggests that some mechanical coupling may have been present between the vibrations of the cryocooler and the disk. Since the measurements of the 520 Hz mode shows a very similar temperature dependence to the 2115 Hz mode, it is possible that the original measurements of the heat-treated disk simply showed features of a similar coupling.

The first measurements of the heat-treated coating, which show several loss peaks, follows the same shape of loss of a mode which demonstrated a lossy

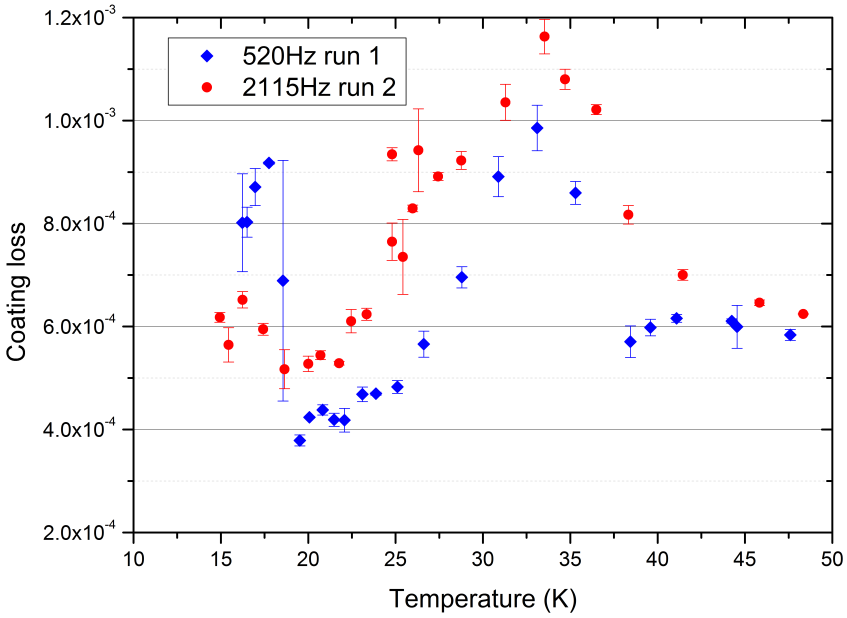

Fig. 5.19 The coating loss calculated from the first measurement run, compared to a set of measurements known to exhibit coupling between the disk and the cooling system.

coupling between the disk and the cooling system. Follow-up measurements of the loss of three vibrational modes, show little temperature dependence in the range 15-50 K. Since this is consistent across multiple modes, the most likely deduction is that the coating loss does not feature any loss peaks in this temperature range. However, to fully determine the behaviour of the coating loss at cryogenic temperatures, futher measurements would be required.

Both the as-deposited and heat-treated coatings show little dependence on temperature under 50 K. This agrees with the behaviour exhibited in measurements by Yamamoto et al. [132]. The difference between the behaviour of the coating and the behaviour predicted by I. Martin [113] may be due to the difference in atomic structure between the coating measured here and those used for the predictions. Alternatively, it may even be that coatings composed of these materials simply behave differently when deposited upon a sapphire substrate. To test this, an identical coating would need to be deposited upon both a silicon and sapphire substrate. It would then be possible to make a direct comparison, since only one parameter would be different between the two: the substrate material.

5.4 Conclusions

The mechanical loss of the Advanced LIGO ETM coating was characterised in the temperature range 10-300 K. At room temperature, the coating shows a loss of 3×10^{-4}. At low temperature, the coating shows a large dissipation peak, with a peak magnitude of 9-10$\times10^{-4}$ at 25 K. Additionally, the coating loss shows some frequency dependence, with higher frequencies showing higher loss. An Arrhenius analysis of the peak gives an activation energy $E_{\mathrm{a}} = (31.8 \pm 7.0)$ meV, which is similar to that calculated for the loss-causing processes in silica, tantala and titania-doped tantala.

The Advanced LIGO ITM coating was also measured at room temperature, exhibiting losses in the range 1-1.4$\times10^{-4}$. Predictions of the losses of the titania-doped tantala and silica layers within the two aLIGO coatings resulted in a non-physical result. This may be evidence that the model used for the calculation does not account for all of the loss exhibited, neglecting any additional losses due to coating interfaces.

A 30-layer silica/tantala coating deposited on a sapphire disk was measured in both an as-deposited and heat-treated condition. Initial results suggested that at low temperatures, the mechanical loss of the as-deposited coating was independent of temperature, but that the 500 °C heat-treated coating had several dissipation peaks in the temperature range 15-45 K. However, follow up measurements showed that the peaks were likely to be due to a mechanical coupling between the disk and the cooling system, and that the loss of the heat-treated coating is actually flat with temperature, with coating loss in the range 4-7$\times10^{-4}$. However, more measurements would be required to verify this behaviour.

Chapter 6

The temperature dependence of the mechanical loss of IBS silica-doped hafnia coatings

6.1 Introduction

As discussed in previous chapters, reducing the mechanical loss of the mirror coatings used in gravitational wave detectors and/or reducing the temperature of the coatings, would decrease the magnitude of coating thermal noise. Decreasing the coating temperature is a viable option, as planned for detectors such as the Einstein Telescope (ET) [19] and KAGRA [59]. These detectors would be operated with the mirrors cooled to around 10-20 K. However, the benefit provided by a reduction in temperature may be reduced by the fact that silica, tantala and titania-doped tantala show evidence of peaks in their mechanical loss at low temperature [4, 115, 116]. Cryogenic studies of the Advanced LIGO ETM coating show a dissipation peak the existence of which is consistent with the existence of dissipation peaks observed in single layer studies [107]. However, in a study using sapphire disks with a coating composed of IBS silica and tantala bilayers, no cryogenic loss peak in the coating was observed [132, 157]. Whether or not there is a dissipation peak at 20 K in a multilayer silica/tantala coating, it is clear that the loss of such based coatings at low temperature is currently higher than that required to obtain the desired sensitivity requirements of future, low-temperature detectors.

Previous research at the University of Glasgow showed that IBS hafnia (HfO_2) had low mechanical loss compared to tantala at cryogenic temperatures, despite having partially crystallised on deposition [6]. Poly-crystalline hafnia is not likely to be suitable for use in gravitational wave detectors since the crystallites would contribute to optical losses in a cavity by scattering the circulating light. The Advanced LIGO reference design requires the coatings to have an optical scatter of 10 ppm or less [158]. Previous research into heat-treatment of tantala shows that when tantala becomes poly-crystalline, the mechanical loss increases [4]. Therefore, since even in a partially crystallised form, IBS hafnia had a lower mechanical loss than tantala heat-treated, it was postulated that if it could be stabilised against crystallisation, hafnia may have a suitably low loss to be a promising alternative high-index material to tantala. Mirror coatings are typically heat-treated after deposition to reduce both stress and optical absorption in order to meet design requirements, which are as low as 0.5 ppm in the case of Advanced LIGO [158]. It was observed that at higher heat treatment temperatures, a higher proportion of the hafnia coating became polycrystalline [6]. Doping hafnia with silica to a 30% cation concentration has been shown previously to stabilise against crystallisation following heat-treatment at temperatures up to 550 °C [159, 160]. Additionally, little effect on the mechanical loss at room temperature was observed as a result of the doping [160]. However, previous mechanical loss measurements involving silica-doped hafnia were of a multilayer silica/silica-doped hafnia coating, and measurements were taken at room temperature only [160].

In this chapter, investigations are reported of the effects of heat-treatment on the mechanical loss of IBS silica-doped hafnia at temperatures in the range 10-300 K, and the loss of silica-doped hafnia compared to that of pure hafnia and of titania-doped tantala. Further, as noted above, optical absorption is an important parameter for mirrors in cavities with high circulating power since absorption limits cavity finesse by contributing to the cavity's optical loss and may heat the mirror, leading to difficulties with temperature control in a cryogenic detector. Thus, the results of measurements of the optical absorption of these films are also presented.

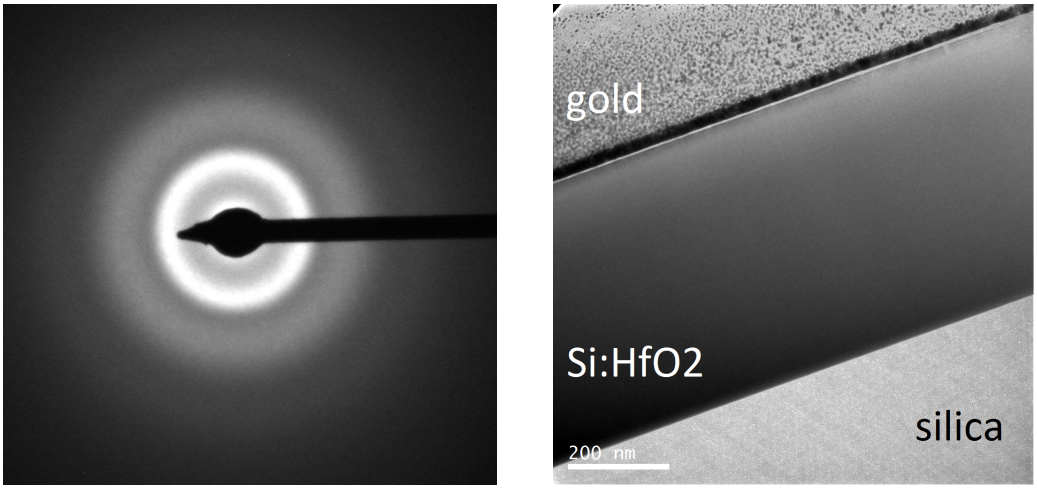

(a) (b)

Fig. 6.1 An electron diffraction pattern (a) of the 600 °C heat-treated coating, and a dark field TEM image of the coating (b). In the right hand image, the dark band in the middle is the coating, while the lighter patch below is the substrate. The speckled band at the top of the image is gold deposited as part of TEM sample preparation. Both images show the coating to be amorphous. Images taken by Martin Hart.

6.2 Measurements

The mechanical loss of the Si:HfO_2 coatings was measured by comparing the mechanical loss of coated silicon cantilever samples with nominally identical un-coated samples. This technique is explained in more detail in Chapter 3. The cantilevers studied here were heated to 1000 °C in air prior to coating deposition. A 500 nm thick coating of silica-doped hafnia was deposited using IBS onto one face of the cantilevers by a commercial vendor - CSIRO [136]. Some of these cantilevers remained uncoated, but were put through the same thermal treatment as the coated cantilevers to produce suitable un-coated control samples for comparison with the coated cantilevers. The coating was also deposited onto one silica cantilever of dimensions $42 \times 5 \times 0.16$ mm.

Since optical coatings are commonly heat-treated to reduce the coating stress and optical absorption [108], the coated cantilevers were also heat-treated post-deposition to study the effects on the mechanical loss. The heat-treatment temperatures chosen were 150, 300, 400 and 600 °C. Transmission electron microscope (TEM) measurements were carried out by M. Hart, and showed that all of the heat-treated coatings remained amorphous. TEM measurements of the coating which had been heat-treated to 600 °C are shown in figure 6.1.

The mechanical loss of several modes (having resonant frequencies between 0.5 and 9.5 kHz) of each cantilever was measured at temperatures between ∼10 K and 295 K. After one complete measurement cycle, the cantilever was reclamped to ensure unintentional variations in the clamping procedure did not adversely affect the results. Of the data taken, cycles showing excess loss compared to other cycles were discarded since it is relatively easy to measure an artificially high loss through excess damping, for example due to the clamp, whereas in most cases it is difficult to measure a lower loss than the intrinsic loss of a sample. From the measurement cycles with the lowest loss, the average loss at each temperature point was calculated. The standard deviation was typically around a few percent.

6.3 Results

6.3.1 Mechanical loss

A comparison of the mechanical loss of a coated and uncoated substrate for the third bending mode of the cantilevers at 1.4 kHz is shown in figure 6.2. For the as-deposited cantilever and the cantilevers heat-treated at 150 °C, 400 °C and 600 °C, the measured loss of the nominally identical uncoated substrates were used to evaluate the coating loss, as per equation 3.7.

However, for the samples heat-treated at 300 °C, the coated cantilevers were found to be significantly thinner than the control samples, by ∼17 µm. The thicknesses of all coated samples are shown in table 6.1. As a result, the mode frequencies differed significantly to those of the un-coated control sample, and thus the un-coated data could not be used to calculate the coating loss. Instead, for these samples it has been assumed that at temperatures under 150 K, the mechanical loss of the substrate is negligible and that the measured loss is solely due to the coating. As shown in figure 6.2, below 150 K the mechanical loss of the substrate is around one tenth of the loss of the coated substrate for all of the coated cantilevers studied. This means that the assumption that the substrate contributes no loss to the coated cantilever gives an upper limit to the coating loss, but introduces a further 10% error in calculations where this assumption is made.

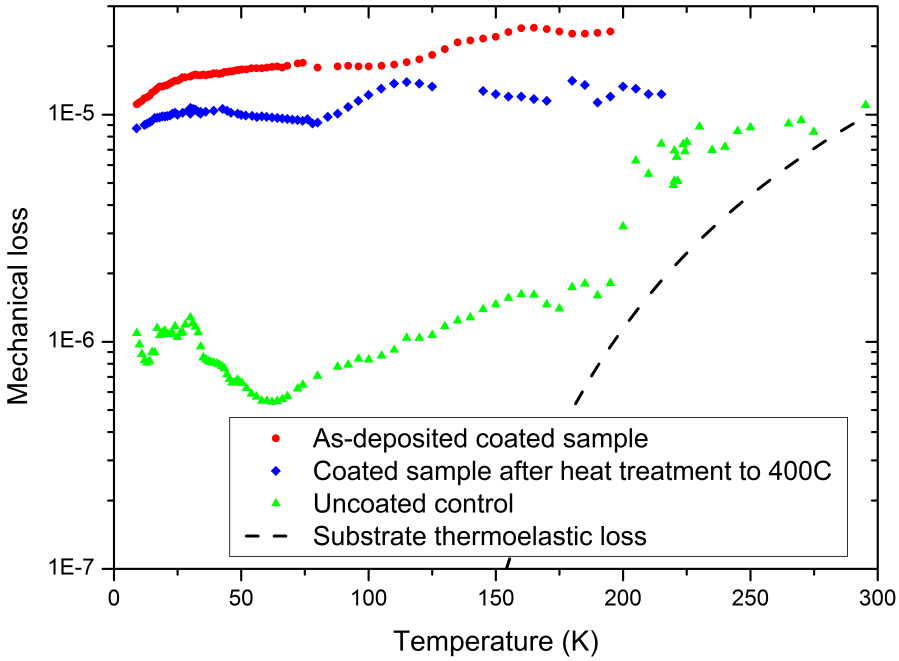

Fig. 6.2 The mechanical loss of the uncoated control sample as a function of temperature for bending mode 3, 1.4 kHz. Also shown is the mechanical loss of the highest loss coated sample, the as-deposited coating, and the lowest loss coated sample, the 400 °C heat-treated cantilever. The dashed line is the thermoelastic loss of the substrate, calculated from [5].

This approximation has also been used for the 6th and 7th modes of all of the cantilevers studied due to the absence of good quality control data for these modes, since the uncoated control data for these modes showed evidence of excess loss and a lot of scatter which can be an indication that the uncoated cantilever was losing energy into the clamp.

Heat-treatment :	As-dep.	150 °C	300 °C	400 °C	600 °C
Substrate thickness (μm):	72	71	54	72	72
$Y_s t_s / 3 Y_c t_c$:	45±4	45±4	34±3	45±4	45±4

Table 6.1 Substrate thicknesses and the ratio of elastic energy stored in the substrate and coating during vibration for all coated samples. Sample thicknesses are calculated from the frequency of the bending modes of the cantilevers using equation (8) in [7] and have an error of ±1 µm.

Since a measured value for the Young's modulus of 30% silica-doped hafnia was not available, an estimated value was calculated from the formula derived by of Barta [8] using the moduli of both silica and hafnia. Barta's formulae allow the Young's modulus and Poission's ratio of a mixture to be calculated

from the properties of the mixture components. First, the material properties X_i and y_i are defined [8]:

$$X_i = \frac{\sigma_i Y_i}{\sigma_i + 1} \quad \text{and} \quad y_i = \sigma_i - 1, \tag{6.1}$$

where Y_i and σ_i are the Young's moduli and Poisson's ratios of the mixture components. The properties X and y of the mixture are then calculated through the system of equations [8]:

$$\sum_i c_i \frac{X - X_i}{2X + (X_i/y_i)(\sigma_i + 1)} = 0 \tag{6.2}$$

and

$$\sum_i c_i \frac{(X/y) - (X_i/y_i)}{2X + (X_i/y_i)(\sigma_i + 1)} = 0, \tag{6.3}$$

where c_i is the fraction of material i within the mixture. Here, silica takes a value of $c = 0.3$, and hafnia of $c = 0.7$. The Poission's ratio of silica was taken to be $\sigma = 0.17$ [103], and the Poisson's ratio of hafnia was taken to be $\sigma = 0.3$ [161].

Values of the Young's modulus of amorphous hafnia found in literature vary greatly depending on deposition technique and heat-treatment. The Young's modulus for a hafnia coating deposited by atomic layer deposition can be as high as (370 ± 20) GPa, which reduces to (240 ± 20) GPa after heat-treatment [162]. The heat-treatments reported in [162] were at 400 °C and 600 °C, each in a rapid thermal annealing system. Both heat-treatments were found to induce crystallisation of the ALD hafnia coatings [162].

The Young's modulus of hafnia deposited at CSIRO by ion beam sputtering was measured by nano-indentation to be (216 ± 16) GPa, however it is known that this coating was poly-crystalline during measurement [137]. This value agrees within error with the value for plasma ion assisted deposition (PIAD) amorphous hafnia found in [163], (220 ± 20) GPa, which was used for calculating the mechanical loss of a pure hafnia film also deposited by CSIRO [6]. The properties of the coating used here for the calculation of coating loss, along with the properties of the substrates, are shown in table 6.2. The error in coating mechanical loss is dominated by the large uncertainty in the elastic modulus of hafnia.

Material:	Silica	Hafnia	Silica-doped hafnia	Silicon
Thickness	N/A	N/A	500 nm	Sample dependent: see table 2
Young's modulus (GPa):	72[164]	(220 ± 20)[163]	180.5±15	166[156]

Table 6.2 Young's moduli used for the coatings and substrates. The Young's modulus of 30% silica-doped hafnia is calculated using the results of Barta [8]

.

The substrate thicknesses calculated from the frequencies of the resonant bending modes, and the calculated energy storage ratios for the coated cantilevers, required for calculating the coating loss, are shown in table 6.1. The coating loss, as calculated from the loss measurements of bending modes 3-5 (where mode 1 is the fundamental mode) is shown as a function of temperature in figures 6.3, 6.4 and 6.5 respectively. The coating losses calculated for modes 6 and 7 using the zero-loss substrate assumption are shown in figures 6.6 and 6.7 respectively. For the thinner 300 °C cantilever, modes 7 and 8 are close in frequency to modes 6 and 7 respectively and have therefore been included in these figures. Additionally, the coating loss of the 300 °C heat-treated coating for bending modes 3-6 are shown in figure 6.8.

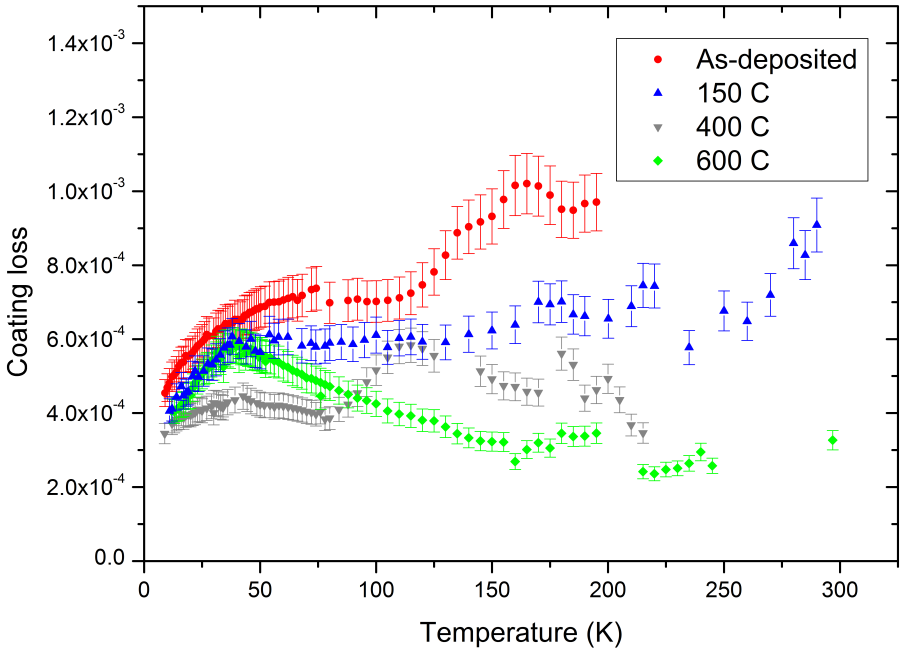

Fig. 6.3 Temperature dependent coating loss calculated from the as-deposited, 150 °C, 400 °C and 600 °C heat-treated cantilevers for bending mode 3, at 1.4 kHz

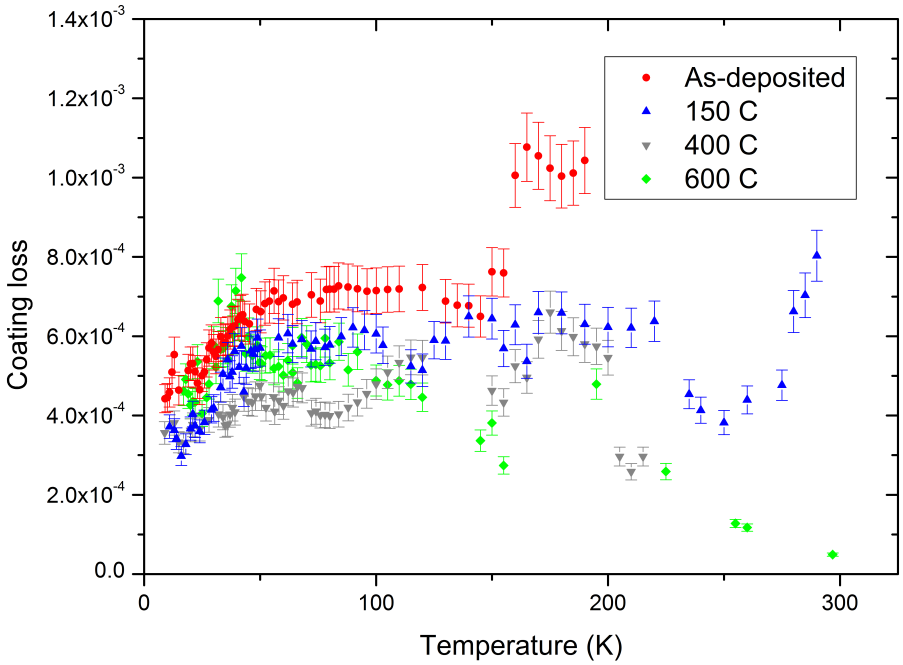

Fig. 6.4 Temperature dependent coating loss calculated from the as-deposited, 150 °C, 400 °C and 600 °C heat-treated cantilevers for bending mode 4, at 2.7 kHz

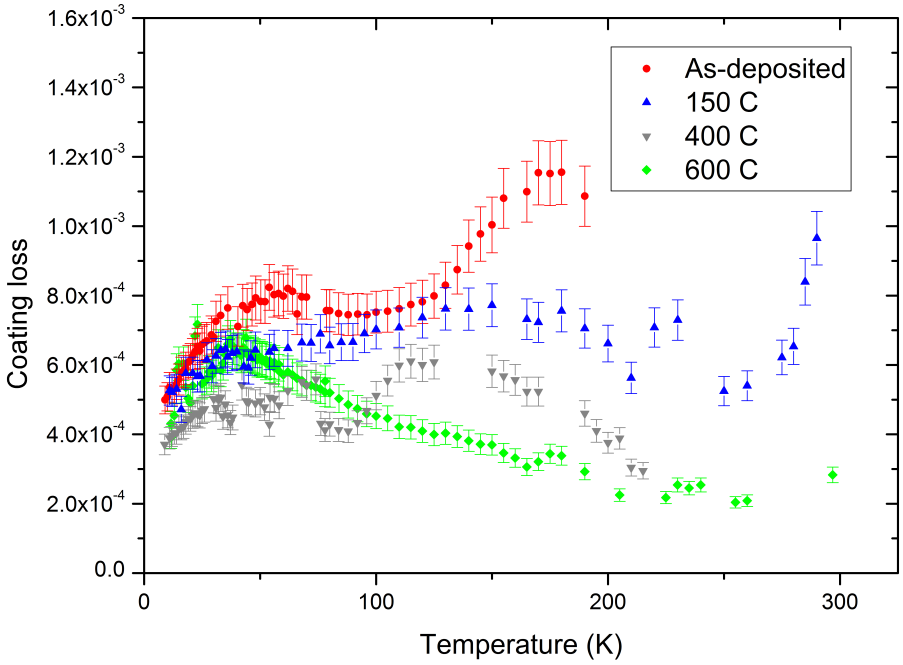

Fig. 6.5 Temperature dependent coating loss calculated from the as-deposited, 150 °C, 400 °C and 600 °C heat-treated cantilevers for bending mode 5, at 4.5 kHz

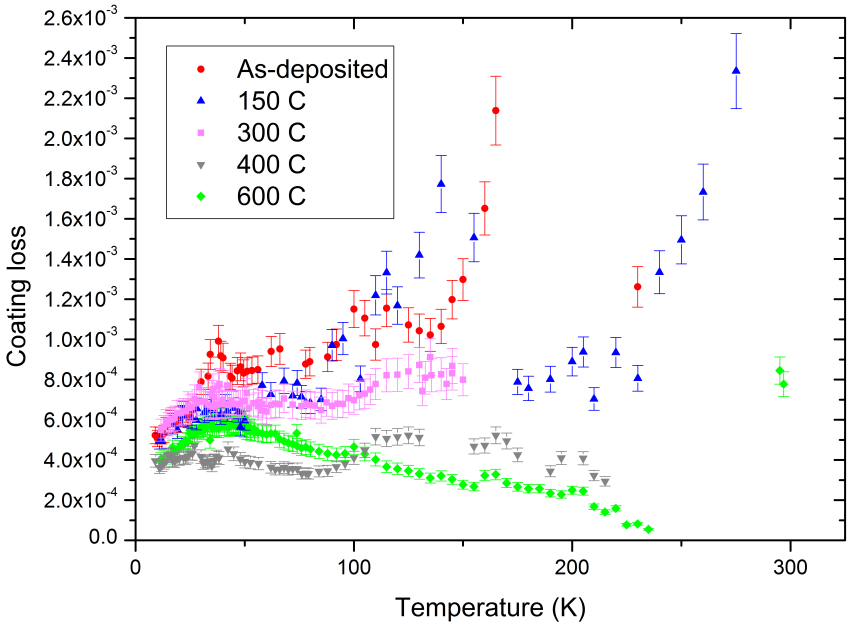

Fig. 6.6 Temperature dependent coating loss calculated from the as-deposited, 150 °C, 400 °C and 600 °C heat-treated cantilevers for bending mode 6, at 6.9 kHz and bending mode 7 of the 300 °C cantilever at 7.1 kHz. This coating loss is an upper limit as it assumes no contribution to the loss from the substrate.

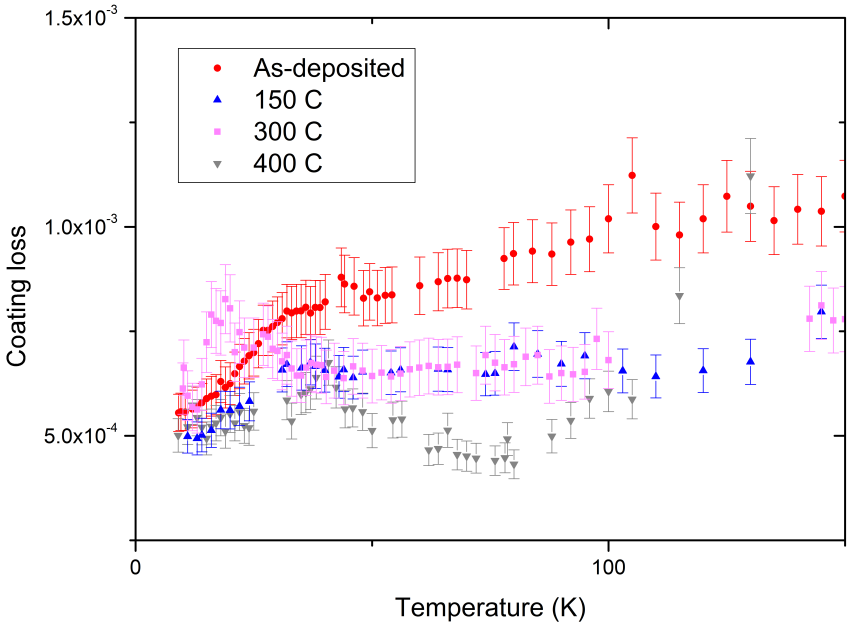

Fig. 6.7 Temperature dependent coating loss calculated from the as-deposited, 150 °C, and 400 °C heat-treated cantilevers for bending mode 7, at 9.5 kHz and bending mode 8 of the 300 °C cantilever, also at 9.5 kHz. This coating loss is an upper limit as it assumes no contribution to the loss from the substrate.

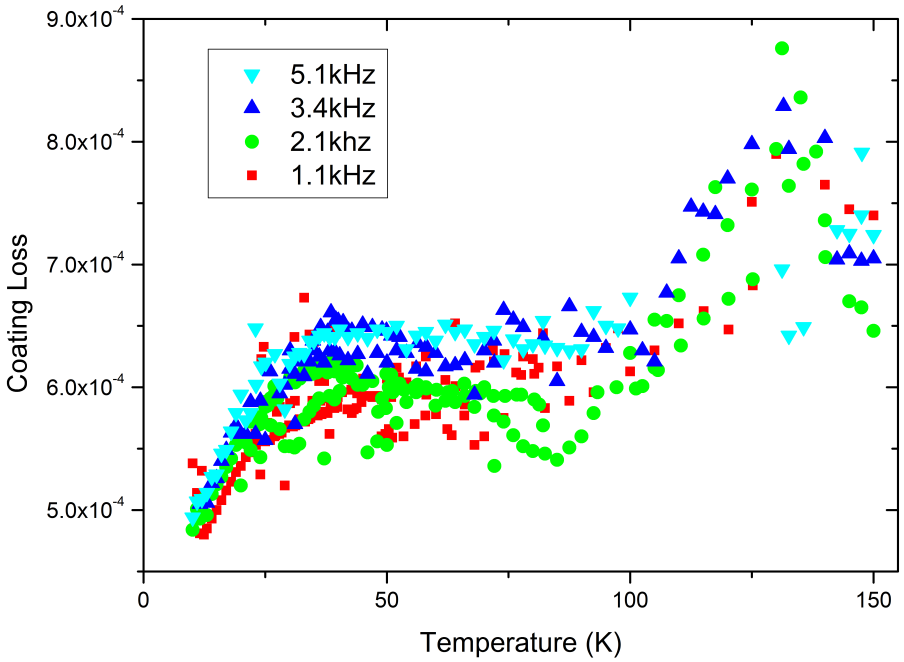

Fig. 6.8 Temperature dependent coating loss of bending modes 3-6 of the 300 °C heat-treated coating, assuming no loss from the substrate. Error bars have been omitted for clarity, but are around 14%, from the uncertainty in the Young's modulus in hafnia and the error arising from the zero-loss substrate assumption.

The loss of the as-deposited coating shows a steady decrease with decreasing temperature under 75 K, with the level of coating loss at 10 K being approximately 5×10^{-4}. The as-deposited coating also shows a peak at 160 K on the data for mode 3, and at 180 K on the data for mode 5. Mode 4 does not show this feature, but the mode 6 data shows a sharp increase in loss starting at 150 K. For all modes, it can be seen that the as-deposited coating has the highest loss, and that, at temperatures below 100K, the loss decreases with heat-treatment at both 150 °C and 400 °C.

The coating loss of the 150 °C heat-treated coating shows the same decrease below 40 K as the as-deposited coating, but exhibits a lower magnitude of loss by less than 10% in this temperature range. The 150 °C heat-treated coating does not exhibit the peak feature seen in modes 3 and 5 of the as-deposited coating data. This suggests that either the heat-treatment has removed this feature, or that the peak is not due to the coating itself but rather the as-deposited coating sample or the measurements carried out upon it. The loss of the 150 °C coating shows no clear frequency dependence, and all modes show an increase in loss with temperature in the range 250-300 K.

The mechanical loss exhibited by the 300 °C heat-treated shows some possible frequency dependence below 50 K, with higher frequencies exhibiting higher loss. However, the variation in coating loss between modes is far below the level of uncertainty. The loss also shows the same decrease below 40 K as the as-deposited and 150 K data, dropping from 6-6.5$\times10^{-4}$ to 5×10^{-4} in the range 10-40 K.

The 400 °C heat-treated coating shows a loss of 4×10^{-4} at 10 K, the lowest loss in the temperature range of interest for the ET and KAGRA detectors. The coating shows the lowest loss up to 100 K, above which the 600 °C coating shows lower loss. The increase in loss under 100 K arising from heat-treatment at 600 °C could possibly be related to changes in the amorphous structure induced by heat-treatment. It should be noted that TEM images have shown that the coating remains amorphous after a 600 °C heat-treatment, illustrated in figure 6.1.

The loss of the coating heat-treated to 600 °C shows a clear peak under 100 K. The dissipation peaks exhibited across the various modes of the 600 °C heat-treated coating are shown in figure 6.9. The temperature of the loss peak shows no evidence of increasing with frequency as would be expected for a peak

arising from a thermally activated process described by an Arrhenius-like law [61].

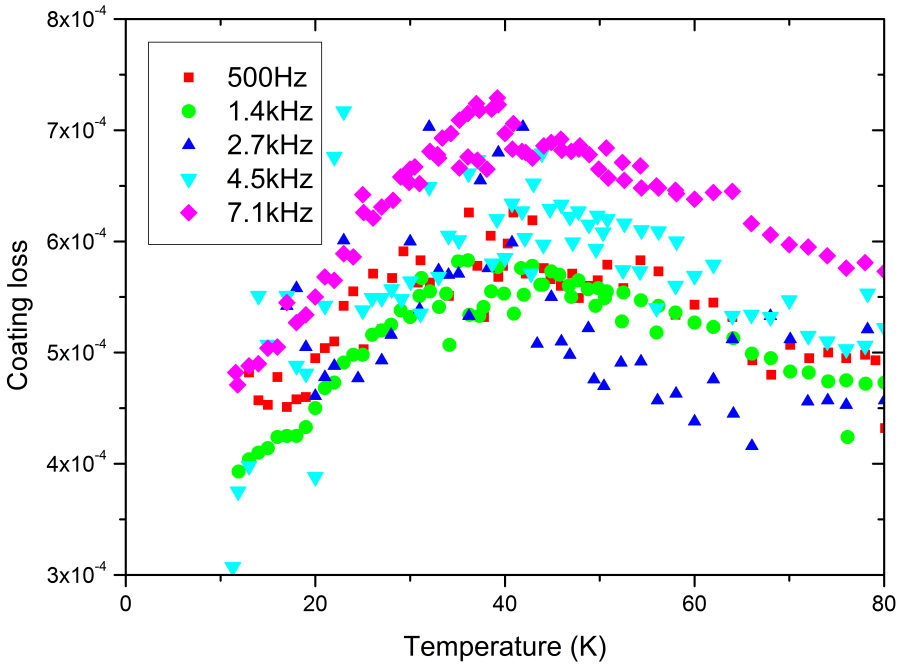

Fig. 6.9 The mechanical loss of the 600 °C heat-treated coating as a function of temperature under 80 K. The coating loss for these modes show clear peaks, apart from that of the 2.7 kHz 4th bending mode.

A comparison of the coating mechanical loss as measured for 400 °C heat-treated hafnia [6] and silica-doped hafnia is shown in figure 6.10. The 400 °C coating shows a similar level of loss at low temperature than that of pure hafnia with a similar heat-treatment. However, unlike the pure hafnia, the silica-doped hafnia remains in a fully amorphous state, making it potentially useful as an optical coating material for GW detectors. The figure also compares silica-doped hafnia to IBS pure tantala heat-treated to 400 °C and 600 °C [4].

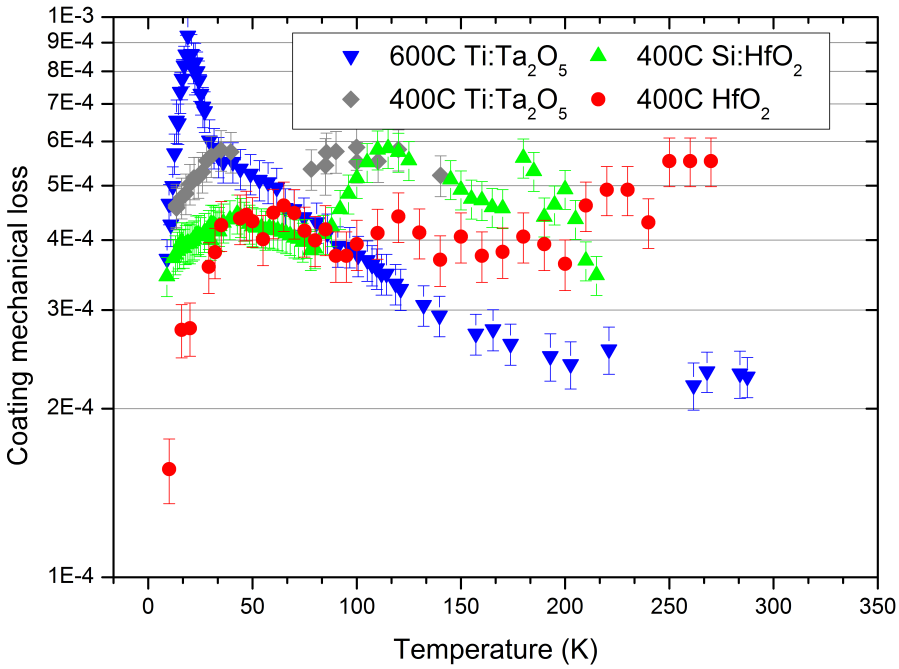

Fig. 6.10 A comparison of the coating mechanical loss of 400 °C heat-treated silica-doped hafnia with 400 °C heat-treated pure hafnia from [6] and IBS titania-doped tantala from [4]. These results are from the second bending mode of the pure hafnia coated cantilever, around 850 Hz, the third mode of the tantala coated cantilever, around 1 kHz and the third mode of the silica-doped hafnia coated cantilever at 1.4 kHz. It can be seen at the extreme low temperatures, the loss of the hafnia drops while that of the silica-doped hafnia does not.

6.3.2 Room temperature loss measurements

The mechanical loss of a 160 µm thick silica cantilever with the as-deposited silica-doped hafnia coating applied is shown in figure 6.11. The loss of the uncoated substrate, as measured prior to coating deposition is also shown. The mechanical loss of the coating shows some frequency dependence, with the lowest loss exhibited at the lowest frequencies. The lowest coating loss observed was on the 4 kHz mode. However, it is likely that this low coating loss is due to the high substrate loss, which does not follow the trend of substrate loss observed for the other modes. The coating loss exhibited by the first three modes is around 1×10^{-3}. The coating loss calculated for the two highest-frequency modes are upper limits, where the measured loss is assumed to be entirely due to the coating in absence of control data for these modes.

In the cryogenic measurements, the 600 °C heat-treated coating shows the lowest loss above 100 K. A 600 °C, 24 hour heat-treatment regime was therefore chosen for the coated silica cantilever, used for measuring the room temperature mechanical loss. The measurements of the 600 °C heat-treated cantilever are shown in figure 6.12. Coating loss calculations made for the heat-treated coating assume the same substrate loss as the as-deposited coating. For the 4 kHz mode, the coated cantilever showed a loss lower than that of the uncoated substrate after heat-treatment, and a coating loss could not be calculated. This may be due to the loss of the substrate improving with heat-treatment, but may also be due to excess loss measured on the uncoated cantilever since the loss of that mode does not follow the general trend of the other modes.

The coating losses of the as-deposited and heat-treated coating are shown in figure 6.13 From the low frequency modes, the loss of silica-doped hafnia as-deposited appears to reduce from 1×10^{-3} to 3×10^{-4} after heat-treatment to 600 °C. This is comparable to the mechanical loss of IBS tantala, which has a mechanical loss at room temperature of 3×10^{-4}, though titania-doped tantala has a lower loss than this [105].

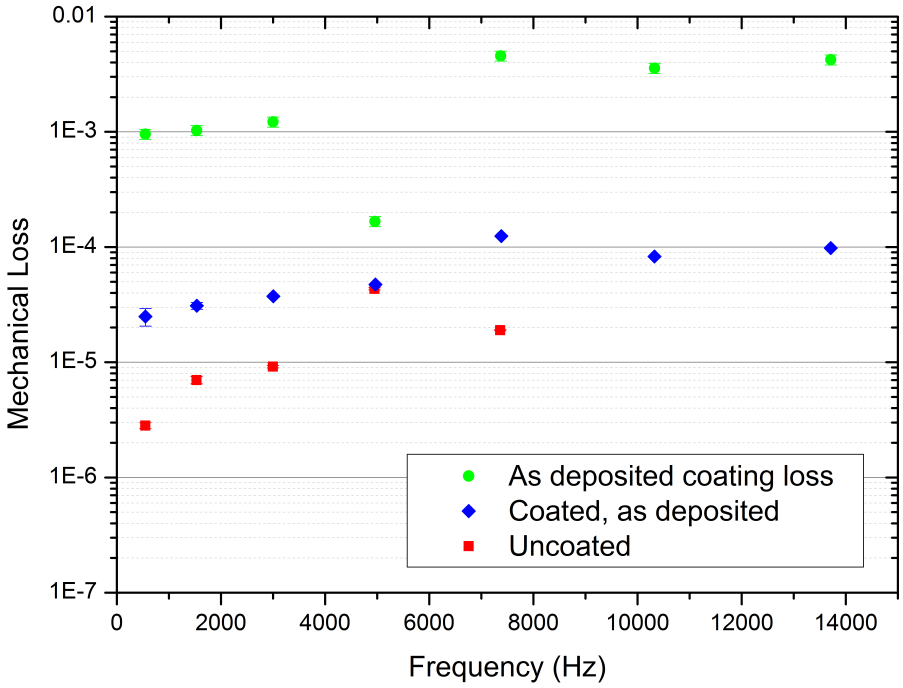

Fig. 6.11 The mechanical loss of a silica cantilever coated with silica-doped hafnia in an as-deposited state. Also shown is the loss of the cantilever prior to coating, and the coating loss calculated from the measurements.

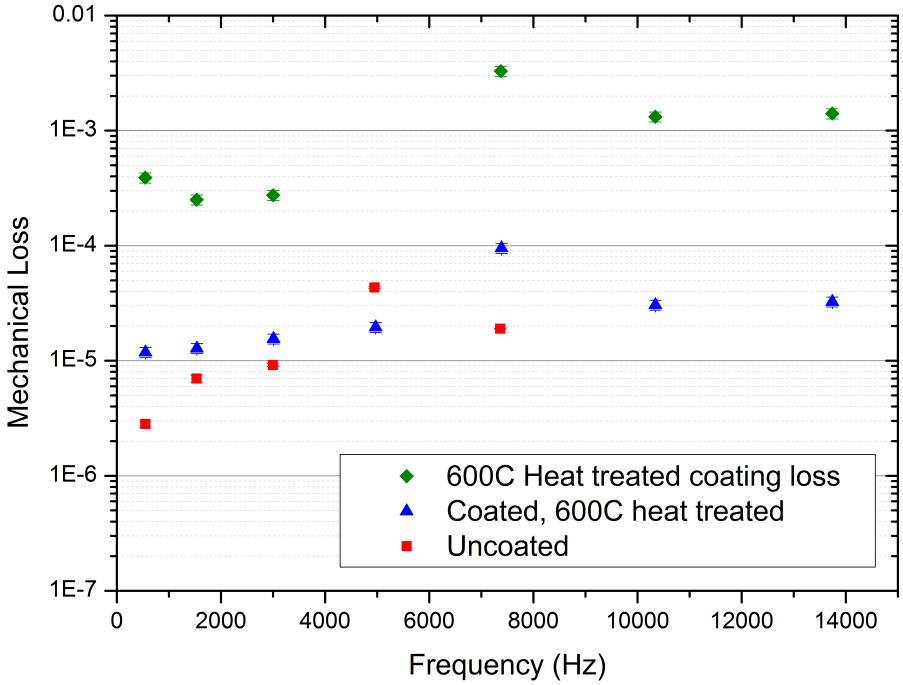

Fig. 6.12 The mechanical loss of a silica cantilever coated with silica-doped hafnia in an as-deposited state. Also shown is the loss of the cantilever prior to coating, and the coating loss calculated from the measurements.

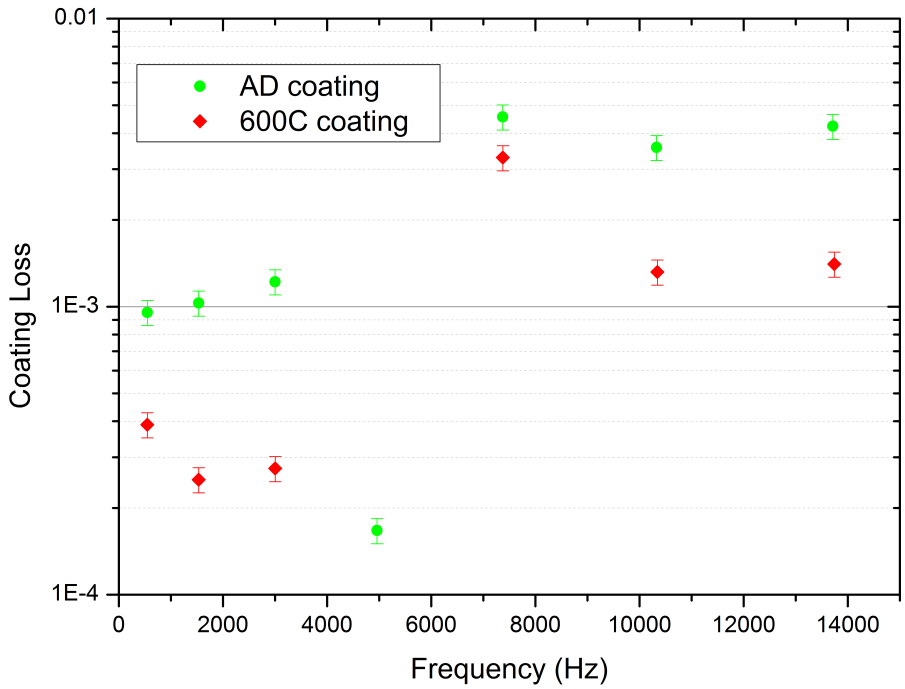

Fig. 6.13 The coating losses of the as-deposited and 600 °C heat-treated silica-doped hafnia coatings.

6.3.3 The thermal noise associated with a silica/silica-doped hafnia mirror coating

The thermal noise arising from a mirror coating in a gravitational wave detector may be calculated from equation 2.23, where the terms $\phi_\perp$ and $\phi_\parallel$ are assumed to be equal for an amorphous coating. For comparison to current amorphous coatings, this calculation has been performed using the properties of the Advanced LIGO ETM coating, the loss of which is presented in Chapter 5. The loss of the aLIGO ETM was taken to be 3×10^{-4} at 300 K and 9×10^{-4} at 20 K. The coating has a thickness of 5.9 μm when deposited for high-reflectivity at 1064 nm and a thickness of 8.6 μm when deposited for reflectivity at 1550 nm. A 1550 nm laser is required for operation at 20 K, assuming that silicon is the choice substrate, as in ET [19]. This coating has an effective Young's modulus of 96 GPa.

A silica/silica-doped hafnia multilayer deposited upon a silicon substrate would require 22 bilayers to match the reflectivity of the aLIGO ETM coating. This assumes the refractive index of silica to be $n_L = 1.443$, and the refractive index of silicon to be $n_{\mathrm{sub}} = 3.5$. The refractive index of silica-doped hafnia was measured by ellipsometry to be $n_H = 1.91$. The mechanical loss of silica was taken to be 8×10^{-4} at 20 K [113, 116], and the loss of a 400 °C heat-treated silica-doped hafnia was taken to be 4×10^{-4} at 20 K.

The displacement thermal noise arising from each of the above coatings was calculated assuming the same laser beam radius as the Advanced LIGO ETM, 6.2 cm. The displacement thermal noise of the aLIGO ETM coating on a silica substrate at room temperature, the aLIGO ETM coating on a silicon substrate at 20 K and of a silica/silica-doped hafnia coating at 20 K is shown in figure 6.14.

The Brownian noise arising from a silica/silica-doped hafnia coating at 20 K is a factor of 2.5 lower than that of the aLIGO ETM at room temperature. However, most of this improvement is due to the reduction in temperature. The silica-doped hafnia based coating also exhibits a factor of 1.14 lower Brownian noise than the aLIGO ETM coating at 20 K. This factor of improvement may be increased using layer-thickness optimisation, which is featured in the aLIGO ETM coatings. Additionally, the calculations here assume a silica/silica-doped hafnia coating. Since amorphous silicon exhibits a very low loss ($\phi_{\mathrm{Si}} = 4 \times 10^{-5}$

at 20 K) and a very high refractive index $n_{\mathrm{Si}} = 3.5$, a low noise coating may be produced using silica-doped hafnia as the low-index material.

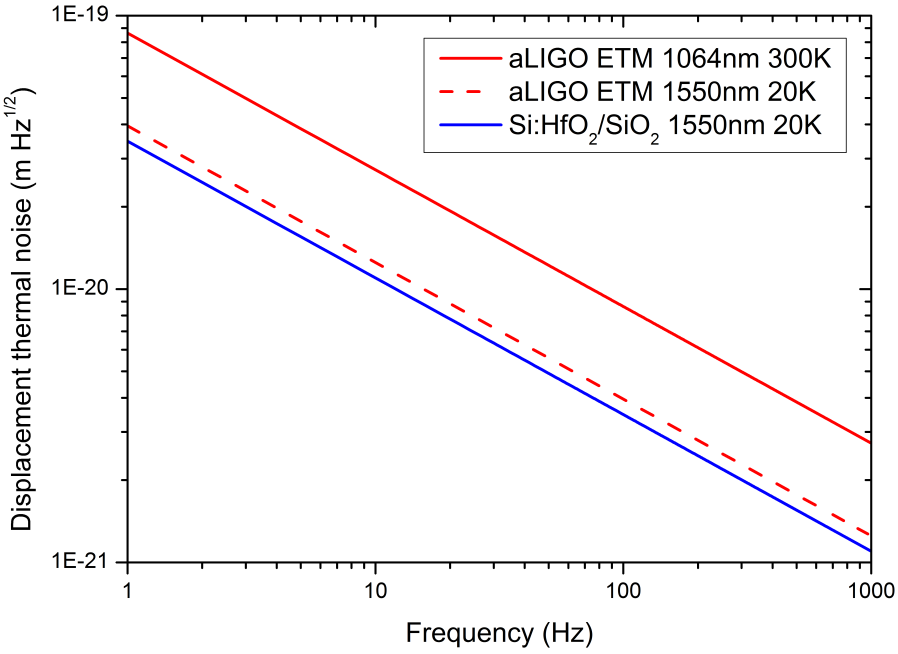

Fig. 6.14 The displacement thermal noise arising from a silica/silica-doped hafnia multilayer on a silicon substrate at 20 K. Also shown is the thermal noise of the Advanced LIGO ETM coating at room temperature, and at 20 K.

6.3.4 Optical absorption

Measurements of the optical absorption of silica-doped hafnia coatings were measured by J. Steinlechner. The absorption at 1550 nm of a 500 nm thick silica-doped hafnia layer deposited onto several silica disks was measured using a Photothermal Common-Path Interferometer (PCI), detailed in [165]. These coatings were deposited onto one inch diameter fused silica discs. The absorption was measured on the as-deposited coating as well as on the 400 °C heat-treated coating, which exhibited the lowest loss at temperatures under 100 K. The absorption of the as-deposited coating was measured to be (36 ± 2) ppm, and heat-treatment reduced this to (26 ± 2) ppm. These values are the mean and standard deviation of five individual measurements, each taken at a different position on the sample surface for each of the as-deposited and heat-treated coatings. Additionally, there is an absolute error of 20% on this measurement series. However, the surface absorption of the uncoated back face of one of these

discs was found to be 22 ppm, regardless of heat-treatment. These results show that the heat-treatment of silica-doped hafnia reduces its optical absorption. However, it is difficult to draw conclusions about the absolute optical absorption of the 400 °C heat-treated coating since, within the absolute error of these measurements, it is hard to distinguish from the uncoated silica substrates used for these measurements. The design study for the Einstein Telescope, places a requirement on coating absorption of a maximum of 5 ppm for a coating to be suitable for the detector mirrors [19]. These measurements show that the 400 °C heat-treated silica-doped hafnia coating shows good potential to match these requirements. However, measurements on lower absorbing substrates would be necessary to confirm this result.

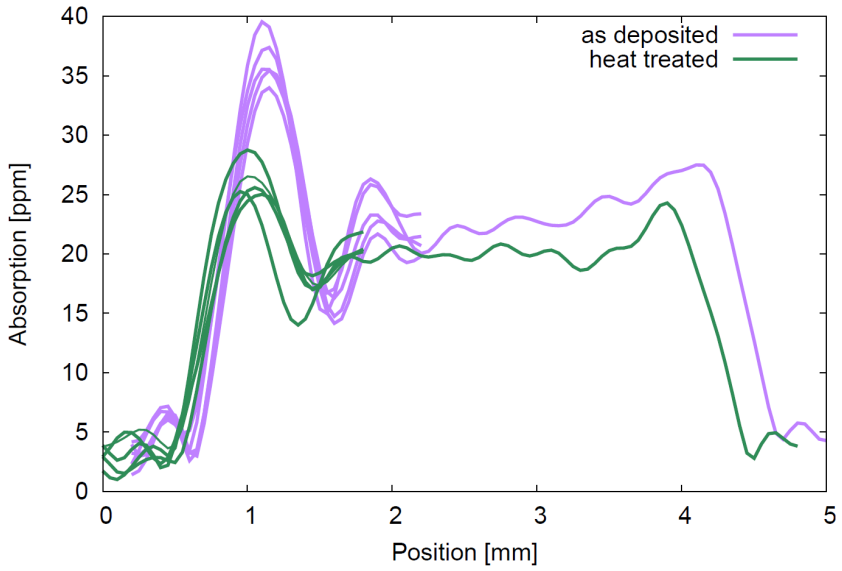

Fig. 6.15 The absorption of the as-deposited and 400 °C heat-treated sample. This plot shows a scan through the thickness of the disk with the coated face around 1 mm and the back face around 4 mm. It should be noted that the uncoated back face of the sample had an absorption of around 22 ppm. The multiple lines of each colour represent measurements of each sample, taken at different locations on the sample surface.

6.4 Conclusions

The temperature dependent mechanical loss of a silica-doped hafnia coating with a range of post-deposition heat-treatments up to 600 °C was measured. This coating has been demonstrated to remain amorphous after heat-treatment.

Under 100 K, the 400 °C heat-treated coating has the lowest loss of this series, and has a factor of 2-3 lower loss than IBS tantala at 10-20 K. Above 100 K, the 600 °C coating has a lower loss than the 400 °C heat-treated coating and was hence chosen for room temperature investigations. At room temperature, heat-treatment at 600 °C clearly reduces the coating loss, but not to a level sufficient to replace coatings on the mirrors of existing room temperature gravitational wave detectors.

The thermal noise of a silica-doped hafnia coating shows a factor of 1.14 improvement over the Advanced LIGO ETM coating at 20 K.

The optical absorption at 1550 nm was measured on the as-deposited and 400 °C heat-treated coatings. The measurements show that heat-treatment to 400 °C reduces the absorption. While the measurement of the heat-treated coating is limited by the absorption of the substrate, there is evidence that the optical absorption may be good enough to meet the ET design study requirements.

Chapter 7

Studies of multilayer single-crystal mirror coatings

7.1 Introduction

Amorphous coatings have relatively high loss when compared to the bulk materials used for the test-masses and their suspensions. Bulk silica, used as the mirror substrates in room temperature gravitational-wave detectors such as Advanced LIGO and Advanced Virgo, has an extremely low mechanical dissipation. Silica produced by thin-film deposition methods such as ion-beam sputtering has a mechanical loss several orders of magnitude larger than that of bulk silica at room temperature [116], but remains one of the lowest loss coating materials produced which meets the strict optical requirements imposed by interferometric gravitational wave detectors.

The high refractive index material tantala, in thin film form, has been improved by vendors over the years by optimisation of deposition parameters, applying post-deposition heat-treatments and by doping with titania [105]. Further improvements are required to enable future detectors such as the Einstein Telescope (ET) to reach their design sensitivities. The ET design study features 6 interferometers with 3 of these having their mirrors cooled 10-20 K [19]. Silicon is a strong candidate material for use as a mirror substrate in a low-temperature detector, since it has lower mechanical loss than fused silica at low temperatures [128, 129], and has a higher thermal conductivity [156], advantageous for faster cooling rates and for handling higher laser powers.

From a decrease in mirror temperature from 300 K to 20 K, from equation 2.21, one would expect the thermal noise to be reduced by a factor of almost 4, assuming a constant mechanical loss. This figure arises since the amplitude spectral density of thermal displacement noise is proportional to the square root of temperature. However, as shown in in Chapters 3 and 4, as well as in previous studies, neither the mechanical losses of tantala, titania-doped tantala and silica, nor the multilayers of these materials, are independent of temperature [4, 107, 115, 116].

Studies of mirror coatings comprised of single crystals have observed coating thermal noise consistent with the crystalline coatings having a factor of 10 lower mechanical loss than a silica/tantala coating at room temperature [88]. The crystalline coating of [88] was a GaAs/AlGaAs multilayer coating bonded to a fused silica substrate. However, the coating cannot be grown directly on a silica substrate. The coating may not be grown on silicon due to the lattice mismatch between the materials. Instead, alternating layers of GaAs and $Al_{0.92}Ga_{0.08}As$ are grown on a (100)-oriented GaAs substrate by molecular beam epitaxy (MBE). The GaAs substrate is then etched, leaving just the coating to be directly bonded onto the fused silica substrate. This process has the draw-back that the bond may feature defects, or areas of non-adhesion compared to a method where a coating is grown directly on the chosen mirror substrate.

An alternative approach is to work with a material system which can be grown epitaxially directly onto silicon substrates, thus avoiding the need for substrate transfer. A multilayer coating comprising of alternating layers of $GaP/Al_{0.9}Ga_{0.1}P$ may be grown directly onto a silicon substrate. This is possible due to the crystal lattice being matched to that of silicon. In order to acheive the lattice matching, the films are grown on offcut (100) silicon wafers with a 4° offcut towards the [110] direction [166].

7.2 Studies of GaAs/AlGaAs crystalline mirror coatings

7.2.1 Introduction

In a study by Cole et al. [167], a set of micromechanical resonators fabricated from AlGaAs multilayer coatings were manufactured by depositing the coating upon a substrate, and etching both the coating and the substrate. The resonators were therefore of pure coating material. Mechanical loss measurements were carried out, and coating loss values of 2×10^{-4} (at room temperature) and 5×10^{-5} (at 4 K) were reported [167]. The mechanical loss of the coating material represents a significant improvement over the Advanced LIGO ETM coatings at low temperature. However, the measurements carried out in [167] are at a frequency range far outside of the detection band of gravitational wave detectors, with the studies looking at resonant frequencies in the range 0.7-2 MHz [167]. Additionally, the coating material is not attached to a substrate, and therefore does not take into account any effect of any attachment procedures [167]. Further development of free-standing AlGaAs-based resonators showed that a loss of may be achieved at room temperature 2.5×10^{-5} [168].

In a further study, a thermal noise limited Fabry-Perot cavity in which both end mirrors comprised of a GaAs/AlGaAs multilayer bonded to a silica substrate was set up, and the mechanical loss of the AlGaAs coating inferred from the level of noise [88]. The thermal noise in the cavity was consistent with a coating mechanical loss between $(0 \pm 4) \times 10^{-5}$ and $(4 \pm 4) \times 10^{-5}$, depending on the assumed dissipation of the silica substrate. This represents an improvement over the mechanical loss of the Advanced LIGO ETM coating at room temperature by a factor approximately 7.5. This shows that an AlGaAs coating may be a viable option for replacing the amorphous coatings within gravitational wave detectors, pending further investigation. However, further developments would be needed since the coatings studied within [88] are of 4 mm radius, and the sampling laser beam is of radius 250 μm By comparison, the laser beam radius incident upon the Advanced LIGO ETMs is approximately 6.2 cm.

Direct measurements of the mechanical loss of an AlGaAs coating bonded to a silica substrate have not previously been published. Therefore, it is of

interest to measure the mechanical loss of the coating after bonding to a relevant substrate.

7.2.2 Room temperature mechanical loss measurements of a GaAs/AlGaAs crystalline coating bonded to a silica disk

Measurements and results

A silica disk measuring 76.2 mm diameter by 1.7 mm thick was sent to CMS, where a GaAs/AlGaAs multilayer coating was bonded to the disk. The coating is composed of 40 layers of GaAs (high refractive index, $n = 3.480$) and 41 layers of $Al_{0.92}Ga_{0.08}As$ (low index, $n = 2.977$) [88]. The AlGaAs coating measures 16.3 mm in diameter, with a thickness of 6.83 μm, and was bonded to the disk as close as possible to the centre of the face of the disk. The substrate transfer process is a direct-bonding process which relies on Van der Waals forces and/or covalent bonding between the coating and the silica disk [169]. The technique is analogous to optical contact bonding [88], and may be strengthened by annealing [169].

The mechanical loss of the disk was measured prior to the coating being applied, and then again after coating. The measured mechanical losses of the coated disk are shown in figure 7.1. The losses of the coated disk used calculate the coating loss are shown in figure 7.2, along with the loss of the uncoated substrate. The energy storage ratios were calculated using an FEA model of the coated disk in order to calculate the coating loss. The energy ratio for each mode is shown in table 7.1. The coating loss calculated from the difference in the loss of the disk before and after coating is shown in figure 7.3.

The coating loss shows a considerable spread with losses between 2.0×10^{-5} and 5.8×10^{-3}, and no clear frequency dependence. The lowest and highest coating losses calculated are separated by a factor of almost 300. This is suspected to be related to a combination of uncertainties in the measurement and the amount of energy stored in the coating during vibration. Figure 7.4 shows the mode shapes of four of the modes used to measure the coating loss, in which one can see the nodes and antinodes during oscillation.

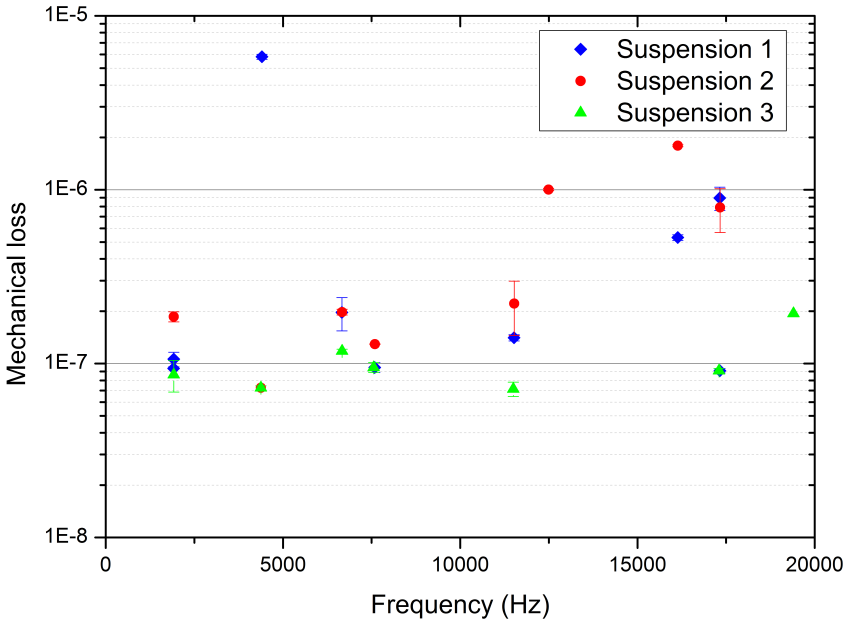

Fig. 7.1 The mechanical loss of a silica disk at room temperature with an AlGaAs multilayer bonded to the centre of one face. The disk was suspended three times, and the loss measured for each is shown.

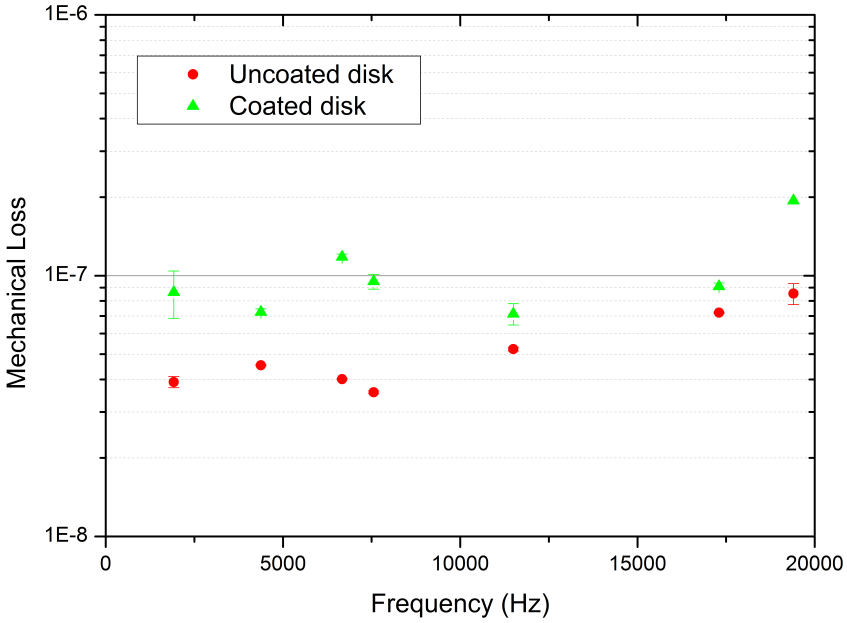

Fig. 7.2 The mechanical loss of a silica disk at room temperature before and after an AlGaAs multilayer was bonded to the centre of one face.

AlGaAs on silica energy ratios	
Mode frequency (Hz)	E_s/E_c
1916	807.1
4376	8751
6665	1945
7561	92720
11528	1039
17324	2808
19359	568.2

Table 7.1 The mode-dependent values of the ratio of energy stored in the substrate to that stored in the coating during oscillation, used to calculate coating loss.

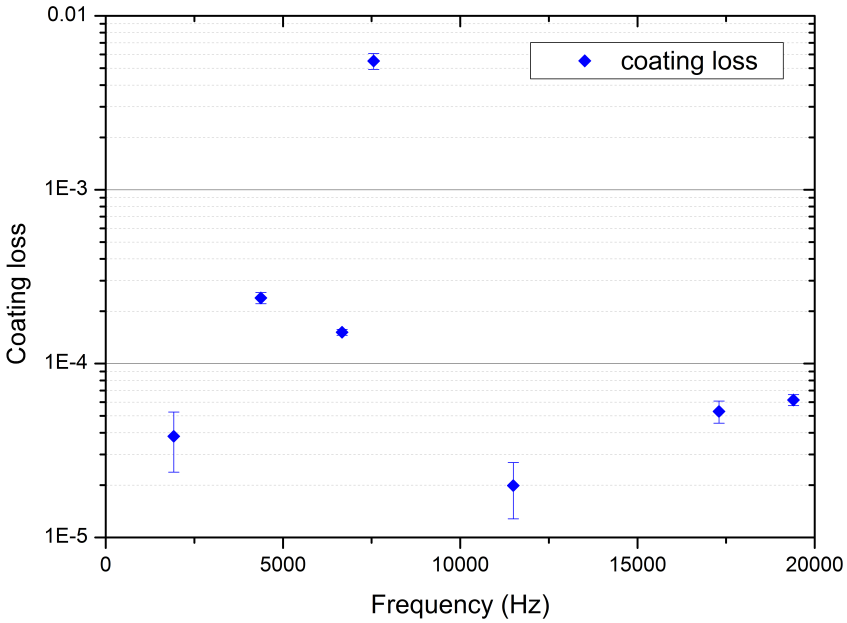

Fig. 7.3 The mechanical loss of an AlGaAs coating, at room temperature. The coating loss was calculated from the difference in mechanical loss of a silica disk before and after coating.

The mode for which the coating loss appears highest is the 7561 Hz mode, in which any motion of the disk during vibration is furthest from the centre of the disk face. This is reflected in the extremely high energy ratio, which represents there being very little energy stored in the coating during oscillation, and means that any small difference between the loss of the coated and uncoated disk will be amplified greatly in calculation of the coating loss. It is thought that the substrate loss used for the calculation of coating loss is artificially low. When the uncoated disk is suspended, the wires at the edges cause the disk vibrations to feature nodes at the contact locations. However, when the disk has a coating applied, it may be that the disk substrate may no longer self determine where the vibrational nodes are, and hence excess loss is exhibited by the coated disk through friction with the suspension elements. This excess loss would act to obscure the loss due arising from the coating.

The coating losses calculated from modes with little energy stored in the coating during oscillation (i.e. higher energy ratios) are considerably higher than those where there is a larger fraction of the system's energy placed in the coating during vibration. The modes with the lowest energy ratios are thought to be more reliable, as the coating is being sampled more effectively during measurements. The four modes with the lowest energy ratios are the 19.4, 1.9, and 11.5 kHz modes in order of increasing energy ratio. These modes exhibit coating losses of $(6.2 \pm 0.2) \times 10^{-5}$, $(3.8 \pm 1.4) \times 10^{-5}$, and $(2.0 \pm 0.7) \times 10^{-5}$ respectively. All of these values agree, within error, with the loss calculated by Cole from measurements of a thermal noise limited Fabry-Perot cavity with AlGaAs end mirrors.

It should be noted that two of the three modes which exhibit the lowest coating losses, the 11528 Hz mode, and the 19359 Hz mode, oscillate with more shear motion than most of the other modes, which are closer to pure bending motion. This bears similarity to the studies of a GaP/AlGaP coating, presented in section 7.3, in which the mode with more shear motion exhibited consistently lower loss than the modes with less shear motion. This may be a focus for future studies, as the different types of motion may be highly important in studies of crystalline coatings, which may have different mechanical properties for their different crystal axes.

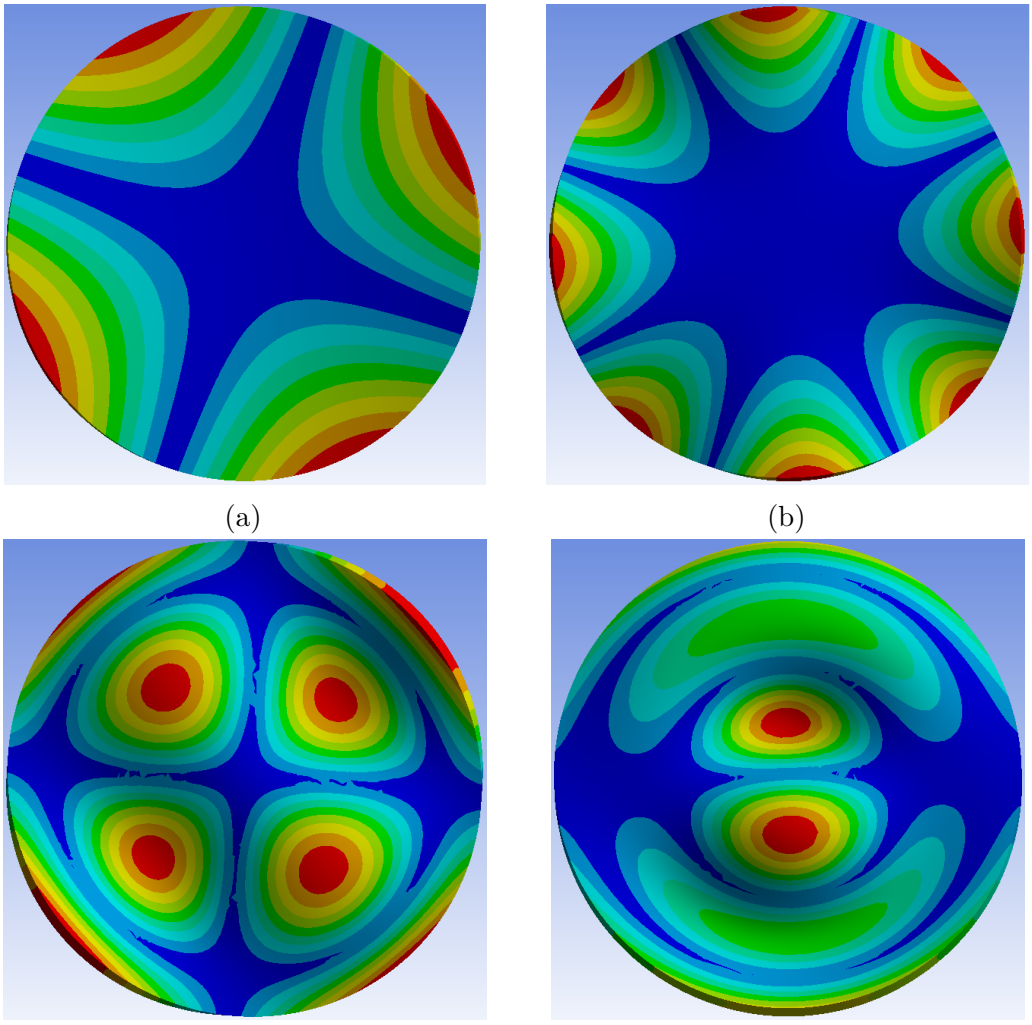

Fig. 7.4 ANSYS finite element models showing the shapes of several vibrational modes of a silica disk excited to measure the mechanical loss of an AlGaAs coating. The blue areas indicate minimal motion, while red areas indicate maximum motion during oscillation. Shown are (a) the 1916 Hz, (b) the 7561 Hz, (c) the 11528 Hz, and (d) the 19359 Hz vibrational modes. The motion of the 7561 Hz mode is concentrated furthest from the centre of the disk, where the coating is located, and this mode shows the highest coating loss. The other modes show motion closer to the coating, and show substantially lower coating loss.

7.2.3 Cryogenic studies of a GaAs/AlGaAs crystalline coating bonded to a silicon substrate

Following the completion of measurements of the AlGaP coated silicon disk and its uncoated counterpart (both samples detailed in section 7.3), the control sample was sent to Crystalline Mirror Solutions GmbH (CMS), [170], to be coated with a GaAs/AlGaAs multilayer coating. Since silicon and AlGaAs are not lattice matched, the coating was grown on a GaAs substrate and then later transferred to the silicon disk. This sample was intended to be used for cryogenic loss measurements of the GaAs/AlGaAs multilayer stack.

The same measurement strategy as that employed in section 7.3, was used. The disk was suspended, placed in a cyostat and cooled to 12 K using contact gas. Unfortunately, however, after the cooling stage of measurements a problem was encountered with the measurement apparatus which meant that the system required warming to room temperature before measurements could proceed. Before recooling, the disk was checked and it was discovered that the coating had partially delaminated during the thermal cycle. The condition of the disk before the thermal cycle is shown in figure 7.5. The disk and coating with signs of delamination after thermal cycling are shown in figure 7.6.

The delaminated parts of the coating are very likely increase the mechanical loss measured, meaning that the coating loss would be impossible to accurately and confidently be determined since the additional loss associated with the delamination would be impossible to distinguish from the coating loss. This along with the potential for futher delamination with more temperature cycles, meant that the decision was taken to cease measurements and to inform the vendor, giving useful feedback for the development of the substrate transfer process applied to coatings for cryogenic measurements.

The substrate-transfer process used for this particular sample is not suitable for depositing AlGaAs coatings onto silicon for cryogenic mirrors, such as those in the proposed ET project. To measure the mechanical loss of the coating, and for the coating to ever be suitable for such cryogenic gravitational wave detectors, the transfer process would need to be developed further.

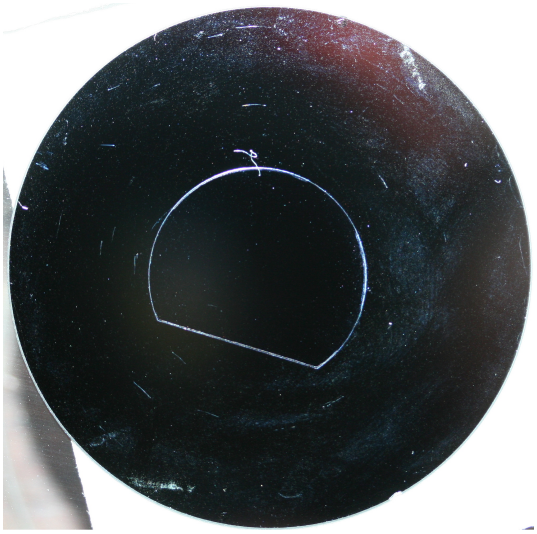

Fig. 7.5 A silicon disk of diameter 39 mm, with a 16.3 mm diameter single-crystal GaAs/AlGaAs multilayer coating placed near the centre of the disk face. The coating shows no signs of delamination. Note that, due to a problem during substrate transfer, the coating has a straight edge rather than being completely circular.

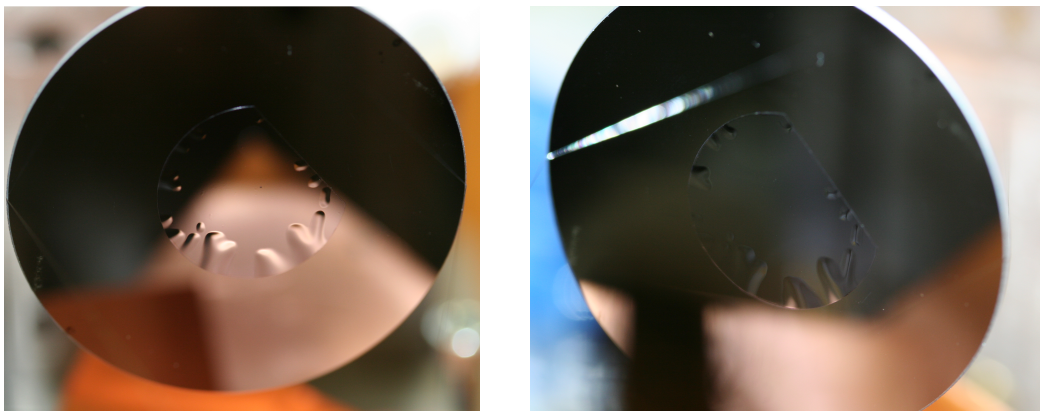

(a) (b)

Fig. 7.6 A silicon disk with an AlGaAs multilayer coating after thermal cycling from 295 K to 12 K, and back to 295 K. Note the bubbles at the edges of the coating where the coating has started to delaminate, presumably due to the differences in thermal expansion coefficients between the coating and substrate. In image (b), the blurred line on the upper left hand side of the substrate is a reflection of one of the 50 µm thick tungsten wires used to suspend the disk.

7.3 Characterisation of a novel GaP/AlGaP crystalline multilayer coating grown on a silicon disk

7.3.1 Sample manufacture

Two thin silicon disks were prepared by collaborators at Stanford University by laser cutting them from silicon wafers. These disks were 39 and 40 mm in diameter, and 450 μm thick. One of these disks was kept un-coated as a control. The other disk was used as a substrate for a coating comprised of 20 layers (10 bilayers) of alternating GaP (each 127 nm thick) and AlGaP (each 140 nm thick), with a 200 nm thick buffer layer of GaP between the substrate and the multilayer mirror coating structure [166, 171]. This gives the coating a total thickness of 2.87 μm. The coating is designed as a Bragg reflector for 1550 nm wavelength light [166].

7.3.2 Measurement setup

The mechanical loss of the samples was measured using the nodal suspension technique described in Chapter 3. As with other loss techniques, the resonant modes of the disk were excited using an electrostatic drive plate, positioned behind the disk. The amplitude of vibration was measured using a commercial SIOS SPS-120/500 laser interferometer [172], and a ring-down technique was employed. After suspension, the hanging disk was placed inside a cryostat.

For cryogenic measurements, the cryostat was cooled using liquid helium, to cool the clamps and the walls surrounding the experimental chamber. The wires used to suspend the disk were 50 μm in diameter, minimising the thermal link between the disk and the clamps. Since the disk could not be cooled significantly through the suspension wires, gaseous helium was injected into the experimental volume to act as a contact gas to cool the disk. To calibrate the temperature/contact gas pressure relationship, a blank disk was suspended with a silicon diode temperature sensor attached to the centre of the disk. The cryostat was then cooled, and contact gas was introduced with varying pressures. When the system reached thermal equilibrium for a given gas pressure, the disk

temperature was recorded. The disk temperatures achieved and the contact gas pressures used to obtain them are catalogued in table 7.2.

Temperature/pressure calibration	
Pressure (mbar)	Disk temperature (K)
7.5×10^{-4}	12
2.5×10^{-4}	17
1×10^{-4}	20
5×10^{-5}	27
2.5×10^{-5}	35
no gas ($\sim10^{-7}$)	43

Table 7.2 Disk temperatures measured using a silicon diode temperature sensor on the centre of the disk as a function of helium contact gas pressure.

7.3.3 Results

The mechanical losses of the two disks were measured for several modes throughout the temperature range 12-43 K. For both disks, the mechanical loss increases above 35 K in a manner consistent with the thermoelastic loss calculated for each mode, which was calculated by collaborators at Friedrich Schiller University Jena.

The measured mechanical losses of the coated and uncoated disks for three modes in the frequency range 5.9-10.3 kHz are shown in figures 7.7, 7.8 and 7.9. To enable the calculation of coating loss, the ratio of energy stored in the coating to that stored in the substrate was calculated using the finite element analysis package ANSYS. The ratios obtained are shown in table 7.3. This calculation requires the value of the Young's modulus of the coating, which was taken to be 103 GPa. This value was taken from the literature values for GaP [173, 174], and was assumed to be the same for AlGaP in the absence of measurements for this material. The Young's modulus was also assumed to have no temperature dependence. Measurements of silicon show that the typical normalised change of Young's modulus with temperature ($\frac{1}{Y}\frac{dY}{dT}$) is of the order of 1×10^{-5}, with a different value for each crystal direction [175]. The coating losses, calculated from the measured data and the energy ratios, are shown in figure 7.10.

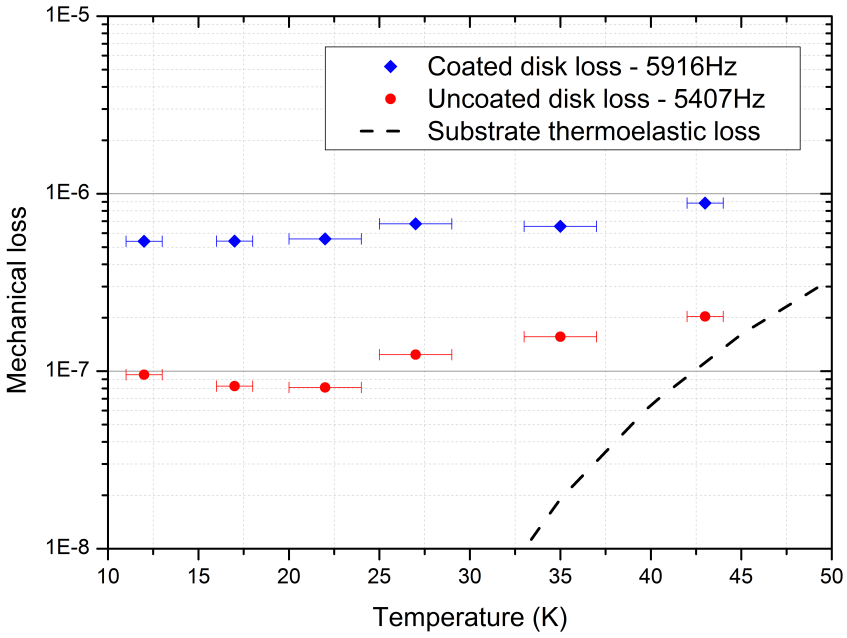

Fig. 7.7 The mechanical loss of a silicon disk with and without an AlGaP coating, measured at 5916 Hz.

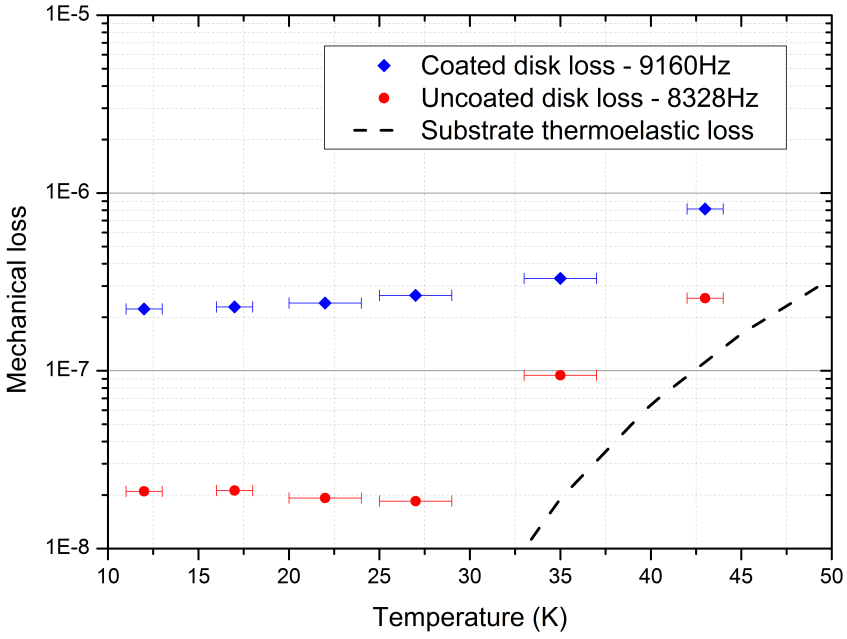

Fig. 7.8 The mechanical loss of a silicon disk with and without an AlGaP coating, measured at 9160 Hz.

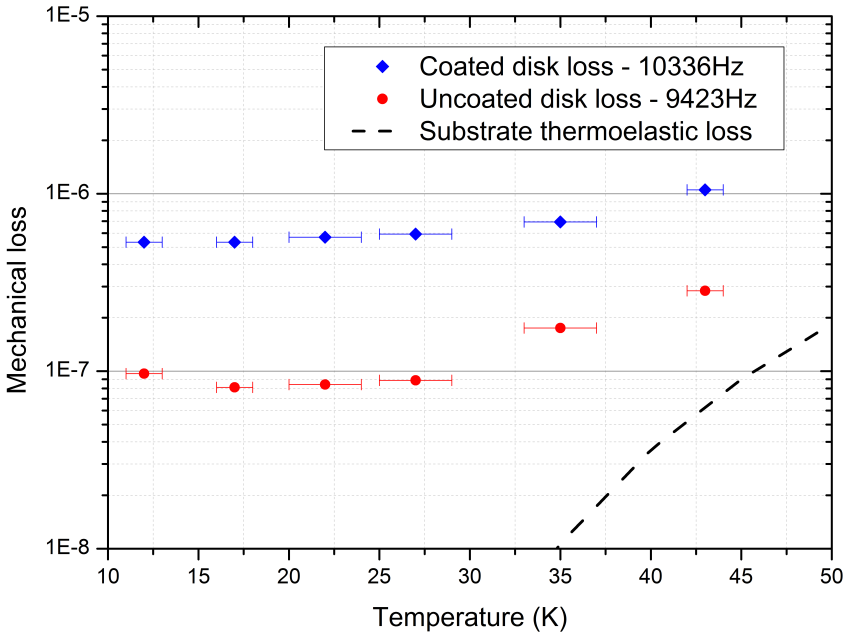

Fig. 7.9 The mechanical loss of a silicon disk with and without an AlGaP coating, measured at 10336 Hz.

AlGaP on silica energy ratios	
Mode frequency (Hz)	E_s/E_c
5917	79.1
9160	70.8
10336	80.5

Table 7.3 The ratio of elastic energy stored in the substrate to that stored in the coating during oscillation, used to calculate coating loss for each mode of a silicon disk coated with an AlGaP multilayer.

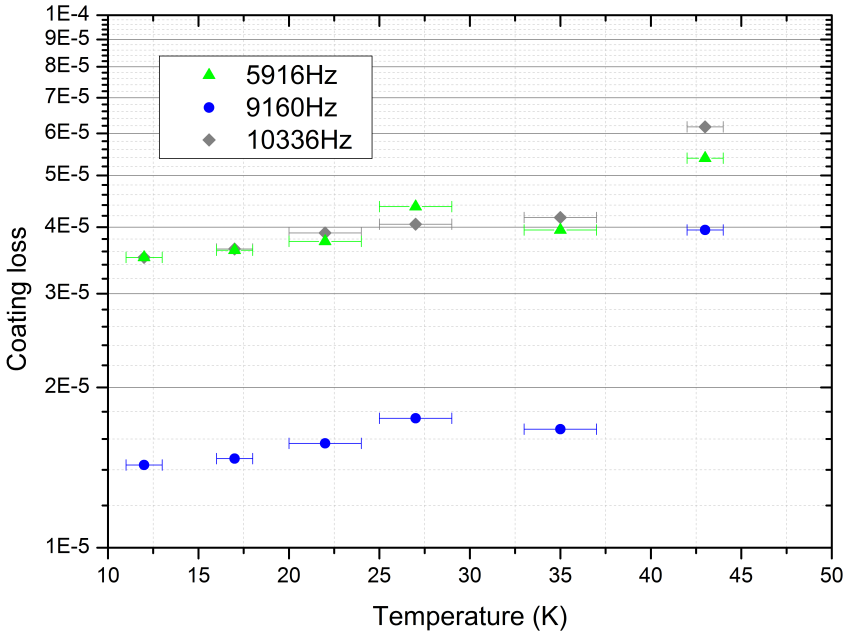

Fig. 7.10 The coating loss of a GaP/AlGaP multilayer crystalline coating as a function of temperature as calculated from measurements of the loss of three modes.

The coating loss shows a small increase over the temperature range 12-35 K, with a larger increase in loss between 35 K and 43 K. At 12 K, the coating loss of the 9160 Hz mode was 1.4×10^{-5}, the lowest coating loss measured, while the highest loss at 12 K was 3.7×10^{-5}, measured at 5916 Hz.

7.3.4 Discussion

The lowest coating loss observed, 1.4×10^{-5} is a factor of ∼14 lower than current IBS silica/titania-doped tantala coatings at room temperature [105], and a factor of ∼64 better than the Advanced LIGO ETM at 20 K, which has a dissipation of approximately 9×10^{-4} [107]. The highest coating loss measured

at 12 K is a factor of ∼5.7 lower than that of silica tantala coatings at room temperature, and a factor of ∼26 improvement in loss over the Advanced LIGO ETM at 20 K.

The coating loss measured for the 9160 Hz mode was consistently lower than the losses of the other two modes. This dependence of coating loss is not yet fully understood. However, a study by Hong et al. has shown that for amorphous coatings, there may be different mechanical losses associated with bulk and shear strains [176]. The same may apply for crystalline materials, with different mechanical losses associated with the different crystal axes, which would be sampled differently by different resonant modes. An illustration of the three mode shapes used to measure the loss of the AlGaP coating are shown in figure 7.11. The two modes measuring the higher coating loss are members of the same mode shape family, whereas the mode measuring a lower coating loss features more shear motion, potentially changing how the coating is sampled during oscillation.

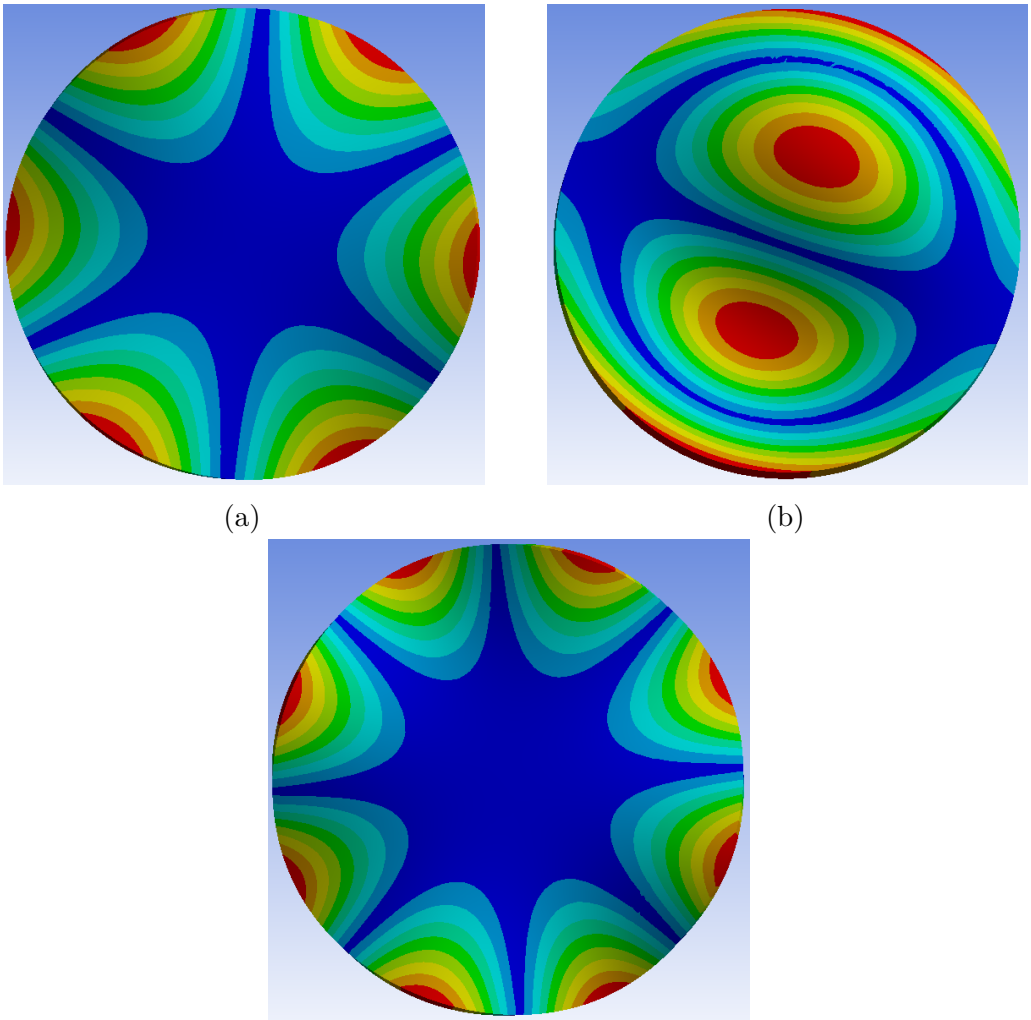

Fig. 7.11 ANSYS finite element models showing the shapes of several vibrational modes of a silicon disk excited to measure the mechanical loss of an AlGaP coating. The blue areas indicate minimal motion, while red areas indicate maximum motion during oscillation. Shown are (a) the 5916 Hz, (b) the 9160 Hz, and (c) the 10336 Hz vibrational modes. The motion of the 9160 Hz mode incorporates more shear motion, potentially sampling the coating in a different manner to the bending motion of the other modes.

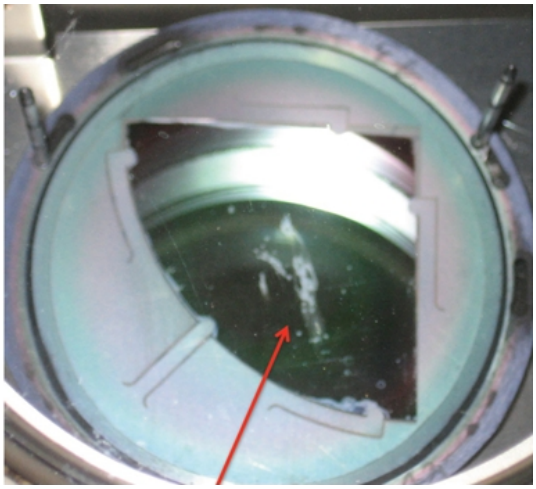

Fig. 7.12 A partial silicon wafer, coated with an MBE GaP/AlGaP crystalline multilayer coating. The disk sample used for loss measurements was later laser cut from this wafer section. The arrow indicates defects seen in the coating after MBE deposition. Note the shape of the defects, which may be seen in the further degraded coating in figure 7.13

The coating showed small visible defects in the as-deposited state. Following one temperature cycle between room temperature and 12 K, further degradation was observed, largely concentrated around existing defects in the coating. A picture of the AlGaP coated silicon wafer, prior to the disk sample being laser cut from it, is shown in figure 7.12 where the defects are clearly visible. The coating after temperature cycling is shown in figure 7.13, where further degradation and the original defects can still be seen. These original defects are likely to have been the starting point for the development of the cooling-related defects and it would hence be desirable for the MBE process involved in growing these coatings to be enhanced in order to reduce the number and size of surface defects from the coating growth process. The coating produced for this study was the first ever prototype coating of this type. The coating exhibits low loss despite the visible defects, so it is likely that future coatings produced will be of a higher quality.

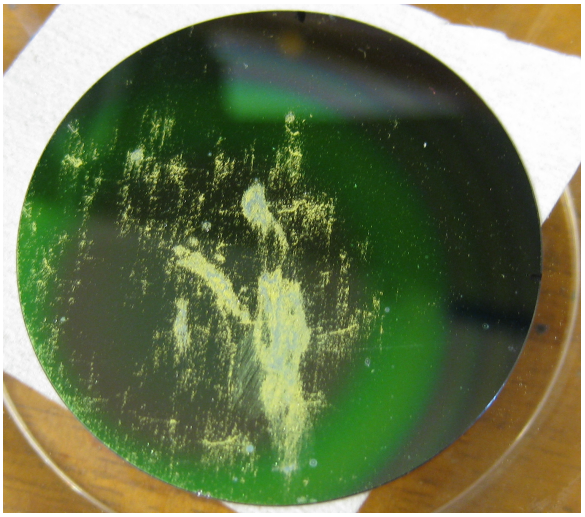

(a)

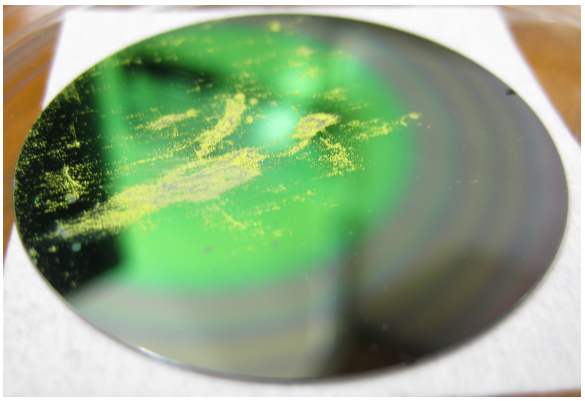

(b)

Fig. 7.13 The AlGaP coated silicon disk after temperature cycling. The coating shows more defects than it did prior to thermal cycling.

7.4 The Brownian thermal noise associated with crystalline coatings

Thermal noise arising from mirror coatings is discused in Chapter 2. In particular, the Brownian noise power spectral density associated with a mirror coating may be calculated from equation 2.23, taking the second term within the brackets to be the thermal noise solely due to the coating.

For the Advanced LIGO ETM coating, which has a mechanical loss of 3×10^{-4} at 300 K and of approximately 9×10^{-4} at 20 K [107] and a total thickness of 5.9 μm when deposited as a coating for high-reflectivity at 1064 nm and a thickness of 8.6 μm for high-reflectivity at 1550 nm. A 1550 nm wavelength laser would be required for operation at 20 K, assuming silicon is the choice substrate, as is proposed for ET [19]. This coating has a Young's modulus approximately 96 GPa.

The AlGaP coating is assumed to have a Young's modulus of 103 GPa, that of GaP. For operation at 20 K, the coating is assumed to be deposited upon a silicon substrate, as per the development of the coating technology thus far. The GaP layers have a refractive index of $n_H = 3.05$, and are the high-index layers within the coating, while the AlGaP layers have a refractive index of $n_L = 2.77$ [177].

For a fair comparison with the aLIGO ETM, the AlGaP coating must be of the required reflectivity, and hence the number of layers needed to satisfy this constraint must be calculated. For the Advanced LIGO ETM, the transmission is stipulated to be 5-10 ppm, with the rest of the light reflected. The reflectivity, R, of a multilayer coating may be calculated from [178]:

$$R = \left(\frac{n_s \left(\frac{n_H}{n_L}\right)^{2N} - n_0}{n_s \left(\frac{n_H}{n_L}\right)^{2N} + n_0} \right)^2 \tag{7.1}$$

where n is the refractive index of the substrate, s, the high index layers, H, the low index layers L, and of a vacuum, 0, denoted by subscript. Here, N is the number of layer pairs. It can be shown that an AlGaP coating requires $N = 58$, giving the coating a thickness of 15.5 μm for high reflectivity at 1550 nm.

The displacement thermal noise associated with the AlGaP coating has been calculated twice, with two different values for the coating loss used. For an

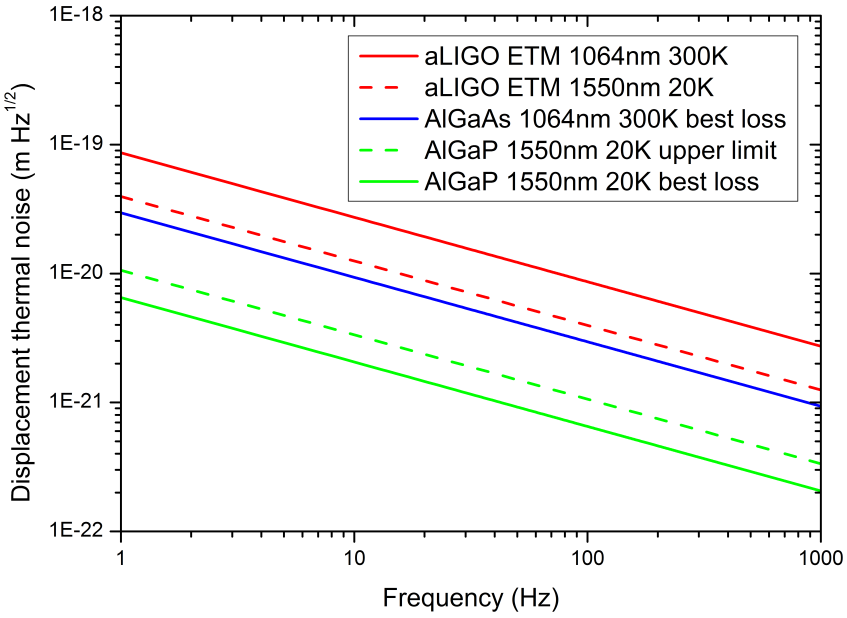

Fig. 7.14 The Brownian thermal noise associated with an Advanced LIGO ETM coating at 300 (silica substrate) and 20 (silicon substrate) Kelvin, compared with the upper and lower estimates of noise associated with an AlGaP crystalline coating on a silicon substrate at 20 K, and an AlGaAs crystalline coating on a silica substrate at 300 K.

upper limit, a coating loss of 3.5×10^{-5} has been taken. To show the potential improvement in thermal noise, a value of 1.4×10^{-5} has also been used, being the lowest loss measured for an AlGaP coating at cryogenic temperatures.

The mechanical loss of an AlGaAs coating at cryogenic temperatures was not obtained. However, coating loss values for the AlGaAs coating at room temperature were measured and have been used to calculate an associated thermal noise. The thickness of an AlGaAs coating meeting the aLIGO ETM design requirements is 6.83μm. The coating Young's modulus was taken to be 100 GPa, and the coating was assumed to have a silica substrate. The mechanical loss used to calculate thermal noise was taken to be 2×10^{-5}, as this was the lowest coating loss measured on a silica disk.

All calculations of thermal noise assume a laser beam radius of 6.2 cm, that of the aLIGO reference design for the ETM. A comparison of the displacement thermal noise associated with the Advanced LIGO ETM coating at 300 K and 20 K, the AlGaP coating at 20 K with calculated upper and lower limits, and the AlGaAs coating at 300 K is shown in figure 7.14.

The AlGaAs coating shows a factor of 2.9 improvement in amplitude displacement thermal noise over the Advanced LIGO ETM coating at room temperature. The aLIGO ETM coating thermal noise may be improved by switching to a silicon substrate cooled to 20 K with a laser wavelength of 1550 nm, but still does not match the improvement associated with an AlGaAs coating at room temperature.

The biggest improvement in thermal noise over the Advanced LIGO ETM coating is calculated to be from the AlGaP coating. The AlGaP coating shows a factor of between 8-13.3 improvement in thermal noise over the aLIGO ETM at room temperature, and a factor of between 3.7-6 over the aLIGO ETM coating operating at 20 K.

7.5 Conclusions

The mechanical novel GaP/AlGaP crystalline coating, grown on a silicon disk, has been characterised at low temperatures. The lowest observed coating loss is 1.4×10^{-5}, measured at 12 K. This is a factor of approximately 14.3 lower than the loss of a silica/tantala multilayer at room temperature and a factor of 64 lower than the loss of the aLIGO ETM coating at 20 K. Thermal noise calculations show that the coating would give a displacement thermal noise improvement of a factor of between 8-13 over the aLIGO ETM at room temperature and a factor of 3.7-6 over the aLIGO ETM at 20 K.

However, the AlGaP coating showed defects in the as-deposited state, which further degraded after several temperature cycles. This coating may be promising for future gravitational wave detectors if developments in manufacturing reduce the density of defects within the coatings. Further studies of the mechanical properties of the coating are also required, including measurements of the Young's modulus of the individual layers and of the mechanical losses which may be associated with the different crystal orientations. Studies of the optical properties of the coating are also of interest.

A substrate-transferred GaAs/AlGaAs coating was studied at room temperature, yielding measurements of the coating mechanical loss. The results showed a wide scatter, however the three lowest values are consistent with previous studies using free-standing AlGaAs structures and resonant Fabry-Perot cavities. The lowest coating loss measured was $(2.0 \pm 0.7) \times 10^{-5}$. It is thought that

the wide range of coating losses obtained is due to the relative sampling of the coating by the various vibrational modes of the disk on which the coating was deposited. Previous studies show the coating to have good optical properties [88], and the coating therefore may be of high-interest to the gravitational wave community. However, the coating produced for measurements here was of 16.3 mm diameter, which is small compared to the 6.2 cm beam radius of the Advanced LIGO ETM. If the coating technology may be appropriately scaled up, the coating will offer a displacement thermal noise improvement by a factor of approximately 2.9 over the existing aLIGO ETM coating at room temperature.

Attempts to study the AlGaAs crystalline coating substrate-transferred onto a silicon disk, at cryogenic temperatures resulted in the partial delamination of the coating. The coating itself remained intact, but further developments in the substrate-transfer process are required for the coating to be considered for low temperature detectors such as ET or KAGRA.

Overall, the two crystalline coatings studied have shown low mechanical loss, but require further development in manufacturing in order to be feasibly used in a gravitational wave detector.

Chapter 8

Conclusions

A network of first-generation interferometric gravitational wave detectors was created in order to make the first direct detection of gravitational waves. Several data runs were carried out, but gravitational waves were not detected. However, the data collected were used to place new constraints on astrophysical models of the sources of gravitational waves. The second generation of interferometric gravitational wave detectors feature numerous upgrades from the first generation detectors. These detectors will begin collecting data soon, and it is widely anticipated that these detectors will make the first direct detection of gravitational waves.

The second generation of interferometric gravitational wave detectors are expected to be limited by a host of fundamental noise sources, including the thermal noise of the optical coatings used to form the mirrors. In particular, coating Brownian noise is expected to form a limit to the sensitivity of third generation detectors at their most sensitive frequency bands. Third generation detectors such as the Einstein Telescope will utilise cryogenic cooling to reduce the magnitude of Brownian noise. Hence, it is necessary to understand the source of Brownian noise in existing coatings by measuring the mechanical properties that contribute to the coating Brownian noise at cryogenic temperatures. It is also important to seek new coating materials which exhibit lower thermal noise than existing coatings.

Previous research has shown that the Brownian thermal noise arising from a coating is dependent upon its mechanical dissipation. Methods of measuring the mechanical loss of coatings deposited upon disks and cantilevers have been described. Using measurements of a tantala layer fabricated by atomic layer

deposition, it has been shown that silicon cantilevers should be oxidised prior to coating deposition in order to prevent excess loss arising from the coating, which is thought to originate from poor coating adhesion. The mechanical loss of a Niobia coating has been measured using the disk and cantilever technique, and with two coating thicknesses. Within error, the same mechanical loss was observed to arise from the coating, independent of substrate geometry and coating thickness.

In previous studies, doping pure tantala coatings has been shown to reduce the mechanical loss of the material. However, it is not well understood how the doping actually reduces the mechanical loss. Therefore, studies of the mechanical loss of tantala doped with titania to a cation concentration of 25% and 55% have been carried out. These doped coatings have been studied before and after heat-treatment, and loss peaks have been observed at cryogenic temperatures in the temperature dependent mechanical loss of the as-deposited 25% and 55% doped coatings and the 55% doped coating heat-treated to 600 °C. The dissipation peaks follow an Arrhenius-like rate law for which an activation energy and rate constant may be calculated. These values have been obtained and a distribution of barrier heights has been calculated for each sample, which suggests that the effect of heat-treatment is greater than the effect of doping on the microscopic structure of the coatings. Structural measurements by X-ray diffraction are a suggested future experiment to correlate observed changes in mechanical loss with changes in molecular stucture.

The Brownian thermal noise arising from the coatings within the Advanced LIGO detector will set a limit to the sensitivity of the detector in a frequency band of a few tens of Hertz to a few hundred Hertz. Measurements of the mechanical loss of the Advanced LIGO ETM and ITM coatings have been made at room temperature, and the mechanical loss of the ETM coating has been characterised at low temperature. The ETM coating exhibits a large dissipation peak at approximately 28 K, which is important if the coating is chosen for detectors designed to operate at low temperatures such as KAGRA or ET.

A discrepancy between the previous studies of the losses of single layer silica and tantala coatings and measurements of a silica/tantala multilayer disk at cryogenic temperatures has been investigated. From the losses of the single layers, it would be expected that the multilayer coating would exhibit a loss

peak at cryogenic temperatures, similar to that seen in the loss of the aLIGO ETM coating. However, previous measurements of the multilayer coating shows the loss to be independent of temperature. The loss of this coating was remeasured before and after heat-treatment at 500 °C. Initial measurements suggested that the heat-treated coating shows a loss peak, however further measurements suggested that the peak was due to loss into the clamp structure. A second measurement showed the loss of the coating to be independent of temperature, although more measurements would be required to confirm this.

Previous research has shown that the mechanical loss of a multilayer silica/tantala coating is typically dominated by the loss of the tantala layers. Hence, it is of interest to seek materials with a lower loss than tantala to create coatings which exhibit lower thermal noise. IBS hafnium dioxide was suggested by previous studies as being a promising material. However, the IBS hafnia studied was found to have partially crystallised upon deposition, which is known to increase loss and degrade optical properties. As such, measurements the mechanical loss of hafnia doped with silica have been carried out since silica is known to prevent crystallisation of hafnia. The IBS silica-doped hafnia films studied exhibit lower mechanical loss than titania-doped tantala at cryogenic temperatures, and show promising optical absorption. The thermal noise arising from a silica/silica-doped hafnia multilayer at 20 K is lower than that calculated for the Advanced LIGO ETM coating at similar temperatures. Therefore, silica-doped hafnia is a promising candidate to be a suitable replacement for the high-index tantala for future cryogenic detectors.

Previous studies at room temperature have shown that the Brownian thermal noise exhibited by a mirror coating fabricated from single crystals is consistent with the coatings having a coating loss lower than that of a silica/tantala multilayer by a factor of ten. The mechanical loss of a GaP/AlGaP multilayer coating grown on a silicon wafer by molecular beam epitaxy was measured at cryogenic temperatures, and subsequent calculations show that the coating would exhibit a factor of 3.7-6 lower thermal noise than an aLIGO ETM coating at 20 K. However, degradation of the coating with thermal cycling means that the deposition process needs further development if the coating is to be a promising candidate for future gravitational wave detectors.

A multilayer GaAs/AlGaAs coating has been studied at room temperature on a silica substrate and at cryogenic temperatures on a silicon substrate. The

coating deposited on a silicon substrate appeared to delaminate after thermal cycling, and so the substrate transfer process used requires further development. The loss of the AlGaAs coating on a silica substrate showed low loss, consistent with previous measurements of a similar coating with a different techinque. However, the current technology is not capable of producing the diameter of coatings required in gravitational wave detectors and needs further development if the coating is to be used in future detectors.

The measurements made within this thesis will greatly aid the study of the mechanical loss causing mechanisms within amorphous thin films. This will guide future investigations into low loss coatings. Further, the studies of crystalline coatings carried out will feed back to coating vendors, enabling them to address current problems with the state of the art technologies such that a coating suitable for use in interferometric gravitational wave detectors may be produced.

Appendix A

Mechanical loss data collection and analysis

A description of the data collection and analysis methods relating to cantilever measurements are presented within this appendix. Once a cantilever has been clamped, the cryostat evacuated and the optics aligned by the methods described in Chapter 3, data may be collected. The electrostatic drive plate is used to drive the motion of the cantilever at the frequency of the a.c. signal applied. To begin with, the chosen a.c. signal frequency is lower than that of the expected resonant frequency. The time series output of the split photodiode is Fourier transformed, and the amplitude of vibration at the driving frequency is recorded by a custom Labview data logging programme. The driving frequency is incrementally increased, typically in steps of 0.01 Hz, and the amplitude of vibration is monitored. When the driving frequency approaches a cantilever resonant frequency, the amplitude of vibration increases significantly. When the driving frequency is larger than that of the resonant frequency, the amplitude of vibration begins to decrease. At this point, the excitation signal is switched off, allowing the signal to decay naturally. Figure A.1 shows the response of the vibrational amplitude of a cantilever in response to a frequency sweep as described above. The large peak indicates that the resonant cantilever motion was excited, and the frequency at which the peak occurs is recorded as the resonant frequency.

Figure A.2 shows the decay of vibrational amplitude after the excitation shown in figure A.1. The data are then fitted as an exponential decay. The mechanical loss is then calculated using equation 3.1.

During one cryogenic measurement cycle, the mechanical loss is measured at each desired temperature step 2-3 times per cycle. The measurement cycle is repeated, with the cantilever removed from the clamp and reclamped between cycles. Figure A.3 shows the data from four measurement cycles of a coated cantilever. Here, two ringdowns were taken per temperature step in each cycle. The data points indicate the mean of the two measurements and the error bars indicate the upper and lower loss values measured within each cycle. The both the green and the grey measurement cycles feature signs of excess loss. These signs include multiple loss peaks, which do not feature upon reclamping, and significantly higher scatter amongst the data. By comparison, the losses shown in blue and red feature little to no variation between ringdowns within each measurement cycles, and the loss does not vary significantly between measurement cycles. In this case, the green and grey points are removed from consideration during further analysis.

With the remaining points, the temperature dependent mechanical loss is calculated using the mean of the losses measured at each temperature step. The uncertainty in loss at each temperature step is then calculated as the standard deviation of the points at each step. The temperature mechanical loss calculated for this data is shown in figure A.4.

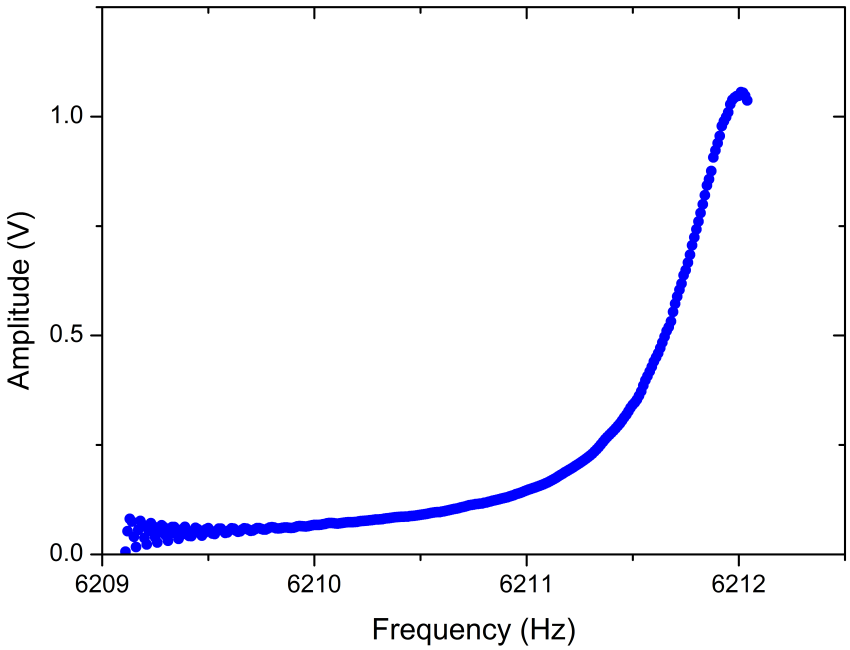

Fig. A.1 The amplitude of vibration of a cantilever in response to an electrostatic drive with increasing frequency. The large peak indicates the excitation of a resonant mode. Once the mode is excited, the driving force is removed.

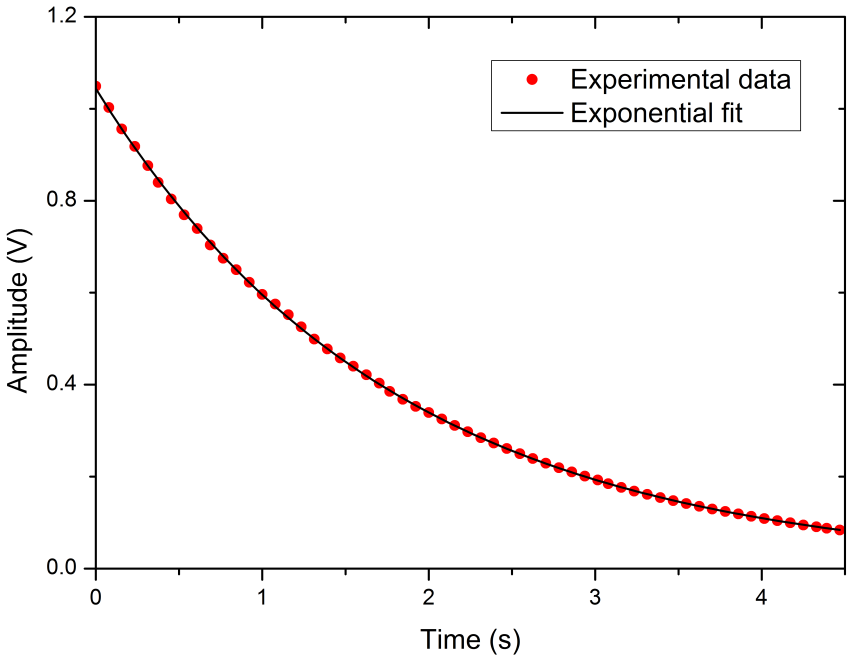

Fig. A.2 After the excitation of a resonant mode, shown in figure A.1, the resonant motion is allowed to decay freely. The experimental data and exponential fit used to determine the ringdown time are shown.

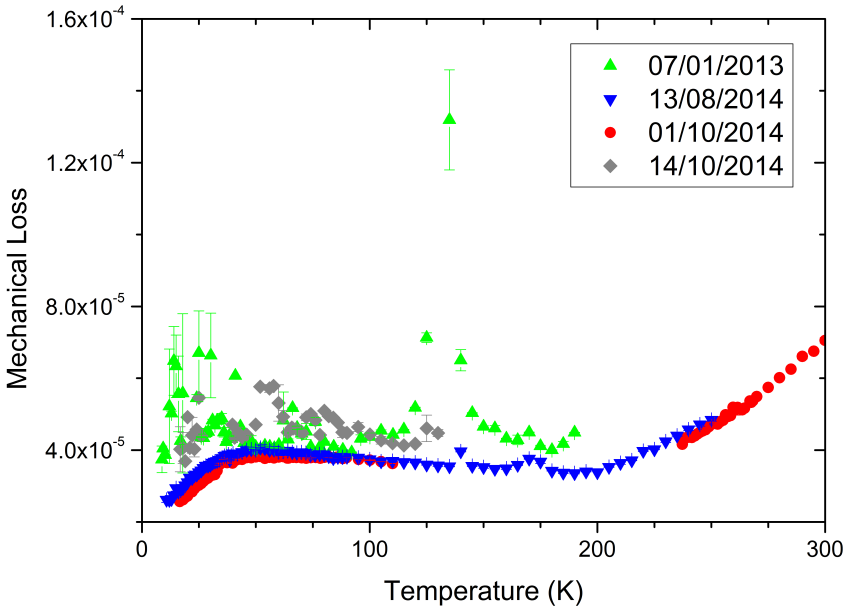

Fig. A.3 The data collected in four measurement cycles for one cantilever. Each data point is the average of two measurements taken during each measurement cycle. The error bars indicate the maximum and minimum losses measured at each temperature during each cycle.

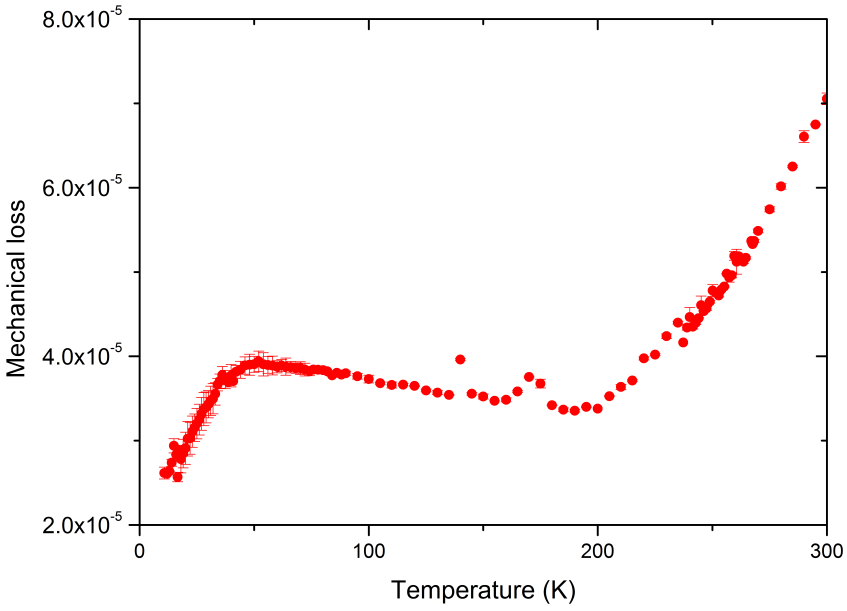

Fig. A.4 In the final data, each data point is the average of the good losses measured at that temperature. The error bars are the standard deviation of the points included in the average.

Appendix B

Silicon cantilever sample preparation and the effects on coating loss

B.1 Introduction

Discussions with commercial vendors of IBS coatings have indicated that some IBS coatings do not adhere properly to the surface of silicon, and that the growth of a very thin thermal oxide layer on the surface of the sample can significantly improve adhesion [130]. Silicon typically has a native surface oxide layer ∼2-3 nm thick. Before coating deposition, the silicon cantilevers studied here were typically placed into an oven at 1000 °C for 15 minutes. This creates a ∼20 nm thick layer of amorphous silicon dioxide on all surfaces of the cantilever, which was measured by ellipsometry.

In this appendix, a comparison of the coating loss arising from an identical coating deposited on cantilevers with and without a thermally grown oxide layer is presented in order to test the hypothesis that depositing a coating on a silicon cantilever with only a native oxide leads to poor coating adhesion. If the coating is poorly adhered to the substrate, the calculated coating loss may exhibit additional loss compared to the loss of a well-adhered coating.

Two silicon cantilevers of nominally identical thicknesses were chosen for this experiment. One was placed in an oven for 15 minutes at 1000 °C (which will hereby be referred to as the oxidised cantilever), the other remained as-

manufactured with only a thin native oxide layer on its surfaces (referred to as the unoxidised cantilever). The two cantilevers were then subsequently coated with a 500 nm thick amorphous tantala layer using the technique of atomic layer deposition (ALD) [110].

B.2 Oxidised cantilever

The mechanical loss of the oxidised cantilever, coated with ALD tantala, is presented in Chapter 4.

B.3 Unoxidised cantilever

The mechanical loss of the unoxidised, coated cantilever for bending modes 3-9 is shown in figures B.1, B.2, and B.3 in order of increasing frequency of resonant mode. The mechanical loss of an uncoated control cantilever of similar thickness was also measured, in order to allow a coating loss to be calculated. The thicknesses and mode frequencies of the coated oxidised, coated unoxidised and oxidised uncoated cantilevers are shown in table B.1.

The same control data was used for the oxidised cantilever as for the unoxidised cantilever, and the uncoated cantilever used was oxidised prior to measurement. The loss of bulk amorphous silica was shown to be of the order of $\phi = 1 \times 10{-}3$ at the cryogenic loss peak [179]. Using equation 3.6, the contribution of a 20 nm oxide layer to the loss of the uncoated cantilever should be of the order of $\phi_{\text{oxide}} = 8 \times 10^{-7}$, which is below the level of loss typically measured for the modes of the uncoated cantilever. The effect of the very thin oxide layer on the uncoated cantilever is therefore negligable in coating loss calculations.

For all modes, the loss of the coated cantilever decreased slightly between 290 K and 200 K, and then rose steadily to a broad peak centred on approximately 50-70 K, mode dependent. The coating loss at the peak was approximately $2{\times}10^{-3}$. The room temperature coating loss was in the range $1\text{-}4{\times}10^{-3}$ for all modes. This is significantly higher than the loss of a comparable IBS film [4].

ALD coated cantilever mode frequencies (kHz)			
Mode	Unoxidised coated cantilever	Oxidised coated cantilever	Oxidised uncoated control sample
3	1.2	1.3	1.2
4	2.5	2.5	2.4
5	4.1	4.1	3.9
6	6.1	6.2	5.9
7	8.5	8.6	8.2
8	11.4	11.4	10.9
9	14.6	14.7	14.0
Total Thickness µm	61.1	61.9	58.5

Table B.1 The mode frequencies and cantilever thicknesses (including the coating) of the oxidised and unoxidised cantilever coated with ALD tantala, as well as the corresponding values of the control sample.

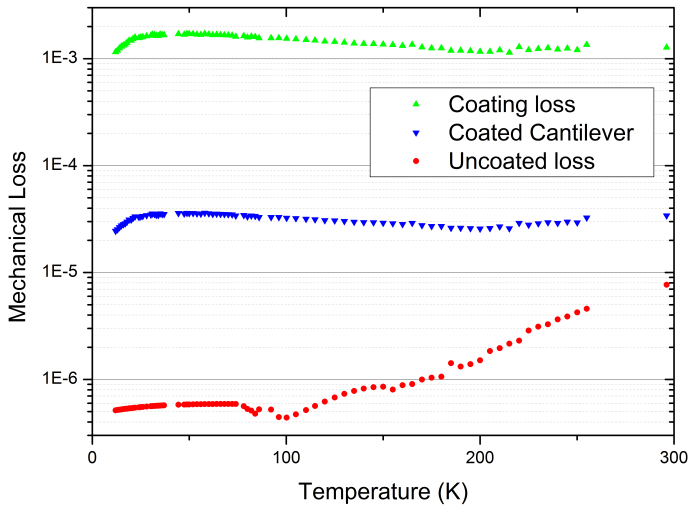

Fig. B.1 Temperature dependent mechanical loss of an ALD tantala coating for bending mode 3 at 1.3 kHz. Also shown are the mechanical loss of the coated, unoxidised cantilever and the control data used in the coating calculation.

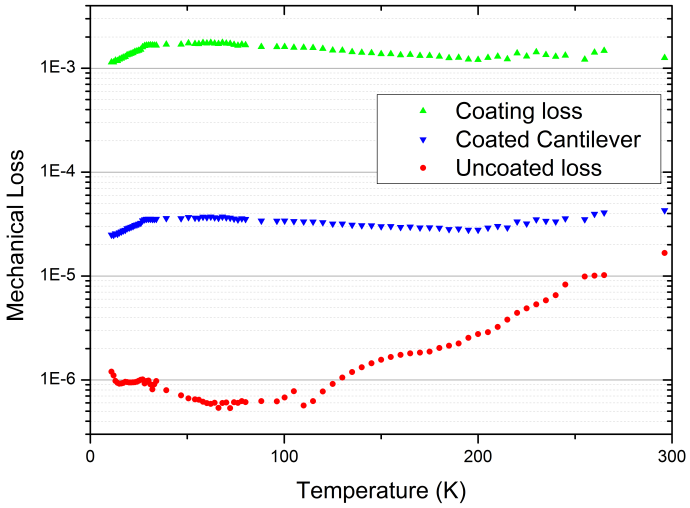

(a) Bending mode 4, 2.5 kHz

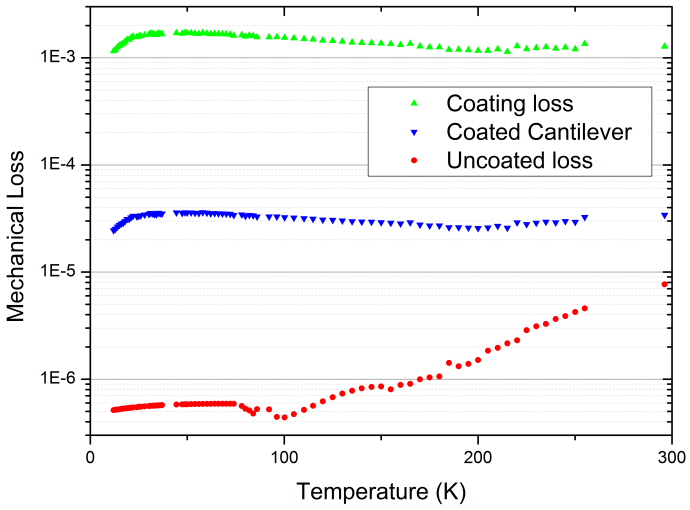

(b) Bending mode 5, 4.2 kHz

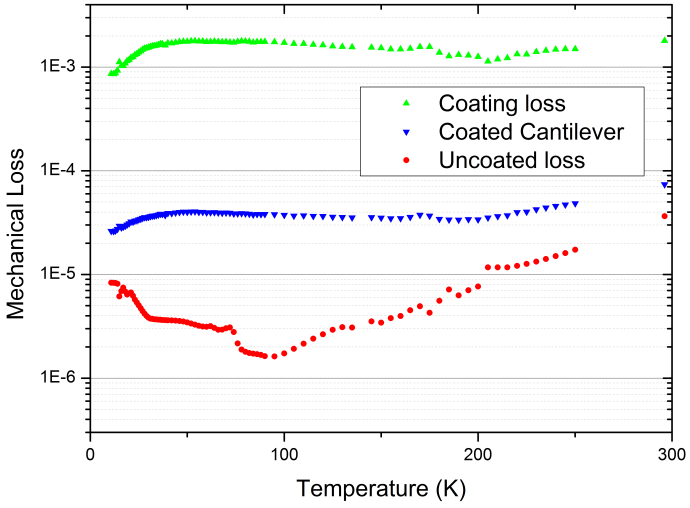

(c) Bending mode 6, 6.2 kHz

Fig. B.2 Temperature dependent mechanical loss of an ALD tantala coating for several bending modes, measured on the unoxidised cantilever. Also shown are the mechanical loss of the coated cantilever and the control data used in the coating calculation.

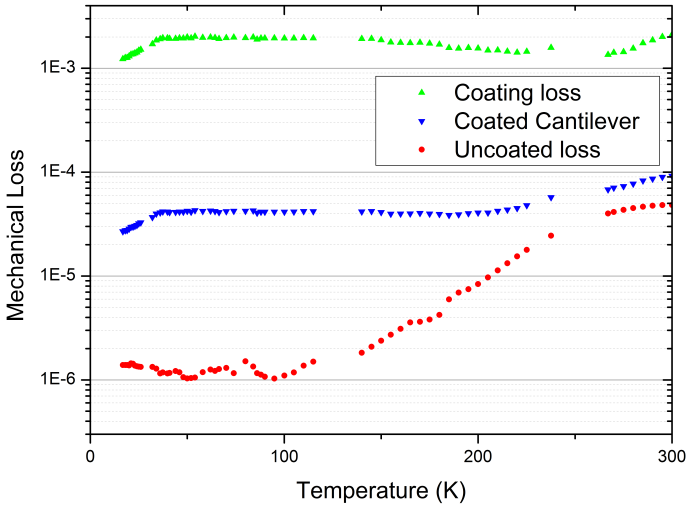

(a) Bending mode 7, 8.7 kHz

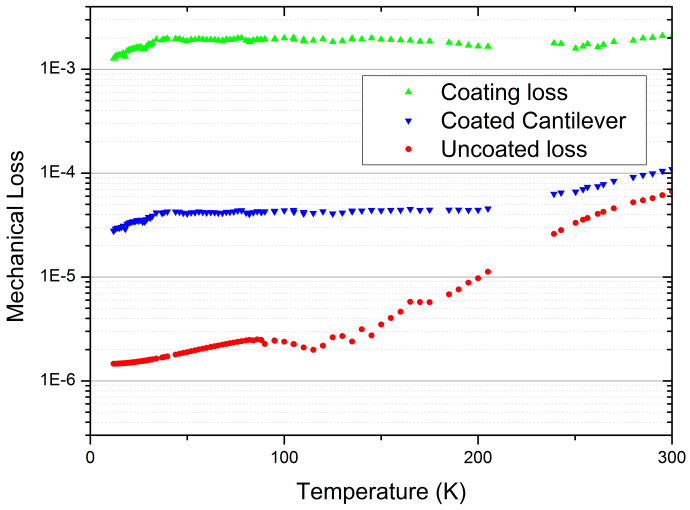

(b) Bending mode 8, 11.5 kHz

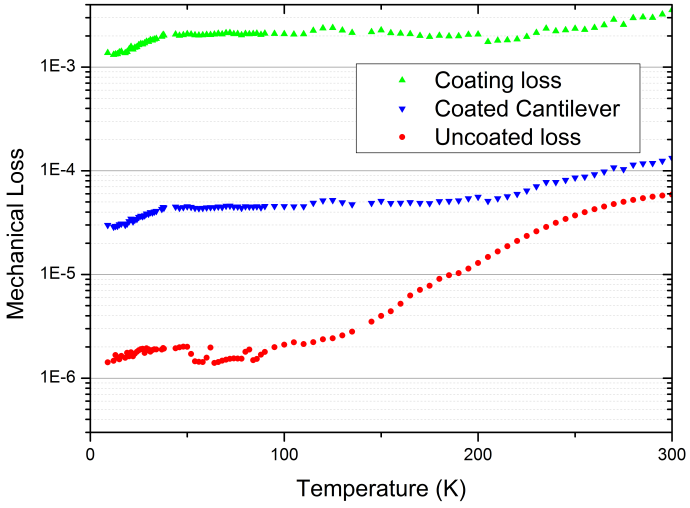

(c) Bending mode 9, 14.8 kHz

Fig. B.3 Temperature dependent mechanical loss of an ALD tantala coating for several bending modes, measured on the unoxidised cantilever. Also shown are the mechanical loss of the coated cantilever and the control data used in the coating calculation.

B.3.1 Comparison

A comparison of the coating mechanical loss as measured using the oxidised and unoxidised cantilevers are presented in figures B.4, B.5, B.6, B.7,B.8, B.9 and B.10. These show a comparison of bending modes 3-9 in order of increasing frequency.

The results for mode 3 show very good agreement between the coating loss exhibited by the two cantilevers. The coating losses exhibited by the fourth mode show good agreement in the low temperature region below 100 K. Above 200 K, the coating loss exhibited by the unoxidised cantilever is higher than exhibited by the oxidised cantilever, with some scatter in the losses measured. The same behaviour is exhibited by the fifth mode, where the losses measured on the unoxidised cantilever show significantly higher loss and scatter in the 200-300 K range compared to the losses measured on the oxidised cantilever. The results of modes 7-9 show similar behaviour, but the temperature region where excess loss is observed extends down to 100 K. The excess loss exhibited by the coating deposited on the unoxidised cantilever shows a frequency dependence, with higher frequencies showing a higher level of loss. This may be due to the higher order bending modes probing more of the interface since higher order modes have more antinodes along the cantilever length than lower order modes.

Since the coating loss exhibited on the oxidised cantilever appears lower and less scattered for many of the modes measured for both cantilevers, cantilevers used for coating loss measurements throughout this thesis have been oxidised prior to coating deposition.

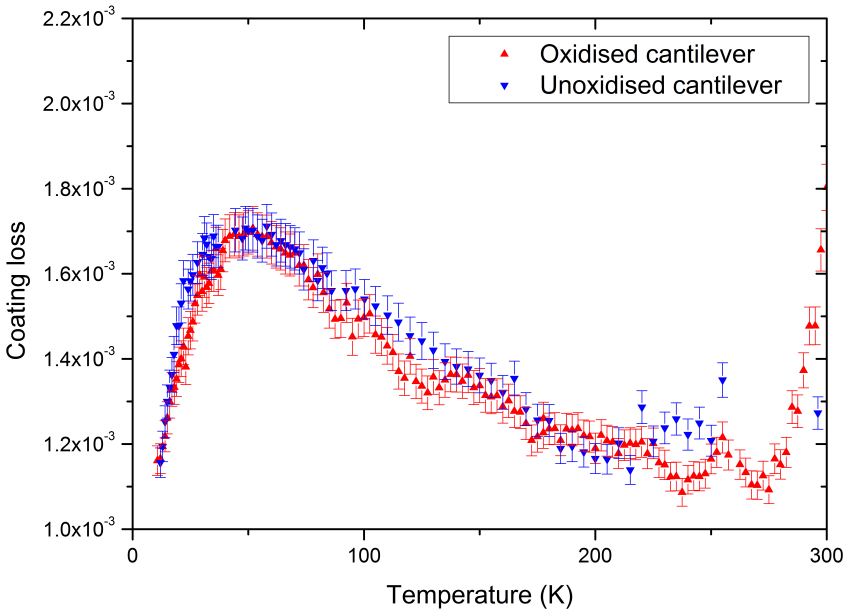

Fig. B.4 A comparison of the mechanical loss of an ALD tantala coating as measured using cantilevers with different surface oxide thicknesses. The coating loss from measurements of mode 3 is shown.

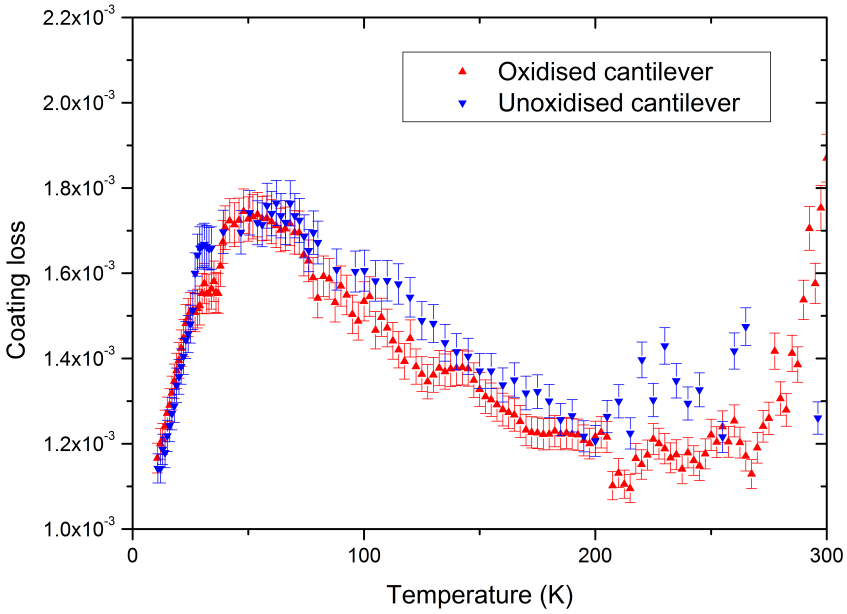

Fig. B.5 A comparison of the mechanical loss of an ALD tantala coating as measured using cantilevers with different surface oxide thicknesses. The coating loss from measurements of mode 4 is shown.

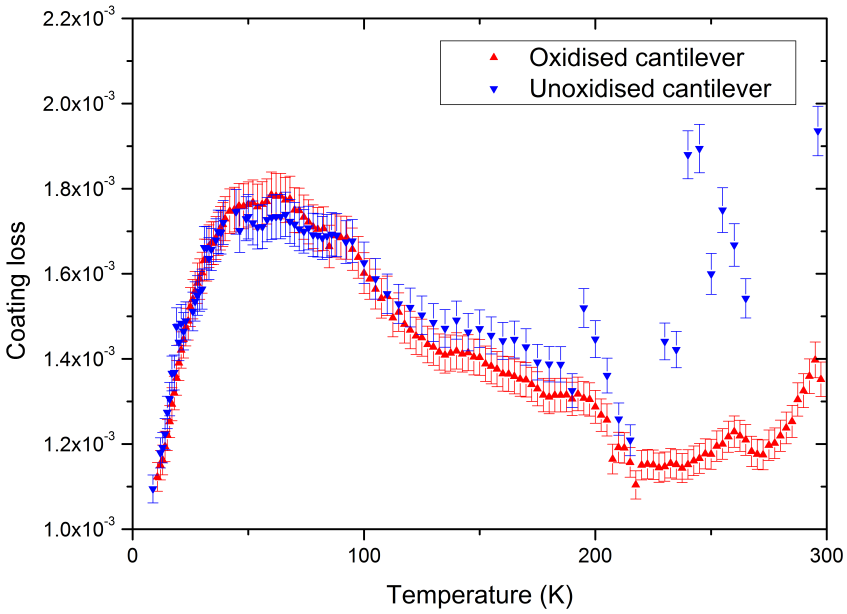

Fig. B.6 A comparison of the mechanical loss of an ALD tantala coating as measured using cantilevers with different surface oxide thicknesses. The coating loss from measurements of mode 5 is shown.

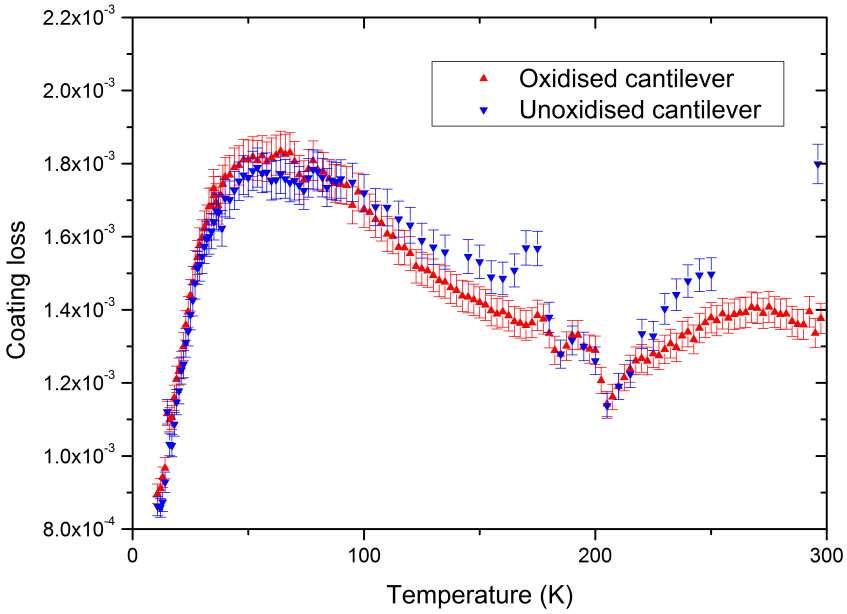

Fig. B.7 A comparison of the mechanical loss of an ALD tantala coating as measured using cantilevers with different surface oxide thicknesses. The coating loss from measurements of mode 6 is shown.

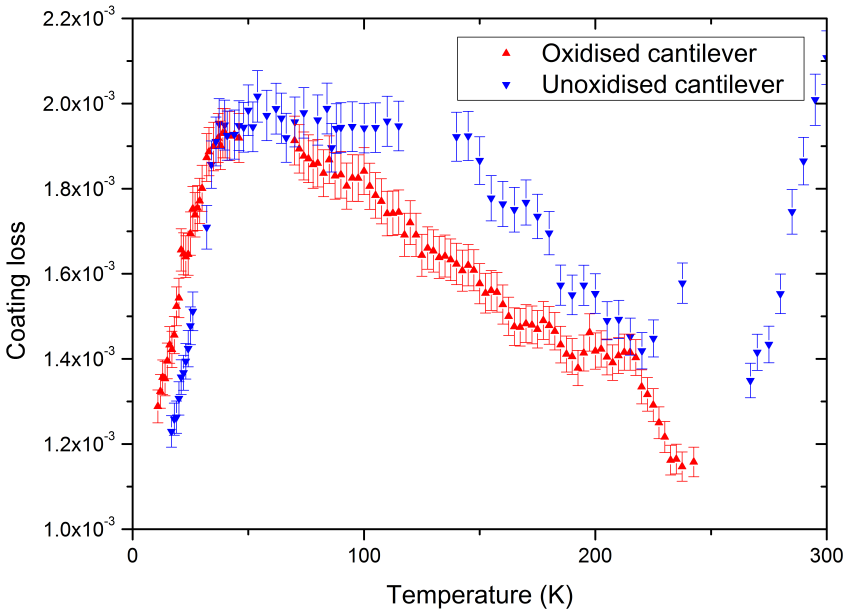

Fig. B.8 A comparison of the mechanical loss of an ALD tantala coating as measured using cantilevers with different surface oxide thicknesses. The coating loss from measurements of mode 7 are shown.

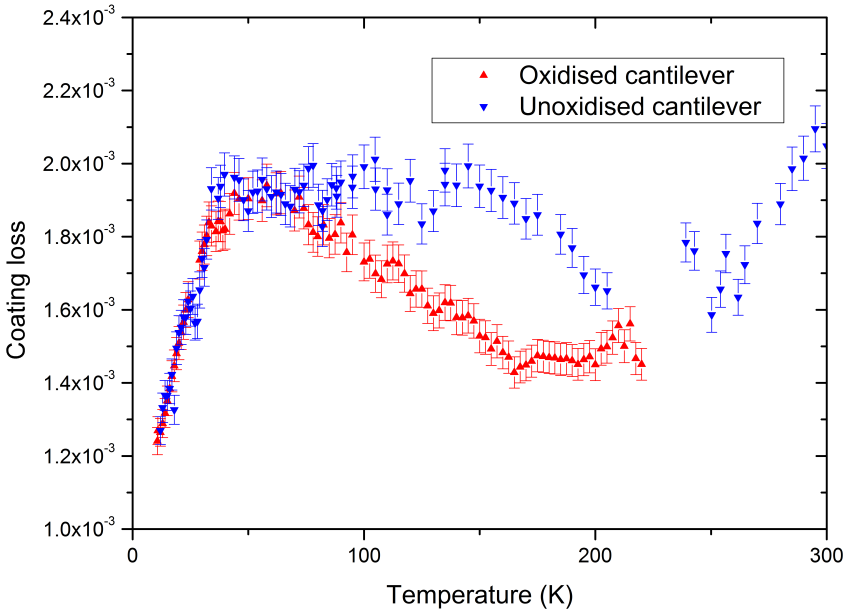

Fig. B.9 A comparison of the mechanical loss of an ALD tantala coating as measured using cantilevers with different surface oxide thicknesses. The coating loss from measurements of mode 8 are shown.

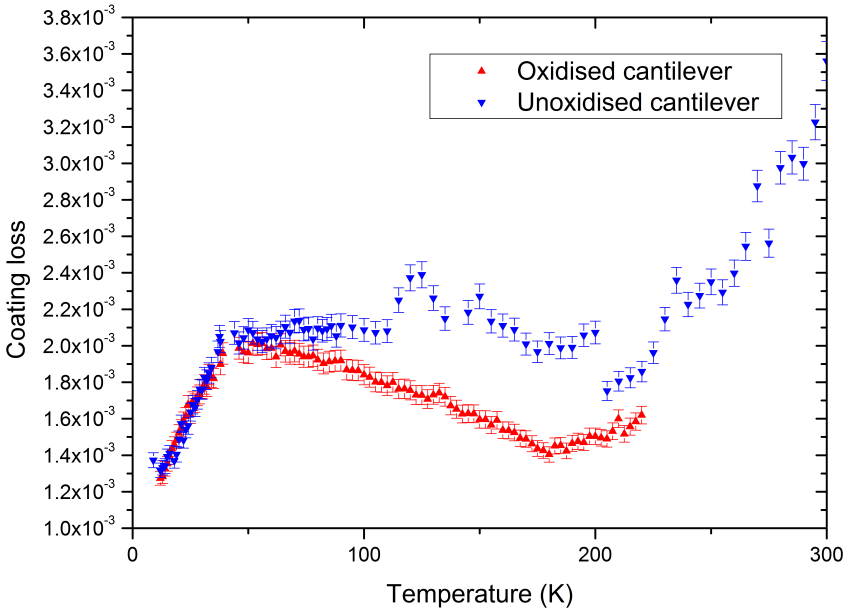

Fig. B.10 A comparison of the mechanical loss of an ALD tantala coating as measured using cantilevers with different surface oxide thicknesses. The coating loss from measurements of mode 9 are shown.

Appendix C

Coating mechanical loss, sample geometry and film thickness

As discussed in Chapter 5, mechanical loss measurements carried out by the commercial coating vendor LMA [153] suggest possible discrepancies between the coating loss exhibited by a coating when measured on different substrate geometries [154]. Measurements were carried out to determine the coating loss of the Advanced LIGO ITM coating using a cantilever. These measurements found that the coating loss was higher than expected, by a factor of approximately 1.6 [154]. In order to verify this result, the ITM coating was deposited upon a silica disk (the same disk used for studies of the ITM coating used in Chapter 5, where further sample details are given), and a silicon wafer of 5 cm diameter and 450 μm thick [154]. Measurements of the ITM coating on a disk showed that the coating loss was lower than the coating loss from cantilever measurements by a factor of approximately 1.4 [154]. These studies suggested that further examination of the coating loss exhibited by coatings deposited on cantilevers and disks should be carried out.

In this appendix, the mechanical loss of a coating deposited on two cantilevers and two disks is studied. One cantilever and one disk were chosen to have a coating, which may be considered to be negligably thin with respect to the cantilever and the disk thicknesses, deposited upon them. The other disk and cantilever had a coating which may be considered to be negligably thin with respect to the disk substrate, but not with respect to the cantilever substrate. This allows a cross-geometry test as well as a check that the film thickness does not affect loss measurements, when made using a cantilever.

This is important for measurements of thick coatings such as those studied in Chapter 5.

C.1 Coating loss measurements using disks and cantilevers

The mechanical losses of two uncoated silica cantilevers and two uncoated silica disks were measured. The silica disks were 76.2 mm in diameter and 1.7 mm thick. The flexing part of the cantilevers were 148 μm and 164 μm thick. One cantilever and one disk was coated with a 0.5 μm thick layer of niobia (Nb_2O_5). This sample set represents the case where the coating can be considered to be of negligable thickness compared to both substrates. The coatings were deposited at the University of the West of Scotland by a DC magnetron process.

The other cantilever and disk were coated with a 5 μm thick niobia coating by an identical process. This sample set represents the case where the coating may be considered negligably thin compared to the disk, but not compared to the cantilever.

C.1.1 Cantilever measurements

The mechanical losses of the two silica cantilevers were measured prior to coating. The mechanical loss of the cantilever with the 0.5 μm coating is shown in figure C.1, along with the loss of the cantilever prior to coating. The loss of the second and fifth modes are higher the level of loss exhibited by the other modes. This could be excess loss into the clamp. However, the excess loss is exhibited both before and after coating, suggesting that the excess loss may be due to a more permanent feature of the cantilever, such as the weld.

The mechanical loss of the cantilever with the 5 μm thick coating is shown in figure C.2, along with the loss of the cantilever prior to coating. For cantilever bending modes 1-4, the loss of the uncoated cantilever is lower than that of the coated cantilever by a factor of around 10 or more. In this range, the coated cantilever shows a consistent level of loss of 8-10$\times 10^{-5}$. For modes 5-7, the loss of the uncoated cantilever is considerably higher than at low frequencies. The loss of the uncoated cantilever exhibits a peak at the sixth mode which is also featured in the loss of the coated cantilever.

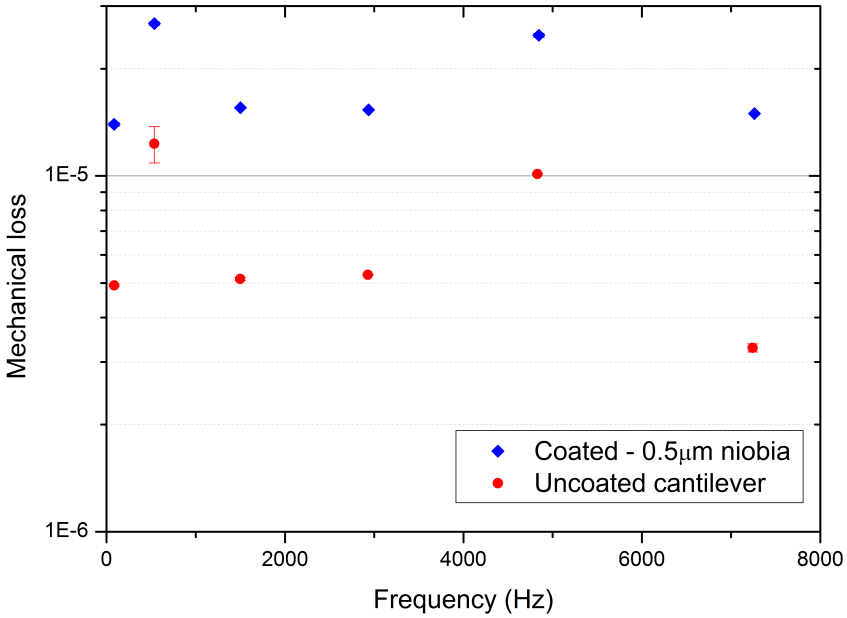

Fig. C.1 The mechanical loss of a silica cantilever before and after the application of a 0.5 μm thick niobia layer.

The coating loss of the 0.5 μm coating was calculated using equations 3.7 and 3.8, where the cantilever thickness was calculated to be 148 μm from the resonant frequencies. The Young's modulus of niobia was taken to be 100 GPa [180], and the Young's modulus of silica to be 72 GPa. For the cantilever with a thin coating, the energy ratio is 67.3.

The ratio of elastic energy stored in the cantilever substrate to that stored in the 5 μm was calculated using finite element analysis. In this case the ratio $\frac{E_{cc}}{E_s}$ was calculated to be 8.91. The coating losses of both the 0.5 μm and 5 μm are shown in figure C.3.

The mechanical loss exhibited by the 0.5 μm thick coating ranges from 6.1×10^{-4} to 9.9×10^{-4}, with a mean of 7.9×10^{-4} and a standard deviation of 1.6×10^{-4}. The coating shows some scatter, with no clear frequency dependence. The mechanical loss of the 5 μm thick coating shows similar scatter to that of the 0.5 μm coating. The mean loss exhibited by the thicker coating was 8.3×10^{-4} with a standard deviation of 3.4×10^{-4}. This value agrees within error with that exhibited by the thinner coating. From these measurements, it appears that the mechanical loss exhibited by the coating is independent of coating thickness when measured using cantilevers.

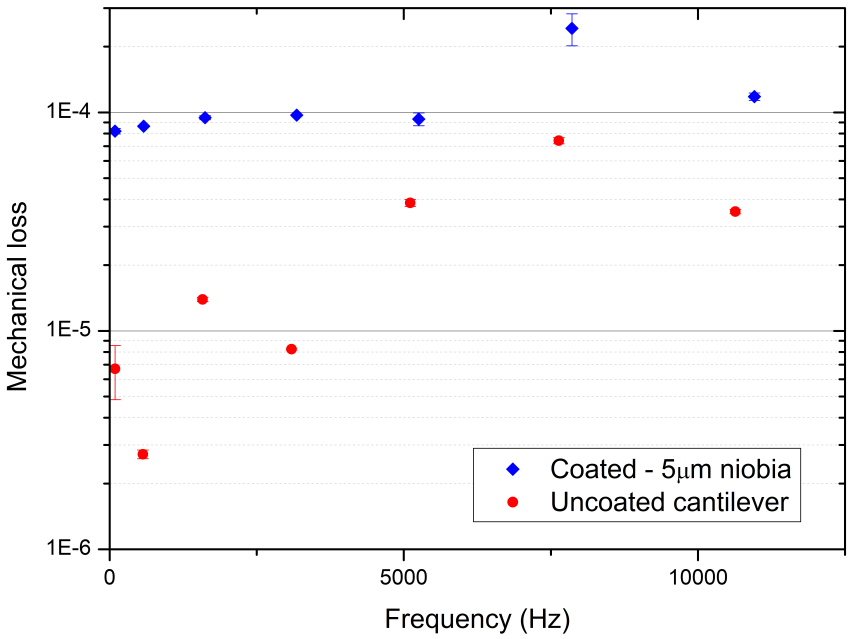

Fig. C.2 The mechanical loss of a silica cantilever before and after the application of a 5 μm thick niobia layer.

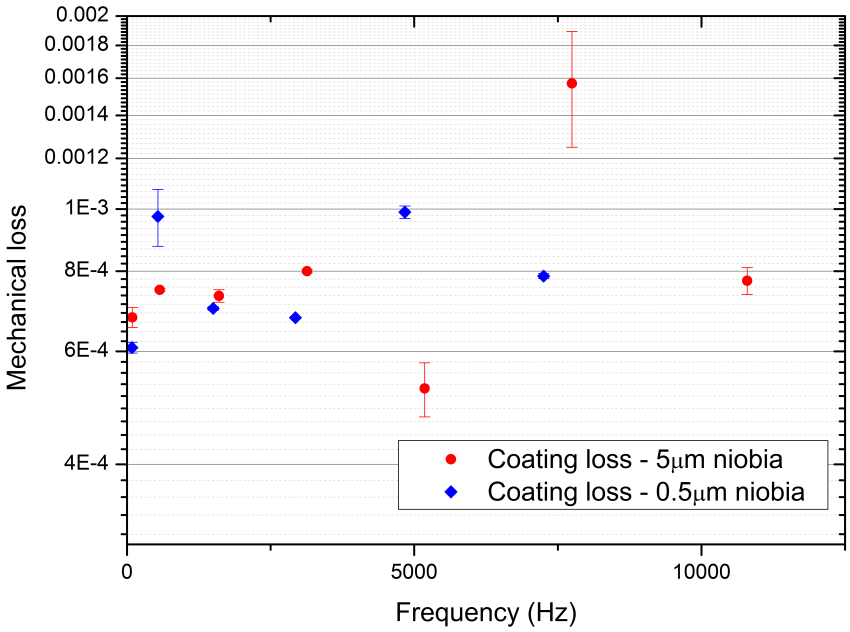

Fig. C.3 The coating losses of a 0.5 μm and a 5 μm thick niobia coating exhibited on silica cantilevers.

C.1.2 Disk measurements

The mechanical losses of the one of the silica disks with flame polished edges were measured prior to coating using the nodal suspension technique with an interferometric displacemtn readout. The mechanical loss of the disk with a 0.5 µm thick coating is shown in figure C.4, along with the coating loss of the disk prior to coating. The loss of the uncoated substrate is very low, with many modes exhibiting losses of 1×10^{-7} and below. This low level of substrate loss gives silica disks high sensitivity to coating loss, with the mechanical loss of the coated disk a factor of around 10 greater than that of the substrate.

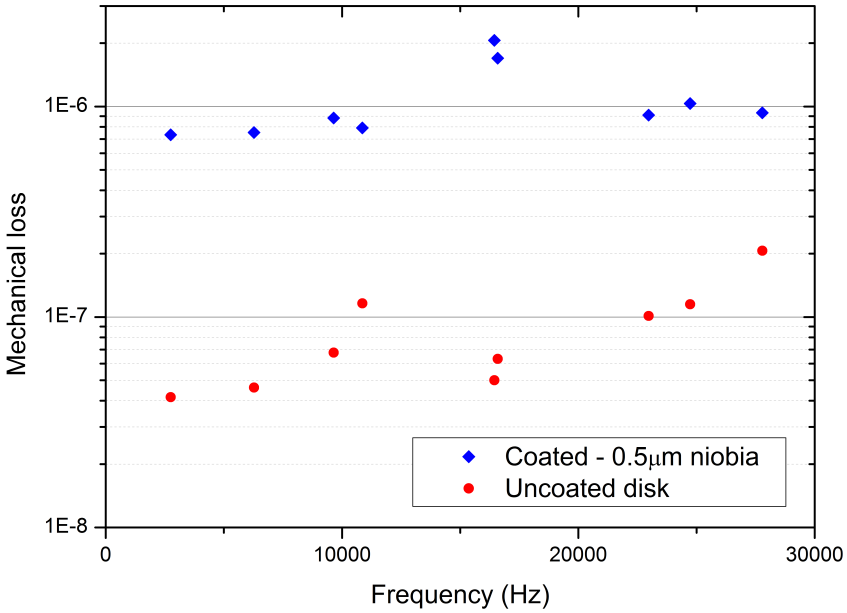

Fig. C.4 The mechanical loss of a silica disk before and after the application of a 0.5 µm thick niobia layer.

The mechanical loss of the disk with a 5 µm thick coating is shown in figure C.5, along with the loss of the uncoated substrate, which is assumed to have an identical loss to that of the first disk. The loss of the coated disk is a factor of over 100 higher than that of the substrate for some modes.

The mechanical loss of each coating was calculated using equation 3.7, and the ratio of elastic energy stored in the coating to that stored in the substrate was evaluated using an FEA model. The energy ratio takes different values for each mode, and are catalogued for each sample in table C.1. The coating losses of the thin and thick niobia coatings are shown in figure C.6. The coating loss of the 0.5 µm thick coating exhibits a loss consistently under 1×10^{-4}, apart

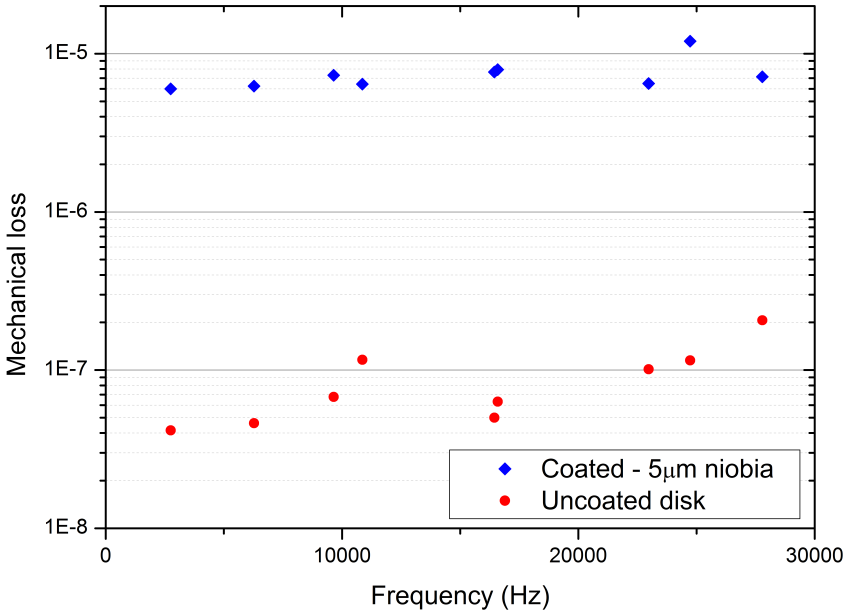

Fig. C.5 The mechanical loss of a silica disk before and after the application of a 5 μm thick niobia layer.

from two modes. These modes are likely to be limited by suspension losses. Excluding the two suspension limited modes, the 0.5 μm thick coating exhibits a mean loss of 8.8×10^{-4} with a standard deviation of 0.9×10^{-4}. The mean loss of the 5 μm thick coating is 8.8×10^{-4}, with a standard deviation of 1.7×10^{-4}. This agrees very well with the coating loss of the thin coating as measured on the disk. The coating loss of the thicker coating appears lower than the thin coating across all modes, apart from one, which increases the loss and the standard deviation of the results. However, the spread of the results from the half-micron coating would be larger if the suspension-limited modes are included. These results suggest that a thicker coating may be beneficial when measuring coating loss using a disk, since the thick coating provides a higher sensitivity to the coating loss by decreasing the energy storage ratios of all modes. The loss of both coatings show no clear frequency dependence.

The mechancal losses of all four niobia coatings, as measured on disks and cantilevers, are shown in figure C.7. The coatings deposited on cantilevers exhibit the lower average loss than the coatings deposited on disks, but the thick coating on a cantilever exhibits the largest spread in coating losses. However, that may be due in part to the high loss of the substrate used for that particular coating. The losses of all four coatings agree within error. The

Niobia energy storage ratios E_s/E_c		
Frequency (kHz)	0.5 μm	5 μm
2.7	1300	136
6.3	1256	131
9.6	992	104
10.9	1234	129
16.4	1224	128
16.6	1044	109
23.0	1222	127
24.7	1078	112
27.8	1042	107

Table C.1 The elastic energy ratios used to calculate the mechanical loss of the 0.5 μm and 5 μm thick niobia coatings.

half micron coating measured on a cantilever exhibits the lowest loss, but the half micron coating on a disk exhibits the smallest spread in results. From these measurements, it can be concluded that the mechanical loss of this niobia coating is independent of substrate geometry and coating thickness.

The studies carried out here are of a DC magnetron coating which exhibits a relatively high loss compared to the IBS coatings used in gravitational wave detector mirror coatings. Further investigations should be carried out in order to verify that the same result is obtained for a lower loss coating, and for coatings more similar to those of gravitational wave detector mirrors.

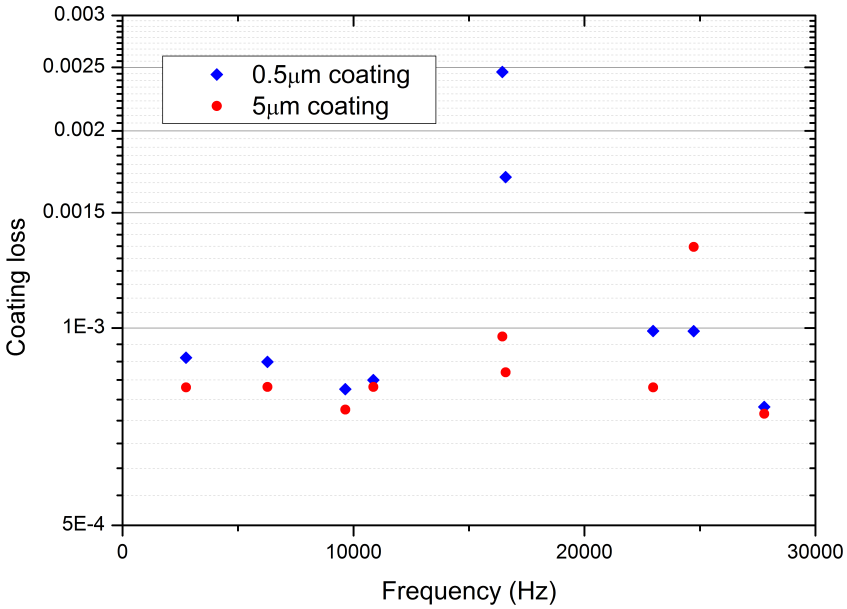

Fig. C.6 The coating losses of a 0.5 µm and a 5 µm thick niobia coating exhibited on silica cantilevers.

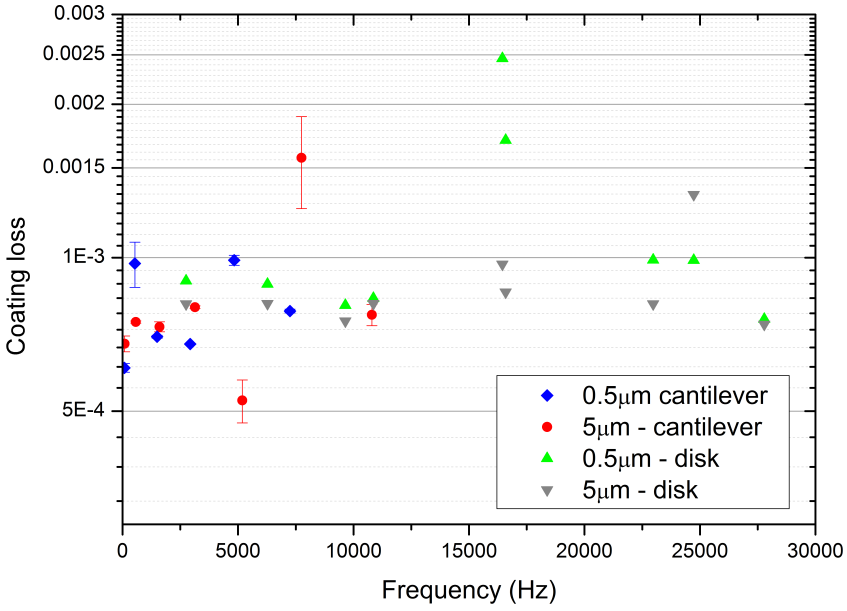

Fig. C.7 The coating losses of a 0.5 µm and a 5 µm thick niobia coating exhibited on silica cantilevers and disks.

Appendix D

The mechanical loss of a thermally cycled bonded cantilever

D.1 Introduction

In the Advanced LIGO interferometers, hydroxide-catalysis bonding was used to attach 'ears' onto the side of the test-masses, and the supporting fused silica suspension elements were then welded to the ears [181, 182]. Additionally, cryogenic detectors such as the Einstein Telescope [19] and KAGRA [59] detector projects may use this bonding technique in the assembly of their respective suspension systems. The thin bond layers between the ears and the test-mass substrates have a non-zero mechanical loss and will therefore contribute to the thermal noise of the detectors. It is therefore of interest to measure the mechanical loss of a hydroxide-catalysis bond, particularly at cryogenic temperatures. Since the mirrors of these cryogenic gravitational wave detectors will likely be thermally cycled between room temperature and their respective operating temperatures several times during the span of each detector project, it is also of interest to investigate the effect of thermal cycling on the dissipation of a bonded system.

To facilitate a loss measurement of a hydroxide-catalysis bond, two silicon cantilevers, with thicknesses 26μm and 66μm were bonded together. The details of the bonding procedure may be found in [183]. A study by Beveridge

placed an upper limit on the mechanical loss of the bond layer of 0.17 ± 0.004 at temperatures below 75 K [183]. The minimum loss obtained for the bond layer was 0.04 ± 0.008, which was observed at 20 K [183]. However, the effect of thermal cycling on the dissipation of the bond layer is unknown. Hence, the bonded cantilever studied by Beveridge was remeasured, in order to investigate the effect of thermal cycling on the bonded cantilever.

D.2 Measurements and results

During the study carried out by Beveridge, the bonded cantilever underwent one thermal cycle [183]. For the purpose of this investigation, the mechanical loss at cryogenic temperatures was measured a further four times. The mechanical losses measured for the second to fourth bending modes are shown in figures D.1, D.2 and D.3 in order of increasing frequency. For all modes, it can be seen that the results of cycle 1 and cycle 2 agree in the temperature range 10-100 K. The results of cycle 1 shows excess loss compared to cycle 2 for modes 2 and 4 in the range 100-225 K. For mode 2, the additional temperature cycles have little effect, although additional loss can be seen in after 4 cycles throughout the temperature range. For modes 3 and 4, the effect is more pronounced with the loss increasing after 3 cycles, and increasing further after 4 cycles. From these results, it was postulated that thermal cycling may act to degrade hydroxide-catalysis bonds.

D.3 Discussion

From the increase observed in the mechanical loss of the bonded cantilever studied here, it is likely that the bond layer has degraded with thermal cycling. The bonded cantilever studied here is known to feature several air bubbles in the bond layer [183]. It is of interest to study the effect of thermal cycling on a bonded system with no such defects in order to determine whether or not the mechanical loss of an ideal bond will resist degradation.

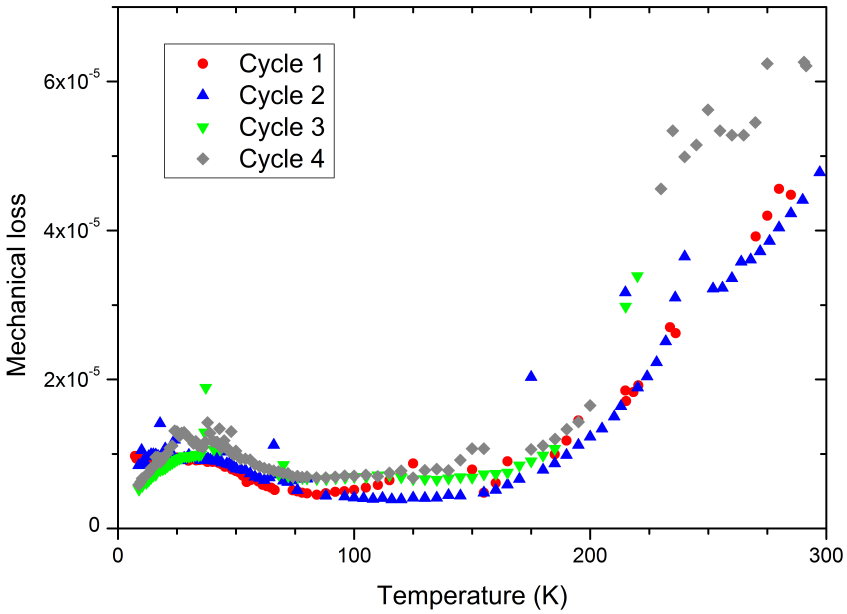

Fig. D.1 The mechanical loss of two silicon cantilevers bonded together. Here, the loss of the 736 Hz bending mode is shown.

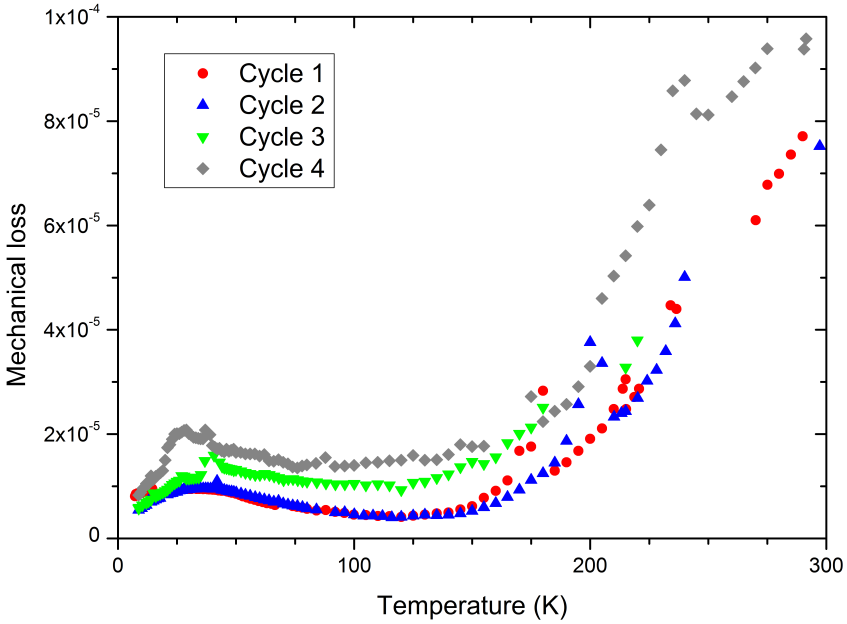

Fig. D.2 The mechanical loss of two silicon cantilevers bonded together. Here, the loss of the 2.1 kHz bending mode is shown.

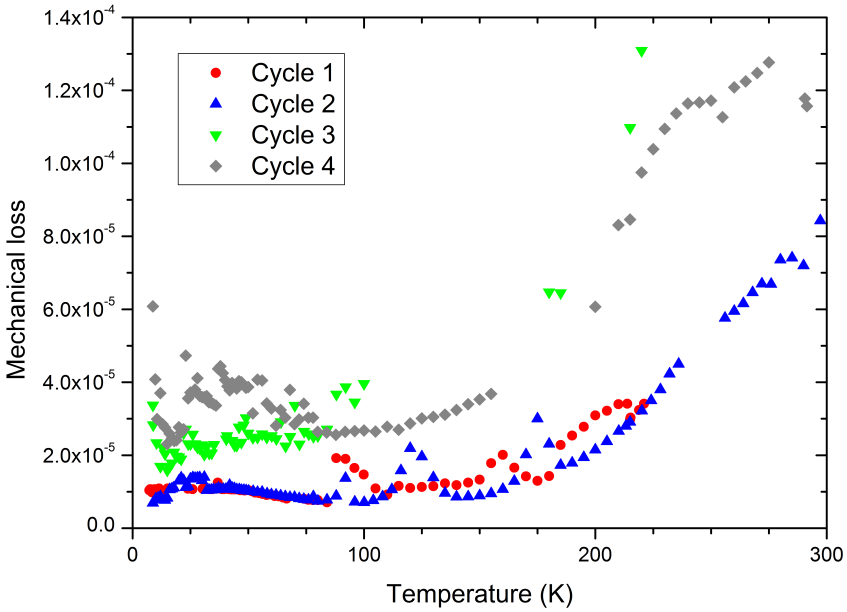

Fig. D.3 The mechanical loss of two silicon cantilevers bonded together. Here, the loss of the 4.2 kHz bending mode is shown.

Bibliography

[1] Picture courtesy of www.ligo.org.

[2] S. Hild. *Beyond the second generation of laser-interferometric gravitational wave observatories. Classical and Quantum Gravity*, 29(124006), 2012.

[3] A. V. Cumming. *Aspects of mirrors and suspensions for advanced gravitational wave detectors.* PhD thesis, University of Glasgow, 2008.

[4] I. W. Martin, R. Bassiri, R. Nawrodt, M. M. Fejer, et al. *Effect of heat treatment on mechanical dissipation in Ta 2 O 5 coatings. Classical and Quantum Gravity*, 27(22):225020, 2010.

[5] C. Zener. *Internal Friction in Solids I. Theory of Internal Friction in Reeds. Phys. Rev.,*, 52(3):230–235, Aug 1937.

[6] M. R. Abernathy, S. Reid, E. Chalkley, R. Bassiri, et al. *Cryogenic mechanical loss measurements of heat-treated hafnium dioxide. Classical and Quantum Gravity*, 28(19):195017, 2011.

[7] B. S. Berry and W. C. Pritchet. *Vibrating reed internal friction apparatus for films and foils. IBM J. Res. Dev.*, **19**:334, 1975.

[8] S. Barta. *Effective Young';s modulus and Poisson's ratio for the particulate composite. Journal of Applied Physics*, 75(7):3258–3263, Apr 1994.

[9] A. Einstein. *Die Grundlage der allgemein Relativitatstheorie. Annalen der Physik*, 49:769, 1916.

[10] P. R. Saulson. *Fundamentals of Interferometric Gravitational Wave Detectors.* World Scientific, Singapore, 1994.

[11] J. Weber. *Detection and generation of gravitational waves. Physical Review*, 117:306–313, 1960.

[12] R. L. Garwin and J. L. Levine. *Single gravity-wave detector results contrasted with previous coincident detections.* 31:176–180, 1973.

[13] J. H. Taylor, L. A. Fowler, and P. M. McCulloch. *Measurements of general relativistic effects in the binary pulsar PSR 1913 + 16. Nature*, 277:437–440, 1979.

[14] J. H. Taylor and J. M. Weisberg. *A new test of general relativity - Gravitational radiation and the binary pulsar PSR 1913+16. The Astrophysical Journal*, 253:908–920, 1982.

[15] J. M. Weisberg and J. H. Taylor. *Relativistic binary pulsar B1913+16: Thirty years of observations and analysis.* In F A Rasio and I H Stairs, editors, *Binary Radio Pulsars: Proc. Aspen Conference*, volume 328, pages 25–31, 2004.

[16] R. A. Hulse and J. H. Taylor. *Discovery of a pulsar in a binary system. The Astrophysical Journal*, 195:L51–L53, 1975.

[17] J. H. Taylor, R. A. Hulse, L. A. Fowler, G. E. Gullahron, and J. M. Rankin. *Further observations of the binary pulsar PSR 1913 + 16. The Astrophysical Journal*, 206:L53–L58, 1976.

[18] R P Feynman, F B Moriniga, and W G Wagner. *Feynman lectures on gravitation.* Westview, Boulder, CO, 2003.

[19] The ET Science Team. *Einstein gravitational wave telescope conceptual design study.* ET technical document number ET-0106A-10, 2011.

[20] B. F. Schutz. *Gravitational-wave sources. Class. Quantum Grav.*, 13:A219–A238, 1996.

[21] C. Messenger and G. Woan. *A fast search strategy for gravitational waves from low-mass X-ray binaries. Classical and Quantum Gravity*, 24(S469), 2007.

[22] L. Lindblom, B. J. Owen, and G. Ushomirsky. *Effect of a neutron-star crust on the r-mode instability. Physical Review D*, 62((8):084030), 2000.

[23] Y. Wu, C. D. Matzner, and P. Arras. *R-modes in neutron stars with crusts: turbulent saturation, spin-down, and crust melting. The Astrophysical Journal*, 549:1011–1020, 2001.

[24] C. Cutler. *Gravitational waves from neutron stars with large toroidal B fields. Physical Review D*, 66(8)(084025), 2002.

[25] B. S. Sathyaprakash and B. F. Schutz. *Physics, astrophysics and cosmology with gravitational waves. Living Reviews in Relativity*, 12(2), 2009.

[26] K. S. Thorne. *Gravitational radiation. Annals of the New York Academy of Sciences*, 759:127–152, 1995.

[27] J. Abadie, B. Abbott, R. Abbott, M. R. Abernathy, et al. *Beating the spin-down limit on gravitational wave emission from the Vela pulsar. The Astrophysical Journal*, 737(2):93, 2011.

[28] J. Abadie, B. Abbott, R. Abbott, M. R. Abernathy, et al. *First search for gravitational waves from the youngest known neutron star. The Astrophysical Journal*, 722(2):1504–1513, 2010.

[29] B. Abbott, R. Abbott, R. Adhikari, P. Ajith, et al. *Beating the spin-down limit on gravitational wave emission from the Crab pulsar. The Astrophysical Journal Letters*, 638(1):L45, 2008.

[30] B. P. Abbott, R. Abbott, R. Adhikari, P. Ajith, B. Allen, G. Allen, et al. *LIGO: The laser interferometer gravitational wave observatory. Reports on Progress in Physics*, 72:076901, 2009.

[31] B. F. Schutz. *A first course in general relativity.* Cambridge University Press, Cambridge, 1985.

[32] B. F. Schutz. *Determining the Hubble constant from gravitational wave observations. Nature*, 323((6086)):310–311, 1986.

[33] B. P. Abbott, R. Abbott, F. Acernese, R. Adhikari, P. Ajith, B. Allen, et al. *An upper limit on the stochastic gravitational wave background of cosmological origin. Nature*, 460(990-994), 2009.

[34] B. Abbott, R. Abbott, R. Adhikari, J. Agresti, et al. *Searching for a stochastic background of gravitational waves with the laser interferometer gravitational-wave observatory. The Astrophysical Journal*, 659:918–930, 2007.

[35] R. L. Forward, D. Zipoy, J. Weber, S. Smith, et al. *Upper limit for interstellar millicycle gravitational radiation. Nature*, 189(473), 1961.

[36] J. Weber. *Observation of the thermal fluctuations of a gravitational-wave detector. Phys. Rev. Lett.*, 20(1307-1308), 1968.

[37] J. L. Levine and R. L. Garwin. *Absence of gravity-wave signals in a bar at 1695 Hz. Phys. Rev. Lett.*, 31:173–176, 1973.

[38] J. A. Tyson. *Null search for bursts of gravitational radiation. Phys. Rev. Lett.*, 31:326–329, 1973.

[39] V. B. Braginsky, A. B. Manukin, E. I. Popov, V. N. Rudenko, et al. *Upper limit of the density of extraterrestrial gravitational radiation. Soviet Physics*, JETP 39:387, 1974.

[40] R. W. P. Drever, J. Hough, R. Bland, and G. W. Lessenhoff. *Search for short bursts of gravitational radiation. Nature*, 246:340–344, 1973.

[41] I. S. Heng, E. Daw, J. Giaime, W. O. Hamilton, et al. *Allegro: noise performance and the ongoing search for gravitational waves. Classical and Quantum Gravity*, 19:1889–1895, 2002.

[42] A. Vinante, R. Mezzena, G. A. Prodi, S. Vitale, et al. *Thermal noise in a high Q ultracryogenic resonator. Rev. Sci. Instrum.*, 76(074501), 2005.

[43] M. E. Gertsenshtein and V. I. Pustovoit. *On the detection of low frequency gravitational waves. Soviet Physics*, JETP 16:433, 1962.

[44] R. Weiss. *Electromagnetically coupled broadband gravitational wave antenna. Quarterly Progress Report 105, Electronics Research Laboratory, MIT*, 1972.

[45] G. E. Moss, L. R. Miller, and R. L. Forward. *Photon-noise-limited laser transducer for gravitational wave antenna. Applied Optics*, 10(2495), 1971.

[46] R. L. Forward. *Wideband laser-interferometer gravitational-radiation experiment. Physical Review D*, 17:379–390, 1978.

[47] H. Billing, K. Maischberger, A. Rudiger, R. Schilling, et al. *An argon laser interferometer for the detection of gravitational radiation. Journal of Physics E: Scientific Instruments*, 12:1043–1050, 1979.

[48] R. W. P. Drever, J. R. Pugh, W. A. Edelstein, H. Ward, et al. In *Proceedings of the Royal Society of London*, volume A368, pages 11–18, 1979.

[49] H. Ward, J. Hough, G P Newton, B. J. Meers, et al. *Laser interferometric sensing techniques for very small displacements with applications to gravitational radiation detectors. IEEE Transactions on Instrumentation and Measurement*, 34:261–265, 1985.

[50] R. L. Ward, R. Adhikari, B. Abbott, R. Abbott, D. Barron, R. Bork, T. Fricke, V. Frolov, J. Heefner, A. Ivanov, O. Miyakawa, K. McKenzie, B. Slagmolen, M. Smith, R. Taylor, S. Vass, S. Waldman, and A. Weinstein. dc readout experiment at the caltech 40m prototype interferometer. *Classical and Quantum Gravity*, 25(11):114030, 2008.

[51] P. Fritschel, G. Gonzalez, B. Lantz, P. Saha, and M. Zucker. *High Power Interferometric Phase Measurement Limited by Quantum Noise and Application to Detection of Gravitational Waves. Phys. Rev. Lett.*, 80(15):3181–3184, 1998.

[52] D. Shoemaker, R. Schilling, L. Schnupp, W. Winkler, et al. *Noise behaviour of the Garching 30-meter prototype gravitational-wave detector. Physical Review D*, 38:423–432, 1988.

[53] M. Beccaria et al. *Relevance of Newtonian seismic noise for the VIRGO interferometer sensitivity. Classical and Quantum Gravity*, 15:3339–3362, 1998.

[54] N. A. Robertson, G. Cagnoli, D. R. M. Crooks, E. Elliffe, J. Faller, P. Fritschel, et al. *Quadruple suspension design for advanced LIGO. Classical and Quantum Gravity*, 19(4043), 2002.

[55] M. V. Plissi, C. I. Torrie, M. E. Husman, N. A. Robertson, K. A. Strain, H. Ward, et al. *GEO 600 triple pendulum suspension system: Seismic isolation and control. Rev. Sci. Instrum.*, 71:2539–2545, 2000.

[56] S. Braccini, C. Casciano, F. Cordero, F. Corvace, M. De Sanctis, R .Franco, et al. *The maraging-steel blades of the Virgo super attenuator. Measurement Science and Technology*, 11:467–476, 2000.

[57] P. R. Saulson. *Terrestrial gravitational noise on a gravitational wave antenna. Physical Review D*, 30:732–736, 1984.

[58] S. A. Hughes and K. S. Thorne. *Seismic gravity-gradient noise in interferometric gravitational-wave detectors. Physical Review D*, 58(122002), 1998.

[59] K. Somiya. *Detector configuration of KAGRA–the Japanese cryogenic gravitational-wave detector. Classical and Quantum Gravity*, 29(12):124007, 2012.

[60] K. Danzmann, T. A. Prince, P. Binetruy, P. Bender, S. Buchman, J. Centrella, et al. *LISA Unveiling a hidden Universe. Technical Report ESA/SRE(2011)3*, 2011.

[61] A.S. Nowick and B.S. Berry. *Anelastic Relaxation in Crystalline Solids*. Academic Press, New York, 1972.

[62] K. Kawabe and The LIGO Scientific Collaboration. *Status of LIGO. Journal of Physics Conference Series*, 120(032003), 2008.

[63] P. Amico, L. Bosi, L. Carbone, L. Gammaitoni, et al. *Fused silica suspension for the VIRGO optics: status and perspectives. Classical and Quantum Gravity*, 19(1669-1674), 2002.

[64] G. Cagnoli and P. A. Willems. *Effects of nonlinear thermoelastic damping in highly stressed fibers. Phys. Rev. B*, 65:174111, Apr 2002.

[65] C. J. Bell, S. Reid, J. Faller, G. D. Hammond, J. Hough, I. W. Martin, S. Rowan, and K. V. Tokmakov. *Experimental results for nulling the effective thermal expansion coefficient of fused silica fibres under a static stress. Classical and Quantum Gravity*, 31(6):065010, 2014.

[66] W. A. Edelstein, J. Hough, J. R. Pugh, and W. Martin. *Limits to the measurement of displacement in an interferometric gravitational radiation detector. Journal of Physics E: Scientific Instruments*, 11(7):710, 1978.

[67] M. Pitkin, S. Reid, S. Rowan, and J. Hough. *Gravitational Wave Detection by Interferometry (Ground and Space). Living Reviews in Relativity*, 14(5), 2011.

[68] C. M. Caves. *Quantum-mechanical noise in an interferometer. Physical Review D*, 23:1693–1703, 1981.

[69] C. M. Caves. *Quantum-mechanical radiation-pressure noise fluctuations in an interferometer. Physical Review D*, 45:75–79, 1980.

[70] V. Henning, S. Chelkowski, B. Hage, A. Franzen, K. Danzmann, and R. Schnabel. *Coherent control of vacuum squeezing in the gravitational-wave detection band. Phys. Rev. Lett.*, 97(011101), 2006.

[71] Gregory M Harry and the LIGO Scientific Collaboration. *Advanced LIGO: the next generation of gravitational wave detectors. Classical and Quantum Gravity*, 27(8):084006, 2010.

[72] R. W. P. Drever et al. *Gravitational wave detectors using laser interferometers and optical cavities: Ideas, principles and prospects.* In P Meystre and M O Scully, editors, *Quantum optics. Experimental gravity, and measurement theory*, Series B: Physics, Proceedings of the NATO Advanced Study Institute held in Bad Windsheim, Germany, August 16-29, 1981. NATO Advanced Science Institutes (ASI), New York: Plennum Press, 1983.

[73] B. J. Meers. *Recycling in laser-interferometric gravitational-wave detectors. Physical Review D*, 38:2317–2326, 1988.

[74] K. A. Strain and B. J. Meers. *Experimental demonstration of dual recycling for interferometric gravitational-wave detectors. Phys. Rev. Lett.*, 66:1391–1394, 1991.

[75] G. Heinzel, K. A. Strain, J. Mizuno, K. D. Skeldon, B. Willke, W. Winkler, R. Schilling, A. Rudiger, and K. Danzmann. *Experimental demonstration of a suspended dual recycling interferometer for gravitational wave detection. Phys. Rev. Lett.*, 81:5493–5496, 1998.

[76] H. Grote and D. H. Reitze. *First generation interferometric gravitational-wave detectors.* In *Proceedings of the 46th Recontres de Moriond QCD and High Energy Interactions Conference*, 2011.

[77] G. Ballardin, L. Bracci, S. Braccini, C. Bradaschia, et al. *Measurement of the VIRGO superattenuator performance for seismic noise suppression. Rev. Sci. Instrum.*, 72(9):3643–3652, 2001.

[78] The Virgo Collaboration. *Advanced Virgo baseline design.* note VIR-027A-09, May 2009.

[79] H. Grote and The LIGO Scientific Collaboration. *The GEO 600 status. Classical and Quantum Gravity*, 27(8):084003, 2010.

[80] B. Willke et al. *The GEO-HF project. Classical and Quantum Gravity*, 23:S207, 2006.

[81] R. Takahashi and the TAMA Collaboration. *Operational status of TAMA300. Classical and Quantum Gravity*, 20(17):S593, 2003.

[82] R. Takahashi and the TAMA Collaboration. *Status of TAMA300. Classical and Quantum Gravity*, 21(5)(S403), 2004.

[83] K. Arai, R. Takahashi, D. Tatsumi, K. Izumi, the CLIO Collaboration, and the LCGT Collaboration. *Status of Japanese gravitational wave detectors. Classical and Quantum Gravity*, 26(20)(204020), 2009.

[84] T. Uchiyama, S. Miyoki, S. Telada, K. Yamamoto, M. Ohashi, K. Agatsuma, K. Arai, M.-K. Fujimoto, T. Haruyama, S. Kawamura, O. Miyakawa, N. Ohishi, T. Saito, T. Shintomi, T. Suzuki, R. Takahashi, and D. Tatsumi. Reduction of thermal fluctuations in a cryogenic laser interferometric gravitational wave detector. *Phys. Rev. Lett.*, 108:141101, Apr 2012.

[85] K. Kuroda and the LCGT Collaboration. *Status of LCGT. Classical and Quantum Gravity*, 27(8)(084004), 2010.

[86] G.M. Harry, A.M. Gretarsson, P. R. Saulson, S.E. Kittelberger, et al. *Thermal noise in interferometric gravitational wave detectors due to dielectric optical coatings. Class. Quantum Grav.*, **19**:897–917, 2002.

[87] M. Evans, S. Ballmer, M. M. Fejer, P. Fritschel, G. Harry, and G. Ogin. *Thermo-optic noise in coated mirrors for high-precision optical measurements. Physical Review D*, 78(102003), 2008.

[88] G. D. Cole, W. Zhang, M. J. Martin, J. Ye, and M. Aspelmeyer. *Tenfold reduction of Brownian noise in high-reflectivity optical coatings. Nature Photonics*, 7:644–650, 2013.

[89] R. Brown. *A Brief account of microscopical observations made in the months of June, July and August 1827 on the particles contained in the pollen of plants. The Philisophical Magazine and Annals of Philosophy, new series*, 4(21), 1828.

[90] A. Einstein. *Uber die von der molekularkinetischen Theorie der Warme geforderte Bewegung von in ruhenden Flussigkeiten suspendierten Teilchen. Annalen der Physik*, 322(8):549–560, 1905.

[91] HB Callen and RF Greene. *On the theorem of irreversible thermodynamics. Physical Review*, 86(702-710), 1952.

[92] P. R. Saulson. *Thermal noise in mechanical experiments. Physical Review D*, 42:2437–2445, 1990.

[93] C. M. Zener. *Elasticity and anelasticity of metals. University of Chicago Press*, 1948.

[94] C. Zener. *Internal friction in solids II. General theory of thermoelastic internal friction. Physical Review*, 53(90-99), 1938.

[95] A. Gillespie and F. Raab. *Thermally excited vibrations of the mirrors of laser interferometer gravitational-wave detectors. Physical Review D*, 52(577), 1995.

[96] Y. Levin. *Internal thermal noise in the LIGO test masses: A direct approach. Phys. Rev. D*, **57**(2):659, 1998.

[97] K. Yamamoto. *Study of the thermal noise caused by inhomogeneously distributed loss.* PhD thesis, University of Tokyo, 2000.

[98] S. Rowan, J. Hough, and D. R. M. Crooks. *Thermal noise and material issues for gravitational wave detectors. Phys. Lett. A*, 347(1-3):25–32, 2005.

[99] F. Bondu, P. Hello, and J.-Y. Vinet. *Thermal noise in mirrors of interferometric gravitational wave antennas. Physical Letters A*, 246(3-4):227–236, 1998.

[100] Y. T. Liu and K. S. Thorne. *Thermoelastic noise and homogeneous thermal noise in finite sized gravitational-wave test masses. Physical Review D*, 62(122002), 2000.

[101] N. Nakagawa, A. M. Gretarsson, E. K. Gustafson, and M. M. Fejer. *Thermal noise in half-finite mirrors with nonuniform loss: A slab of excess loss in a half-infinite mirror. Physical Review D*, 65:102001, 2002.

[102] V. B. Braginsky and S. P. Vyatchanin. *Thermodynamical fluctuations in optical mirror coatings. Physics Letters A*, 312(3-4)(244-255), 2003.

[103] M. M. Fejer, S. Rowan, G. Cagnoli, D. R. M. Crooks, A. Gretarsson, G. M. Harry, J. Hough, S. D. Penn, P. H. Sneddon, and S. P. Vyatchanin. *Thermoelastic dissipation in inhomogeneous media: loss measurements and displacement noise in coated test masses for interferometric gravitational wave detectors. Physical Review D*, 70(082003), 2004.

[104] V. B. Braginsky, M. L. Gorodetsky, and S. P. Vyatchanin. *Thermo-refractive noise in gravitational wave antennae. Physics Letters A*, 372(12):1941–1944, 2000.

[105] G. M. Harry, M. R. Abernathy, A. E. Becerra-Toledo, H. Armandula, et al. *Titania-doped tantala/silica coatings for gravitational-wave detection. Class. Quantum Grav.*, **24**:405–415, 2007.

[106] R Flaminio, J Franc, C. Michel, N. Morgado, et al. *A study of coating mechanical and optical losses in view of reducing mirror thermal noise in gravitational wave detectors. Class. Quantum Grav.*, 27(8):084030, 2010.

[107] M. Granata, K. Craig, G. Cagnoli, C. Carcy, et al. *Cryogenic measurements of mechanical loss of high-reflectivity coating and estimation of thermal noise. Opt. Lett.*, 38(24):5268–5271, Dec 2013.

[108] R. P. Netterfield, M. Gross, F. N. Baynes, K. L. Green, et al. *Low mechanical loss coatings for LIGO optics: progress report. Proc. SPIE*, **5870**(1):58700H, 2005.

[109] Krishna Seshan, editor. *Handbook of thin-film deposition processes and techniques - principles, methods, equipment and applications*. William Andrew Publishing/Noyes, Norwich, NY, 2002.

[110] R. W. Johnson, A. Hultqvist, and S. F. Bent. A brief review of atomic layer deposition: from fundamentals to applications. *Materials Today*, 17(5):236 – 246, 2014.

[111] P.J Kelly and R.D Arnell. *Magnetron sputtering: a review of recent developments and applications. Vacuum*, 56(3):159 – 172, 2000.

[112] P. H. Sneddon. *Investigations of internal mechanical loss factors of test mass materials for interferometric gravitational wave detectors*. PhD thesis, University of Glasgow, 2001.

[113] I. W. Martin. *Studies of materials for use in future interferometric gravitational wave detectors*. PhD thesis, University of Glasgow, 2009.

[114] S. Reid. *Studies of materials for future ground-based and space-based interferometric gravitational wave detectors*. PhD thesis, University of Glasgow, 2006.

[115] I. W. Martin, H. Armandula, C. Comtet, M. M. Fejer, et al. *Measurements of a low-temperature mechanical dissipation peak in a single layer of Ta 2 O 5 doped with TiO 2. Classical and Quantum Gravity*, 25(5):055005, 2008.

[116] I. W. Martin, R. Nawrodt, K. Craig, C. Schwarz, et al. *Low temperature mechanical dissipation of an ion-beam sputtered silica film. Classical and Quantum Gravity*, 31(3):035019, 2014.

[117] N. W. McLachlan. *Theory of Vibrations*. Dover, 1952.

[118] D. R. M. Crooks. *Mechanical loss and its significance in the test mass mirrors of gravitational wave detectors*. PhD thesis, University of Glasgow, 2002.

[119] F. R. Blom, S. Bouwstra, M. Elwenspoek, and J. H. J. Fluitman. *Dependence of the quality factor of micromachined silicon beam resonators on pressure and geometry. J. Vac. Sci. Technol. B*, 10(1), 1991.

[120] $http://www.struers.com/default.asp?doc\_id = 364$.

[121] https://shop.buehler.com/consumables/grinding-polishing/polishing-suspensions/alumina-suspensions.

[122] http://www.lakeshore.com/products/cryogenic-temperature-sensors/silicon-diodes/dt-670/pages/specifications.aspx. April 2015.

[123] V. B. Braginsky, V. P. Mitrofanov, and V. I. Panov. *Systems with small dissipation*. University of Chicago Press, Chicago, 1985.

[124] A. Ageev, B. C. Palmer, A. Felice, and S. D. Penn. *Very high quality factor measured in annealed fused silica. Classical and Quantum Gravity*, 21(16):3887, 2004.

[125] T.J. Quinn, C.C. Speake, R.S. Davis, and W. Tew. *Stress-dependent damping in CuBe torsion and flexure suspensions at stresses up to 1.1 {GPa}. Physics Letters A*, 197(3):197 – 208, 1995.

[126] O. L. Anderson and H. E. Bommel. *Ultrasonic absorption in fused silica at low temperatures and high frequencies. Journal of the American Ceramic Society*, 38:125–131, 1955.

[127] R. E. Strakna. *Investigation of low temperature ultrasonic absorption in fast-neutron irradiated SiO2 glass. Physical Review*, 123:2020–2026, 1961.

[128] D.F. McGuigan, C.C. Lam, R.Q. Gram, A.W. Hoffman, et al. *Measurements of the mechanical Q of single-crystal silicon at low temperatures. Journal of Low Temperature Physics*, 30(5-6):621–629, 1978.

[129] R. Nawrodt, C. Schwarz, S. Kroker, I. W. Martin, R. Bassiri, F. Brückner, L. Cunningham, G. D. Hammond, D. Heinert, J. Hough, T. Käsebier, E.-B. Kley, R. Neubert, S. Reid, S. Rowan, P. Seidel, and A. Tünnermann. *Investigation of mechanical losses of thin silicon flexures at low temperatures. Classical and Quantum Gravity*, 30(11):115008, 2013.

[130] M. Granata. Private communication, 2013.

[131] K. Numata, G. Bertolotto Bianc, N. Ohishi, A. Sekiya, S. Otsuka, K. Kawabe, M. Ando, and K. Tsubono. *Measurement of the intrinsic mechanical loss of low-loss samples using a nodal support. Physics Letters A*, 276(1–4):37, 2000.

[132] K. Yamamoto, S. Miyoki, T. Uchiyama, H. Ishitsuka, et al. *Measurement of the mechanical loss of a cooled reflective coating for gravitational wave detection. Phys. Rev. D*, 74:022002, 2006.

[133] R. Bassiri, K.B. Borisenko, D.J.H. Cockayne, J. Hough, I. MacLaren, and S. Rowan. *Probing the atomic structure of amorphous Ta2O5 coatings. Applied Physics Letters*, 98(3):–, 2011.

[134] R. Bassiri, K. Evans, K.B. Borisenko, M. M. Fejer, J. Hough, I. MacLaren, I. W. Martin, R. K. Route, and S. Rowan. *Correlations between the mechanical loss and atomic structure of amorphous TiO2-doped Ta2O5 coatings. Acta Materialia*, 61(4):1070 – 1077, 2013.

[135] R. Bassiri, F. Liou, M. R. Abernathy, A. C. Lin, N. Kim, A. Mehta, B. Shyam, R. L. Byer, E. K. Gustafson, M. Hart, I. MacLaren, I. W. Martin, R. K. Route, S. Rowan, J. F. Stebbins, and M. M. Fejer. *Order within disorder: The atomic structure of ion-beam sputtered amorphous tantala (a-Ta2O5). APL Materials*, 3(3):–, 2015.

[136] Industrial Physics Division, Commonwealth Scientific and Industrial Research Organisation, West Lindfield, NSW, Australia.

[137] M. R. Abernathy. *Mechanical properties of coating materials for use in the mirrors of interferometric gravitational wave detectors.* PhD thesis, University of Glasgow, 2012.

[138] M. Goldstein. *Amorphous Materials.* Wiley, New York, 1970.

[139] M. R. Vukcevich. *A new interpretation of the anomalous properties of vitreous silica. Journal of Non-Crystalline Solids*, 11:25–63, 1972.

[140] J. Y. Duquesne and G. Bellessa. *Internal-friction peak in amorhpous selenium at low temperature. Journal of Physics C: Solid State Physics*, pages L215–L219, 1980.

[141] K. S. Gilroy and W. A. Phillips. *Philos. Mag. B*, **43**:735–746, 1981.

[142] K. A. Topp and D. G. Cahill. *Elastic properties of several amorphous solids and disordered crystals below 100 K. Z. Phys. B: Condens. Matter*, 101:235–245, 2004.

[143] J. E. V. Cleve, A. K. Raychaudhuri, and R. O. Pohl. *Glasslike elastic properties in the alloys. Zeitschrift fur Physik B*, 93:479–490, 1994.

[144] J. P. Trinastic, R. Hamdan, Y. Wu, L. Zhang, and Hai-Ping Cheng. *Unified interatomic potential and energy barrier distributions for amorphous oxides. The Journal of Chemical Physics*, 139(15):–, 2013.

[145] W.A. Phillips. *Tunneling states in amorphous solids. Journal of Low Temperature Physics*, 7(3-4):351–360, 1972.

[146] A. Nittke, M. Scherl, P. Esquinazi, W. Lorenz, Junyun Li, and F. Pobell. *Low temperature heat release, sound velocity and attenuation, specific heat and thermal conductivity in polymers. Journal of Low Temperature Physics*, 98(5-6):517–547, 1995.

[147] O. L. Krivanek, T. C. Lovejoy, N. Dellby, T. Aoki, R. W. Carpenter, P. Rez, E. Soignard, J. Zhu, P. E. Batson, M. J. Lagos, R. F. Egerton, and P. A. Crozier. *Vibrational spectroscopy in the electron microscope. Nature*, 514(7521):209, 10 2014.

[148] S. D. Penn, P. H. Sneddon, H. Armandula, J. C. Betzwieser, G. Cagnoli, J. Camp, D. R. M. Crooks, M. M. Fejer, A. M. Gretarsson, G. M. Harry, J. Hough, S. E. Kittelberger, M. J. Mortonson, R. K. Route, S. Rowan, and C. C. Vassiliou. *Mechanical loss in tantala/silica dielectric mirror coatings. Classical and Quantum Gravity*, 20(13):2917, 2003.

[149] M. R. Abernathy, G. M. Harry, F. Travasso, I. W. Martin, S. Reid, S. Rowan, J. Hough, M. M. Fejer, R. K. Route, S. D. Penn, H. Armandula, and A. Gretarsson. *The effects of heating on mechanical loss in tantala/silica optical coatings. Physics Letters A*, 372(2):87 – 90, 2008.

[150] A. E. Villar, E. D. Black, R. DeSalvo, K. G. Libbrecht, C. Michel, N. Morgado, L. Pinard, I. M. Pinto, V. Pierro, V. Galdi, M. Principe, and I. Taurasi. *Measurement of thermal noise in multilayer coatings with optimized layer thickness. Phys. Rev. D*, 81:122001, Jun 2010.

[151] D. R. M. Crooks, G. Cagnoli, M. M. Fejer, A. Gretarsson, G. Harry, J. Hough, N. Nakagawa, S. Penn, R. K. Route, S. Rowan, and P. H. Sneddon. *Experimental measurements of coating mechanical loss factors. Classical and Quantum Gravity*, 21(5):S1059, 2004.

[152] D. R. M. Crooks, G. Cagnoli, M. M. Fejer, G. Harry, J. Hough, B. T. Khuri-Yakub, S. Penn, R. K. Route, S. Rowan, P. H. Sneddon, I. O. Wygant, and G. G. Yaralioglu. *Experimental measurements of mechanical dissipation associated with dielectric coatings formed using SiO 2 , Ta 2 O 5 and Al 2 O 3. Classical and Quantum Gravity*, 23(15):4953, 2006.

[153] Laboratoire des Materiaux Avances. 7, Avenue Pierre de Coubertin, 69622 VILLEURBANNE Cedex.

[154] R. Flaminio. Development of the coatings for the advanced ligo and advanced virgo mirrors. Amaldi10, Warsaw, Poland, July 2013.

[155] D. G. Blair and J. Ferreirinho. *Thermoelastic Effect in Niobium at the Superconducting Transition. Phys. Rev. Lett.*, 49(6), 1982.

[156] Y. S. Touloukian and E. H. Buyco. *Thermo-physical Properties of Matter.* Plenum, New York, 1970.

[157] E. Hirose, K. Craig, H. Ishitsuka, I. W. Martin, N. Mio, S. Moriwaki, P. G. Murray, M. Ohashi, S. Rowan, Y. Sakakibara, T. Suzuki, K. Waseda, K. Watanabe, and K. Yamamoto. *Mechanical loss of a multilayer tantala/silica coating on a sapphire disk at cryogenic temperatures: Toward the KAGRA gravitational wave detector. Phys. Rev. D*, 90:102004, Nov 2014.

[158] LIGO Scientific Collaboration. *Advanced LIGO Reference Design. LIGO DCC document number M060056.*

[159] S. V. Ushakov, A. Navrotsky, Y. Yang, S. Stemmer, et al. *Crystallization in hafnia- and zirconia-based systems. physica status solidi (b)*, 241(10):2268–2278, 2004.

[160] R. Bassiri. *The atomic structure and properties of mirror coatings for use in gravitational wave detectors.* PhD thesis, University of Glasgow, 2012.

[161] S. L. Dole, O. Hunter Jr., and C. J. Wooge. *Elastic properties of monoclinic hafnium oxide at room temperature. Journal of the American Ceramic Society*, 60(11-12):488, 1977.

[162] K. Tapily, J. E. Jakes, D. Gu, H. Baumgart, and A. A. Elmustafa. *Nanomechanical study of amorphous and polycrystalline ALD HfO2 thin films. Int. J. of Surface Science and Engineering*, 5(2/3):193–204, 2011.

[163] R. Thielsch, A. Gatto, and N. Kaiser. *Mechanical Stress and Thermal-Elastic Properties of Oxide Coatings for Use in the Deep-Ultraviolet Spectral Region. Appl. Opt.*, 41(16):3211, Jun 2002.

[164] S Musikant. *Optical Materials: An Introduction to Selection and Application.* Dekker, New York, 1985.

[165] A. Alexandrovski, M. M. Fejer, A. Markosian, and R. Route. Photothermal common-path interferometry (pci): new developments, 2009.

[166] A. C. Lin, R. Bassiri, K. Craig, A. V. Cumming, M. M. Fejer, J. S. Harris, K. A. Haughian, J. Hough, A. S. Markosyan, I. W. Martin, S. Reid, R. K. Route, and S. Rowan. *Epitaxial integration of monocrystalline III-V coatings on silicon for thermal noise reduction.* In *Optical Interference Coatings*, page MA.2. Optical Society of America, 2013.

[167] G. D. Cole, S. Groblacher, K. Gugler, S. Gigan, and M. Aspelmeyer. *Monocrystalline AlGaAs heterostructures for high-reflectivity high-Q micromechanical resonators in the megahertz regime. Applied Physics Letters*, 92(261108), 2008.

[168] G. D. Cole. *Cavity optomechanics with low-noise crystalline mirrors. Proc. SPIE*, 8458:845807–845807–11, 2012.

[169] G. D. Cole and M. Aspelmeyer. *Substrate transferred monocrystalline Bragg mirrors. European Patent no. EP2607935*, 2014.

[170] *http* : *//www.crystallinemirrors.com/*.

[171] A. C. Lin and J. S. Harris. *Two-dimensional III-V nucleation on Si for nonlinear optics. J. Vac. Sci. Technol. B*, 28(3)(03C120), 2011.

[172] *www.sios.de/englisch/produkte/sp*1*_e.htm*.

[173] W. F. Boyle and R. J. Sladek. *Elastic constants and lattice anharmonicity of GaSb and GaP from ultrasonic-velocity measurements between 4.2 and 300 K. Phys. Rev. B*, 11:2933–40, 1975.

[174] M. Levinshtein and M. Shur. *Ternary and Quaternary A3B5 Semiconductors*, volume vol 2. Singapore: World Scientific, 1995.

[175] C.-H. Cho. *Characterization of Young's modulus of silicon versus temperature using a "beam deflection" method with a four-point bending fixture. Current Applied Physics*, 9(2):538 – 545, 2009.

[176] T. Hong, H. Yang, E. K. Gustafson, R. Adhikari, and Y. Chen. *Brownian thermal noise in multilayer coated mirrors. Phys. Rev. D*, 87:082001, Apr 2013.

[177] A. V. Cumming, K. Craig, I. W. Martin, R. Bassiri, L. Cunningham, M. M. Fejer, J. S. Harris, K. A. Haughian, D. Heinert, B. Lantz, A. C. Lin, A. S. Markosyan, R. Nawrodt, R. K. Route, and S. Rowan. *Measurement of the mechanical loss of prototype GaP/AlGaP crystalline coatings for future gravitational wave detectors. Classical and Quantum Gravity*, 32(3):035002, 2015.

[178] O. S. Heavens. *Thin Film Physics*. London: Methuen and Co. Ltd, 1970.

[179] P. D. Vu, Xiao Liu, and R. O. Pohl. Phonon scattering and internal friction in dielectric and metallic films at low temperatures. *Phys. Rev. B*, 63:125421, Mar 2001.

[180] G. M. Harry, T. P. Bodiya, and R. DeSalvo, editors. *Optical Coatings and Thermal Noise in Precision Measurement*. Cambridge University Press, Cambridge, 1 edition, 2012.

[181] S. Rowan, S.M. Twyford, J. Hough, D.-H. Gwo, and R. K. Route. *Mechanical losses associated with the technique of hydroxide-catalysis bonding of fused silica. Physics Letters A*, 246(6):471 – 478, 1998.

[182] A. V. Cumming, A. S. Bell, L. Barsotti, M. A. Barton, G. Cagnoli, D. Cook, L. Cunningham, M. Evans, G. D. Hammond, G. M. Harry, A. Heptonstall, J. Hough, R. Jones, R. Kumar, R. Mittleman, N. A. Robertson, S. Rowan, B. Shapiro, K. A. Strain, K. Tokmakov, C. Torrie, and A. A. van Veggel. *Design and development of the advanced LIGO monolithic fused silica suspension. Classical and Quantum Gravity*, 29(3):035003, 2012.

[183] N. L. Beveridge. *Characteristics of silicon-silicon hydroxide catalysis bonds for future gravitational wave detectors*. PhD thesis, University of Glasgow, 2012.